Raman Spectroscopic Studies of Carbon Nanotube Composite Fibres

A thesis submitted to The University of Manchester for the degree of Doctor of Philosophy in the Faculty of Engineering and Physical Sciences

2010

Libo Deng

School of Materials

Contents

Word count: 52, 006

Abstract

Raman Spectroscopic Studies of Carbon Nanotube Composite Fibres

The University of Manchester
Libo Deng
Doctor of Philosophy
11 November, 2010

The project has been concerned with structure/property relationships in a series of different carbon nanotube (CNT) composite fibres. Raman spectroscopy has been proved to be a powerful technique to characterise the CNT-containing fibres.

Electrospinning has been used to prepare poly(vinyl alcohol) (PVA) nanofibres containing single-wall carbon nanotubes (SWNTs). The effect of the processing conditions including the polymer concentration, electric voltage, tip-to-collector distance, nanotube concentration and the collection method upon the morphology, diameter and the alignment of the fibres have been investigated.

Raman spectroscopy of individual SWNTs dispersed in PVA electrospun fibres have been studied systematically in terms of the Raman band frequency, intensity and linewidth. The G'-band shift per unit strain during tensile deformation has been found to be dependent on the nanotube chirality.

A detailed study has been undertaken of the efficiency of reinforcement in PVA/SWNT nanocomposites. The stress-induced Raman band shifts in the nanocomposites have been shown to be controlled by both geometric factors such as the angles between the nanotube axis, the stressing direction and the direction of laser polarisation, and by finite length effects and bundling. A theory has been developed that takes into account all of these factors and enables the behavior of the different forms of nanocomposite, both fibres and films, to be compared.

The effects of dispersion and orientation of nanotubes and the interfacial adhesion on mechanical properties of poly(p-phenylene terephthalamide) (PPTA)/SWNTs composite fibres have been investigated. It has been shown the change of orientation of the polymer molecules upon incorporating nanotubes had direct effect on mechanical properties of the PPTA fibres. An in-situ Raman spectroscopy study during fibre deformation has revealed good stress transfer from the matrix to nanotubes in low strain range, and the interface failed when the strain exceeded 0.5%. Raman spectroscopy has also been employed to investigate the microstructure and micromechanical process of neat carbon nanotube (CNT) fibres. It has been found the fibres consisted of both SWNTs and MWNTs and varied in composition at different locations. High efficiency of stress transfer both within the fibre and in composites has been observed, suggesting the promising potential of CNT fibres in reinforcing polymers.

List of symbols

a_n	Proportion of fillers lying at different directions relative to the longitudinal direction of the composite
a_0	Length of the lattice vector
$\vec{a_1}$	The first lattice vector of a graphite sheet
$\vec{a_2}$	The second lattice vector of a graphite sheet
b	Average thickness of the nanotube-nucleated crystalline polymer
$\vec{C_h}$	Chiral vector defining the nanotube circumference
C_i	Diameter dependence of the G'-band frequency
d_t	Diameter of the nanotube
D	Bending deflection of the cantilever
E_a	Modulus of the amorphous polymer
E_c	Modulus of the composite
E_{ii}	Transition energy between the ith pair of van Hove singularities for nanotubes
E_{laser}	Laser excitation energy
E_{NT}	Modulus of the nanotube
F_{pull}	Force to pull out nanotubes from the matrix
E_χ	Modulus of the crystalline polymer
E_{11}^M	Energy transition between the first pair of van Hove singularities for metallic nanotubes
E_{22}^S	Energy transition between the second pair of van Hove singularities for semiconducting nanotubes
E_{33}^S	Energy transition between the third pair of van Hove singularities for semiconducting nanotubes
E_{44}^S	Energy transition between the fourth pair of van Hove singularities for semiconducting nanotubes
f	Herman's orientation factor
I	Raman intensity

I_{HH}	Raman band intensity obtained using an HH configuration
I_{HV}	Raman band intensity obtained using an HV configuration
I_p	Intensity of Raman peaks
I_{VH}	Raman band intensity obtained using a VH configuration
I_{VV}	Raman band intensity obtained using a VV configuration
K	Spring constant of the cantilever
l	Length of the nanotube
l_c	Critical length
l_{emb}	Length of the nanotube embedded in matrix
l_f	Length of the fibre
l_p	Length of the nanotube pulled out from the matrix
l_0	Initial length of the fibre
(n, m)	Indices defining the nanotube structure
P	Qualitative orientation factor of polymer molecules
r_t	Radius of the nanotube
R_i	Electrical resistance of the strain gauge during deformation
R_0	Initial electrical resistance of the strain gauge at 0% strain
s	Aspect ratio of the nanotube
S	Raman band shift rate
S_{hex}	Separation between nanotubes
S_0	Raman band shift rate for uniaxially-aligned fillers
$S(0)$	Raman band shift rate for the sample parallel to the strain direction
V_{NT}	Volume fraction of the nanotube
α	Angle between the nanotube axis and the fibre axis
β	Angle between the molecular axis and the fibre axis
Δ	Full width at half maximum of the orientation distribution function
ε	Strain
ε_m	Tensile strain of the matrix
Γ	Half width at half maximum of the Raman band

ϕ	Angle between the strain axis and the axis of laser polarisation
η_l	Length efficiency factor
η_o	Orientation efficiency factor
η_s	Strength efficiency factor
φ	Angle between the sample axis and the axis of laser polarisation
κ	Depolarisation ratio
λ	Wavelength
μ	Mean spacing between nanotubes
ν	Poisson's ratio
θ	Angle between the strain axis and nanotube axis
σ_c	Strength of the composite
σ_{eff}	Effective strength of the nanotube
σ_{NT}	Strength of the nanotube
σ_p	Strength of the polymer
τ	Interfacial shear stress
τ_i	Interfacial shear strength
τ_{ave}	Average interfacial shear stress
ω	Frequency of the Raman band
ω_G	Frequency of the G-band
ω_{G^+}	Frequency of the G$^+$ peak
ω_{G^-}	Frequency of the G$^-$ peak
$\omega_{G'}$	Frequency of the G'-band
ω_{RBM}	Frequency of the radial breathing mode
ω_0	Frequency of the G'-band of 2D graphite
ξ	Diameter dependence of the G-band frequency
Ψ	Angle between the filler axis and the longitudinal direction of the composite

List of abbreviations

AFM	Atomic force microscopy
BWF	Breti-Wigner-Fano
℃	Celsius degree
CCD	Charge coupled device
CNT	Carbon nanotube
cm^{-1}	Wavenumber
CVD	Chemical vapour deposition
DSC	Differential scanning calorimetry
DOS	Density of states
DR	Draw ratio
DWNT	Double-wall carbon nanotube
FWHM	Full width at half maximum
GPa	GigaPascal
h	Hour
HiPco	High-pressure decomposition of carbon oxide
IFSS	Interfacial shear strength
nm	Nanometre
NMP	N-methylpyrrolidone
min	Minute
MPa	MegaPascal
MWNT	Multi-wall carbon nanotube
Ref	Reference
s	second
μm	micrometre
PA6	Nylon-6
PAN	Polyacrylonitrile
PBO	Poly(p-phenylene benzobisoxazole)
PC	Polycarbonate

PDMS	Poly(dimethyl siloxane)
PEEK	Poly(ether ether ketone)
PEO	Poly(ethylene oxide)
PMMA	Poly(methyl methacrylate)
PP	Polypropylene
PPTA	Poly(p-phenylene terephthalamide)
PS	Polystyrene
PVA	Poly(vinyl alcohol)
RBM	Radial breathing mode
rpm	Revolutions per minute
SANS	Small angle neutron scattering
SDS	Sodium dodecyl sulfate
SEC	Size exclusion chromatography
SEM	Scanning electron microscope
SPM	Scanning probe microscopy
SWNT	Single-wall carbon nanotube
TB1	Tight-binding model including only the interactions with the nearest-neighbouring carbon atoms in the hexagonal lattice
TEM	Transmission electron microscopy
TPa	TeraPascal
vol%	Volume%
W	Watt
wt%	Weight%

Acknowledgements

Declaration

No portion of the work referred to in the thesis has been submitted in support of an application for another degree or qualification of this or any other university or other institute of learning.

Copyright Statement

Chapter 1   Raman spectroscopy of carbon nanotubes

1.1 Introduction

Two scientists were awarded the Nobel Prize in Physics for 2010, for their pioneering work regarding two-dimensional graphene, a one-atom thick planar sheet of sp^2-bonded carbon atoms. Rolling the two-dimensional graphene sheets into cylinders gives rise to a fascinating material, carbon nanotubes (CNTs), which has been attracting great research interest in the last two decades due to the impressive properties and wide range of potential applications. The applications in mechanical reinforcement and electronic device are particularly promising. The excellent mechanical properties of nanotubes are related to the strong sp^2 hybridized carbon-carbon bonds and the perfect hexagonal structure in the graphene sheet from which they are built up, while the unique electronic properties are due largely to the one-dimensional confinement of electronic and phonon states which results in van Hove singularities in density of states (DOS) of nanotubes [1].

Raman spectroscopy has become an important technique to characterise the electronic structure and to follow the deformation behaviour of CNTs. This technique can provide insight into the intrinsic properties and the interaction of nanotubes with the surrounding environment, as well as the mechanical reinforcing efficiency of nanotubes in composites.

This chapter aims to give a brief introduction to the structure, preparation and properties of carbon nanotubes, and to review the background and main properties of nanotube Raman bands, with an emphasis on the effect of environment on the Raman bands. More comprehensive reviews on physical properties and Raman spectroscopy of CNTs can be found in Refs. [1-3].

1.2 Structure and preparation of CNTs

CNTs are long cylinders of covalently-bonded carbon atoms. The carbon atoms are arranged on a hexagonal network and each of them has three neighbours with which they form strong sp^2 hybridized carbon-carbon bonds. There are basically two main

types of CNTs according to the numbers of graphene cylinder in their structure: single-wall carbon nanotubes (SWNTs) and multi-wall carbon nanotubes (MWNTs); double-wall carbon nanotubes (DWNTs) are a special case of MWNTs [3-5].

An SWNT can be considered as a seamless roll of a single graphene sheet. The nanotube is one atom in thickness, tens of atoms in circumference, and up to a few millimetres in length. The different ways of rolling graphene into tubes are described by the chirality as defined by the circumferential vector [3-5]:

$$\vec{C}_h = n\vec{a}_1 + m\vec{a}_2 \tag{1.1}$$

where n and m are the steps along the unit vectors of the two lattice vectors, respectively, as shown in Figure 1.1. MWNTs are made up of many coaxial SWNTs with an interlayer separation of 0.34 nm and each of the walls may possess different chiralities.
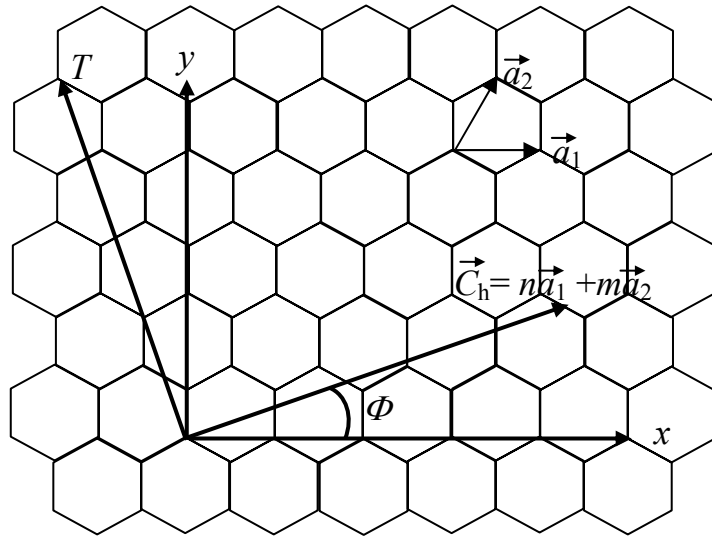
Figure 1.1 Schematic of a graphene sheet and the chiral vectors [4].

The diameter and chiral angle are two important parameters that define the nanotube structure, which can be derived from the chirality indices (n, m). The diameter d_t is given by [3, 4]:

$$d_t = a_0 \sqrt{\left(n^2 + mn + m^2\right)} / \pi \tag{1.2}$$

where a_0 is the length of lattice vector and has a value of 0.249 nm. The chiral angle Φ is defined as the angle between the chiral vector and the zigzag direction x (Figure

1.1). It varies in the range of 0 - 30° and is given by [3, 4]:

$$\Phi = \tan^{-1}\frac{\sqrt{3}n}{2m+n}$$ (1.3)

Three types of SWNT can be distinguished depending on their chiral angles: a) armchair nanotubes ($n = m$) which have a chiral angle of 30°, b) zigzag nanotubes ($m = 0$) with a chiral angle of 0°, and c) chiral nanotubes ($n \neq m \neq 0$) with the chiral angle ranging from 0° to 30° (Figure 1.2).
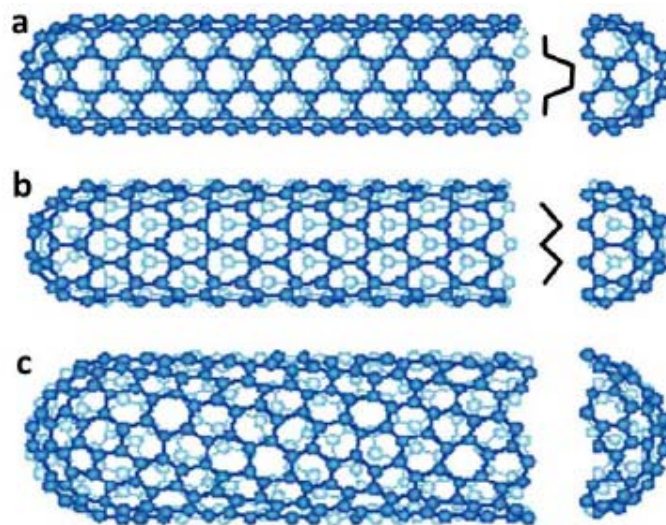
Figure 1.2 Three types of SWNT: (a) armchair, (b) zigzag, and (c) chiral nanotubes [6].

Three methods are employed widely to prepare nanotubes: arc-discharge, laser ablation, and chemical vapour deposition (CVD) [5]. The first two methods involve the condensation of hot gaseous carbon atoms generated from the evaporation of solid carbon, while in the CVD process, a gaseous carbon source is decomposed catalytically to form the nanotubes. CVD-grown nanotubes have fewer impurities but have more defects than the arc-grown nanotubes. The arc-grown CNTs are therefore mechanically stronger than the CVD-CNTs, but the latter will almost certainly find more applications. This is because the length and structure of the nanotubes are more controllable in a CVD process than in other methods, and this process is also more amenable to being scaled-up for industrial production [5].

1.3 Properties of CNTs

The high aspect ratio, strong sp^2 carbon-carbon bonds and the one-dimensional confinement of electronic states, confer CNTs with a range of interesting physical properties such as unique electronic properties, excellent mechanical properties, and good thermal conductivity and electrical conductivity.

SWNTs behave as either semiconductors or metals, which can be distinguished according to the remainder of (n - m) divided by 3: those with n - m = $3k$ are metallic nanotubes while those with n - m = $3k\pm1$ are semiconducting nanotubes (where k is integer) [4, 5]. Therefore, approximately one third of SWNTs are metallic and the rest are semiconducting. For semiconducting nanotubes, the band gap generally decreases as the diameter increases [4].

Deformation has a significant effect on the electronic structure of nanotubes. The effect of strain on the electronic structure depends on the deformation mode (i.e. uniaxial strain, torsional strain or radial deformation) and the nanotube chirality. For example, uniaxial strain can open the band gap of non-armchair metallic nanotubes but has no effect on armchair nanotubes; while torsional strain can change the electronic structure of armchair nanotubes but does not affect zigzag nanotubes [4].

Nanotubes and graphite share the same hexagonal network of sp^2 carbons in their structure. The mechanical properties of nanotubes are therefore expected to be comparable with those of graphite which has an in-plane Young's modulus of 1.06 TPa and a strength of 130 GPa [7, 8]. The first actual mechanical measurement on nanotubes was performed using transmission electron microscopy (TEM) in 1996 [9]. Since then, bending tests using an atomic force microscopy (AFM) tip have been developed and used widely [10]. A modulus for SWNTs of 1.0 TPa and 0.3 - 0.9 TPa for MWNTs, and a tensile strength of 50 - 150 GPa for SWNTs and 10 - 50 GPa for MWNTs are generally quoted by the scientific community. The actual values vary from nanotube to nanotube, cover a wide range, and depend on many factors such as the nanotube type, preparation method, purity and diameter.

Theoretical work has predicted a very high thermal conductivity for CNTs (of

approximately 6000 W m^{-1} K^{-1}), while experimental work has recorded a value of 3000 W m^{-1} K^{-1}. MWNTs have been found to also exhibit good electrical conductivity, which is in the range of 10^6 - 10^7 S/m (As a comparison, the copper has an electrical conductivity of 6×10^7 S/m) [11]. The physical properties of CNTs and a comparison with typical engineering materials are summarised in Table 1.1.

Table 1.1 Physical properties of CNTs and typical engineering materials [11].

Material	Mechanical properties		Thermal conductivity (W m^{-1} K^{-1})	Electrical conductivity (S/m)
	Modulus (GPa)	Strength (GPa)		
Carbon nanotubes	1000	30 - 100	200 – 3000 [12]	10^6 - 10^7 [13]
Carbon fibre (Pitch)	300 - 700	5 - 7	1000	2 - 8.5×10^6
Copper	110 - 128		400	6×10^7

1.4 Introduction to Raman spectroscopy

Raman spectroscopy is a powerful technique for studying the structural and dynamic information on the molecular level. This technique possesses many advantages in materials characterisation [14-16]. Firstly, a very small amount of sample and little or no sample-preparation is required for materials to be characterised by Raman spectroscopy. Secondly, the laser can be focused on a spot as small as 1 μm and so it is possible to study the local properties of a material. Most of all, as a probe it is non-destructive and is reliable in revealing the actual properties of the materials when subjected to external perturbation.

1.4.1 Principle of Raman scattering

When a light wave, which can be considered as a stream of photons, passes through a molecule, it can interact and distort the cloud of electrons round the nucleus [15]. This incident light can either be absorbed, which forms the basis of infrared

absorption spectroscopy, or be scattered either elastically (known as the Rayleigh scattering) or inelastically (Raman scattering). Rayleigh scattering is a process with no energy transfer between the incident photon and the molecule, the scattered light has therefore the same frequency as the incident light. About one in 10^3 incident photons is involved in this elastic scattering, and represents most of the observed scattering process [15]. Raman scattering, or the Raman effect, is a process in which the molecule either gains or emits energy upon interacting with the incident light, which gives rise to a change in the frequency of the incident light [15]. The incident photons can excite the molecule to either higher (Stokes Raman scattering) or to lower energy level (anti-Stokes Raman scattering), depending on whether the process starts with a molecule in the ground state or from a molecule in a vibrationally-excited state (Figure 1.3). For a Raman-active vibration, the change of polarisability with respect to the nuclear displacement is required. The Raman spectrum from a material is actually a record of the shift of light frequency relative to the excitation radiation, and reflects the vibrational modes of molecules.
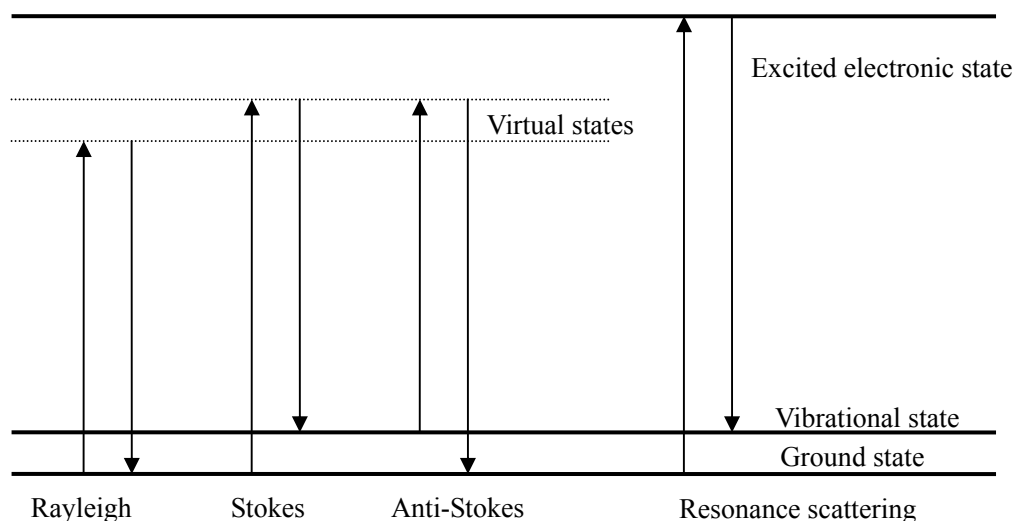
Figure 1.3 Schematic of Rayleigh, Stokes-Raman and anti-Stokes Raman and resonance Raman scattering [15].

1.4.2 Resonance Raman scattering

Resonance Raman scattering occurs when the energy of the excitation photon

matches the electronic transition energy of a molecule and the photon excites an electron to enter a real electronic state instead of virtual states. The resonance scattering process can enhance the intensity by up to 10^6 (normally of the order of 10^3) relative to the non-resonance scattering. In addition to the vibrational information one can learn from the normal Raman scattering, the electronic properties can also be probed using resonance Raman spectroscopy as the electronic transition is involved in this process. Table 1.2 summarises the main differences between the non-resonance and resonance Raman scattering processes. Resonance Raman spectroscopy is particularly useful in characterising SWNTs, as will be discussed in the following sections.

Table 1.2 The main differences between normal Raman scattering and resonance Raman scattering [15].

Normal Raman scattering	Resonance Raman scattering
No overtone	Overtone common
No electronic information	Electronic information present
More modes observed in the spectrum	Some modes selectively enhanced
Weak scattering	Stronger scattering

1.5 Raman spectroscopy of SWNTs

The Raman spectroscopy of SWNTs has become an important research topic since 1997 [17]. This technique is particularly useful for investigation of the properties of SWNTs due to the resonance effects and the discussion in the following section is confined to SWNTs (Raman spectroscopy of MWNTs is not discussed here).

A typical Raman spectrum of SWNTs is shown in Figure 1.4. Four characteristic Raman bands, namely the radial breathing modes (RBMs), G-band, D-band and G'-band (also called the 2D band) carry a large amount of structural information and have been studied in most detail, although several other weaker and broader features have also been observed in the nanotube spectra [4]. The main properties of these Raman bands are summarised as follows.
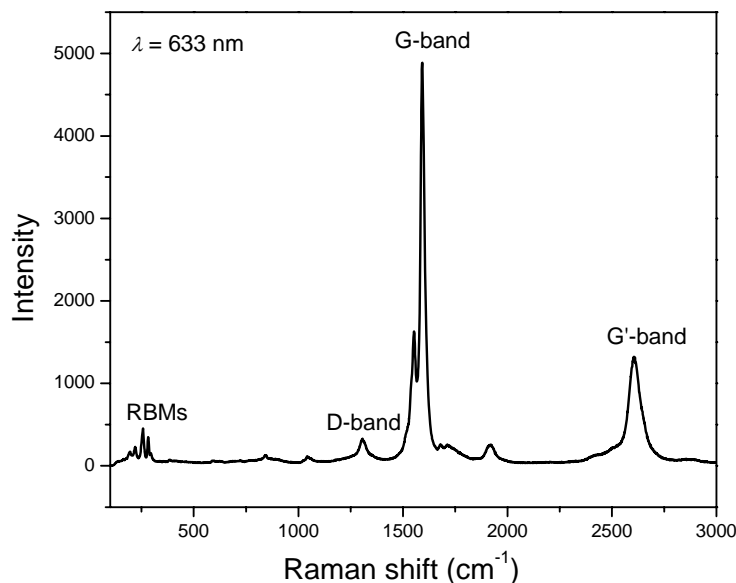
Figure 1.4 A typical Raman spectrum of SWNTs showing the four characteristic bands.

1.5.1 RBMs

The RBM features appear between 100 and 500 cm^{-1} and are vibrational modes in which all the carbon atoms move radially, perpendicular to the nanotube axis, as if the nanotube was breathing. The lineshape of the RBM peak for a single nanotube is a simple Lorentzian line and the natural linewidth is 3 cm^{-1}. The RBM peak is quite often broadened to exhibit a linewidth of 4 - 10 cm^{-1} due to the interaction of nanotubes with the environment [2].

The RBM frequency ω_{RBM} is independent of the chiral angle Φ but depends linearly on the reciprocal of nanotube diameter d_t through the relation [1, 2]:

$$\omega_{RBM} = \frac{A}{d_t} + B \qquad (1.4)$$

where the parameters A and B (B is associated with the effect of environment on the ω_{RBM}) are determined experimentally. Although the form of the relation is well established, a variety of values for the parameters A and B have been found by different groups with different samples. The interaction between the nanotubes and the surrounding environment leads to each sample having its own set of parameters to determine d_t from ω_{RBM}. Table 1.3 lists the typical values of the parameters for the ω_{RBM}/d_t relation reported in the literature.

Table 1.3 The A and B values for Equation (1.4) reported in the literature.

Sample	A (nm cm^{-1})	B (cm^{-1})	Reference
SWNTs on a silicon substrate	248	0	[18]
SDS-dispersed HiPco SWNTs	223.5	12.5	[19]
SDS-dispersed HiPco SWNTs	218	17	[20]
Alcohol-assisted CVD-SWNTs	217	15	[21]
Laser ablation bundled SWNTs	232	0	[22]

The most important information one can determine from the RBMs is the nanotube chirality, which is given by the (n, m) indices. The identification of the (n, m) indices is based on resonance theory which gives rise to the so-called Kataura plot which is a plot of the electronic transition energies (E_{ii}) versus nanotube diameter (or the ω_{RBM}) [23]. The diameter can be determined from ω_{RBM} using Equation (1.4). The transition energies for the Kataura plot can be determined using resonance Raman spectroscopy equipped with a tuneable laser (this method gives a precision of 3 meV for each E_{ii}), photoluminescence spectroscopy (with the precision of 20 - 30 meV) and theoretical approaches [19, 20].

The value of the transition energy is influenced by many factors such as whether the nanotubes are in bundles or isolated, whether they are wrapped by surfactants, the type of solvent in which nanotubes are dispersed, the type of substrate and the temperature. As for the influence of intertube interaction, the E_{ii} transition shifts to lower energies and RBM peaks shift to lower frequencies by 1 - 10 cm^{-1} when isolated individual nanotubes aggregate into bundles. Theoretical studies predicted that the value of E_{ii} can shift as much as 0.25 eV upon bundling [24] and O'Connell *et al.* determined experimentally an average value of 86 meV for the down-shift [25]. The down-shift of the E_{ii} may lead to the so-called "roping effect" on RBM peaks, that is, some RBMs that are seen in the isolated state disappear when in bundles (there is an opposite case: some RBMs that are absent for isolated nanotubes appear when they are in bundles) [26, 27]. Figure 1.5 illustrates the roping effect upon the RBMs for

two nanotubes: the (10, 2) and (11, 3) nanotubes that are off resonance and in resonance with a 785 nm laser, respectively, when isolated, are brought into and outside the resonance window ($E_{laser}\pm 0.1$ eV) when in bundles due to the changes of transition energies.
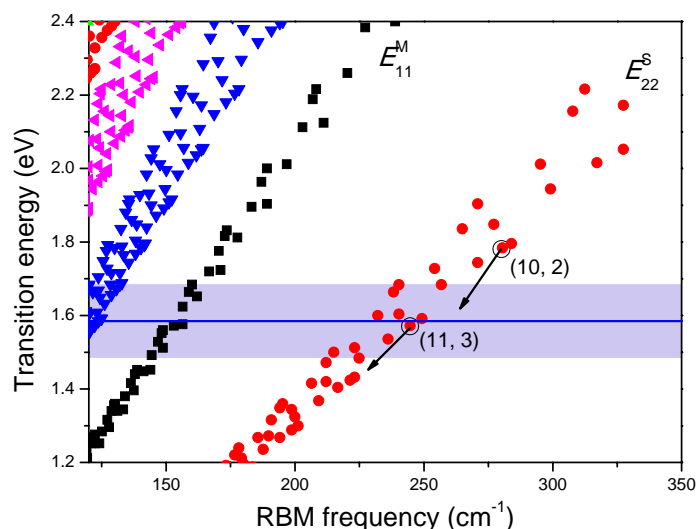
Figure 1.5 A theoretical Kataura plot for individual SWNTs. The blue box indicates a resonance window ($E_{laser}\pm 0.1$ eV) for an excitation laser with energy of 1.58 eV. The arrows indicate the down-shift of E_{22}^{S} for two individual nanotubes when they aggregate into bundles, showing the roping effect on the RBMs. All E_{ii} values were calculated using the nearest-tight binding (TB1) model [4].

The uncertainties in E_{ii} values and ω_{RBM}/d_t relation bring difficulty in identifying nanotube chirality. Additional information for identification of the nanotube chirality can be provided by deforming nanotubes which affects the electronic structure and consequently influence the Raman band intensity. Lucas and Young managed to assign a unique nanotube structure to each RBM separated by just 1 - 2 cm^{-1} by studying the effect of deformation upon the RBM intensity [4].

1.5.2 G-band

The G-band originates from the vibrations of neighbouring carbon atoms in opposite directions along the nanotube axis and its circumference and is observed in

the 1500 - 1605 cm^{-1} region for SWNTs. In most cases, the G-band can be fitted with the two most intense peaks labelled by G$^+$, for atomic vibration along the tube axis; and G$^-$, for modes with atomic vibration along the circumferential direction [2]. ω_{G^+} is independent of the diameter while ω_{G^-} decreases with decreasing diameter. The dependence of ω_G on nanotube diameter can be described as:

$$\omega_{G^-} = \omega_{G^+} - \xi / d_t^2 \tag{1.5}$$

where ξ has a value of 47.7 nm^2 cm^{-1} for semiconducting and 79.5 nm^2 cm^{-1} for metallic nanotubes, respectively [1]. This equation allows the determination of nanotube diameter when the RBM is absent, although the information is less accurate than direct RBM measurement.

The lineshape of the G$^-$ peak of semiconducting nanotubes is quite different from that of metallic nanotubes, which allows one to readily distinguish between semiconducting and metallic nanotubes [1]. For semiconducting nanotubes, both the G$^+$ and G$^-$ peaks are of a Lorentzian profile with linewidths of 6 - 15 cm^{-1}. While for metallic nanotubes, the G$^+$ peak has a Lorentzian lineshape similar to the semiconducting tubes, but the G$^-$ peak is a broad and asymmetry peak and is usually fitted using a Briet-Wigner-Fano (BWF) function [2]. The BWF broadening is related to free electrons in nanotubes with metallic character. There are, however, conflicting reports in the G$^-$ lineshape of metallic nanotubes. Paillet *et al.* demonstrated that the BWF line is an intrinsic feature of metallic nanotube bundles but the BWF component vanishes in isolated metallic nanotubes [28]. In contrast, Bose *et al.* predicted the BWF lineshape to be intrinsic in single metallic nanotubes [29].

Interactions between the nanotubes and the environment have a significant effect upon the G-band. Important environmental factors include the aggregation state (i.e. whether the nanotubes are isolated or in bundles), the charge transfer arising from doping a SWNT and the substrate of nanotubes. When the nanotubes are debundled with the assistance of dispersant, the dispersant molecules wrapping the nanotube can suppress the vibration in the circumferential direction, giving rise to weakening of the G$^-$ peak [30]. In addition, the G$^+$ linewidth decreases significantly when nanotube

bundles are well separated. As for the influence of charge transfer, removing charge from a SWNT (i.e. p-doping) leads to an up-shift of the G^+ peak around 1592 cm^{-1}, while adding charge (i.e. n-doping) to a SWNT results in a down-shift [31].

1.5.3 D-band and G'-band

The D-band and its second order overtone G'-band (also called the 2D band) are observed in the 1250 - 1450 cm^{-1} and 2500 - 2900 cm^{-1} regions, respectively. The D-band scattering involves one-phonon emission while the G'-band scattering involves emission of two phonons. The causes of these two bands both involve a double resonance Raman process as shown in Figure 1.6. The D-band scattering consists of one-elastic and one-inelastic scattering process, in which the elastic scattering arises from defects (such as vacancies, impurities and hetero-atoms) in the crystal. On the other hand, the G'-band is due to two-inelastic scattering process, in which the two emitted phonons possess vectors of $+q$ and $-q$, respectively. The momentum constant is therefore automatically preserved in the G'-band scattering and no defect is required to observe the G'-band.
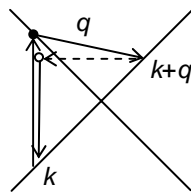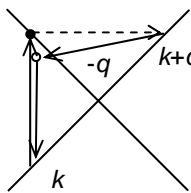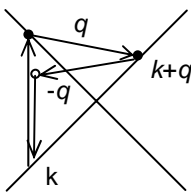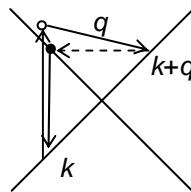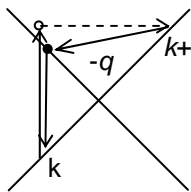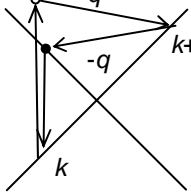
Figure 1.6 Second-order resonance Raman spectral processes for the D-band and G'-band. The dashed lines indicate elastic scattering. Resonance points are shown as solid circles [1].

27

The D- and G'- bands are known as dispersive bands because they change their frequencies when the laser excitation energy changes. For example, a function $\omega_{G'}=2420+106E_{laser}$ has been found for the dependence of G'-band position on E_{laser} [2]. The dependence of the ω_D and $\omega_{G'}$ on E_{laser} is associated with the dependence of phonon energy on E_{laser}.

Both the ω_D and $\omega_{G'}$ are found to depend also on both the nanotube diameter d_t and the chiral angle Φ, a property unique to nanotubes. The diameter dependence is a more complex issue. When considering the $\omega_{G'}/d_t$ dependence in a broad range of d_t where different E_{ii} interband transitions are involved in resonance, the value of the $\omega_{G'}$ decreases as the d_t decreases and follows the relation: $\omega_{G'}= 2708.1-35.4/d_t$. On the other hand, when analysing the $\omega_{G'}$ data within the same interband transition where the d_t varies over a small range, $\omega_{G'}$ decreases with increasing d_t through the dependence: $\omega_{G'}= \omega_0+C_i/d_t$, where the parameter C_i has a value of 34 nm cm^{-1} for E_{33}^S and 182 nm cm^{-1} for E_{44}^S [32].

In most cases, the G'-band shows a single Lorentzian peak, but double-peak G'-bands have also been observed from individual SWNTs. The double-peak structure of the G'-band is observed when two independent double resonance processes are involved. Specifically, for semiconducting SWNTs this occurs when one level of the E_{ii} transition is in resonance with the incident laser while a lower level of interband transition is in resonance with the scattered photon. While for metallic SWNTs, each E_{ii} transition is split into an upper and lower subbands, and both the upper and lower subbands can be involved simultaneously in the two independent resonance processes [33, 34]. There are 16 (n, m) nanotubes that exhibits a double-peak G'-band when excited with a 514 nm laser.

For individual SWNTs, the linewidth ranges from 7 to 40 cm^{-1} for the D-band and from 11 to 56 cm^{-1} for the G'-band [35]. The G'-band linewidth is a measure of the aggregation state as its value decreases with the decrease of bundle size [36]. The G'-band frequency is sensitive to stress and is usually employed to follow the deformation of nanotubes. The effect of both the aggregation state and deformation on

the nanotube Raman bands are important topics in this study and will be discussed in Chapter 4.

1.6 References

1. M. S. Dresselhaus, G. Dresselhaus, R. Saito, and A. Jorio, *Raman spectroscopy of carbon nanotubes,* Phys. Rep., 2005, **409**, 47-99.

2. M. S. Dresselhaus, G. Dresselhaus, A. Jorio, A. G. Souza, and R. Saito, *Raman spectroscopy on isolated single wall carbon nanotubes,* Carbon, 2002, **40**, 2043-2061.

3. R. Satio, G. Dresselhaus, and M. S. Dresselhaus, *Physical properties of carbon nanotubes*, London: Imperial College Press. 1998.

4. M. Lucas, *Effect of deformation upon the intensity of the Raman radial breathing modes of single-wall carbon nanotubes in epoxy/SWNT composites,* PhD Thesis, University of Manchester, 2005.

5. M. Moniruzzaman and K. I. Winey, *Polymer nanocomposites containing carbon nanotubes,* Macromolecules, 2006, **39**, 5194-5205.

6. P. J. F. Harris, *Carbon nanotube composites,* Int. Mater. Rev., 2004, **49**, 31-43.

7. J. N. Coleman, U. Khan, W. J. Blau, and Y. K. Gun'Ko, *Small but strong: A review of the mechanical properties of carbon nanotube–polymer composites,* Carbon, 2006, **44**, 1624-1652.

8. J. N. Coleman, U. Khan, and Y. K. Gun'Ko, *Mechanical reinforcement of polymers using carbon nanotubes,* Adv. Mater., 2006, **18**, 689-706.

9. M. M. Treacy, T. W. Ebbesen, and T. M. Gibson, *Exceptionally high Young's modulus observed for individual carbon nanotubes,* Nature, 1996, **381**, 680-687.

10. E. W. Wong, P. E. Sheehan, and C. M. Lieber, *Nanobeam mechanics: Elasticity, strength, and toughness of nanorods and nanotubes,* Science, 1997, **277**, 1971-1975.

11. Z. Wang, *Reinforcing efficiency of carbon nanotubes in Poly(vinyl alcohol) composites,* PhD thesis, Queen Mary, University of London, 2007.

12. P. Kim, L. Shi, A. Majumdar, and P. L. McEuen, *Thermal transport measurements of individual multiwalled nanotubes,* Phys. Rev. Lett., 2001, **87**,

215502 1-4.

13.   http://www.nanocyl.com/en/CNT-Expertise-Centre/Carbon-Nanotubes, 2010.

14. C. A. Cooper, *Structure/property relationships in particulate composites,* PhD Thesis, University of Manchester, 2000.

15. E. Smith and G. Dent, *Modern Raman spectroscopy-A practical approach*, Chichester: John Wiely & Sons, Ltd, 2005.

16. W. Y. Yeh, *Structure-property Relationship in engineering polymer fibres,* PhD Thesis, University of Manchester, 1995.

17. A. M. Rao, R. Richter, S. Bandow, B. Chase, P. C. Eklund, K. A. Williams, S. Fang, K. R. Subbaswamy, M. Menon, A. Thess, R. E. Smalley, G. Dresselhaus, and M. S. Dresselhaus, *Diameter-selective Raman scattering from vibrational modes in carbon nanotubes,* Science, 1997, **275**, 187-191.

18. A. Jorio, R. Saito, J. H. Hafner, C. M. Lieber, M. Hunter, T. McClure, G. Dresselhaus, and M. S. Dresselhaus, *Structural (n, m) determination of isolated single-wall carbon nanotubes by resonant Raman scattering,* Phys. Rev. Lett., 2001, **86**, 1118-1121.

19. S. M. Bachilo, M. S. Strano, C. Kittrell, R. H. Hauge, R. E. Smalley, and R. B. Weisman, *Structure-assigned optical spectra of single-walled carbon nanotubes,* Science, 2002, **298**, 2361-2366.

20. C. Fantini, A. Jorio, M. Souza, M. S. Strano, M. S. Dresselhaus, and M. A. Pimenta, *Optical transition energies for carbon nanotubes from resonant Raman spectroscopy: Environment and temperature effects,* Phys. Rev. Lett., 2004, **93**, 147406 1-4.

21. P. T. Araujo, S. K. Doorn, S. Kilina, S. Tretiak, E. Einarsson, S. Maruyama, H. Chacham, M. A. Pimenta, and A. Jorio, *Third and fourth optical transitions in semiconducting carbon nanotubes,* Phys. Rev. Lett., 2007, **98**, 067401 1-4.

22. M. Milnera, J. Kurti, M. Hulman, and H. Kuzmany, *Periodic resonance excitation and intertube interaction from quasicontinuous distributed helicities in single-wall carbon nanotubes,* Phys. Rev. Lett., 2000, **84**, 1324-1327.

23. H. Kataura, Y. Kumazawa, Y. Maniwa, I. Umezu, S. Suzuki, Y. Ohtsuka, and Y.

Achiba, *Optical properties of single-wall carbon nanotubes,* Synthetic Met., 1999, **103**, 2555-2558.

24. S. Reich, C. Thomsen, and P. Ordejon, *Electronic band structure of isolated and bundled carbon nanotubes,* Phys. Rev. B, 2002, **65**, 155411 1-11.

25. M. J. O'Connell, S. Sivaram, and S. K. Doorn, *Near-infrared resonance Raman excitation profile studies of single-walled carbon nanotube intertube interactions: A direct comparison of bundled and individually dispersed HiPco nanotubes,* Phys. Rev. B, 2004, **69**, 235415 1-15.

26. S. K. Doorn, M. S. Strano, E. H. Haroz, K. L. Rialon, R. H. Hauge, and R. E. Smalley, *Capillary electrophoresis separations of bundled and individual carbon nanotubes,* J. Phys. Chem. B, 2003, **107**, 6063-6069.

27. D. A. Heller, P. W. Barone, J. P. Swanson, R. M. Mayrhofer, and M. S. Strano, *Using Raman spectroscopy to elucidate the aggregation state of single-walled carbon nanotubes,* J. Phys. Chem. B, 2005, **108**, 6905-6909.

28. M. Paillet, P. Poncharal, A. Zahab, and J. L. Sauvajol, *Vanishing of the breit-wigner-fano component in individual single-wall carbon nanotubes,* Phys. Rev. Lett., 2005, **94**, 237401 1-4.

29. S. M. Bose, S. Gayen, and S. N. Behera, *Theory of the tangential G-band feature in the Raman spectra of metallic carbon nanotubes,* Phys. Rev. B, 2005, **72**, 153402 1-4.

30. H. Kawamoto, H. Uchida, T. Kojima, and M. Tachibana, *G band Raman features of DNA-wrapped single-wall carbon nanotubes in aqueous solution and air,* Chem. Phys. Lett., 2006, **432**, 172-176.

31. K. E. Wise, C. Park, E. J. Siochi, and J. S. Harrison, *Stable dispersion of single wall carbon nanotubes in polyimide: the role of noncovalent interactions,* Chem. Phys. Lett., 2004, **391**, 207-211.

32. A. G. S. Filho, A. Jorio, G. Samsonidze, G. Dresselhaus, M. A. Pimenta, M. S. Dresselhaus, A. K. Swan, M. Ünlü, B. B. Goldberg, and R. Saito, *Competing spring constant versus double resonance effects on the properties of dispersive modes in isolated single-wall carbon nanotubes,* Phys. Rev. B, 2003, **67**, 035427 1-7.

33. A. G. S. Filho, A. Jorio, M. S. Dresselhaus, J. H. Hafner, C. M. Lieber, and M. A. Pimenta, *Probing the electronic trigonal warping effect in individual single-wall carbon nanotubes using phonon spectra,* Chem. Phys. Lett., 2002, **354**, 62-68.

34. A. G. S. Filho, A. Jorio, A. K.Swan, M. S.Ünlü, B. B.Goldberg, R. Saito, J. H. Hafner, C. M. Lieber, M. A. Pimenta, G. Dresselhaus, and M. S. Dresselhaus, *Anomalous two-peak G′-band Raman effect in one isolated single-wall carbon nanotube,* Phys. Rev. B, 2002, **65**, 085417 1-6.

35. A. Jorio, C. Fantini, M. S. S. Dantas, M. A. Pimenta, M. S. Dresselhaus, A. K. Swan, and R. Saito, *Linewidth of the Raman features of individual single-wall carbon nanotubes,* Phys. Rev. B, 2002, **66**, 115411 1-8.

36. J. Cardenas, F. Juan, and A. Gromov, *The effect of bundling on the G' Raman band of single-walled carbon nanotubes,* Nanotechnology, 2009, **20**, 465703 1-8.

Chapter 2   Carbon nanotube composites

2.1 Introduction

One of the best ways to fulfil the enormous potential of carbon nanotubes (CNTs) is to incorporate them into polymers. It has been demonstrated that CNTs can improve the mechanical properties, electrical conductivity, thermal conductivity, thermal stability and fire-retardant ability of polymers significantly [1]. There has been impressive progress and interest is still growing in this area since the first polymer/CNT composite was prepared by Ajayan *et al.* in 1994 (their initial purpose, though, was not to make a composite but to prepare a TEM sample) [2].

Mechanical reinforcement on polymers is probably one of the most promising applications of nanotubes and is of particular interest in this study. In fact, CNTs have shown reinforcement in Young's modulus, tensile strength and toughness for a variety of polymers and the amount of nanotubes required to achieve significant improvement is much lower than the conventional fillers such as high performance fibres and clay. The extraordinary mechanical properties, high specific surface area, and high aspect ratio make nanotubes ideal candidates for polymer reinforcement [3-5].

This chapter reviews the preparation method, mechanical properties, the factors that determine the mechanical properties of polymer/CNT composites and the techniques to characterise these factors. The preparation and properties of polymer/CNT bulk composites and composite fibres are considered separately. While there are numerous articles dealing with mechanical reinforcement of polymers by nanotubes, only a few typical examples are summarised.

2.2 Preparation and properties of bulk composites

Most studies on CNT composites have been carried out with bulk composites due to their ease of preparation. The basic methods to produce CNT composites are solution processing and melt processing, and other methods have been developed, by firstly dispersing and integrating nanotubes with polymers and then by using solution or melt processing to prepare the final composites.

Solution processing is probably the most common method for the preparation of polymer/CNT composites. In a typical process [1, 3, 6], the nanotubes are firstly dispersed in a solvent, the nanotube dispersion is then mixed with the polymer solution by energetic agitation and finally the composite is obtained by either controlled evaporation or coagulation. Any polymers that are soluble can be processed using this method in theory and small quantity of nanotubes leads to significant improvement in mechanical properties of the polymer in most cases. For example, Ryan *et al.* incorporated different types of nanotubes into a poly(vinyl alcohol) (PVA) matrix and prepared thin films by solution processing. They observed a three-fold increase in Young's modulus and two-fold increase in tensile strength for the composites containing only 0.1% of Elicarb SWNTs [7]. The exceptionally-high efficiency of reinforcement is thought to be related to crystallisation of the polymers nucleated by the nanotubes. Zhang *et al*. also observed a 60% increase in Young's modulus and a 200% increase in tensile strength of the PVA by adding 5% of HiPco SWNTs [8]. Figure 2.1 shows typical stress-strain curves of the neat PVA and PVA/SWNT composite films.
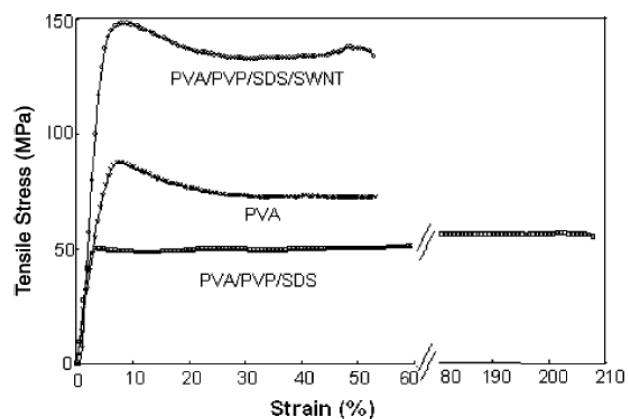
Figure 2.1 Typical stress-strain curves of PVA and PVA/SWNT films [8].

Melt processing is a common alternative to prepare polymer nanocomposites for polymers that are insoluble in a solvent but melt when heated and it is most suitable for industrial production [6]. This method includes three steps [1, 3, 6]: the polymers are firstly melted to form a viscous liquid, nanotubes are then added into the melt and

dispersed by a high shear force and finally composites are obtained by compression moulding or extrusion. Good mechanical reinforcing efficiency has been observed in a range of composites that are fabricated using this technique. Liu *et al.* prepared a nylon-6 (PA6)/MWNTs composite and found that the elastic modulus and yield strength were improved by 214% and 162%, respectively, for composites containing 2% of MWNTs [9]. The significant reinforcement was explained as a consequence of strong interfacial adhesion in the composite. Díez-Pascual *et al.* produced a poly(ether ether ketone) (PEEK)/SWNT composite using a similar method and observed a 27% increase in storage modulus at 1% loading of arc-SWNTs [10]. Nanotubes have also been incorporated into other polymers such as polypropylene (PP), poly(methyl methacrylate) (PMMA), polycarbonate (PC) and polystyrene (PS) using this process.

Other methods such as in-situ polymerization and solid-state pulverization have also been employed to prepare CNT composites. In an in-situ polymerization process, polymerization of the monomers occur on the nanotube surface such that the polymers are grafted onto the nanotubes, the polymer-modified nanotubes are then processed by solution or melt processing. The main advantage of this method is that it provides a better dispersion of nanotube and stronger interface between the nanotubes and the polymer matrix. Velasco-Santos *et al.* introduced chemically-functionalised MWNTs into a PMMA matrix by in-situ polymerization. With 1% of MWNTs, the storage modulus and tensile strength were improved by 66% and 40%, respectively [11].

2.3 Preparation and properties of composite fibres

Polymer fibres such as the polyacrylonitrile (PAN) and poly(p-phenylene benzobisoxazole) (PBO) are favoured over bulk polymers for many applications [6]. Generally, CNTs show more promising reinforcement in fibres than in bulk composites due to the possibility of improved alignment. The most important methods to fabricate polymer/CNT composite fibres include melt spinning, coagulation spinning and electrospinning.

The process for melt spinning of fibres is similar to the melt processing of bulk

composites except that the dopes are extruded through a smaller nozzle and fibres are drawn further. Kearns *et al.* prepared PP/SWNT composite fibres by melt spinning [12]. The modulus and strength of the matrix were increased by 56% and 45%, respectively, by adding 1% of SWNTs, and the elongation at break was also seen to increase by 30%, which is of particular significance for the composite fibres.

Coagulation spinning is a new method which was first reported by Vigolo *et al.* in 2000 [13]. This method disperses SWNTs using a surfactant solution and coagulates the nanotubes into a mesh by spinning it into an aqueous PVA solution. Dalton *et al.* optimized this method and prepared super-tough PVA/SWNT composite fibres containing 60% of SWNTs, which had a tensile strength of 1.8 GPa, comparable to that of spider silk [14]. What leads to this simple method attracting much attention is the extraordinary toughness of the fibre, of 570 J/g, which is much higher than that of any existing high-performance fibre.

Electrospinning is the simplest method to prepare fibres as small as several nm in diameter and it is particularly effective in orienting nanotubes in composites [15, 16]. In the electrospinning process, a high electric voltage is applied to a polymer solution (or melt) such that the solution is charged. When the electrostatic force overcomes the surface tension, a charged jet emanates from the nozzle, the solvent evaporates and fibres are deposited on a collector (see Figure 2.2 for a schematic diagram of the process). The nanotubes in the fibres are aligned by the strong drawing force exerted by the electric field. Young *et al.* demonstrated recently that the nanotube orientation has a dominant effect on the fibre strength [17]. The good orientation achieved in the electrospun fibres is thus expected to enhance the fibre strength greatly. Almecija *et al.* measured the mechanical properties of individual PVA/SWNT electrospun nanofibres and observed an effective modulus of 27 TPa and effective strength of 600 GPa for the nanotubes, suggesting a superb reinforcing efficiency that has never been achieved in less-aligned CNT composites. These values are much higher than the theoretical values for individual nanotubes. Nanotube-nucleated polymer ordering and crystallisation might be responsible for this extraordinary reinforcement [18].
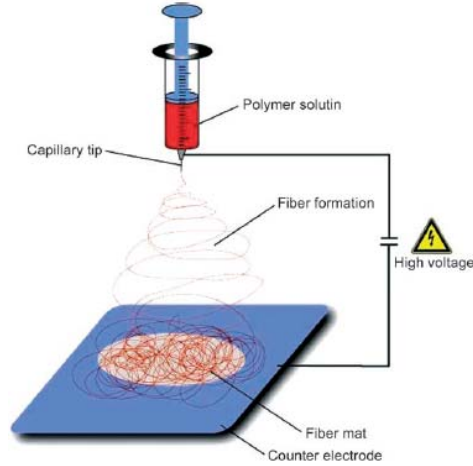
Figure 2.2 A laboratory set-up for an electrospinning experiment [15].

2.4 Reinforcing mechanisms and modelling

For composites for which the properties of the polymer matrix are unaffected by the nanotubes, the mechanical reinforcement is associated with stress transfer from the matrix to the nanotubes. In an ideal case where long and highly aligned nanotubes are embedded in polymers, the mechanical properties of the composite can be described by the simple rule of mixtures [19]:

$$E_c = V_{NT}E_{NT} + (1-V_{NT})E_m \tag{2.1}$$

$$\sigma_c = V_{NT}\sigma_{NT} + (1-V_{NT})\sigma_m \tag{2.2}$$

where E_c, E_{NT}, and E_m are the modulus of the composite, nanotubes, and the polymer matrix, respectively; σ_c, σ_{NT}, and σ_m are the strength of the composite, nanotubes, and the polymer matrix, respectively; and V_{NT} is the volume fraction of nanotubes.

When all nanotubes are not aligned in the same direction and the length is too short such that the stress is non-uniform in the majority part of the nanotube, the rule of mixtures needs to be modified to take into account the length and orientation effects, which can be described as [6]:

$$E_c = \eta_o\eta_l V_{NT}E_{NT} + (1-V_{NT})E_m \tag{2.3}$$

$$\sigma_c = \eta_s V_{NT}\sigma_{NT} + (1-V_{NT})\sigma_m \tag{2.4}$$

where η_o is the orientation efficiency factor, η_l is the length efficiency factor, and η_s is

the strength efficiency factor. The effective modulus E_{eff} of nanotubes, which is defined as $E_{eff} = \eta_l E_{NT}$ (similarly, σ_{eff} is defined as $\sigma_{eff} = \eta_s \sigma_{NT}$), accounts for the length and bundling effect on nanotube modulus. The E_{eff} and σ_{eff} allow the efficiency of mechanical reinforcement in different composite systems to be compared.

The important results for mechanical properties of bulk composites and composite fibres reported in the literature are summarised in Table 2.1 and Table 2.2, respectively. The effective modulus (E_{eff}) and strength (σ_{eff}) in these tables were back-calculated using the rule of mixtures assuming that: 1) the matrices were unaffected by the nanotubes in all these cases and 2) the nanotubes were distributed randomly in two-dimension in the bulk composites. It is noted although nanotubes display reinforcing effects on a range of polymers, only few of them have values of E_{eff} and σ_{eff} approaching the theoretical values for individual nanotubes (i.e. 1000 GPa for the modulus and 30 - 100 GPa for the strength). Moreover, the degree of strength improvement is less than that of the modulus improvement in most cases, which is possibly due to the shortened length and bundling effect of the nanotubes in composites. This suggests the mechanical performance of CNT composites can be further improved. A better understanding of the structure/property relationships is needed and this requires powerful techniques to characterise the composites, which will be reviewed in the following sections.

Table 2.1 Mechanical properties of CNT-reinforced bulk composites.

CNT type	Polymer	CNT% (vol%)	E_c (GPa)	E_m (GPa)	E_{eff} (GPa)	σ_{eff} (GPa)	Reference
SWNT	PVA	5	4	2.5	87	2	[8]
DWNT	Epoxy	10	10.9	3	220	0.3	[20]
MWNT	PP	0.5	1.12	0.77	180	2.8	[21]
MWNT	PC	2	2.6	2	85	0.46	[22]
MWNT	PA6	1	1.24	0.4	225	3	[9]
MWNT	PS	0.5	1.69	1.19	270	0.64	[23]
MWNT	PMMA	0.5	2.6	1.6	540	2.4	[24]

Table 2.2 Mechanical properties of CNT-reinforced polymer fibres.

CNT type	Polymer	CNT% (Vol)	E_c (GPa)	E_m (GPa)	E_{NT} (GPa)	σ_{NT} (GPa)	Reference
SWNT	PVA	3	35.8	25.6	366	7.6	[25]
SWNT	PA6	0.1	0.54	0.44	100	45	[26]
SWNT	PP	0.7	1	0.4	86	--	[27]
SWNT	PBO	12	167	138	380	16	[28]
SWNT	PAN	0.9	1.07	0.9	730	19	[29]

Nanotubes can nucleate some polymers such as PVA to crystallise on their surfaces and the crystalline layer is much stiffer than the surrounding amorphous polymers. In this case the modulus and strength of the composites are higher than those predicted by the simple rule of mixtures, which is due to the contribution of the stiffer crystalline phase. Coleman *et al.* modified the rule of mixtures to calculate the composite modulus considering the contribution of the three phases [4]:

$$E_c = \eta_o E_{eff} V_{NT} + E_a \left(1 - V_{NT}\right) + \left(E_\chi - E_a\right) \left(\frac{b^2 + 2r_t b}{r_t^2}\right) V_{NT} \qquad (2.5)$$

where E_a is the modulus of the amorphous polymer, E_χ is the modulus of the crystalline phase, b is the average thickness of the nanotube-nucleated crystalline layer and r_t is the nanotube radius.

When the nanotube-induced crystallisation occurs, the fracture of the composite occurs at the interface between the bulk polymer and the crystalline layer. The composite strength can be described as a sum of the strength of the bulk polymer and the interface. Coleman *et al.* developed another form of the rule of mixtures to calculate the composite strength which is given by [30]:

$$\sigma_c = \tau_i \frac{(r_t + b) l_p}{r_t^2} V_{NT} + \sigma_m \left[1 - \frac{(r_t + b) V_{NT}}{r_t^2}\right] \qquad (2.6)$$

where τ_i is the interfacial shear strength, σ_m is the tensile strength of the polymer, and l_p is the pull out length of the nanotubes. Equations (2.5) and (2.6) suggest that the

crystalline layer has a significant effect on mechanical properties of the composites when *b* is large, and the simple rule of mixtures is invalid when the properties of the polymer matrix are affected by adding nanotubes.

2.5 Fundamental aspects of CNT composites

Although nanotubes have exhibited their promising reinforcing effect in composites, there is still a gap between the measured and the theoretical values of modulus and strength. It is recognized that the dispersion state, orientation and the interfacial adhesion have significant effect on the mechanical properties of composites [31]. This section discusses how these factors influence the properties and how to optimize them in the composite structure.

2.5.1 Dispersion

The state of dispersion is an important factor that determines the mechanical properties of composites and good dispersion of nanotubes is crucial for any composite. The state of dispersion of nanotubes can influence the mechanical properties through the following aspects [31]:

1) The surface area decreases when individual nanotubes aggregate into ropes (or bundles). The surface area is important for mechanical reinforcement because: a) it acts as an interface for stress transfer, and larger surface area leads to higher efficiency of stress transfer; b) when the nanotubes are in ropes, the load is carried mainly by the nanotube on the perimeter of each rope which is evidenced by the intertube sliding when subjected to external stress [32]. Hence, larger nanotube ropes result in smaller effective volume fraction for the reinforcing fillers; and c) nanotubes can induce polymers to crystallise on their surface. The crystalline layer, which is related to the nanotube surface area, can determine the mechanical performance for some semi-crystalline polymer composites [4, 30].

2) Good dispersion gives rise to a uniform distribution of stress and minimises the stress concentration centres in the composites. Poor dispersion which results in stress

concentrations, in turn, leads to a smaller degree of strength improvement than that of the modulus improvement.

3) The mechanical properties of nanotube bundles are much poorer than those of individual nanotubes. Salvetat *et al.* measured the modulus of nanotube ropes by bending the nanotubes with an atomic force microscopy (AFM) tip [33]. It was found the modulus decreased from over 1 TPa for the nanotube rope with a diameter of 3 nm to 149 GPa for the rope with a diameter of 13.5 nm.

The aforementioned theoretical analysis of the effect of dispersion has been supported by a range of experimental work. For example, Song *et al.* observed a greater improvement in tensile strength and elongation at break for epoxy composites with good MWNTs dispersion compared to a poorly-dispersed system [34]. Zhu *et al.* investigated the mechanical properties of epoxy composites containing both pristine (poor dispersion) and functionalized SWNTs (good dispersion). The mechanical properties of the poorly-dispersed system were shown to be worse than those of the neat epoxy, whereas the modulus and strength were increased by 18% and 30%, respectively, for the composite with good dispersion of nanotubes [35].

Nanotube exfoliation can be accomplished by stirring, shear mixing and/or ultrasonication [6]. Stable and uniform dispersions of pristine nanotubes are, however, difficult to achieve using these techniques alone. Compared to MWNTs, SWNTs are even more difficult to disperse due to a larger specific surface area and a stronger tendency for aggregation. In addition, intensive mechanical agitation can induce defects and damage the sidewall structure, which consequently degrades the mechanical properties of the nanotubes. Two main methods have thus been developed to facilitate the dispersion of nanotubes in polymers:

1) Dispersing nanotubes with the aid of surfactants or other dispersants. The dispersant molecule wrapping around the nanotubes can induce strong non-covalent bonding with the matrix, giving rise to stable dispersion. Gong *et al.* prepared epoxy/CNT composites using a non-ionic surfactant to assist dispersion of nanotubes. They found the elastic modulus was increased by 30% by adding 1% of nanotubes, while the incorporation of nanotubes without the surfactant had only a moderate effect

on mechanical properties [36].

2) Introducing covalent bonding between nanotubes and the matrix by chemically functionalising the nanotubes. This can be achieved by introducing functional groups (such as carboxyl group) or by grafting matrix polymers onto the nanotube surface through in-situ polymerization. Improving the dispersion via chemical functionalisation confers extra benefit, i.e. better interfacial adhesion in the composites.

It should be pointed out, however, there is a maximum volume fraction for isolated nanotubes in the polymer matrix, assuming the minimum separation between the nanotubes is the radius of a polymer molecule. For nanotubes arranged in hexagonal arrays, the separation S_{hex} between the nanotubes is given by [37]:

$$S_{hex} = d_t \left[\sqrt{\frac{\pi}{2\sqrt{3} \cdot V_{NT}}} - 1 \right] \qquad (2.7)$$

where d_t is the nanotube diameter. The typical radius for a polymer is of the order of 5 nm [37]. For SWNTs with an average diameter of 1 nm, more than 2.5% of nanotubes in the polymer will naturally lead to nanotube aggregation, and in the case of MWNTs with a diameter of ~10 nm, the maximum volume fraction for individual nanotubes is ~40%.

2.5.2 Orientation

Carbon nanotubes show highly anisotropic mechanical properties, e.g. the longitudinal modulus is ~1000 GPa while the transverse modulus is only ~15 GPa [38, 39]. The mechanical properties of composites are thus strongly dependent on nanotube orientation. The mechanical reinforcing efficiency is lower when all nanotubes are not aligned in the same direction. Cox introduced an orientation efficiency factor, η_o, to the rule of mixtures to take into account the effect of orientation distribution of the reinforcing fillers on the properties of the composites [40, 41]. The parameter η_o can be considered as a summation of contribution of all fillers (nanotubes in this case) lying at any angle Ψ with respect to the longitudinal direction of the composite:

$$\eta_o = \sum_n a_n \cos^4 \Psi \tag{2.8}$$

where a_n is the proportion of fillers lying at the angle Ψ and is given by $\sum_n a_n = 1$.

For fillers randomly distributed in a plane (two-dimensional distribution), the η_o is an integration over the range of -π/2 to π/2 and is given by [42]:

$$\eta_o = \frac{1}{\pi} \int_{-\pi/2}^{\pi/2} \cos^4 \Psi d\Psi = 3/8 \tag{2.9}$$

while for fillers distributed randomly in three dimensions, the η_o can be determined by [41]:

$$\eta_o = \frac{1}{\pi} \int_0^{\pi/2} \sin \Psi \cos^4 \Psi d\Psi = 1/5 \tag{2.10}$$

This indicates the modulus and strength of the nanotubes is 3/8 (for two-dimensional distribution) or 1/5 (for three-dimensional distribution) of those of the uniaxially-aligned nanotubes. Some reports are consistent with these theoretical values. For example, Thostenson *et al.* prepared PS/SWNT composites and observed an increase of 49% in storage modulus for an aligned composite, whereas for a randomly-oriented composite the modulus was increased by only 10% compared to the bulk polymer [43]. This means a five-fold relative increase for the aligned system over the randomly-oriented system.

A number of methods have been developed to align the nanotubes in composites. These techniques can be generally classified into two categories:

1) Aligning nanotubes using fibre spinning techniques such as melt spinning, coagulation spinning and most efficiently, electrospinning. In the electrospinning process, there are tremendous drawing forces acting on tiny jets of the polymer solution, which leads to the rigid-rod like nanotubes rotating around their centre of gravity and orienting along the drawing direction to minimise the torque applied to them. Similarly, the shear force in a melt spinning process and the drawing force in a mechanical stretching process can also orient the nanotubes in the composites. Fibre spinning processes together with the mechanical stretching are the most common methods to align nanotubes in composites.

2) Aligning nanotubes using external fields such as magnetic and electric fields. A

high magnetic field is efficient to align nanotubes along the field axis when the diamagnetic susceptibilities parallel to the nanotube axis is larger than that perpendicular to the nanotube axis. In 2002, Kimura *et al.* firstly demonstrated the magnetic field induced orientation of MWNTs in a PS matrix [44]. In this process, MWNTs were dispersed in a monomer solution of unsaturated polyester, and then a constant magnetic field of 10 T was applied to align the nanotubes. Polymerization under the strong magnetic filed yielded good alignment of the nanotubes, and this was revealed by the anisotropic properties of the composites. This procedure was followed and modified by a number of groups to achieve good orientation.

It should be pointed out that good orientation can only be achieved when the nanotubes are well separated because nanotubes bundles are often entangled during growth. Aligned nanotube arrays can be grown directly on substrates, but few examples that transfer the arrays yet preserve their orientations in composites have been reported [45].

2.5.3 Interfacial adhesion

The interfacial adhesion between the polymer matrix and nanotubes is a key factor for the properties of nanocomposites because it determines the efficiency of stress transfer from the matrix to the reinforcing fillers [3, 6]. Adequate interfacial stress transfer from the matrix to the nanotubes is only possible when the interface has not failed during composite loading [46-48].

The interfacial shear strength (IFSS) is defined as the maximum shear stress before the interface fails. It governs the maximum stress transferred to the nanotube and is quite sensitive to the nanotube and matrix types, as well as the bonding type, i.e. whether it is covalent bonding or non-covalent bonding [5-6]. Liao *et al.* demonstrated that in the absence of covalent bonding between the nanotubes and the matrix, the nanotube/matrix adhesion comes from a) electrostatic and van der Waals interactions and b) stress/deformation arising from the mismatch in the coefficients of thermal expansion between the two phases [49].

There are four mechanisms for composite fracture, namely fibre fracture, fibre pull

out, fibre/matrix debonding and matrix cracking (Figure 2.3) [5]. Which kind of fracture occurs depends on the relative strength among the polymer matrix, the interface between the bulk polymer and the interfacial polymer and the nanotube-matrix interface.
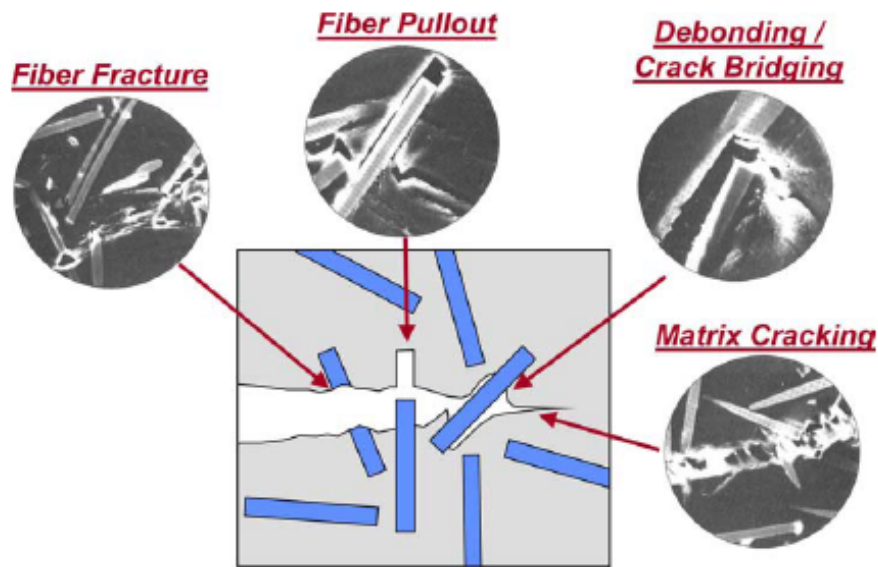
Figure 2.3 Schematic diagram showing the fracture mechanisms of nanocomposites [5].

For non-covalently-bonded systems, the nanotube-polymer interfacial strength is around 50 MPa, and for covalently-bonded systems this value is typically of a few hundred MPa although a large variation has been found in the literature [47]. Barber *et al.* determined that the average stress to pull out a single MWNT from a polyethylene-butene/MWNT composite was 47 MPa, which is about ten times higher than the system made up of the same polymer and carbon fibres [47]. They inferred that covalent bonding existed between the polymer matrix and the defects of MWNTs. Cooper *et al.* determined that the interfacial strength for epoxy/CNT composites ranged from 42 MPa to ~300 MPa and concluded that substantial adhesion between nanotubes and the epoxy resin existed in some cases, probably originated from the defects on the nanotubes [48]. Coleman *et al.* found a value of 95 MPa for the IFSS of their PVA/MWNT films [30]. The strong interfacial adhesion was ascribed to the nucleation effect of nanotubes which induced the polymer to form a crystalline coating around the nanotubes.

The interface can be tailored by introducing different functional groups onto the nanotube surface. Barber *et al.* functionalised MWNTs with carboxylic groups and found that the IFSS increased from 30 MPa for the epoxy/pristine-MWNT interface to 150 MPa for the chemically-functionalised system [50]. Duncan *et al.* modified MWNTs with epoxide terminated groups which can further react with the matrix polycarbonate through thermal trans-esterification reaction [51]. They found that the IFSS was improved by nearly two-fold upon chemical functionalisation, from the range of 5 - 14 MPa for the untreated MWNTs to the range of 11 - 38 MPa for the functionalised system.

Other factors such as the nanotube type and the preparation method of nanotubes can also influence the mechanical properties of the composites. Essentially, these factors influence the mechanical reinforcing efficiency through the more fundamental aspects, namely the dispersion, orientation and the interfacial stress transfer. For example, Chae *et al.* compared the reinforcing efficiency of different types of nanotubes on PAN and observed a general trend of SWNT~MWNT > DWNT [52]. This was explained as a result of a better dispersion and orientation of SWNTs (or MWNTs) than those of DWNTs (because the DWNTs they used were highly entangled and were difficult to align) in the composites.

The nanotube aspect ratio has a more profound effect on the reinforcing efficiency. When a CNT composite is deformed, the stress is transferred to the nanotubes through a shear mechanism and the stress in the nanotubes builds up from the ends to the midsection. The length required for the stress to build up until the nanotube has a strain equal to that of the matrix is called the stress transfer length. At a critical nanotube length l_c, the stress transferred to the nanotube is large enough to break the nanotube. If the interfacial shear stress along the nanotube is assumed to be constant (the Kelly-Tyson model), the critical length can be determined by [51]:

$$l_c = \frac{d_t \sigma_{NT}}{\tau_{ave}} \qquad (2.11)$$

where σ_{NT} is the nanotube tensile strength and τ_{ave} is the average interfacial shear stress. The profiles of stress along nanotubes that possess different lengths, *l*, are

shown in Figure 2.4. It can be seen the regions of the nanotubes near the ends are less heavily stressed and the nanotubes do not carry the maximum load when they are too short ($l < l_c$). Hence, the reinforcing efficiency decreases as the fibre length (or the aspect ratio) is reduced [19].
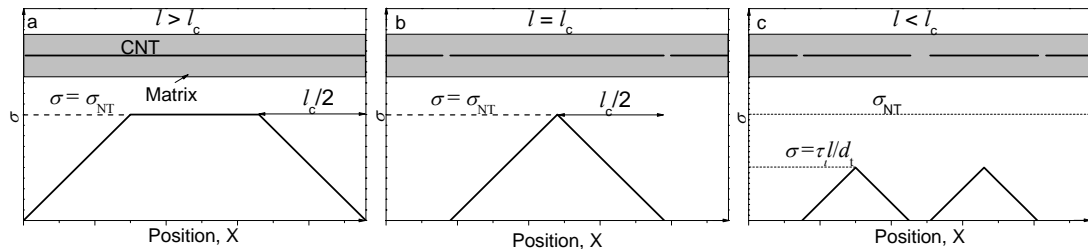
Figure 2.4 The idealised profile of stress in nanotube composites that contain nanotubes with different lengths: (a) nanotubes are longer than the critical length, (b) nanotubes are equal to the critical length, and (c) nanotubes are shorter than the critical length [51].

2.6 Characterisation of CNT composites

2.6.1 Characterisation of the dispersion

Despite the unanimously recognized importance of nanotube dispersion on mechanical properties of the composites, the assessment of dispersion state relies largely on qualitative and subjective interpretation of TEM and SEM images [53]. Efforts have been made to quantify the dispersion by analysing the microscopy images. Lillehei *et al.* established a quantitative approach by analysing the frequency of spatial features in SEM images to evaluating the dispersion quality [54]. Their approach allowed the estimation of diameter of nanotube bundle, the segment length and bundle spacing. Luo *et al.* employed ImageJ software to measure the free-path spacing between the nanotubes in TEM images and used a parameter $D_{0.1}$ to quantify the dispersion quality. This parameter is defined as the probability of the free-path distance distribution in the range of 0.9μ - 1.1μ, where μ is the mean spacing [55]. Figure 2.5 shows an example of the process of quantitative assessment based on the TEM images.
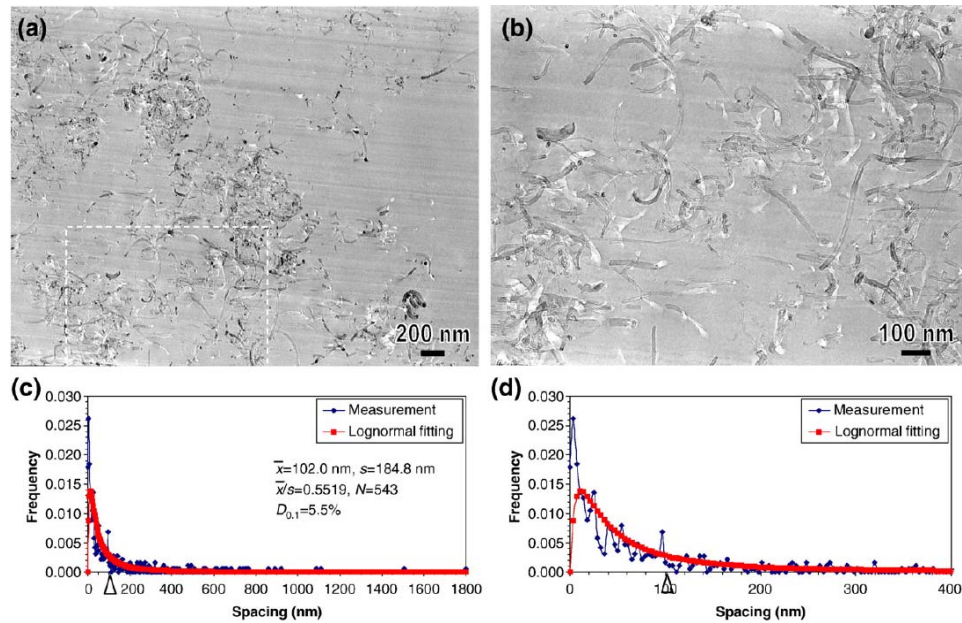
Figure 2.5 (a) A TEM image of a thermoset polymer/MWNT composite. (b) Enlargement from the framed area in (a). (c) Histogram of the filler free-path spacing measured from (a). (d) Enlarged histogram from (c) showing the short spacing range [55].

Fluorescence spectroscopy is another useful technique to assess the dispersion state. When a semiconducting nanotube absorbs excitation light via a E_{22} transition, it emits the light through a $c_1 \rightarrow v_1$ transition (where c_1 and v_1 are the first conduction and valence bands, respectively) and the emission is quenched when the nanotubes are in bundles. Only truly debundled nanotubes can therefore be detected by fluorescence spectroscopy and this can be obtained only for an extremely low loading of nanotubes in composites. Such composites are not of particular interest for mechanical reinforcement but are of great importance for studying the intrinsic properties and the interaction with the environment at the single nanotube level.

Other techniques such as optical microscopy, UV-Vis spectroscopy, small angle neutron scattering (SANS), size exclusion chromatography (SEC) [56] and differential scanning calorimetry (DSC) [57] have also been employed to examine the dispersion quality. Fagan *et al.* compared the reliability of four techniques, i.e. SANS, fluorescence spectroscopy, optical absorption spectroscopy and Raman spectroscopy for evaluating the dispersion [58]. They demonstrated that the first two techniques both offer reliable measures due to their sensitivity to bundling or clustering of

nanotubes and are more definitive than the latter two techniques. While the SANS technique is powerful in evaluating the local dispersion quality on the nanoscale, it does not give information as to the distribution of bundle spacing which is a measure of the uniformity of the dispersion.

2.6.2 Characterisation of the orientation

TEM is the most common characterisation technique which provides a direct view of the arrangement of nanotubes in composites. It is difficult, however, to image SWNTs using TEM due to the low contrast between polymers and SWNTs. This is made even more difficult when SWNTs are well separated. Salalha *et al.* used a reactive ion etching process to etch the polymer matrix so that SWNTs are exposed (Figure 2.6) [59]. The processing time needs to be carefully controlled to reduce the matrix thickness without damaging the SWNTs. Characterising the orientation using TEM requires tedious and careful sample-preparation and it should be noted cutting the composites into slices using a diamond knife (a common method for TEM sample preparation) may lead to the nanotubes orienting along the cutting direction, as has been demonstrated by Ajayan *et al.* in an early example [2].
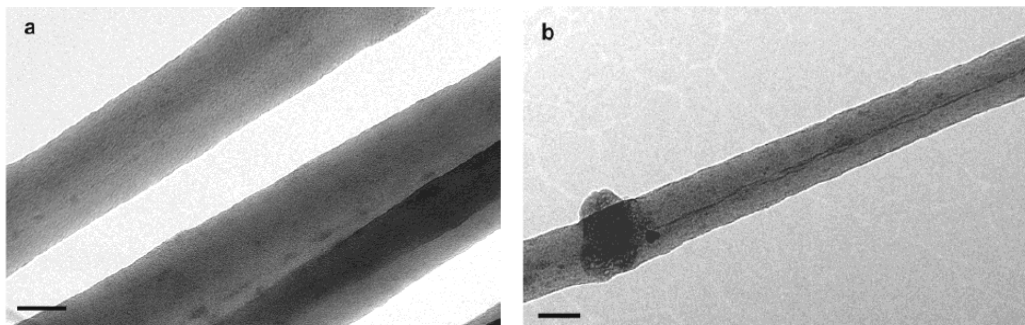
Figure 2.6 TEM images of poly(ethylene oxide) (PEO)/SWNT electrospun fibres: (a) before etching and (b) after etching, showing the good orientation of SWNTs. Bar= 50 nm [59].

Orientation of the nanotubes, particularly of MWNTs, can also be characterised using X-ray diffraction. Figure 2.7 shows the wide angle X-ray diffraction (WAXD) pattern of PAN/MWNT composite nanofibres. The arc at $2\Phi = 26.5º$ is identified as the diffraction of (002) crystal plane of MWNTs. By azimuthal scanning of the (002)

diffraction arc, the average value of the angle β between the molecular axis and the fibre axis can be determined. A quantitative parameter, i.e. the Herman's orientation factor f, can then be determined by:

$$f = \left(3\left\langle \cos^2 \beta \right\rangle - 1\right)/2 \qquad (2.12)$$

Using this method, Ge *et al.* determined the orientation factor of both the polymer molecules and the nanotubes in PAN/MWNT nanofibres and concluded that the nanotubes were better oriented than the polymer molecules [60]. To acquire appreciable intensity requires a relatively high loading of nanotubes in the composites, and for some type of SWNTs, there is no Bragg peak at all.
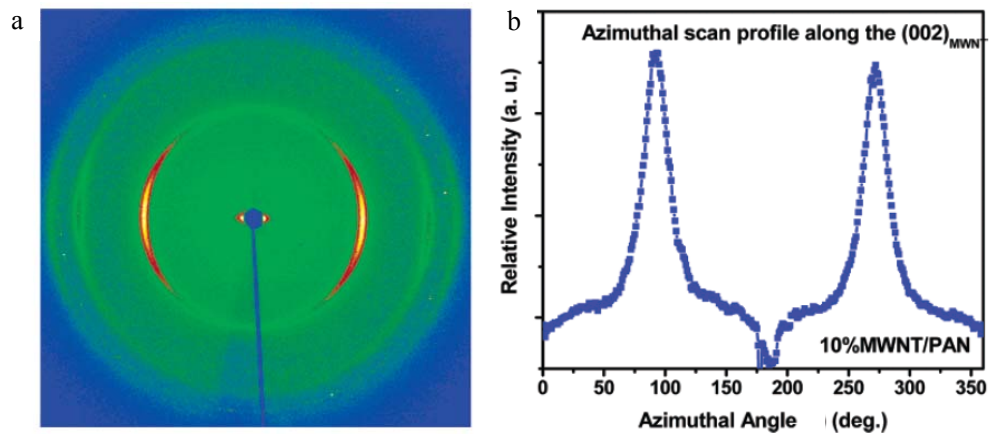
Figure 2.7 (a) Two-dimensional WAXD pattern of PAN/MWNT composite fibres. (b) The azimuthal scan of (002) diffraction ring from (a) [60].

2.6.3 Characterisation of the interfacial adhesion

The interfacial adhesion and strength can be examined qualitatively by SEM observation of the fracture surface which gives information on the failure mechanism (i.e. whether the composite fails due to nanotube pull out, nanotube fracture or matrix failure). TEM allows the investigation of the wetting of nanotubes in a polymer and crystallisation of the polymer on the nanotube surface. These all produce indirect information on the interfacial adhesion.

AFM and scanning probe microscopy (SPM) tips can be utilized to apply small and accurate force to the nanotubes. Combining these tips with electron microscopy, the IFSS in CNT composites can be determined quantitatively. Barber *et al.* carried out a

nanopullout experiment on CNT composites. For a typical measurement, an individual nanotube is attached to the end of an AFM tip and is then pushed into a liquid epoxy polymer. After curing of the epoxy, the nanotube is pulled away from the matrix by the tip which is driven by a cantilever (Figure 2.8). The embedded length l_{emb} (or equivalently the pull out length l_p) can be measured using SEM (by measuring the free length of nanotube before and after pull out), TEM (by measuring the empty cylinder in the matrix upon pull out) and AFM (by measuring the depth of the hole). The pull out force applied by the cantilever is determined by: $F_{pull}= KD$, where K is the spring constant and D is the bending deflection of the cantilever. The average interfacial shear stress τ_{ave} is then given by:

$$\tau_{ave} = \frac{F_{pull}}{\pi d_t l_{emb}} \tag{2.13}$$

Using this method, Barber *et al.* measured the IFSS for polyethylene-butene/MWNT to be 47 MPa [47], for epoxy/MWNT to be 30 MPa and a much higher IFSS for epoxy/MWNT-COOH, to be 150 MPa [50]. Cooper *et al.* used an SPM tip to pull the nanotubes out from the epoxy matrix and showed that the IFSS for epoxy/MWNT composites was in the range of 35 - 380 MPa [48].
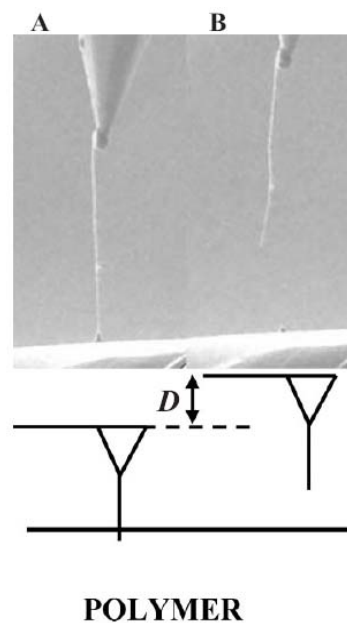
Figure 2.8 SEM images of a MWNT: (A) before and (B) after pulling out from an epoxy by an AFM tip. The bottom shows a schematic movement of the AFM tip [50].

2.7 Characterisation of CNT composites using Raman spectroscopy

Raman spectroscopy has been proved to be a powerful technique to characterise polymer/CNT composites. This technique has advantages over the other techniques in that the rich information it can provide, the capability of studying the composites structure on the molecular scale and simple sample-preparation. In fact, Raman spectroscopy has been employed to study almost all aspects that influence the mechanical properties of nanocomposites.

2.7.1 Characterisation of the dispersion

Raman spectroscopy provides a qualitative but convenient way to assess the dispersion of nanotubes in composites. For composites containing a single type of nanotube (i.e. SWNTs or MWNTs), the Raman band intensity is proportional to the quantity of nanotubes in the laser spot. The dispersion of nanotubes can therefore be monitored by mapping out the Raman band intensity across the composite. The spatial resolution depends on the laser spot size, which is mostly on the order of a few μm.

Rasheed *et al.* prepared a poly(styrene-*co*-vinyl phenol) (PSVPh)/SWNT composite and examined the dispersion of nanotubes using Raman spectroscopy combined with optical microscopy. They mapped out the nanotube G-band intensity (Figure 2.9) and concluded that the oxidized nanotubes were more evenly distributed than the pristine nanotubes in the composite [61]. Sochi *et al.* employed Raman spectroscopy to study the distribution of nanotubes in the radial direction of the polyimide/SWNT fibres. It was noted the G-band became more intense as the laser moved from the centre to the outermost surface, which indicated a higher concentration of nanotubes near the fibre surface [62].

Assessment of the dispersion on the nanoscale (i.e. individual nanotubes) is a more complicate issue. When SWNTs are separated into individual ones, the Raman features including the band frequency, intensity and lineshape are different from those of nanotube bundles. For example, the RBM peaks shift to higher frequencies by 1 - 9 cm^{-1} upon debundling, and some RBM peaks (e.g. the 267 cm^{-1} peak when excited

with a 785 nm laser) seen in nanotube bundles are absent when the SWNTs are individualised. Raman features of well-dispersed SWNTs in PVA/SWNT electrospun fibres will be presented in Chapter 4.
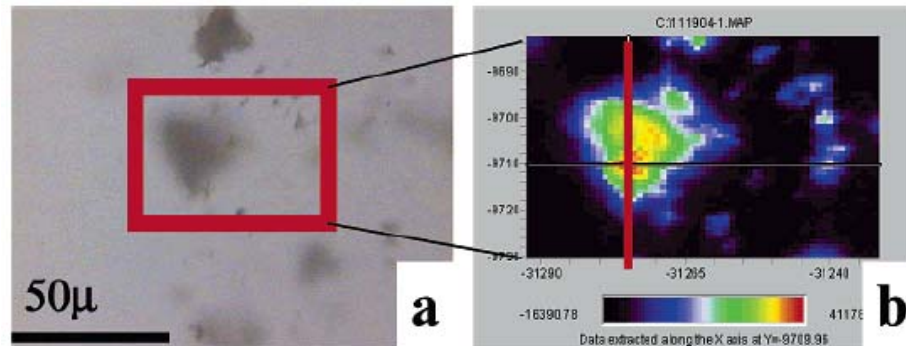
Figure 2.9 (a) Optical micrographs of a PSVPh/SWNT composite on a glass substrate. (b) Colour-coded map of the integrated area under the G-band for this micrograph. The dark areas correspond to lowest SWNT content whereas the red area corresponds to the highest SWNT content [61].

2.7.2 Characterisation of the orientation

Raman spectroscopy is an important technique in characterising the orientation of nanotubes. It is particularly powerful in determining the orientation of individual SWNTs which is difficult to achieve by other techniques such as TEM or XRD.

The degree of alignment of SWNTs can be determined quantitatively using polarized Raman spectroscopy. This is based on the orientation-dependent Raman band intensity of nanotubes (also known as the antenna effect): the Raman band intensity is a maximum when the nanotube axis is parallel to both the incident and scatter laser and is a minimum when the nanotube is perpendicular to the axis of laser polarisation (an example of intensity variation with angle is shown in Figure 2.10) [63]. This orientation-dependence of the Raman scattering is ascribed to the polarisation behaviour of nanotubes. The absorption of the light polarized parallel to the nanotube axis is up to ~20 times stronger than for perpendicularly-polarized light, which in turn influences the resonance enhancement for the Raman spectra of nanotubes [64].

Characterisation of the orientation is usually performed using a polarized Raman

spectroscopy with the VV configuration where the incident light and scattered light are both parallel to the principal axis of the spectrometer, the VH configuration where the incident light is parallel and the scattered light is perpendicular to the principal axis, and the HH configuration where the incident light and scattered light are both perpendicular to the principal axis of the spectrometer.
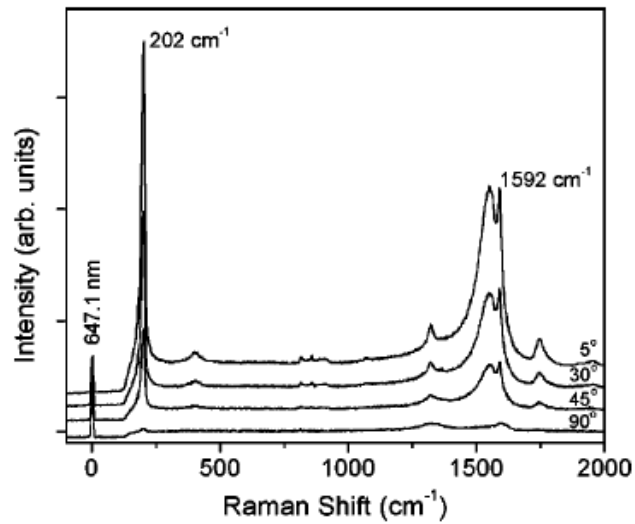
Figure 2.10 Polarized Raman spectra of a PMMA/SWNT fibre at different angles relative to the axis of laser polarisation [63].

Several mathematical models describing the dependence of Raman band intensity upon the nanotube orientation have been proposed. A typical model based on resonance theory is briefed as follows: for perfectly-aligned nanotubes using a VV configuration, the dependence of scattering intensity upon the angle, α, between the nanotube axis and the axis of laser polarisation is found to be [63]:

$$I_{VV} \propto \cos^4 \alpha \qquad (2.14)$$

For a composite comprising nanotubes over a range of angles the total Raman band intensity can be integrated to sum the contribution from nanotubes at each angle. The Raman band intensity $I(\varphi)$ at a sample angle, φ, is given by [63]:

$$I(\varphi) \propto \int_{\varphi-\pi/2}^{\varphi+\pi/2} F(\alpha-\varphi, \Delta) \cos^4 \alpha \, d\alpha \qquad (2.15)$$

where φ is the composite angle with respect to the axis of laser polarisation, $F(\alpha-\varphi, \Delta)$ is an orientation distribution function (ODF). The degree of alignment is characterised

by the parameter Δ which indicates the average orientation angle. Hwang *et al.* found a special Lorentzian function fitted their data well [63]:

$$F(\alpha - \varphi, \Delta) = \frac{\Delta / 2\pi}{(\alpha - \varphi)^2 - (\Delta / 2)^2} \tag{2.16}$$

Anglaret *et al.* used both Lorentzian and Gaussian functions as the ODF [65] and obtained slightly different results when using different ODFs. The method based on Equation (2.15) can give the orientation factor as well as the fraction of nanotubes that make an angle Δ with respect to the sample axis. It has been used by a number of groups with a variety of samples [63, 66].

Liu *et al.* proposed another model to calculate the orientation factor of nanotubes. Considering that the Raman band intensity of SWNTs is determined by its polarisability tensor rather than the derivative of the polarisability tensor, and assuming a uniaxial orientation of the sample, the dependence of the Raman band intensity on the angle φ is given by [67]:

$$I_{VV}(\varphi) \propto \left(\cos^4 \varphi - \frac{6}{7}\cos^2 \varphi + \frac{3}{35} \right)\langle P_4(\cos\beta)\rangle + \left(\frac{6}{7}\cos^2 \varphi - \frac{2}{7} \right)\langle P_2(\cos\beta)\rangle + \frac{1}{5} \tag{2.17}$$

$$I_{VH}(\varphi) \propto \left(-\cos^4 \varphi + \cos^2 \varphi - \frac{4}{35} \right)\langle P_4(\cos\beta)\rangle + \frac{1}{21}\langle P_2(\cos\beta)\rangle + \frac{1}{15} \tag{2.18}$$

where $\langle P_2(\cos\beta)\rangle$ and $\langle P_4(\cos\beta)\rangle$ are the second-order and fourth-order orientation parameters, respectively. Specifically, $\langle P_2(\cos\beta)\rangle$ is known as the Herman's orientation factor, which has a value of 1 for perfect orientation, 0 for random distribution, and -0.5 for the vibration perpendicular to the main axis. Using this method, the orientation factors can be determined by recording the Raman band intensity at different angles and then fitting the data using Equation (2.17) and/or Equation (2.18). For uniaxially-oriented samples, only the VV and VH intensities at 0º and 90º are needed to determine the orientation factor accurately. This provides a simple and straightforward method to quantify the orientation.

Zamora-Ledezma *et al.* also developed a method to assess the orientation assuming that: a) the system is uniaxial and b) only the *zz* component (*z* is the coordinate along

the nanotube axis) of the SWNT Raman polarisation tensor is non-zero. For a 3-D orientation of the nanotubes which has a uniaxial symmetry, the orientation factor f is given by [68]:

$$f = \frac{3I_{VV} + 3I_{VH} - 4I_{HH}}{3I_{VV} + 12I_{VH} + 8I_{HH}} \quad\quad (2.19)$$

while for a 2-D orientation, the orientation factor is given by [68]:

$$f = \frac{I_{VV} - I_{HH}}{I_{VV} + I_{VH} + 2I_{HH}} \qu\quad (2.20)$$

To determine the orientation factor using Zamora-Ledezma's method does not require rotating the sample relative to the laser polarisation, as only the intensities obtained using VV, VH and HH configurations at 0° are needed. The errors brought by heterogeneities in the sample can therefore be eliminated.

It should be noted the orientation factors determined using these methods are not identical to each other due to the different assumptions made in different models. Generally, the intensity ratio $I_{VV}^{0°} / I_{VV}^{90°}$ can be used for a quick and qualitative assessment of the orientation; a higher intensity ratio indicates a better orientation.

2.7.3 Characterisation of the interfacial adhesion

Raman spectroscopy can be used to probe the load transfer from the matrix to nanotubes and the interfacial slippage in the composites. This is based on the well known stress-dependent Raman G-band and G'-band frequencies, where both bands shift to lower wavenumber under tensile stress and to higher wavenumber under compression. Larger Raman band shift rate (the shift rate is defined as the slope of the linear region in the Raman band frequency-strain curve) indicates higher efficiency of stress transfer.

The Raman band shift rate depends on many factors such as the nanotube type, preparation method, state of dispersion and orientation. The factors that influence the shift rate and have been studied in the literature are listed in Table 2.3. This is certainly not a full list, e.g. the G' shift rate for individual SWNTs is likely to be

dependent on the nanotube chirality, and the aspect ratio of nanotube should also influence the Raman band shift rate, but how these factors influence the shift rate is still unclear. A systematic investigation of the effect of these factors is needed if the shift rate is to be used properly in assessing the interfacial adhesion and the efficiency of reinforcement.

Table 2.3 Factors that influence the Raman band shift rate of nanotubes in composites.

Factor	Influence on the G'-band shift rate	Reference
Nanotube type	SWNTs > MWNTs	[41]
Preparation method	CVD-CNTs > arc-discharge CNTs	[41]
Bonding type	Covalent bonding > Non-covalent bonding	[69]
Dispersion state	Good dispersion > Poor dispersion	Chapter 5
Polymer type	Stiff polymers > Elastomers	[70]
Nanotube orientation	Aligned > Random	Chapter 5

While it is difficult to compare the Raman band shift rate in different composite systems, the strain at which the nanotube Raman bands cease to shift during deformation is a measure of the interfacial shear strength. Roy *et al.* incorporated both collagen-modified SWNTs and pristine SWNTs into a PVA matrix. They observed a down-shift of the nanotube G'-band in the collagen-modified system during deformation, while no shift was observed in the unmodified system [69]. The strain at which interfacial slippage occurred for the PVA/Collagen-SWNT film was determined to be 3.5%. This strain value was then used to calculate the IFSS which turned out to be 187.5 MPa [69]. Kao *et al.* investigated the deformation behaviour of an epoxy/SWNT composite under cyclic loading by following the nanotube G'-band [71]. It was shown the deformation was completely reversible over a low strain range (< 0.4%); when a larger strain (e.g. 1%) was released, residual compression was observed, due to friction at the damaged interface in the composite [71].

The stress transfer between the nanotubes inside a nanotube bundle and between the graphene layers in an individual MWNT is also important; intertube sliding in

nanotube ropes and interlayer sliding in individual MWNTs are both detrimental to the mechanical performance of the composites. Kumar *et al.* deformed nanotube bundles by stretching a poly(dimethyl siloxane) (PDMS) substrate on which nanotube were sitting. They observed the shifts of the Raman bands such as: a) a discrete jump of the G-band frequency at certain strains; b) the relative intensity I_D/I_G remained constant during deformation; c) the strain-induced G-band shift rate for bundles was significantly lower than those of individual nanotubes; and d) the RBM frequency of metallic nanotubes shifted to higher-wavenumber by 4 cm^{-1} [32]. These phenomena suggested that only a fraction of the strain applied to the bundle was transferred to the individual nanotubes within the bundles and the main effect of deformation was to debundle the nanotubes [32]. Cui *et al.* studied the interlayer stress transfer in MWNTs using an epoxy/DWNT composite as a model material [72]. By deforming the composite using a four-point bending rig, the higher-frequency component of the G'-band which corresponds to the outer wall, was found to shifted at a rate of -9.2 cm^{-1}/%strain, whereas the lower-frequency component which originates from the inner wall shifted at a much lower rate, of -1.1 cm^{-1}/%strain. They demonstrated that the efficiency of stress transfer from the outer wall to the inner wall was rather low such that the inner wall did not carry load, which is consistent with the previous theoretical predictions [73, 74] and experimental findings [75]. It was also predicted that the effective modulus of MWNTs in composites would decrease as the number of walls increases, and cross linking the walls may possibly increase the resistance of the walls to the shear process.

2.8 Aims of this project

Investigation of the vibrational and electronic properties of SWNTs using Raman spectroscopy has been carried out mostly on nanotube bundles which are an ensemble of nanotube chiralities. Study of effects of both the environment and deformation on the Raman bands of individual nanotube is of great importance. To examine these effects at the single nanotube level requires appropriate samples, and this is

accomplished by the electrospinning of PVA/SWNT composite fibres in this study.

The G'-band shift rate has been used to estimate the effective modulus of nanotubes in composites for over a decade, but the influence of the nanotube orientation and the effect of the configuration of laser polarisation on this important parameter is unclear and needs to be addressed.

While CNTs have been shown to have a reinforcing effect on many polymers, very few reports dealt with the mechanical reinforcement of high-performance aramid fibres by nanotubes. The structure/property relationships for the aramid/SWNT composite fibres are yet to be established.

Fibres made up of neat CNTs are expected to have excellent mechanical properties but only a small proportion of the potential has been fulfilled. The influence of the microstructure on mechanical properties and the reinforcing efficiency on polymers needs to be assessed.

The aims of this project include:

1) To optimize the processing conditions for the dispersion of SWNTs in PVA and the conditions for electrospinning of PVA/SWNT fibres;

2) To study the Raman spectroscopy of SWNTs and the effect of deformation on the Raman bands of SWNTs at the single nanotube level;

3) To study the effect of dispersion, orientation and configuration of laser polarisation on the nanotube Raman band shift rate, and to correlate the G'-band shift rate with the effective nanotube modulus in composites;

4) To study the mechanical reinforcement of aramid fibres by SWNTs and to characterise the interface in aramid/SWNT fibres using Raman spectroscopy;

5) To characterise the microstructure of neat CNT fibres and the efficiency of stress transfer in polymer/CNT fibre composites.

2.9 References

1.　M. Moniruzzaman and K. I. Winey, *Polymer nanocomposites containing carbon nanotubes,* Macromolecules, 2006, **39**, 5194-5205.

2. P. M. Ajayan, O. Stephan, C. Colliex, and D. Trauth, *Aligned carbon nanotube arrays formed by cutting a polymer resin—nanotube composite,* Science, 1994, **265**, 1212-1214.

3. J. N. Coleman, U. Khan, and Y. K. Gun'Ko, *Mechanical reinforcement of polymers using carbon nanotubes,* Adv. Mater., 2006, **18**, 689-706.

4. J. N. Coleman, M. Cadeka, K. P. Ryan, A. Fonseca, J. B. Nagy, W. J. Blau, and M. S. Ferreira, *Reinforcement of polymers with carbon nanotubes. The role of an ordered polymer interfacial region. Experiment and modeling,* Polymer, 2006, **47**, 8556-8561.

5. E. T. Thostenson, C. Li, and T. W. Chou, *Nanocomposites in context,* Compos. Sci. Technol., 2005, **65**, 491-516.

6. J. N. Coleman, U. Khan, W. J. Blau, and Y. K. Gun'Ko, *Small but strong: A review of the mechanical properties of carbon nanotube–polymer composites,* Carbon, 2006, **44**, 1624-1652.

7. K. P. Ryan, M. Cadek, V. Nicolosi, and J. N. Coleman, *Carbon nanotubes for reinforcement of plastics? A case study with poly(vinyl alcohol),* Compos. Sci. Technol., 2007, **67**, 1640-1649.

8. X. Zhang, T. Liu, T. V. Sreekumar, S. Kumar, V. C. Moore, R. H. Hauge, and R. E. Smalley, *Poly(vinyl alcohol)/SWNT composite film,* Nano Lett., 2003, **3**, 11285-1288.

9. T. Liu, I. Y. Phang, L. Shen, S. Y. Chow, and W. Zhang, *Morphology and mechanical properties of multiwalled carbon nanotubes reinforced nylon-6 composites,* Macromolecules, 2004, **37**, 7214-7222.

10. A. M. Díez-Pascuala, M. Naffakha, M. A. Gómeza, C. Macro, G. Ellis, M. T. Martinez, A. Anson, Y. Martínez-Rubic, and B. Simard, *Development and characterization of PEEK/carbon nanotube composites,* Carbon, 2009, **47**, 3079-3090.

11. C. Velasco-Santos, A. L. Martínez-Hernández, F. T. Fisher, R. Ruoff, and V. M. Castaño, *Improvement of thermal and mechanical properties of carbon nanotube composites through chemical functionalization,* Chem. Mater., 2003, **15**, 447-4475.

12. J. C. Kearns and R. L. Shambaugh, *Polypropylene fibers reinforced with carbon nanotubes,* J. Appl. Poly. Sci., 2002, **86**, 2079-2084.

13. B. Vigolo, A. Penicaud, C. Coulon, C. Sauder, R. Pailler, C. Journet, P. Bernier, and P. Poulin, *Macroscopic fibers and ribbons of oriented carbon nanotubes,* Science, 2000, **290**, 1331-1334.

14. A. B. Dalton, S. Collins, E. Munoz, J. M. Razal, V. H. Ebron, J. P. Ferraris, J. N. Coleman, B. G. Kim, and R. H. Baughman, *Super-tough carbon-nanotube fibres - These extraordinary composite fibres can be woven into electronic textiles,* Nature, 2003, **423**, 703-703.

15. A. Greiner and J. H. Wendorff, *Electrospinning: A fascinating method for the preparation of ultrathin fibres,* Angew. Chem., Int. Ed., 2007, **46**, 5670-5703.

16. Z. Huang, Y. Zhang, M. Kotaki, and S. Ramakrishna, *A review on polymer nanofibers by electrospinning and their applications in nanocomposites,* Compos. Sci. Technol., 2003, **63**, 2223-2253.

17. K. Young, F. M. Blighe, J. J. Windle, A. K. I, L. Dend, R. J. Young, and J. N. Coleman, *Strong dependence of mechanical properties on fibre diameter for polymer-nanotube composite fibres: Differentiating defect from orientation effects,* ACS Nano, **2010**, 4, 6989-6997.

18. D. Almecija, D. Blond, J. E. Sader, J. N. Coleman, and J. J. Boland, *Mechanical properties of individual electrospun polymer-nanotube composite nanofibers,* Carbon, 2009, **47**, 2253-2258.

19. D. Hull and T. W. Clyne, *An introduction to composite materials*, Cambridge: Cambridge University Press, 1996.

20. S. R. Brownlow, A. P. Moravsky, N. G. Kalugin, and B. S. Majumdar, *Probing deformation of double-walled carbon nanotube (DWNT)/epoxy composites using FTIR and Raman techniques,* Compos. Sci. Technol., 2010, **70**, 1460-1468.

21. B. Yang, J. Shi, K. P. Pramoda, and S. H. Goh, *Enhancement of the mechanical properties of polypropylene using polypropylene-grafted multiwalled carbon nanotubes,* Compos. Sci. Technol., 2008, **68**, 2490-2497.

22. A. Eitan, F. T. Fisher, R. Andrews, L. C. Brinson, and L. S. Schadler, *Reinforcement mechanisms in MWCNT-filled polycarbonate,* Compos. Sci. Technol., 2006, **66**, 1162-1173.

23. D. Qian, E. C. Dickey, R. Andrews, and T. Rantell, *Load transfer and deformation mechanisms in carbon nanotube-polystyrene composites,* Appl. Phys. Lett., 2000, **76**, 2868-2870.

24. C. Velasco-Santos, A. L. Martinez-Hernandez, F. T. Fisher, R. Ruoff, and V. M. Castano, *Improvement of thermal and mechanical properties of carbon nanotube composites through chemical functionalization,* Chem. Mater., 2003, **15**, 4470-4475.

25. X. Zhang, T. Liu, T. Screekumar, S. Kumar, X. Hu, and K. Smith, *Gel spinning of PVA/SWNT composite fibre,* Polymer, 2004, **45**, 8801-8807.

26. J. B. Gao, M. E. Itkis, A. Yu, E. Bekyarova, B. Zhao, and R. C. Haddon, *Continuous spinning of a single-walled carbon nanotube-nylon composite fiber,* J. Am. Chem. Soc., 2005, **127**, 3847-3854.

27. T. E. Chang, L. R. Jensen, A. Kisliuk, R. B. Pipes, R. Pyrz, and A. P. Sokolov, *Microscopic mechanism of reinforcement in single-wall carbon nanotube/polypropylene nanocomposite,* Polymer, 2005, **46**, 439-444.

28. S. Kumar, T. D. Dang, F. E. Arnold, A. R. Bhattacharyya, B. G. Min, X. F. Zhang, R. A. Vaia, C. Park, W. W. Adams, R. H. Hauge, R. E. Smalley, S. Ramesh, and P. A. Willis, *Synthesis, structure, and properties of PBO/SWNT composites,* Macromolecules, 2002, **35**, 9039-9043.

29. H. G. Chae, M. L. Minus, and S. Kumar, *Oriented and exfoliated single wall carbon nanotubes in polyacrylonitrile* Polymer, 2006, **47**, 3494-3504.

30. J. N. Coleman, M. Cadek, R. Blake, V. Nicolosi, K. P. Ryan, C. Belton, A. Fonseca, J. B. Nagy, Y. K. Gun'ko, and W. J. Blau, *High-performance nanotube-reinforced plastics: Understanding the mechanism of strength increase,* Adv. Func. Mater., 2004, **14**, 791-798.

31. X. L. Xie, Y. W. Mai, and X. P. Zhou, *Dispersion and alignment of carbon nanotubes in polymer matrix: A review,* Mat. Sci. Eng. R, 2005, **49**, 89-112.

32. R. Kumar and S. B. Cronin, *Raman scattering of carbon nanotube bundles under axial strain and strain-induced debundling,* Phys. Rev. B, 2007, **75**, 155421 1-4.

33. J. P. Salvetat, G. A. D. Briggs, J. M. Bonard, R. R. .Bacsa, A. J. Kulik, T. Stockli, N. A. Burnham, and L. Forro, *Elastic and shear moduli of single-walled carbon*

nanotube ropes, Phys. Rev. Lett., 1999, **82**, 944-947.

34. Y. S. Song and J. R. Youn, *Influence of dispersion states of carbon nanotubes on physical properties of epoxy nanocomposites,* Carbon, 2005, **43**, 1378-1385.

35. J. Zhu, J. D. Kim, H. Q. Peng, J. L. Margrave, V. N. Khabashesku, and E. V. Barrera, *Improving the dispersion and integration of single-walled carbon nanotubes in epoxy composites through functionalization,* Nano Lett., 2003, **3**, 1107-1113.

36. X. Gong, J. Liu, S. Baskaran, R. D. Voise, and J. S. Young, *Surfactant-assisted processing of carbon nanotube/polymer composites,* Chem. Mater., 2000, **12**, 1049-1052.

37. B. Fiedler, F. H. Gojny, M. H. G. Wichmann, M. C. M. Nolte, and K. Schulte, *Fundamental aspects of nano-reinforced composites,* Compos. Sci. Technol., 2006, **66**, 3115-3125.

38. T. Liu and S. Kumar, *Effect of orientation on the modulus of SWNT films and fibers,* Nano Lett., 2003, **3**, 647-650.

39. V. N. Popov, V. E. V. Doren, and M. Balkanski, *Elastic properties of crystals of single-walled carbon nanotubes,* Solid State Commun., 2000, **114**, 395-399.

40. C. A. Cooper, *Structure/property relationships in particulate composites,* PhD Thesis, University of Manchester, 2000.

41. C. A. Cooper, R. J. Young, and M. Halsall, *Investigation into the deformation of carbon nanotubes and their composites through the use of Raman spectroscopy,* Compos. Part A, 2001, **32**, 401-411.

42. H. Krenchel, *Fibre reinforcement.* Copenhagen: Akademisk, 1964.

43. E. T. Thostenson and T. W. Chou, *Aligned multi-walled carbon nanotube-reinforced composites: processing and mechanical characterization,* J. Phys. D: Appl. Phys., 2002, **35**, L77-L80.

44. T. Kimura, H. Ago, M. Tobita, S. Ohshima, M. Kyotani, and M. Yumura, *Polymer composites of carbon nanotubes aligned by a magnetic field,* Adv. Mater., 2002, **14**, 1380-1383.

45. W. Feng, X. D. Bai, Y. Q. Lian, J. Liang, X. G. Wang, and K. Yoshino, *Well-aligned polyaniline/carbon-nanotube composite films grown by in-situ aniline*

polymerization, Carbon, 2003, **41**, 1551-1557.

46. A. H. Barber, S. R. Cohen, S. Kenig, and H. D. Wagner, *Interfacial fracture energy measurements for multi-walled carbon nanotubes pulled from a polymer matrix,* Compos. Sci. Technol., 2004, **64**, 2283-2289.

47. A. Barber, S. Cohen, and H. Wagner, *Measurement of carbon nanotube–polymer interfacial strength,* Appl. Phys. Lett., 2003, **82**, 4140-4142.

48. C. A. Cooper, S. R. Cohen, A. H. Barber, and H. D. Wagner, *Detachment of nanotubes from a polymer matrix,* Appl. Phys. Lett., 2002, **81**, 3873-3875.

49. K. Liao and S. Li, *Interfacial characteristics of a carbon nanotube-polystyrene composite system,* Appl. Phys. Lett., 2001, **79**, 4225-4227.

50. A. H. Barber, S. R. Cohen, A. Eitan, L. S. Schadler, and H. D. Wagner, *Fracture transitions at a carbon-nanotube/polymer interface,* Adv. Mater, 2006, **18**, 83-87.

51. R. K. Duncan, X. G. Chen, J. B. Bult, L. C. Brinson, and L. S. Schadler, *Measurement of the critical aspect ratio and interfacial shear strength in MWNT/polymer composites,* Compos. Sci. Technol., 2010, **70**, 599-605.

52. H. G. Chae, T. V. Sreekumar, T. Uchida, and S. Kumar, *A comparison of reinforcement efficiency of various types of carbon nanotubes in poly acrylonitrile fiber,* Polymer, 2005, **46**, 10925-10935.

53. H. S. Khare and D. L. Burris, *A quantitative method for measuring nanocomposite dispersion,* Polymer, 2010, **51**, 719-729.

54. P. T. Lillehei, J. Kim, L. J. Gibbons, and C. Park, *A quantitative assessment of carbon nanotube dispersion in polymer matrices,* Nanotechnology 2009, **20**, 325708 1-7.

55. Z. P. Luo and J. H. Koo, *Quantitative study of the dispersion degree in carbon nanofiber/polymer and carbon nanotube/polymer nanocomposites,* Mater. Lett., 2008, **62**, 3493-3496.

56. B. J. Bauer, M. L. Becker, V. Bajpai, J. A. Fagan, and W. R. Blair, *Measurement of single-wall nanotube dispersion by size exclusion chromatography,* J. Phys. Chem. C, 2007, **111**, 17914-17918.

57. S. H. Kim, W. I. Lee, and J. M. Park, *Assessment of dispersion in carbon*

nanotube reinforced composites using differential scanning calorimetry, Carbon, 2009, **47**, 2699-2703.

58. J. A. Fagan, B. J. Landi, B. J. Bauer, R. Raffaelle, and E. K. Hobbie, *Comparative measures of single-wall carbon nanotube dispersion,* J. Phys. Chem. B, 2006, **110**, 23801–23805.

59. W. Salalha, Y. Dror, R. L. Khalfin, Y. Cohen, A. L. Yarin, and E. Zussman, *Single-walled carbon nanotubes embedded in oriented polymeric nanofibers by electrospinning,* Langmuir, 2004, **20**, 9852-9855.

60. J. Ge, H. Hou, Q. Li, M. J. Graham, A. Greiner, D. H. Reneker, F. W. Harris, and S. Cheng, *Assembly of well-aligned multiwalled carbon nanotubes in confined polyacrylonitrile environments: Electrospun composite nanofiber sheets,* J. Am. Chem. Soc., 2004, **126**, 15754-15761.

61. A. Rasheed, M. D. Dadmun, I. Ivanov, P. F. Britt, and D. B. Geohegan, *Improving dispersion of single-walled carbon nanotubes in a polymer matrix using specific interactions,* Chem. Mater., 2006, **15**, 3513-3522.

62. E. J. Siochi, D. C. Working, C. Park, and S. Kumar, *Melt processing of SWCNT-polyimide nanocomposite fibers,* Compos. Part B, 2004, **35**, 439-446.

63. J. Hwang, H. H. Gommans, A. Ugawa, H. Tashiro, R. Haggenmueller, K. I. Winey, J. E. Fischer, D. B. Tanner, and A. G. Rinzler, *Polarized spectroscopy of aligned single-wall carbon nanotubes,* Phys. Rev. B, 2000, **62**, R13310-R13313.

64. W. C. Ren, F. Li, and H. M. Cheng, *Polarized Raman analysis of aligned double-walled carbon nanotubes,* Phys. Rev. B, 2005, **71**, 115428 1-5.

65. E. Anglaret, A. Righi, J. L. Sauvajol, P. Bernier, B. Vigolo, and P. Poulin, *Raman resonance and orientational order in fibers of single-wall carbon nanotubes,* Phys. Rev. B, 2002, **65**, 165426 1-7.

66. R. Haggenmueller, H. H. Gommans, A. G. Rinzler, and K. I. Winey, *Aligned single-wall carbon nanotubes in composites by melt processing methods,* Chem. Phys. Lett., 2000, **330**, 219-225.

67. T. Liu and S. Kumar, *Quantitative characterization of SWNT orientation by polarized Raman spectroscopy,* Chem. Phys. Lett., 2003, **378**, 257-262.

68. C. Zamora-Ledezma, C. Blanc, M. Maugey, C. Zakri, P. Poulin, and E. Anglaret, *Anisotropic thin films of single-wall carbon nanotubes from aligned lyotropic nematic suspensions,* Nano Lett., 2008, **12**, 4103-4107.

69. D. Roy, S. Bhattacharyya, A. Rachamim, A. Plati, and M. L. Saboungi, *Measurement of interfacial shear strength in single wall carbon nanotubes reinforced composite using Raman spectroscopy,* J. Appl. Phys, 2010, **107**, 043501 1-6.

70. M. D. Frogley, D. Ravich, and H. D. Wagner, *Mechanical properties of carbon nanoparticle-reinforced elastomers,* Compos. Sci. Technol., 2003, **63**, 1647-1654.

71. C. C. Kao and R. J. Young, *Assessment of interface damage during the deformation of carbon nanotube composites,* J. Mater. Sci., 2010, **45**, 1425-1431.

72. S. Cui, I. A. Kinloch, R. J. Young, L. Noé, and M. Monthioux, *The effect of stress transfer within double-walled carbon nanotubes upon their ability to reinforce composites,* Adv. Mater., 2009, **21**, 3591-3595.

73. A. F. Fonseca, T. Borders, R. H. Baughman, and K. Cho, *Load transfer between cross-linked walls of a carbon nanotube,* Phys. Rev. B, 2010, **81**, 045429 1-7.

74. L. Zalamea, H. Kim, and R. B. Pipes, *Stress transfer in multi-walled carbon nanotubes,* Compos. Sci. Technol., 2007, **67**, 3425-3433.

75. L. S. Schadler, S. C. Giannaris, and P. M. Ajayan, *Load transfer in carbon nanotube epoxy composites,* Appl. Phys. Lett., 1998, **73**, 3842-3844.

Chapter 3   Electrospinning of PVA/SWNT fibres

3.1 Introduction

Electrospinning is the simplest method to produce fibres with the diameter ranging from tens of nm to a few μm. This technique has been attracting increasing research interest due to the wide range of potential applications of nanofibres. Electrospinning has also been proved to be an effective technique to disperse and orient carbon nanotubes (CNTs) in polymers. Kannan and co-workers demonstrated that individual and perfectly-aligned nanotubes can be achieved in electrospun fibres [1, 2]. This fibre-preparation technique, therefore, makes it possible to investigate the intrinsic properties of nanotubes and their interactions with polymers at the single nanotube level.

Although the set-up of electrospinning is simple, the process is complex with the resulting fibre diameter being influenced by many factors and variables [3]. A variety of theoretical and experimental investigations have been carried out to understand the effect of spinning conditions on fibre diameter. There are some conflicting conclusions as for the electro-spinability and governing parameters for the morphology and diameter of the fibre. For example, Fridrikh *et al.* found that the final diameter of the fibre was a function of surface tension, electric current and surface charge repulsion and they proposed a model to quantify the influence of these factors [4]. Thompson *et al.* considered many collection parameters for electrospinning and determined that five parameters including the volumetric charge density, distance from nozzle to collector, initial jet/orifice radius, relaxation time and viscosity of the solution have the most significant effect on the jet radius [5]. The other parameters such as the initial polymer concentration, solution density, electric voltage, perturbation frequency and solvent vapour pressure have moderate effects on the jet radius, and parameters such as the relative humidity, surface tension and vapour diffusivity have only minor effects on the jet radius.

Electrospun fibres deposited on a metal collector are obtained mostly in the form of randomly-oriented non-woven mats. For many applications, fibres macroscopically

aligned in one direction are required and macroscopical orientation can be achieved using electrostatic methods such as a directed electric field and mechanical methods such as a rotating drum [6]. For example, Li *et al.* designed a collector consisting of two conductive strips separated by a void gap of variable width [7]. They demonstrated that electrospun fibres could be aligned uniaxially over long length scales during spinning process. Zussman *et al.* used a high-speed rotating disk to collect aligned fibres. In their analysis they simulated the electrostatic field and found the applied electric field was concentrated on the tapered edge of the disk and hence the charged polymer jet was pulled towards the edge of the disk [8]. The fibres attracted to the disk were wound around the perimeter and were thus highly aligned, owing to the tangential force produced from the rotation of the disk.

In this study, poly(vinyl alcohol) (PVA) was chosen as the matrix for the preparation of polymer/CNT fibres due to the broad range of spinning conditions of the PVA, as well as its ability to stabilize the dispersion of nanotubes. This chapter aims to prepare PVA/SWNT fibres that are visible under the optical microscope so that the deformation process of individual fibre can be followed using Raman spectroscopy. The ideal sample would be individual fibres with a diameter of ~1μm spanning over and aligned perpendicular to the edge of a paper window. To this end, the spinning conditions need to be optimized to prepare fibres with the expected diameter. The spinning variables considered in this study include the electric voltage, the tip-to-collector distance, the polymer concentration and nanotube concentration. In addition, two different methods were employed to collect uniaxially-aligned isolated fibres.

3.2 Experimental

3.2.1 Materials

SWNTs were purchased from Carbon Nanotechnology Inc., and were grown by a high-pressure decomposition of carbon oxide (HiPco) process. The HiPco SWNTs were supplied in the form of "Bucky pearls" and the batch number was P0171. The

poly(vinyl alcohol) (PVA) was 98-99% hydrolyzed, with the average molecular weight of 85,000 - 124,000 g/mol, purchased from Sigma-Aldrich and used as received.

3.2.2 Preparation and characterisation of the PVA/SWNT solution

PVA/SWNT solutions with different concentrations of PVA polymer and nanotubes were prepared. Typically, 1.4 g of PVA was dissolved in 7.6 g of deionised water in a glass vial in which the temperature was maintained at 80 ℃. 1.4 mg of SWNTs was dispersed in 4 g of deionised water using a sonic probe (Cole-Parmer Ultrasonic processor CPX 750) with a power of 350 W. The probe was used for 2 min and left to rest for 2 min before the power was applied again. The SWNT/water suspension was ultrasonicated for a total of 30 min, with 30 min of rest. 1 g of the nanotube/water suspension was then added into the PVA solution (the concentration of nanotubes was approximately 0.03wt% in this case) and stirred intensively for 15 min. The PVA/SWNT blend solution was then ultrasonicated again using the sonic probe for another 60 min, with 60 min of rest.

To prepare a blend solution with a relatively high loading of SWNTs (0.2wt%), 2.8 mg of SWNTs were dispersed in 8.6 g of deionized water using the sonic probe for 30 min. 1.4 g of PVA was then added to the nanotube suspension and stirred at 80 ℃ for 3 hr. The mixture was ultrasonicated again using the sonic probe for another 60 min. An ice bath was employed to prevent excessive heating of the samples all the time during sonication.

The conductivity of the solution was measured using a SevenMulti conductivity meter (Mettler Toledo).

3.2.3 Electrospinning of PVA and PVA/SWNT composite fibres

The basic set-up for electrospinning consists of three components:

a) A flow controller, which was a multiple syringe Infusion/Withdrawal pump purchased from World Precision Instruments;

b) A high voltage power supply, which was a FC-series purchased from Glassman

High Voltage, Inc.;

c) A collector, which was a piece of grounded metal.

A syringe of 2 ml capacity and a needle with an outer diameter of 0.8 mm was attached to the pump. Electrospinning was then carried out under different processing conditions, e.g. the electric voltage was set between 5 and 25 kV, the tip-to-collector distance was in the range of 6 - 20 cm, and the concentration of PVA in water varied from 5 to 14% by weight.

To collect isolated and macroscopically-aligned fibres that are suitable for further deformation testing, a collector was designed following the method described in Ref. [9]. Two pieces of parallel aluminium foil which serve as two electrodes were placed on a polystyrene (PS) substrate and were separated by a gap of 8 mm. A paper window was put on top of the aluminium foils to collect fibres and the collection time was 3 - 5 s.

A rotary disk which could rotate at speeds ranging from 0 to 1700 rpm was also employed to collect the fibres. The actual speed used is described in the text. A poly(methyl methacrylate) (PMMA) beam was attached to the disk to collect the fibre in different orientations by setting the beam at different angles.

3.2.4 Scanning electron microscope (SEM)

A Philips XL30 FEG SEM was employed to investigate the surface morphology and diameter of the electrospun fibres. For SEM observation, fibres deposited on aluminium foil were stuck to the SEM stubs which were then sputter coated with gold. SEM was operated with an accelerating voltage of 5 kV and images were acquired with a secondary electron mode. The images were then analysed using ImageJ.

3.2.5 Electric field simulation

The electric field strength between the syringe tip and the collector were calculated using the Maxwell finite element modelling software, Ansoft Maxwell 2D SV (academic product) [10].

3.3 Results and discussion

3.3.1 Fibre surface

The surface morphology of the PVA electrospun fibres was investigated using SEM and a typical image is shown in Figure 3.1. The surfaces were generally smooth and the diameter uniform along the axis for each single fibre. For different fibres, the diameter varied over a broad range and fibre branching were observed. The formation of branches is due to the primary jet splitting into multiple jets when travelling from the pipette to the collector. The branches and merged fibres make it complicated to analyse the diameter distribution of the fibre. In this study, all branches except those that were far smaller and shorter than the average values were counted in when measuring the average fibre diameter.
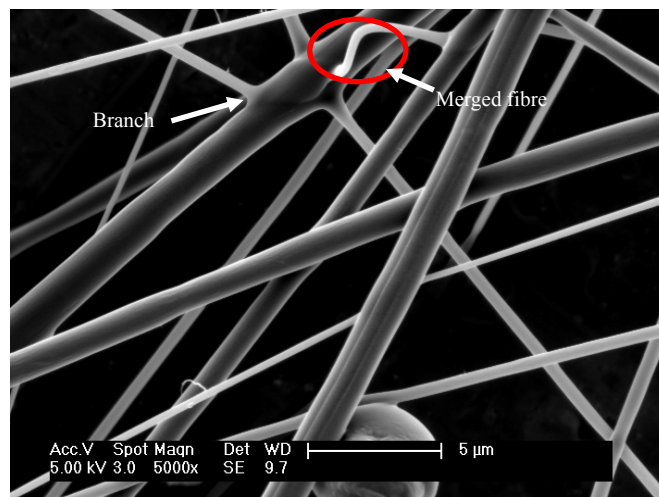
Figure 3.1 SEM micrograph of the PVA electrospun fibres showing the smooth surface, branches and diameter distribution of the fibres.

3.3.2 Effect of processing conditions on the fibre diameter

3.3.2.1 Effect of the PVA concentration

Concentration of the polymer solution is an important parameter that influences the morphology and diameter of the resultant fibres. Fibres spun from solutions with different concentrations of PVA without nanotubes were examined using SEM as shown in Figure 3.2. The fibre develops from a bead-on-string structure at low concentration (5wt%) to smooth and bead-free surface at higher concentrations, which

is related to the viscosity of the solution and to the polymers available for fibre formation.

The formation of beads on the fibre can be understood considering the interplay between the three most important forces acting on a polymer jet, i.e. the Coulomb force, the viscoelastic force and the surface tension [11]. For low-concentration solutions that have a low viscosity, the viscoelastic force is comparatively smaller than the Coulomb force. This results in the over-stretching of a charged jet, hence the break-up of the charged jet into many small spherical droplets as a result of their surface tension [11]. The viscosity increases with the concentration of the solution and the viscoelastic force becomes larger than the Coulomb force at higher concentrations. A smooth surface for the fibre can be obtained when the viscoelastic force is sufficient to prevent a charged jet from breaking up into small droplets [11].
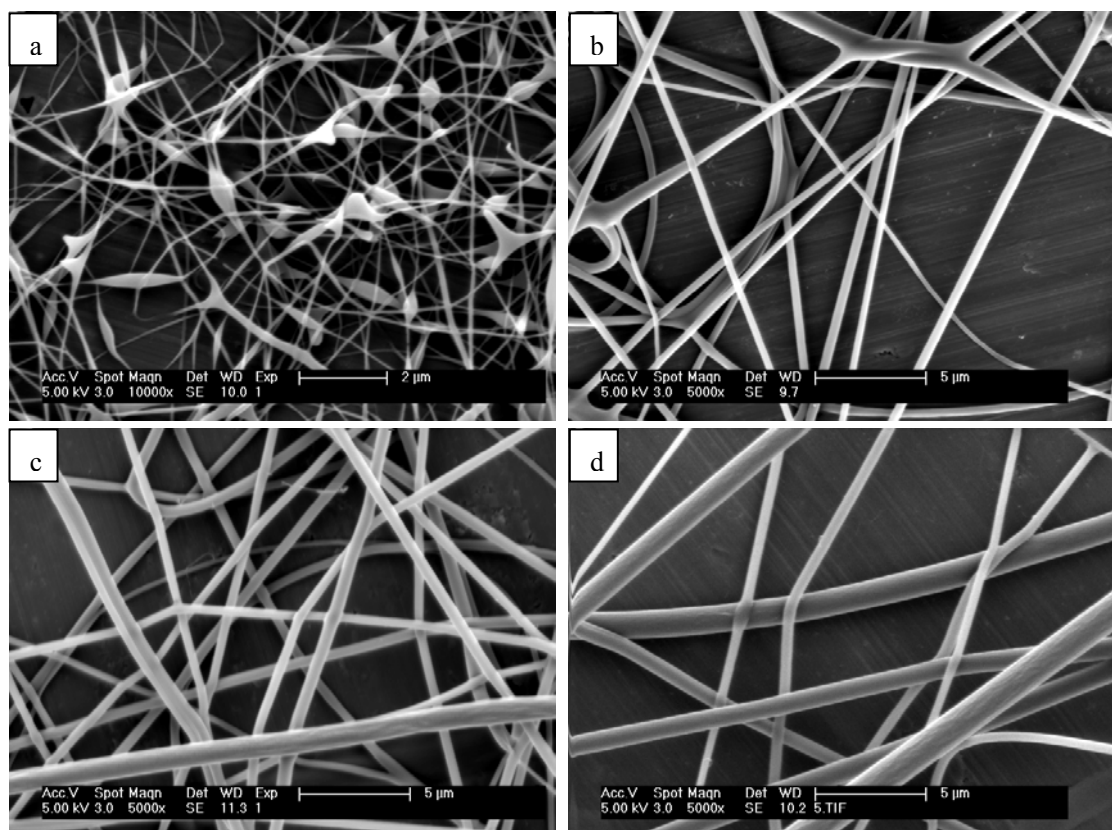
Figure 3.2 SEM images of PVA electrospun fibres with different polymer concentrations: (a) 5wt%, (b) 9wt%, (c) 12wt% and (d) 14wt%.

When smooth fibres can be produced, the diameter increases with the solution

concentration as can be seen from Figure 3.3. This is because when the solutions are more concentrated, there are more polymers available to be spun at the point where the droplet breaks down. Fibres with a diameter up to ~1.2 μm which are visible by eye and ideal for further manipulation can be spun from a solution using a concentration of 14%. This concentration was therefore chosen in this study as the standard solution for electrospinning.
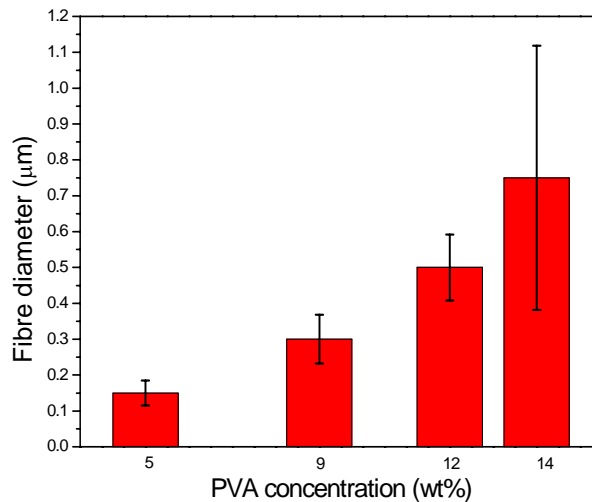
Figure 3.3 Effect of the polymer concentration upon the fibre diameter.

3.3.2.2 Effect of the SWNT concentration

Smooth fibres were also spun from the PVA/SWNT blend solutions. The morphology of the PVA fibres was unaffected by adding a small quantity of SWNTs as can be seen from Figure 3.4. The fibre diameter, however, was found to decrease slightly compared to the neat PVA fibres. This is possibly due to the change of physical properties such as the conductivity and surface tension of the solution induced by the nanotubes. The conductivity measured using a SevenMulti conductivity meter was found to increase from 0.55 mS/cm for the pure PVA solution to 1.07 mS/cm for the blend solution containing 0.2wt% of SWNTs. The net charge density on the jet increases as the conductivity increases, which leads to a stronger charge repulsion on the jet and consequently the enhanced force can stretch the jet thinner [12]. Recently, Molnar *et al.* demonstrated that the surface tension of the PVA solution decreases by adding nanotubes [13]. The effect of nanotubes on surface

tension of the solution might also be responsible for the decrease of the fibre diameter.
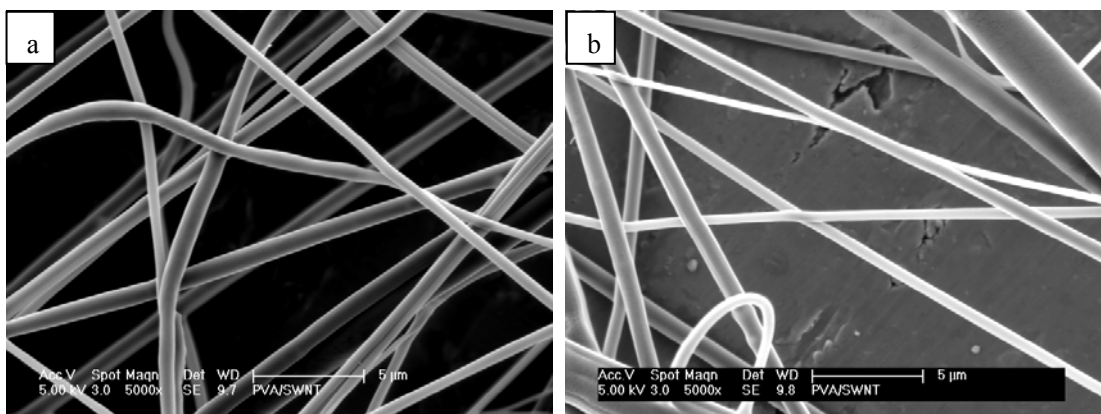
Figure 3.4 SEM images of PVA/SWNT fibres with different concentrations of nanotubes: (a) 0.03wt% and (b) 0.2wt% (PVA = 14wt%, voltage = 20 kV, tip-to-collector distance = 8 cm).

3.3.2.3 Effect of the electric voltage

The applied voltage can influence the electrospinning process through the charge density on the polymer jet and fibres spun at different voltages are shown in Figure 3.5. Ribbon-like structures were observed when a voltage of 5 kV was employed while circular fibres were obtained in the voltage range of 10 - 25 kV.

Flattened fibres are produced when a fraction of the solvent is trapped inside the fibres spun at a low electric voltage [14]. When the trapped solvent evaporates, the fibre collapses, giving rise to flat ribbons. As the voltage exceeded 10 kV in this case, the solvent has evaporated sufficiently before the fibres reached the collector, circular and smooth fibres were thus obtained.

The fibre diameter is presented as a function of the electric voltage in Figure 3.6 and it can be seen the voltage does not influence the fibre diameter significantly in the range of 10 - 25 kV. This is in agreement with the findings reported in Ref. [15]. Increasing the voltage increases the electric field strength and the repulsive force on the polymer jet which in turn thins down the fibres. This effect is, however, counteracted by the fact that the jets reach the collector quicker at higher voltages which results in larger fibres. It appears the voltage has a more pronounced effect on the deposition rate than on the fibre diameter [16].
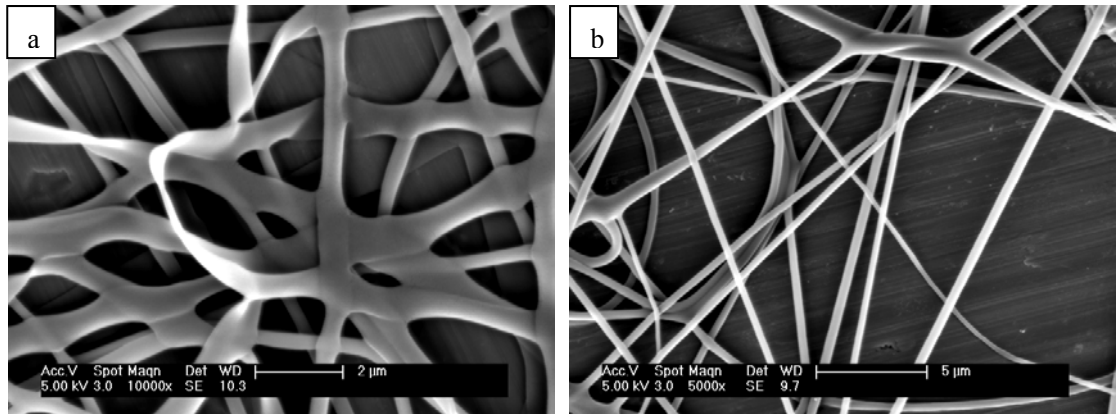
Figure 3.5 PVA fibres spun at different voltages: (a) 5 kV and (b) 20 kV (PVA concentration= 14wt%, tip-to-collector distance = 8 cm).
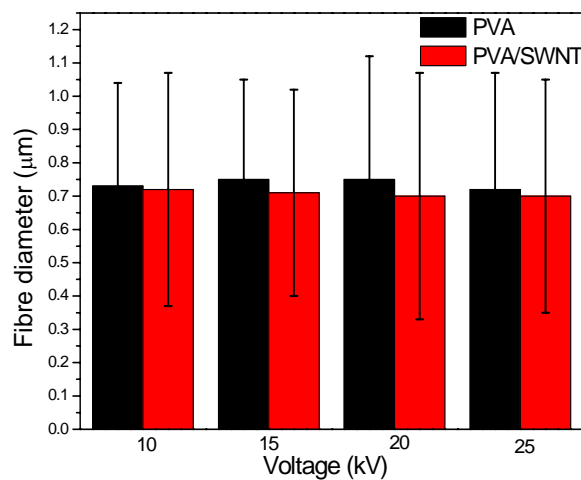
Figure 3.6 Fibre diameter as a function of the electric voltage (PVA = 14wt%, SWNT = 0.03wt%, tip-to-collector distance = 8 cm).

3.3.2.4 Effect of the tip-to-collector distance

The gap between the nozzle and the collector controls the travelling time for the polymer jet and is an important parameter that influences the electrospinning process. A significant decrease of the fibre diameter with increasing collection distance has been observed by a number of groups with different polymers [5, 17].

The tip-to-collector distance was changed in the range of 6 - 20 cm while keeping all other parameters constant to collect the fibres and it was found that smooth fibres could be obtained throughout this distance range. Diameters of the fibres produced under different separation distances are shown in Figure 3.7 and it can be seen the

effect of separation distance on the fibre diameter is negligible for both types of fibre. This suggests the electrospinning of the PVA and PVA/SWNT solutions can be carried out over a broad range of processing conditions.
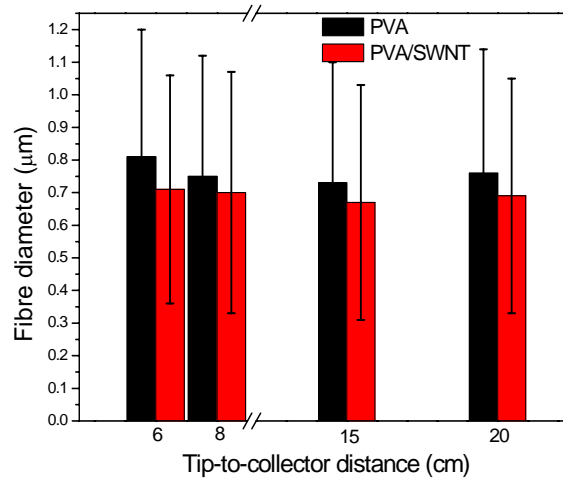
Figure 3.7 Fibre diameter as a function of the tip-to-collector distance (PVA = 14wt%, SWNT = 0.03wt%, voltage = 20 kV).

3.3.3 Uniaxially-aligned fibres

3.3.3.1 Fibres collected using parallel electrodes

Li et al. demonstrated that parallel electrodes separated by an insulator can direct the electric field such that fibres collected between the electrodes are uniaxially aligned [7]. Following their idea, a collector in which a pair of parallel aluminium strips sitting on a polystyrene (PS) substrate and separated by 8 mm was prepared to collect the fibres. Figure 3.8 shows the schematic of the set-up for collection of aligned fibres using Li's method [7].
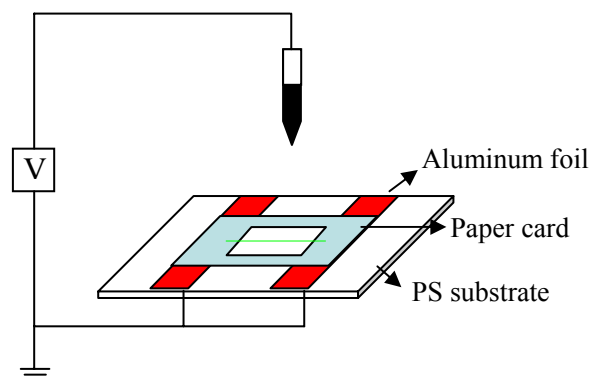
Figure 3.8 Schematic diagram of the parallel-strip collector used for fibre collection.

To prepare samples for deformation testing, a paper frame was placed on top of the parallel aluminium foils to collect the fibres. It can be seen from Figure 3.9 that fibres collected using the paper frame are mostly perpendicular to the edges of the window. The diameter of isolated fibres observed under the optical microscope was ~1 μm. These fibres are suitable to follow the deformation process of single electrospun fibres.
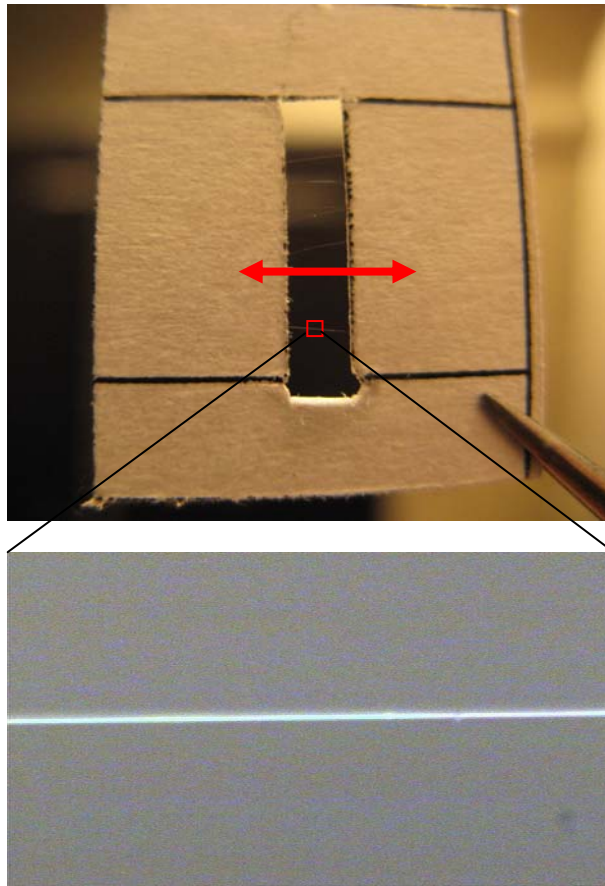
Figure 3.9 PVA /SWNT electrospun fibres collected over a paper frame and an optical microscope image of a single fibre.

The electric field strengths for both the plate collector and the parallel-strip collector were calculated using an Ansoft Maxwell program and the results are shown in Figure 3.10. For the plate collector, most of the electric field lines point towards the grounded plate, hence there is no preferred orientation for the fibres deposited on the plate. When using a pair of parallel strips as the collector, the electric field lines in the

vicinity of the electrodes are split into two components pointing towards opposite edges of the gap (Figure 3.10b). Placing a paper frame on top of the electrodes does not influence the electric field significantly as illustrated in Figure 3.10c.
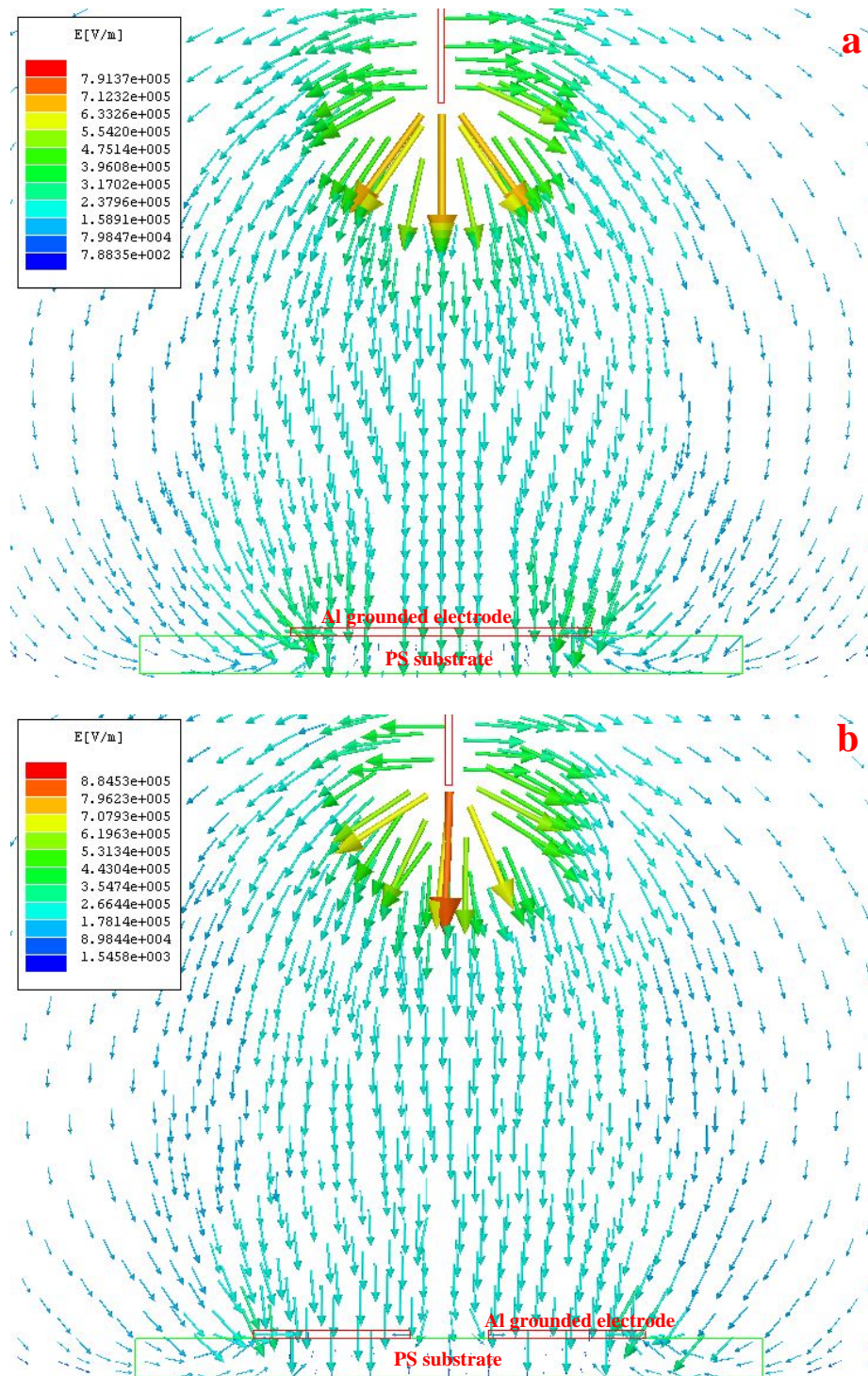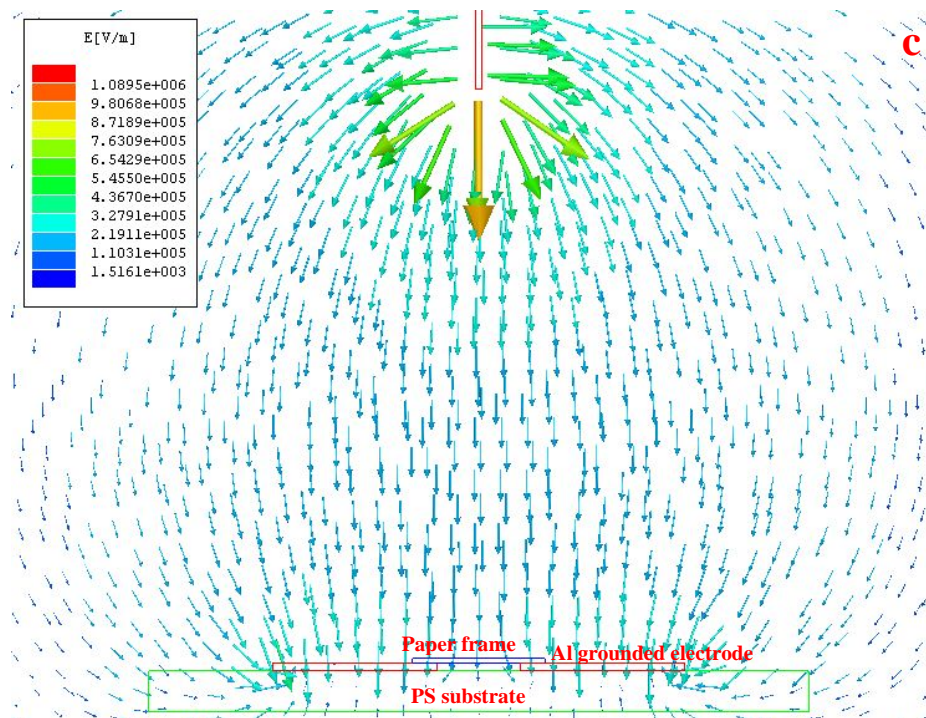
Figure 3.10 Calculated electric field strengths in the region between the needle and the collector: (a) a plate collector, (b) a separated parallel-strip collector and (c) a paper frame on top of the parallel-strip collector.

The orientation of the electric field lines has significant effect on the alignment of the electrospun fibres. There are three forces that ensure that the fibres deposited on the paper frame are aligned along the longitudinal direction (indicated as the red arrow in Figure 3.9) [7, 9]: firstly, the electric forces acting on the fibre between the two strips are in the same direction as the electric field lines; secondly, the positively-charged fibres induce image charges (i.e. negative charge) on the grounded electrodes, giving rise to strong Coulomb interaction at the two ends of the fibres, which further stretches the fibres to span over the gap; furthermore, the positively-charged fibres in the gap area repel each other to make a parallel alignment between them [7, 9].

3.3.3.2 Fibres collected using a rotary disk

A rotary disk was also employed to collect the fibres in this study and the schematic of the set-up is shown in Figure 3.11. A PMMA beam with dimensions of

6.8×1.4×0.25 cm was attached to the disk so that fibres could be collected directly on the beam for further characterisation.
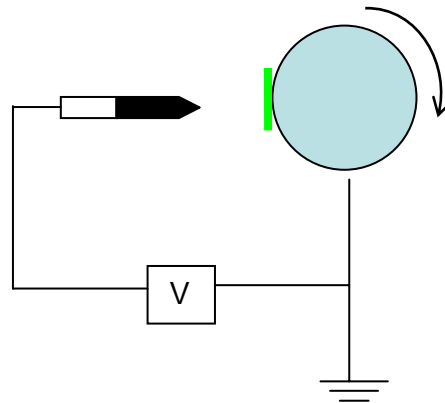
Figure 3.11 Schematic diagram of the rotary disk used for fibre collection.

Fibres collected with a rotation speed of 300 rpm and 1700 rpm are shown in Figure 3.12a and Figure 3.12b, respectively. It can be seen that the macroscopic orientation improves with the rotation speed. During electrospinning, the electric field is concentrated on the edge of the disk where the jets are attracted to. When the rotation speed is too low, the tangential forces are too weak to align the fibres such that the fibres are poorly-oriented on the collector (Figure 3.12a). The tangential forces increase with the rotation speed and at a certain speed the forces are high enough to align the fibres (Figure 3.12b) [6].
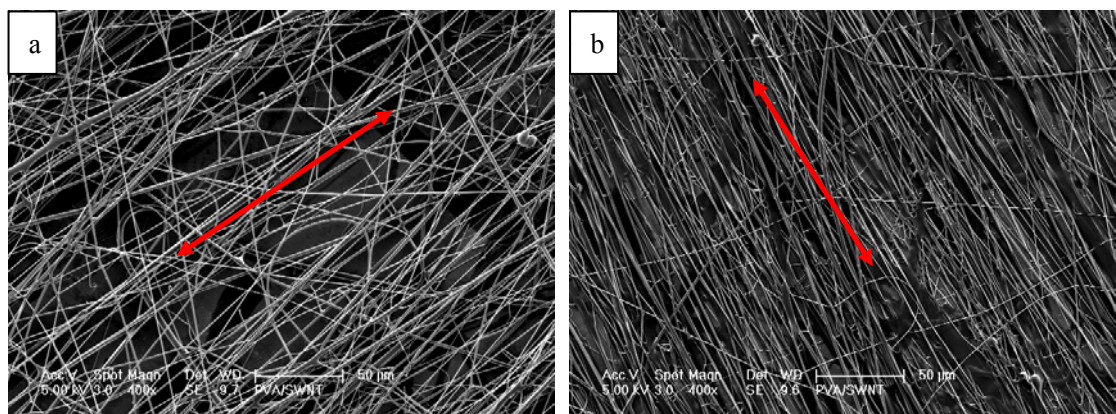
Figure 3.12 SEM micrographs of PVA/SWNT electrospun fibres collected using a disk rotating at a speed of: (a) 300 rpm and (b) 1700 rpm (PVA = 14wt%, SWNT = 0.03wt%, voltage = 20 kV).

The standard experimental conditions for electrospinning used in this study are

listed in Table 3.1. Two different types of nanofibres were prepared with different nanotube concentrations: a) a very low loading, of 0.03wt%, was used so that the nanotubes could be well separated and Raman spectra could be obtained from individual nanotubes in the electrospun fibres (Chapter 4); b) a relatively high loading (0.2wt%) of nanotubes was employed to achieve significant mechanical reinforcement for the polymer (Chapter 5).

Table 3.1 Standard conditions for electrospinning of PVA/SWNT fibres used in this study.

Fibre collection method	PVA concentration (wt%)	SWNT concentration (wt%)	Electric voltage (kV)	Tip to collector distance (cm)	Flow rate (ml/min)
Parallel-electrode	14%	0.03%	20	8	0.02
Rotary disk	14%	0.2%	20	8	0.02

3.4 Conclusions

Electrospinning is a complex process that is influenced by a large number of parameters. Smooth and circular PVA and PVA/SWNT fibres could be obtained under a broad range of conditions, i.e. with a PVA concentration of 6% - 14%, a voltage of 10 - 25 kV, and a tip-to-collector distance of 6 - 20 cm. The diameter of the fibres spun in these processing windows was found to vary from 0.1 to 1.2 μm, while outside these processing windows, irregular fibres were observed. Fibres spun from a solution with a PVA concentration of 5% exhibited bead-on-string structure, while using a voltage of 5 kV, ribbon-like structure was observed.

The average diameter of the fibre was found to decrease from 0.75 μm for neat PVA to 0.69 μm for fibres containing 0.2% of SWNTs and this could be caused by the increase of conductivity and decrease of the surface tension upon adding nanotubes. The effect of the tip-to-collector distance on fibre diameter was found to be negligible.

Macroscopically-aligned fibres were collected using both electrostatic and mechanical methods. A pair of parallel electrodes sitting on an insulator substrate can direct the electric field such that uniaxially-aligned fibres were obtained. A rotating disk which makes use of the tangential force on its sharp edge was also found to align the fibres efficiently. The effects of these processing conditions upon the morphology, diameter and alignment of the fibres were analysed in terms of the forces acting on the jet during fibre formation.

3.5 References

1. P. Kannan, S. J. Eichhorn, and R. J. Young, *Deformation of isolated single-wall carbon nanotubes in electrospun polymer nanofibres,* Nanotechnology, 2007, **18**, 235707-235713.

2. P. Kannan, R. J. Young, and S. J. Eichhorn, *Debundling, isolation, and identification of carbon nanotubes in electrospun nanofibres,* Small, 2008, **4**, 930-933.

3. S. R. Coles, D. K. Jacobs, J. O. Meredith, G. Barker, A. J. Clark, K. Kirwan, J. Stanger, and N. Tucker, *A design of experiments (DoE) approach to material properties optimization of electrospun nanofibers,* J. Appl. Polym. Sci., 2010, **117**, 2251-2257.

4. S. V. Fridrikh, J. H. Yu, M. P. Brenner, and G. C. Rutledge, *Controlling the fiber diameter during electrospinning,* Phys. Rev. Lett., 2003, **90**, 144502 1-4.

5. C. J. Thompson, C. G. G, A. L. Yarin, and D. H. Reneker, *Effects of parameters on nanofiber diameter determined from electrospinning model,* Polymer, 2007, **48**, 6913-6922.

6. D. Li and Y. Xia, *Electrospinning of nanofibers: reinventing the wheel?,* Adv. Mater., 2004, **16**, 1151-1170.

7. D. Li, Y. Wang, and Y. Xia, *Electrospinning of polymeric and ceramic nanofibers as uniaxially aligned arrays,* Nano Lett., 2003, **3**, 1167-1171.

8. A. Theron, E. Zussman, and A. L. Yarin, *Electrostatic field-assisted alignment of electrospun nanofibres,* Nanotechnology, 2001, **12**, 384-390.

9. D. Li, Y. Wang, and Y. Xia, *Electrospinning nanofibers as uniaxially aligned arrays and layer-by-layer stacked films,* Adv. Mater., 2004, **16**, 361-366.

10. http://www.ansoft.com/academic/, 2010.

11. C. Mit-uppatham, M. Nithitanakul, and P. Supaphol, *Effects of solution concentration, emitting electrode polarity, solvent type, and salt addition on electrospun polyamide-6 fibers: a preliminary report,* Macromol. Symp., 2004, **216**, 293-299.

12. T. Lin, H. Wang, H. Wang, and X. Wang, *The charge effect of cationic surfactants on the elimination of fibre beads in the electrospinning of polystyrene,* Nanotechnology, 2004, **15**, 1375-1381.

13. K. Molnar, E. Kost'akova, and L. Meszaros, *Electrospinning of PVA/carbon nanotube composite nanofibers: the effect of processing parameters,* Mater. Sci. Forum., 2008, **589**, 221-226.

14. A. Baji, Y. W. Mai, S. C. Wong, M. Abtahi, and P. Chen, *Electrospinning of polymer nanofibers: Effects on oriented morphology, structures and tensile properties,* Compos. Sci. Technol., 2010, **70**, 703-718.

15. C. Zhang, X. Yuan, L. Wu, Y. Han, and J. Sheng, *Study on morphology of electrospun poly(vinyl alcohol) mats,* Eur. Polym. J., 2005, **41**, 423-432.

16. P. Kannan, *Stress transfer in carbon nanotube composite films and fibres,* PhD Thesis, University of Manchester, 2008.

17. T. Jarusuwannapoom, W. Hongrojjanawiwat, S. Jitjaicham, L. Wannatong, M. Nithitanakul, C. Pattamaprom, P. Koombhongse, R. Rangkupan, and P. Supaphola, *Effect of solvents on electro-spinnability of polystyrene solutions and morphological appearance of resulting electrospun polystyrene fibers,* Eur. Polym. J., 2005, **41**, 409-421.

Chapter 4   Raman spectroscopy of individual SWNTs in electrospun fibres

4.1 Introduction

Resonance Raman spectroscopy is a powerful tool to investigate the vibrational behaviour and electronic properties of SWNTs. It is particularly interesting to study the features of nanotube Raman bands at the single nanotube level as the intrinsic properties of SWNTs are chirality-dependent. Raman bands of individual nanotubes can be significantly different from those of nanotube bundles due to the effect of bundling on the electronic transition energies of nanotubes. In addition to the effect of aggregation state, other environmental factors such as the sample substrate and whether the nanotube is wrapped by a surfactant or other species, can also influence the E_{ii} transition energies, which in turn influence the features of Raman spectra [1, 2]. For example, it is well established that the frequency of the Raman radial breathing mode (RBM), ω_{RBM}, is dependent on nanotube diameter through the relation $\omega_{RBM}=A/d_t+B$, but various values for the parameter A and B have been proposed in the literature [1]. This means a systematic study of the effect of the environment is required if Raman spectroscopy is to be used in assessing the dispersion state and the composition of the sample.

Deforming a nanotube can change the C-C bond length and the E_{ii} transition energy. The deformation process, if followed using resonance Raman spectroscopy, can give insight into the electronic properties of the nanotubes. This is made even more powerful when deformation tests are performed on individual nanotubes. Moreover, when the strain is applied through deforming a nanocomposite in which nanotubes are embedded, the shift of the nanotube Raman bands allows the efficiency of stress transfer to be monitored [3].

In this chapter, Raman spectra of nanotubes that were well dispersed in electrospun fibres were studied. The effect of the environment on the RBMs, G-band and G'-band in terms of the band frequency, intensity and linewidth was investigated systematically. The Raman spectra of individual nanotubes in poly(vinyl alcohol)

(PVA)/SWNT electrospun fibres were compared with those of single nanotubes reported in the literature. The Raman spectra of individual nanotube during deformation were also studied and the response of the G'-band to tensile strain was found to depend on the nanotube chirality.

4.2 Experimental

4.2.1 Electrospinning of PVA/SWNT fibres

Electrospinning was carried out using a standard condition as listed in Table 3.1 in Chapter 3. The nanotubes were grown by a high-pressure decomposition of carbon oxide (HiPco) process and the concentration (relative to the PVA) in the blend solutions was approximately 0.03wt%. A paper frame was placed on top of a pair of grounded electrodes which were separated by 8 mm to collect the fibres. The collection time was limited to 5 s so that only a few isolated fibres were collected.

4.2.2 Deformation of the fibres

Optical micrographs of the PVA/SWNT electrospun fibres were shown in Figure 3.9 in Chapter 3. The two ends of the electrospun fibre were fixed using super glue to achieve good adhesion. The sample was then mounted on a tensile rig shown in Figure 4.1. Both sides of the paper frame were burnt away prior to tensile deformation. The gauge length of the window was 2 mm and a minimum strain step of 0.125% could be applied by turning the micrometer.
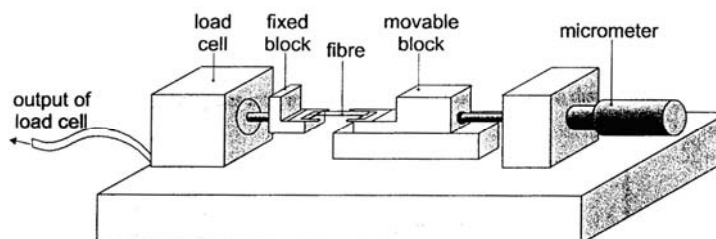
Figure 4.1 The tensile rig for deformation of single fibre [4].

4.2.3 SEM

A Philips XL30 FEG SEM was employed to investigate the aggregation state of the

nanotubes. Nanotubes dispersed using different sonication times were deposited on SEM stubs without coating and were observed directly using SEM which was operated at 20 kV. Images were acquired with a secondary electron mode.

4.2.4 Raman spectroscopy

Raman spectra were obtained using a Renishaw 1000 Raman spectroscopy system. A schematic diagram of the Raman spectrometer is shown in Figure 4.2. Two different laser lines were used in this study:

a) a He-Ne laser of wavelength $\lambda = 633$ nm ($E_{laser} = 1.96$ eV);

b) a near-infrared laser of wavelength $\lambda = 785$ nm ($E_{laser} = 1.58$ eV).

The laser beam was focused on the sample surface with a 50× objective lens and the diameter of the laser spot was about 2 μm. To prevent heating induced by the laser, a minimum laser power, of ~1mW was used. The exposure time was set at 10 s and an accumulation of 30 times was used. For deformation testing, a local reference point on the fibre was followed to return to the same location during straining.
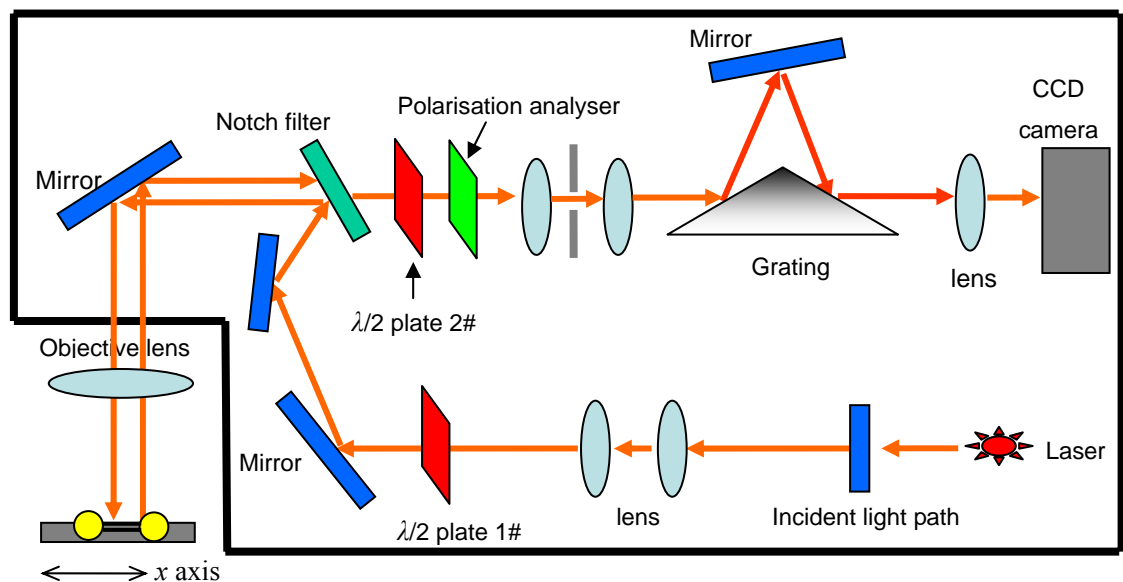
Figure 4.2 Schematic diagram of the Renishaw Raman spectrometer [5].

Polarized Raman spectroscopy was used to characterise the orientation of nanotubes in the fibres. Here, polarized Raman means the scattered light is polarized in one specific direction as the incident laser is always polarized in the Raman system.

Six different polarisation configurations can be achieved by adjusting the positions of the $\lambda/2$ plate and polarisation analyser. For the system equipped with the He-Ne laser, the direction of the incident and scattered laser relative to the reference x axis of the stage and the corresponding positions of the optical components for different polarisation configurations are listed in Table 4.1.

A rotary stage was employed to change the angle between the sample axis and the direction of laser polarisation and Raman spectra were recorded at different angles.

Table 4.1 Direction of the incident and scattered lasers relative to the reference x axis and the position of the optical components for different polarisation configurations [5].

	VN	VV	VH	HN	HH	HV
Direction of incident laser	//	//	//	⊥	⊥	⊥
Direction of scattered laser	No orientation	//	⊥	No orientation	⊥	//
$\lambda/2$ Plate 1#	In	In	In	Out	Out	Out
$\lambda/2$ Plate 2#	Out	Out	In	Out	In	Out
Polarisation analyser	Out	In	In	Out	In	In

// : Laser parallel to the x axis.

⊥: Laser perpendicular to the x axis.

4.2.5 Raman data analysis

A Lorentzian function was used to fit the Raman spectra to determine the parameters of the bands. The function is written as:

$$I = \frac{I_p (2\Gamma)^2}{(2\Gamma)^2 + (\Delta v - \omega)^2}$$

(4.1)

where I is the intensity of the peak between any given wavenumber Δv, ω is the peak position in cm^{-1}, I_p is the intensity at peak point, and 2Γ is the full width at half maximum (FWHM) of the peak (also called the linewidth).

4.3 Results and discussion

4.3.1 Raman spectroscopy of individual SWNTs

4.3.1.1 Full spectrum of the electrospun fibres

Raman spectra of the HiPco SWNT powder and a single electrospun fibre are shown in Figure 4.3. For the Raman measurements, a minimum laser power, of ~1mW was used to prevent sample damage induced by the laser. The Raman spectra acquired at different times from the same area in the sample were found to be identical, suggesting that the sample damage effects were excluded. Characteristic Raman bands of the SWNTs can be seen clearly in the fibre even with an extremely low loading of SWNTs, which is due to the resonance effect which enhances the signal greatly [2]. It was noted the D-band intensity did not increase significantly in the electrospun fibre compared to that in the starting SWNT powder, indicating that the rigorous ultrasonication, which exfoliated the nanotubes efficiently, did not damage the sidewall structure of the nanotubes. As will be shown in the following sections, the nanotubes in the electrospun fibre have been exfoliated into individual ones or small bundles. The vibrational and electronic properties of nanotubes with different chiralities, and the effect of dispersion state on the Raman bands could be investigated with these fibres.
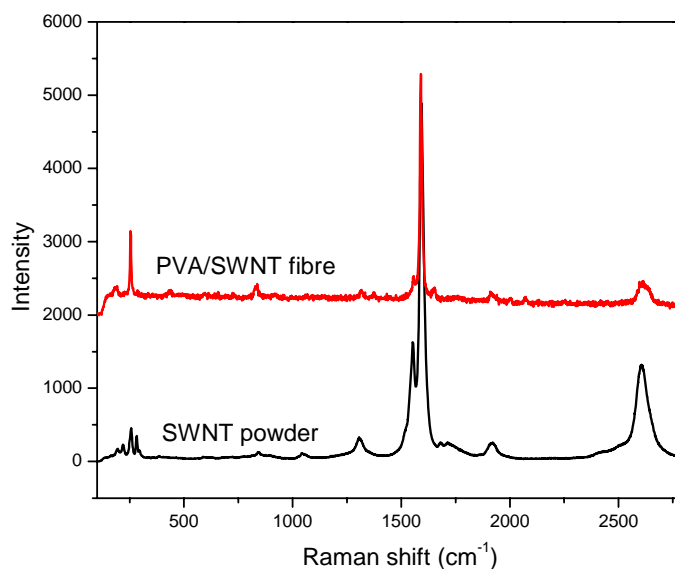
Figure 4.3 Raman spectra of the HiPco SWNT powder and PVA/SWNT electrospun fibre. Excitation laser: He-Ne 633 nm.

4.3.1.2 RBMs

Figure 4.4 shows a Raman spectrum in the radial breathing mode region taken for the HiPco SWNT powder. With the 633 nm laser (E_{laser}= 1.96 eV), resonance occurs for energy transition between the first valence band and conduction band (E_{11}^{M}) for metallic nanotubes and between the second pair of sub-bands (E_{22}^{S}) for semiconducting nanotubes. The peaks below 230 cm^{-1} are from metallic nanotubes whereas the peaks above 240 cm^{-1} are from semiconducting nanotubes. The natural linewidth of the RBM peak of an individual nanotube is 3 cm^{-1} [2], thus each of the broad bands in Figure 4.4, centred at 195 cm^{-1} (2Γ = 14 cm^{-1}), 219 cm^{-1} (2Γ = 11 cm^{-1}) and 257 cm^{-1} (2Γ = 12 cm^{-1}), has contributions from a group of nanotubes. The question arises as how many peaks should be used to fit the spectrum? This can be determined if the chiralities of the resonant nanotubes are known. We determined this by scanning the laser along the electrospun fibres as will be described in the following sections.

The nanotube chirality is characterised by a pair of indices (n, m), and those with the same value of ($2n + m$) can be classified into the same family [2]. The family members are close in RBM frequency (sometimes overlapping each other), which usually makes the RBM bands broad in the spectra of SWNT bundles. The RBM family bands become separated as the nanotube diameter decreases, such as for the peaks at 282 cm^{-1} and 295 cm^{-1} in Figure 4.4. As will be shown in the following sections, there are four nanotube families identified in the HiPco bundles when excited with the 633 nm laser, i.e. ($2n + m$) = 30, 27, 23 and 19, respectively. Within a single nanotube family, both the diameter and chiral angle decrease with increasing RBM frequency [2]. This important rule helps to identify the chirality of nanotubes that are close in RBM band frequency.
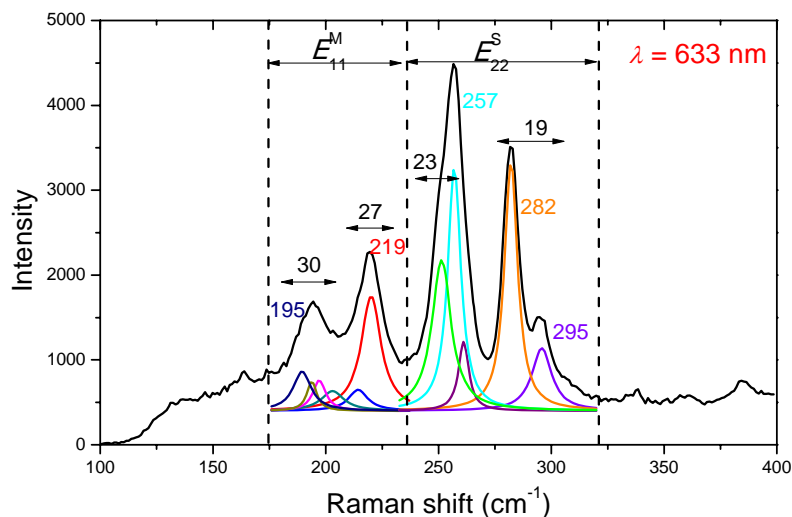
Figure 4.4 Low-frequency Raman spectrum of the HiPco SWNT powder excited with the 633 nm laser. The black numbers denote the values of (2n+m) for the family of nanotubes contributing to the Raman peaks.

In contrast to the SWNT powder which shows multiple RBM peaks and uniform spectra throughout the sample, the PVA/SWNT (0.03wt%) electrospun fibres exhibit a single peak, double peaks, multiple peaks or no peak at all in the low-frequency region from different areas in the fibres. The areas which exhibit single RBM peak are of particular interest because single RBM peak implies nanotubes of single chirality are being probed. Twelve different RBM peaks, with a typical linewidth of 5 cm^{-1}, were observed using the 633 nm laser. These RBM peaks, along with their corresponding G-bands and G'-bands are shown in Figure 4.5. Also shown in Figure 4.5 are the spectra acquired from neat PVA electrospun fibres, from which broad and square peaks can be seen. These peaks are not associated with PVA polymers but are ascribed to the laser plasma lines. The generation of gas lasers, which involves the application of electrical current across a dielectric gas, also generates a great number of plasma lines. The Raman peaks for the He-Ne laser plasma lines are generally weak but are comparable with the nanotube bands when the resonance condition for nanotubes is not so good. It is relatively easy, however, to distinguish them from the nanotube bands as the plasma line peaks are broad and square, moreover, they do not overlap with the main bands of nanotubes as can be seen from Figure 4.5.
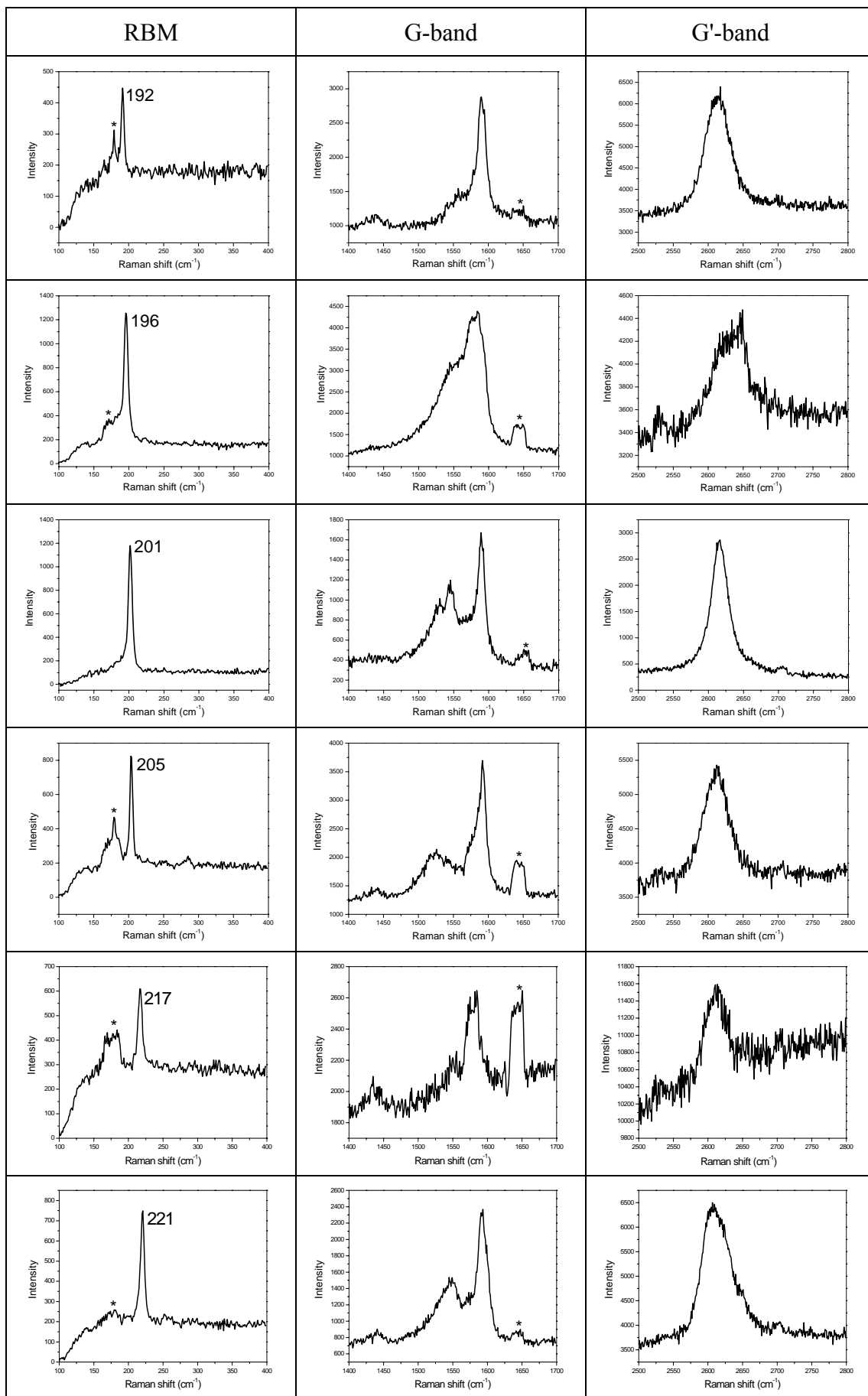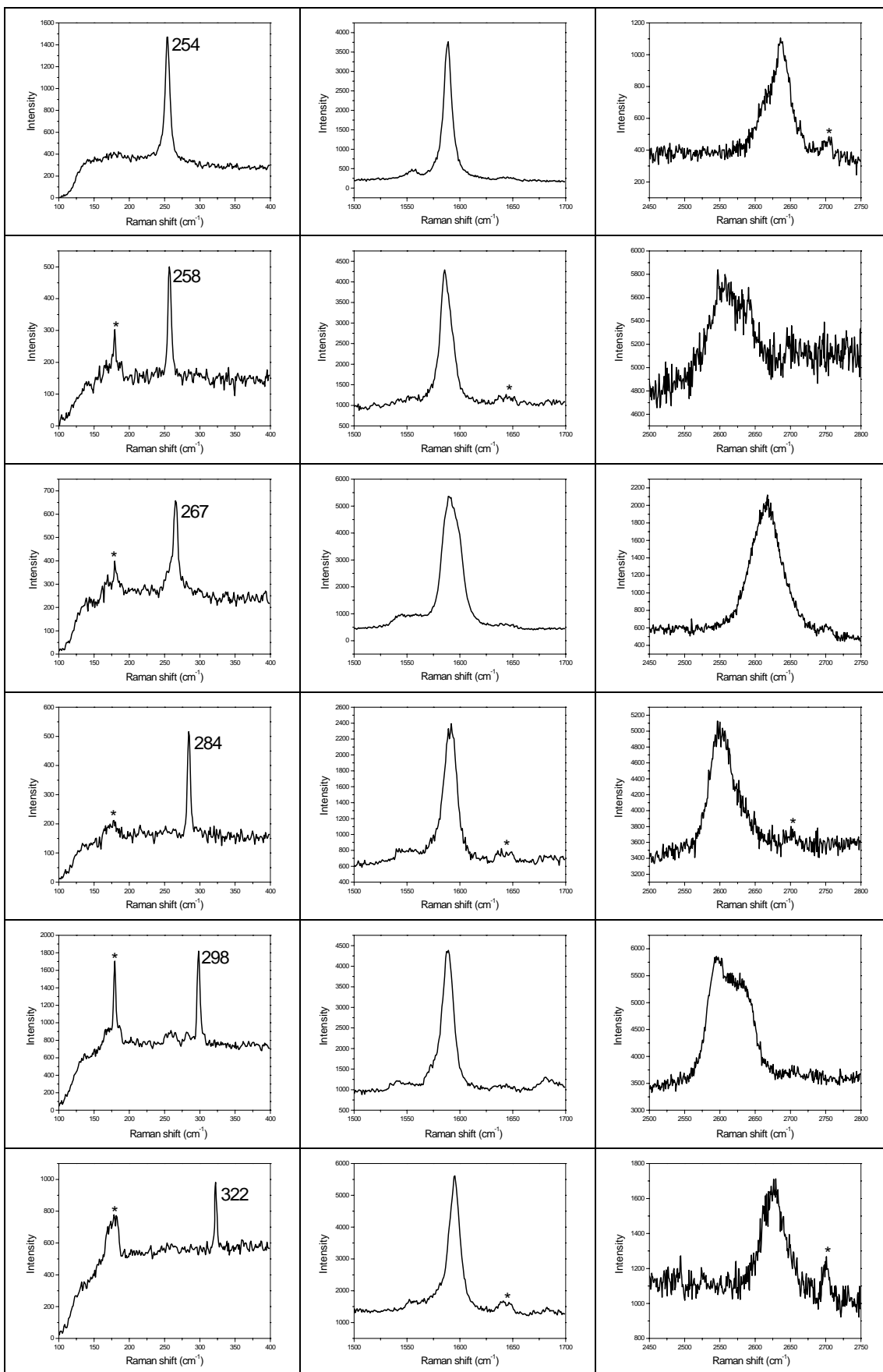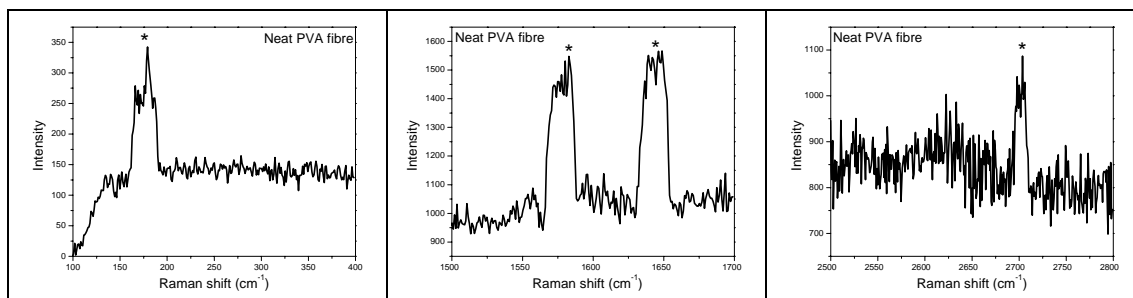
Figure 4.5 RBM peaks and their corresponding G-bands and G′-bands obtained using the 633 nm laser for the PVA/SWNT electrospun fibres. Raman spectra of neat PVA electrospun fibres in different frequency ranges are shown in the bottom row. The stars in the spectra denote peaks from the laser plasma lines.

The single RBM peaks observed in electrospun fibres means only one (*n*, *m*) species contributes to the Raman spectrum, which indicates the nanotubes are probably separated into individual ones in the fibres. Considering the volume fraction of nanotubes in the fibre of approximately 0.03% (since the SWNTs and PVA have about the same density ~1.3 g/cm^3), there are roughly 300 nanotubes on average in the cross section of the fibre (assuming the average $d_t = 1$ nm, and the nanotubes are arranged end-to-end in the fibres so that nanotubes have the same length as the fibres). This means there are on average 300 nanotubes in the laser spot from which the Raman spectra were taken. Among the multiple nanotubes, only one nanotube which was in resonance with the excitation laser was picked up (a schematic diagram is shown in Figure 4.6 in which the resonant nanotube is indicated as the shaded one) [6]. The non-resonant nanotubes contributed weakly to the Raman signal and were not seen in the spectrum. The reason we can obtain a signal from a single nanotube is due to the massive enhancement of resonance effect, which occurs when the excitation energy of the laser matches the electronic transition energy between the valence and conduction bands [2]. Even when the nanotubes were not truly individualised in the electrospun fibres, the vibrational and electronic properties of nanotubes with single chirality could still be investigated due to the resonance enhancement effect. In fact, some other evidence of the presence of single nanotubes in the electrospun fibres was found from the RBMs, G-band and G'-band, which will be discussed later.
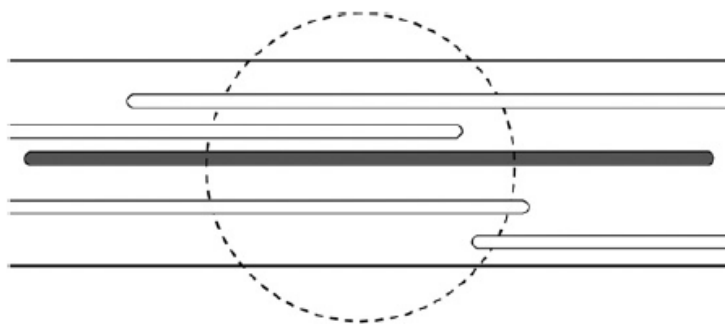
Figure 4.6 Schematic diagram of a single SWNT "seen" by the Raman microscope in an electrospun fibre (not to scale). The dashed circle represents the laser spot with a diameter of 2 μm [6].

The Raman spectrum excited with the near-infrared 785 nm laser provided strong evidence of individual nanotube in the fibres. Figure 4.7 shows a Raman spectrum obtained using the 785 nm laser for the HiPco SWNT powder, from which five RBM peaks centred at 204, 213, 223, 231 and 265 cm^{-1} can be seen. With the 785 nm laser (E_{laser} = 1.58 eV), resonance occurs for energy transition between the second valence band and conduction band of semiconducting nanotubes (E_{22}^S) and no metallic nanotube is in resonance with this laser.
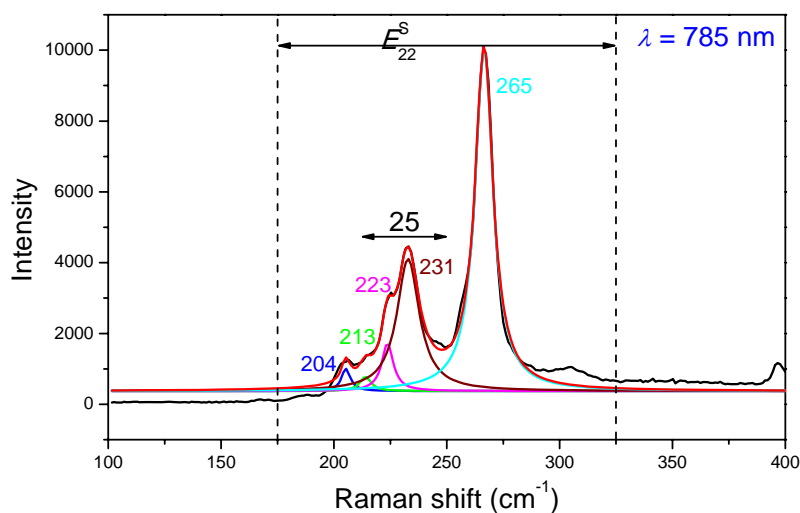
Figure 4.7 Low-frequency Raman spectrum excited with the 785 nm laser for the HiPco SWNT powder. The black number refers to the (2n + m) value for a nanotube family.

Figure 4.8 shows the RBM peaks of the SWNT powder together with those observed from a PVA/SWNT film and electrospun fibres prepared from the same

solution. In Figure 4.8a, the RBM peaks of the film are shifted to higher wavenumber by 2 - 6 cm^{-1} and the relative intensities of the RBM peaks are different compared to those of the SWNT powder. The dominant 265 cm^{-1} peak found in the SWNT powder becomes weaker than the 231 cm^{-1} peak in the film due to debundling of the nanotubes [7]. By scanning the laser along an electrospun fibre, single RBM peaks with a typical linewidth of 5 cm^{-1} were seen from different areas as shown in Figure 4.8b. This suggests the nanotubes vary in composition and dispersion state along the electrospun fibres. With the 785 nm laser, the G'-band was too weak to be resolved when single RBM peak was observed and is not discussed further in this work.
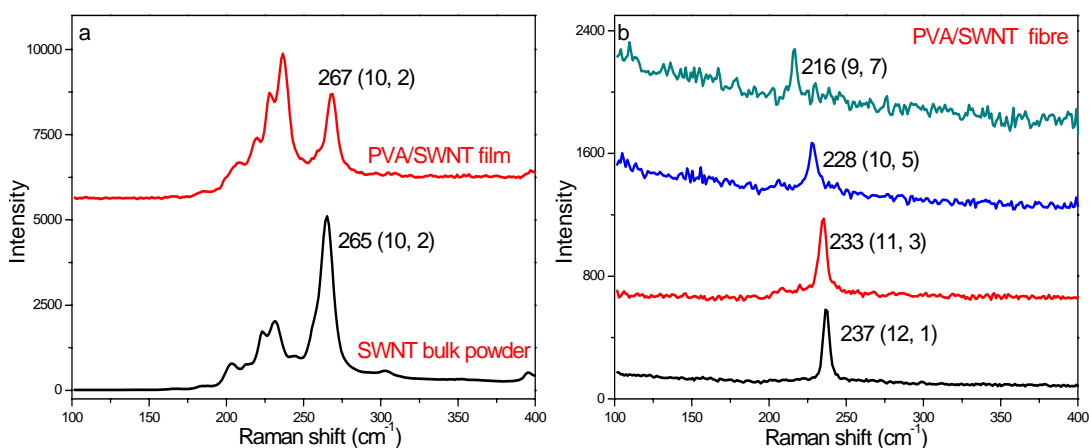
Figure 4.8 (a) RBM peaks of the SWNT powder and a PVA/SWNT film. (b)The single RBM peaks observed from the electrospun fibres. Excitation laser: 785 nm.

It has been found that when using the 785 nm excitation laser, the 267 cm^{-1} peak which corresponds to a (10, 2) nanotube appears only in nanotube bundles and it disappears when the nanotube is isolated [7-9]. This peak is thus known as the "roping peak" [7-9]. The "Roping in" behaviour is due to the effect of bundling on electronic transition energy (E_{ii}) of the nanotube. The strong intertube interaction in nanotube bundles results in a decrease in the energy gap of the van Hove singularities for semiconducting nanotubes. Theoretical studies have predicted that the value of E_{ii} can shift as much as 0.25 eV upon bundling [10]. Different (*n, m*) species may exhibit different degrees of down-shift and this effect is particularly strong for the (10, 2) nanotube [7, 8]. As the bundle size decreases, the E_{22}^{S} of the (10, 2) nanotube shifts

away from the laser excitation energy (which is 1.58 eV), which gives rise to a drop of the 267 cm^{-1} peak intensity; when the nanotube is isolated from others, the 267 cm^{-1} peak disappears completely.

The absence of the 267 cm^{-1} peak in Figure 4.8b is strong evidence that a fraction of nanotubes have been exfoliated into individual ones in the electrospun fibres. It is noted that the nanotubes in the film are still in bundles as indicated by the 267 cm^{-1} peak (Figure 4.8a), while individual nanotubes can be detected in the electrospun fibre in which no extra sonication was applied. This suggests the electrospinning process can exfoliate the nanotubes efficiently.

To identify the chirality of the RBM peaks, the electronic transition energies E_{ii} for different nanotubes (the Kataura plot) need to be known. A large number of values of transition energies for a large range of nanotube chiralities have been reported in the literature. The E_{ii} values for the same nanotube species in different samples can be significantly different. It appears each specific sample has its own set of E_{ii} values for the nanotubes [1, 11-13], which is attributed to the environmental effect. There are no E_{ii} data for HiPco SWNTs dispersed in PVA available to date. It is assumed that the PVA has an effect similar to sodium dodecyl sulphate (SDS)/water upon the E_{ii} values of HiPco SWNTs, and the data reported in Refs. [11, 14] for aqueous solutions of SDS/SWNT have been adapted here. The assumption will be justified later through a similar ω_{RBM}/d_t relation determined for the PVA/SWNT electrospun fibres to that found for the SDS/SWNT/water solution.

The experimental Kataura plot adapted from Refs. [11, 14] for isolated SWNTs is shown in Figure 4.9. As mentioned above, resonance occurs when the E_{ii} transition energy of nanotubes matches the E_{laser}, and the RBM intensity becomes weaker when the two energies deviate from each other. The maximum deviation of the E_{ii} transition energy from the E_{laser} that a nanotube can be detected is described by the so-called resonance window. This parameter can be determined by measuring the RBM intensity at different E_{laser} and is influenced by many factors such as the aggregation state and the chiral angle of nanotubes. The resonance window is 0.1 eV for nanotube bundles, while for isolated nanotubes dispersed in water and wrapped by SDS, it is

around 0.06 eV [2]. A value of 0.1 eV is used here as the resonance window for nanotubes dispersed in polymers can be broadened. We will revisit the broadening of resonance condition in Section 4.3.3 by following the RBM intensity during deformation.

The resonance window ($E_{laser}\pm0.1$ eV) around the red laser line (633 nm) is indicated by an orange box in Figure 4.9. Each of the eleven RBM peaks that are seen in Figure 4.5 (except for the 322 cm^{-1} peak) is then associated with a specific (n, m) species, and the assignment procedure is also shown in Figure 4.9. It should be noted that the RBM frequency for a single chirality determined from different areas in the fibres was not a constant value, due possibly to the environmental effect and the resolution of the Raman spectrometer. Slightly-different RBMs were assigned to the same nanotube species when they met some basic criteria such as [15]: 1) the spectrum could be fitted by a single Lorentzian peak; 2) the difference between the band frequency from the average value was less than 2 cm^{-1}; 3) the linewidth was lower than 10 cm^{-1}.

The chirality assignments of the RBMs and the experimentally determined E_{ii} energies are listed in Table 4.2 for metallic nanotubes and in Table 4.3 for semiconducting nanotubes. For the metallic nanotubes, each interband transition is split into upper and lower levels due to the trigonal warping effect, and Raman spectroscopy only probes the lower energy component of the transition [2]. The E_{ii} energies calculated using a theoretical model developed by Lucas *et al.* [16] are also listed in these tables as a comparison.

The chirality assignments for these eleven nanotubes are reliable because there are only 14 nanotube species in the resonance window (the orange box) and the E_{22}^{S} values are well separated from each other. The 322 cm^{-1} peak can be tentatively assigned to a (6, 4) nanotube. This nanotube has a small diameter and there is a large deviation between the E_{22}^{S} for this nanotube obtained by Raman and photoluminescence spectroscopies [2], which bring uncertainty in structural assignment of this RBM peak.

The nanotubes seen in the electrospun fibres should also be present in the starting SWNTs. The spectrum shown in Figure 4.4 has therefore been fitted with eleven peaks. As can be seen from Figure 4.9, other nanotube species such as the (11, 8) and (11, 5) nanotubes are expected to be in resonance with the 633 nm laser but have not been detected from the electrospun fibres. This may be due to their low populations in the electrospun fibres. It is also possible these nanotubes become off-resonance upon interacting with the polymer matrix.

Figure 4.9 The experimental Kataura plot for isolated HiPco SWNTs [11, 14]. The circles and squares denote semiconducting and metallic nanotubes, respectively. The red line indicates the excitation energy of the 633 nm laser and the orange box represents the resonance window. The black numbers denote the nanotube family by (2n + m) and the red numbers denote the nanotube chiralities of the RBMs observed from the electrospun fibres.

Table 4.2 Isolated metallic SWNTs observed in the PVA/SWNT fibres using the 633 nm laser.

RBM in PVA/SWNT fibre (cm⁻¹)	RBM in HiPco powder (cm⁻¹)	Chirality	Experimental E_{11}^{M} (eV)		Theoretical E_{11}^{M} (eV) [16]	
			Lower [11, 14]	Upper	Lower	Upper
192[a]	189	(12, 6)	1.92	--	1.90	2.01
196±0.3	193	(13, 4)	1.93	--	1.93	2.11

201±0.6	197	(14, 2)	1.92	--	1.96	2.19
205±0.5	203	(15, 0)	1.88	--	1.96	2.22
217[a]	217	(12, 3)	2.04	--	2.14	2.38
221±1.0	220	(13, 1)	2.02	--	2.16	2.46

--a: The standard deviation was not available.

Table 4.3 Isolated semiconducting SWNTs observed in PVA/SWNT fibres using the 633 nm laser.

RBM in PVA/SWNT fibre (cm^{-1})	RBM in HiPco powder (cm^{-1})	Chirality	Experimental E_{ii} (eV)		Theoretical E_{ii} (eV) [16]	
			E_{11}^{S} [13]	E_{22}^{S} [11, 14]	E_{11}^{S}	E_{22}^{S}
254±0.8	250	(10, 3)	0.99	1.96	0.87	1.84
258±0.9	257	(11, 1)	0.98	2.03	0.89	1.90
268±1.3	261	(7, 6)	1.11	1.92	0.92	1.85
284±0.9	282	(7, 5)	1.21	1.92	1.01	1.94
298[a]	296	(8, 3)	1.30	1.87	1.08	2.02
322[a]	--	(6, 4)	--	--		--

--a: The standard deviation was not available.

Using a similar method, chiralities of the RBMs that were observed using the 785 nm laser can be identified. Figure 4.10 shows the experimental Kataura plot along with the resonance window for the 785 nm laser as indicated by a blue box. Seven (*n, m*) species are found in the resonance window and six of them have been observed from the films and electrospun fibres. The (14, 1) nanotube is in the resonance window but has not been detected due probably to its low population. The chirality assignments are listed in Table 4.4 and it can be seen the broad band at 220 - 240 cm^{-1} in Figure 4.8 belongs to a nanotube family with ($2n + m$) = 25.
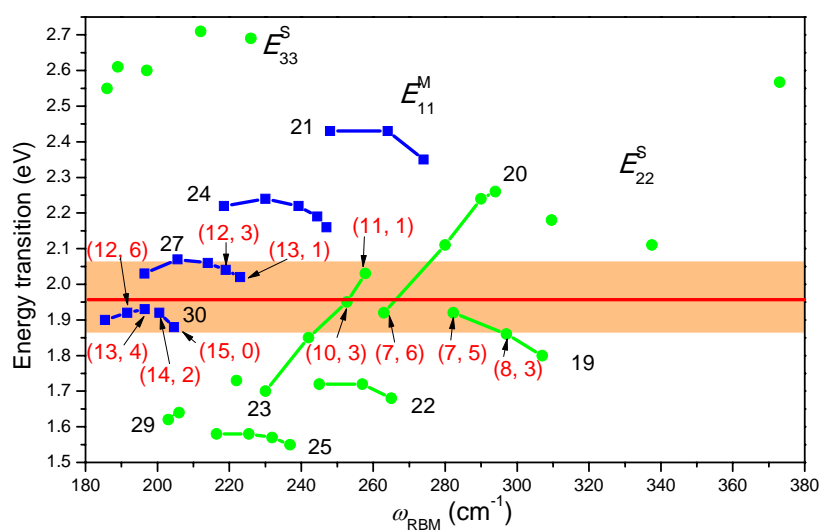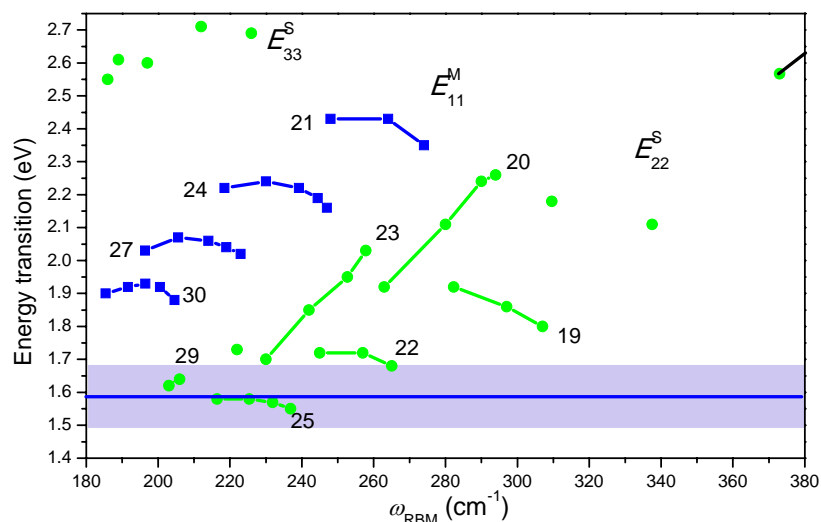
Figure 4.10 The experimental Kataura plot for isolated HiPco SWNTs [11, 14]. The circles and squares denote semiconducting and metallic nanotubes, respectively. The blue line indicates the excitation energy of the 785 nm laser and the light blue box represents the resonance window. The black numbers denote the nanotube family by (2n + m).

Table 4.4 Assignment of the RBMs observed using the IR785 nm laser.

RBM in PVA/SWNT fibre (cm^{-1})	RBM in HiPco powder (cm^{-1})	Chirality	Experimental E_{ii} (eV)		Theoretical E_{ii} (eV) [16]	
			E_{11}^{S} [13]	E_{22}^{S} [11, 14]	E_{11}^{S}	E_{22}^{S}
206[a]	204	(13, 3)	0.83	1.62	0.7	1.47
216±1.1	213	(9, 7)	0.94	1.58	0.76	1.48
228±0.9	223	(10, 5)	0.99	1.58	0.80	1.54
233±0.8	231	(11, 3)	1.04	1.57	0.84	1.57
237±0.9	--	(12, 1)	1.06	1.55	0.86	1.59
267±0.7	265	(10, 2)	1.18	1.68	0.96	1.78

--a: The standard deviation was not available.

The frequency and linewidth of the RBM peaks seen in the electrospun fibre are comparable to both those observed in the SDS/SWNT/water solutions [11, 14], and

are up-shifted by 1 - 6 cm^{-1} in frequency and narrowed by ~5 cm^{-1} in linewidth compared to those in the SWNT powder. The up-shift of the RBM frequency compared to the powder can be due to both the interaction of the nanotubes with the surrounding environment and the residual compression in the fibres. The similarity found in the electrospun fibres and in the SDS/SWNT/water solutions suggests similar environmental effect on nanotubes in these two samples. It also suggests the nanotubes are well debundled in the electrospun fibres.

The relative population of the nanotube species can be assessed by scanning the laser along the fibres. Figure 4.11 shows the possibility of appearance of all RBM peaks seen with the 633 nm laser and the 785 nm laser. Among the 62 single RBM peaks observed using the 633 nm laser from different areas, the peaks at 284 cm^{-1} and 254 cm^{-1} are the most frequently seen, which is in accordance with the strong intensity of these two peaks in the spectrum of bulk bundles. There is no obvious relation between the nanotube population and the chiral angle or diameter for the 11 nanotubes shown in Figure 4.11a. On the other hand, when using the IR 785 nm laser, it seems nanotubes with lower chiral angles are more abundant than those with higher chiral angles (54 single RBMs were recorded from random areas in this case), which is consistent with the findings in Ref. [7]. It should be pointed out the data indicates only the relative population of the nanotubes that are in resonance with these two lasers, and does not represent the overall trend or distribution of other nanotube species in the original HiPco powder. Ding *et al.* have predicted using a theoretical approach that high chiral angles are favoured during the nanotube growth for all preparation methods (Figure 4.11c) [17]. Dumlich et al. [18] and Miyauchi et al. [19] have also found that nanotubes with higher chiral angles are more abundant than those with lower chiral angles.
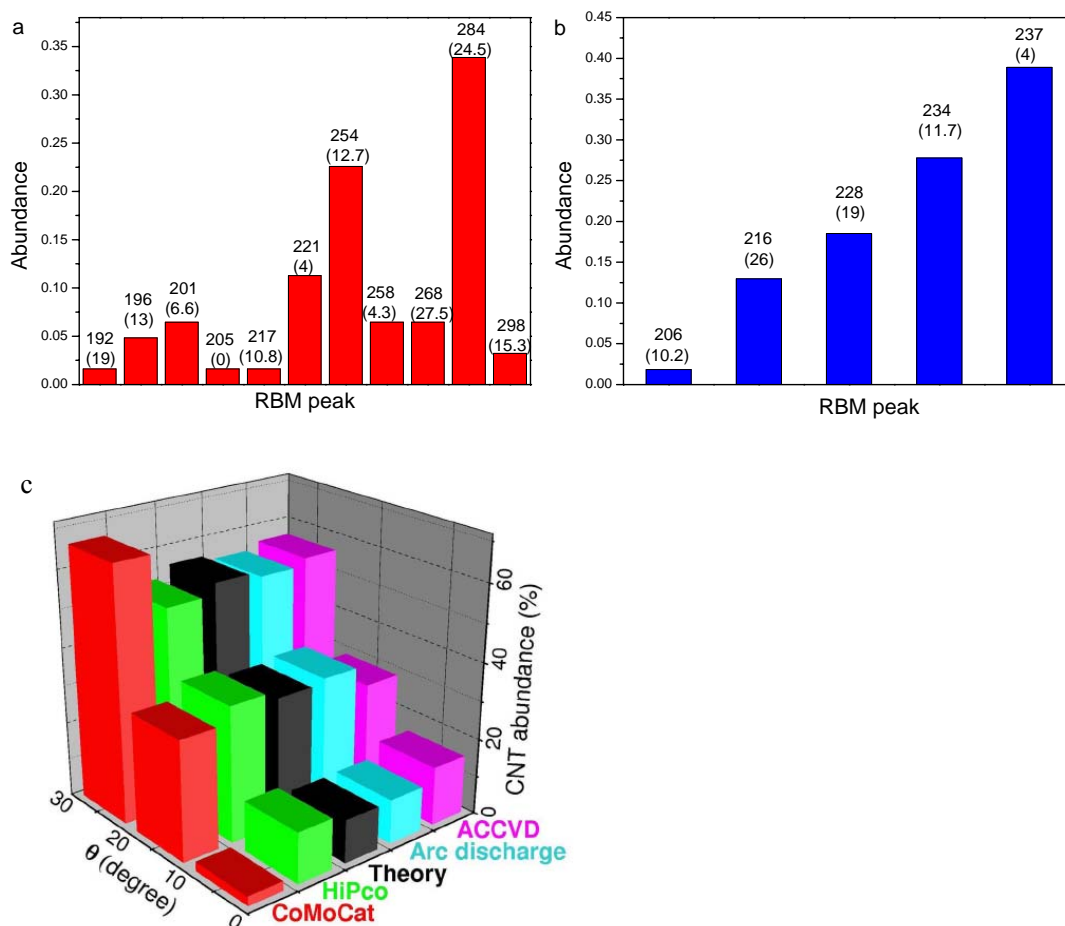
Figure 4.11 Relative abundance of nanotubes in the PVA/SWNT electrospun fibres observed using the 633 nm laser (a) and the 785 nm laser (b). The chiral angles are indicated in the brackets uder the RBMs in (a) and (b). (c) The distribution of SWNTs as a function of chiral angle reported in the literature [17].

4.3.1.3 The ω_{RBM}/d_t dependence

Although the RBM frequency is known to be dependent on the nanotube diameter through the relation: $\omega_{RBM} = A/d_t + B$, there is no unanimous agreement on the values of A and B. As discussed in Chapter 1, due to the different effects of environment on the RBMs, each nanotube sample has its own set of parameters to determine d_t from the RBM frequencies, which leads to uncertainty in chirality assignment.

As the chiralities have been assigned without using the ω_{RBM}/d_t relation, the values of A and B for the nanotubes dispersed in the electrospun fibres can actually be back-determined. The ω_{RBM} is plotted as a function of $1/d_t$ as shown in Figure 4.12, in

which the diameters were derived from the nanotube chirality (n, m) through:

$$d_{t} = 0.142\sqrt{3\left(n^2 + mn + m^2\right)}\Big/\pi \qquad (4.2)$$

A least-square fit to the data gives values of 219 nm cm^{-1} and 15 cm^{-1} for A and B, respectively. These values are in good agreement with those found in SDS/SWNT/water solutions (ω_{RBM}= 218/d_t+17) in Ref. [11]. This indicates the environmental effect on E_{ii} transition exerted by the PVA polymers is similar to that exerted by the SDS solutions.
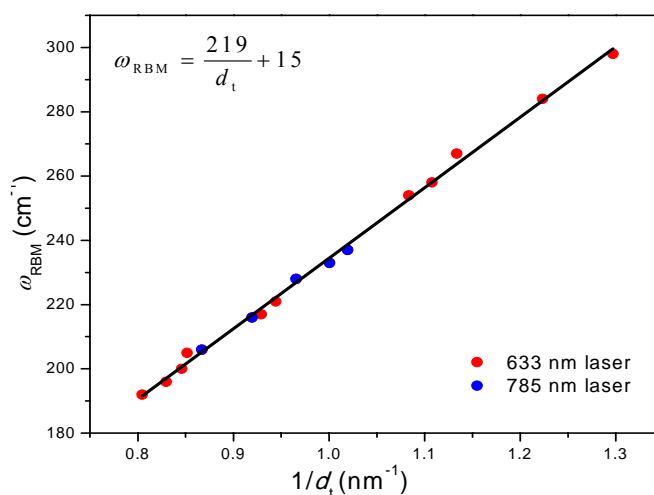
Figure 4.12 Experimental RBM frequencies as a function of the reciprocal of the nanotube diameter.

4.3.1.4 G-band

The G-band is a first-order Raman scattering process involving one-phonon emission. The information we can learn from the G-band of SWNTs includes [2]: 1) the nanotube diameter, 2) its electronic nature, i.e. whether it is metallic or semiconducting and 3) the charge transfer arising from doping a SWNT. The G-band can also reveal the state of dispersion of nanotubes as its lineshape for individual nanotubes is different from that for nanotube bundles [20, 21].

Figure 4.13 shows the G-bands and their corresponding RBMs obtained from the SWNT powder and PVA/SWNT electrospun fibres with different levels of dispersion. In Figure 4.13b, the nanotubes were ultrasonicated for a relatively short time (20 min) and were thus poorly dispersed in the fibres. While in Figure 4.13c, the nanotubes were ultrasonicated for a longer sonication time (90 min) and separated into

individual ones as evident by the single-narrow RBM peak. The G-band of the SWNT powder shows a dominating semiconducting nature and can be fitted with four Lorentzian lines, with the peaks centred at 1541, 1553, 1591 and 1600 cm^{-1}. The two higher-frequency peaks originate from the vibration along the nanotube axis and the two lower-frequency peaks are related to the vibration in the circumferential direction. The fitting parameters and the intensity ratio of the G-peaks for the G-band of different samples are listed in Table 4.5.
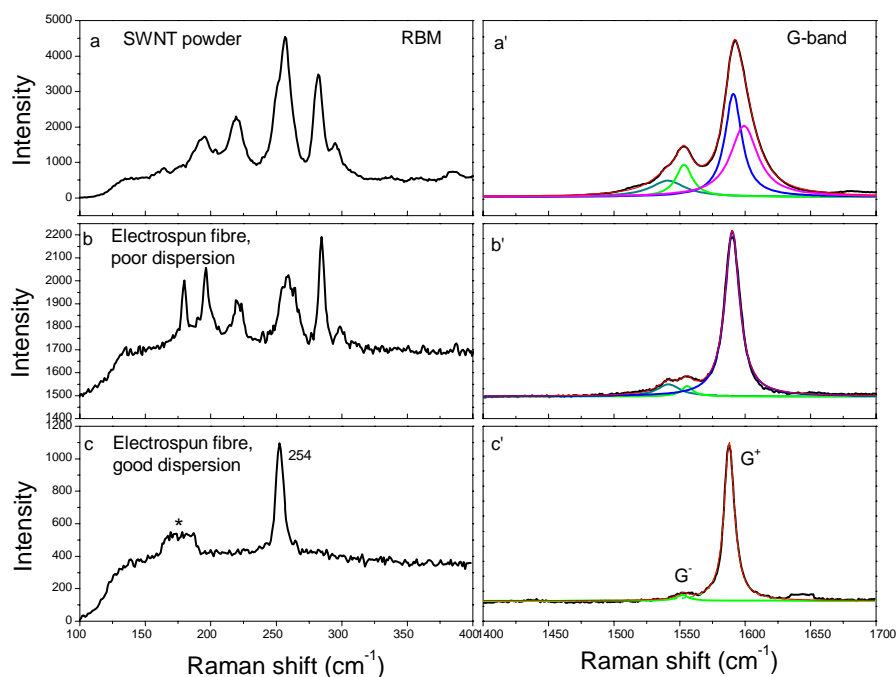
Figure 4.13 The G-bands and their corresponding RBMs at different dispersion states: (a) SWNT powder; (b) nanotubes poorly dispersed in an electrospun fibre (ultrasonicated for 20 min); and (c) an individual semiconducting nanotube in an electrospun fibre. The star denotes a laser plasma line. Spectra were obtained using the 633 nm laser.

The 1600 cm^{-1} peak vanishes as the bundle size decreases, as can be seen from Figures 4.13b and 4.13c. When a single nanotube is in incident resonance, the corresponding G-band can be fitted with two peaks locating at ~1588 cm^{-1} and ~1552 cm^{-1} which are denoted as the G$^+$ and G$^-$ peaks, respectively, as shown in Figure 4.13c [2]. The G$^+$ linewidth decreases from 16 cm^{-1} for the SWNT powder to 9 cm^{-1} for a single nanotube. The G$^+$ linewidth observed here, of 9 cm^{-1}, is comparable to those

found from individual nanotubes on a Si substrate, which is typically in the range of 5 - 10 cm^{-1} [22]. It is also noted the G^{-} intensity decreases significantly (or disappears completely in some cases) as the dispersion improves. This suggests the PVA polymers surrounding the nanotubes can suppress the vibration in the circumferential direction [20]. The vanishing of the G^{-} peak and narrowing of the G^{+} peak are important features of individual nanotubes, which have also been observed by other groups with individual nanotubes exfoliated by different dispersants [9, 20].

Table 4.5 The fitting parameters and intensity ratio I_{G^+}/I_{G^-} for the G-band of different samples.

Component	SWNT powder		PVA/SWNT fibre (Poor dispersion)		PVA/SWNT fibre (Good dispersion)	
	ω (cm^{-1})	2Γ (cm^{-1})	ω (cm^{-1})	2Γ (cm^{-1})	ω (cm^{-1})	2Γ (cm^{-1})
G^{-}	1541	32	1541	20	--	--
G^{-}	1553	15	1555	10	1552	11
G^{+}	1591	16	1590	13	1588	9
G^{+}	1600	25	--	--	--	--
I_{G^+}/I_{G^-}	3.2		16		28	

4.3.1.5 G'-band

The G'-band scattering involves a double resonance Raman process and provides valuable information on electronic structures of nanotubes. Figure 4.14 shows the G'-bands of the nanotube powder and a PVA/SWNT electrospun fibre. It is noted when multiple nanotubes are in resonance with the excitation laser, the G'-band appears as a single peak (or a broad peak containing a small shoulder) with the linewidth varies depending on the size of the nanotube bundle. The G'-band is broad when a large range of nanotubes with different diameters contribute to this band.
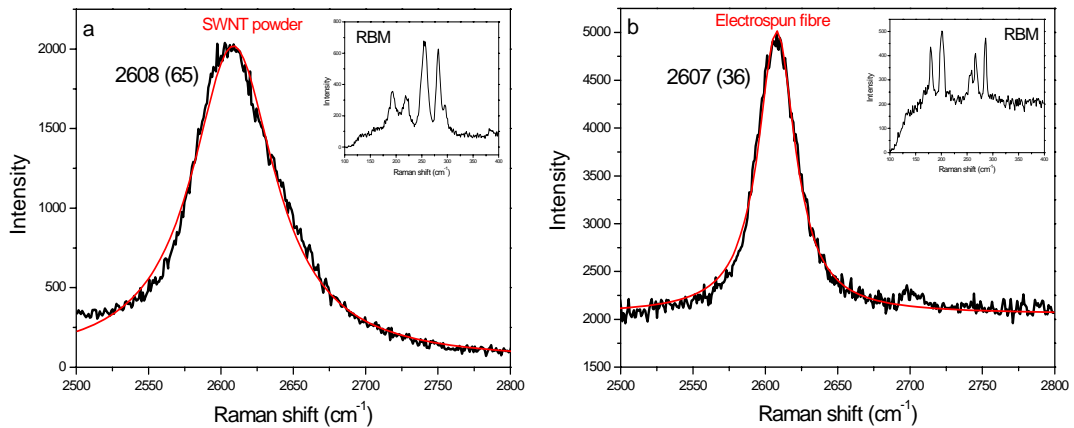
Figure 4.14 G'-band of: (a) SWNT powder and (b) electrospun fibres. Numbers in brackets denote the linewidth of the band and the inserts show the corresponding RBM peaks. Excitation laser: 633 nm.

In contrast to the single G'-peak observed for nanotube bundles, a double-peak structure for the G'-band was seen frequently when a single (n, m) nanotube was in resonance as can be seen from Figure 4.5. The double-peak structure of the G'-band has also been observed by a number of groups with different samples [23-25]. For SWNTs, there are three possible reasons responsible for the double-peak structure:

1) Two independent double resonance processes are involved for a single nanotube. This happens when one level of interband transition of a SWNT is in resonance with the incident laser while a lower level of interband transition is in resonance with the scattered photon [23, 24]. Two phonons, each having an energy of 0.165 eV are emitted in a G' scattering process, the energy of scattered photon is thus 0.33 eV lower than that of the incident photon. For individual semiconducting SWNTs, the two resonance processes happen when the different interband transitions are separated by ~0.33 eV, while for individual metallic nanotubes, as the E_{ii} transition are split into upper and lower bands due to the trigonal warping effect, both the upper and lower bands of the same interband transition can be involved simultaneously in the double resonance process. The E_{ii} energies for the 11 nanotubes that are listed in Table 4.2 and Table 4.3 were analysed using the experimental data or theoretical approach (for metallic nanotubes, a tight-binding model developed by Lucas has been used to calculate both the upper and lower E_{11}^{M}). Figure 4.15 gives two examples of the E_{ii}

transitions along with resonance windows for the (7, 5) semiconducting nanotube and the (13, 4) metallic nanotube. None of the 11 nanotubes shown in Figure 4.5 are expected to display a double-peak G'-band at the single nanotube level. The double-peak structures of the G'-band are therefore assumed to originate from multiple nanotubes.
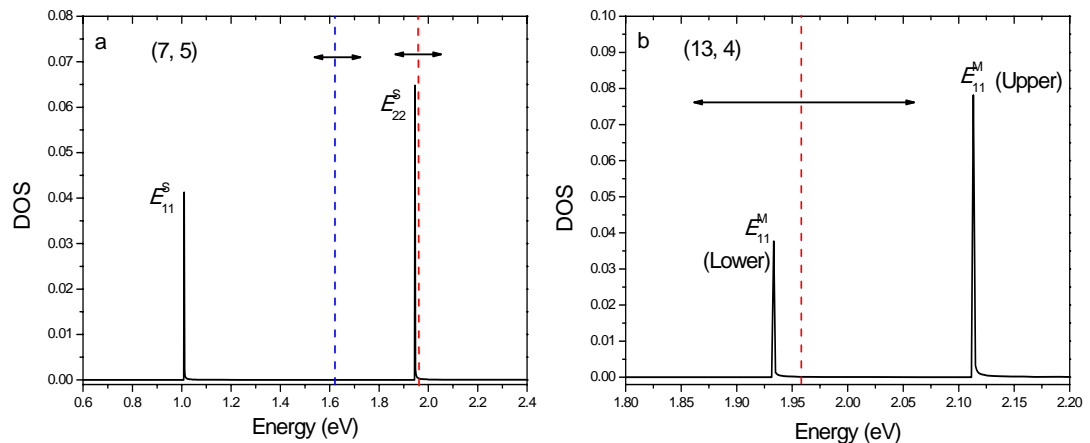
Figure 4.15 Density of electronic states as a function of the energy for: (a) the (7, 5) semiconducting nanotube and (b) the (13, 4) metallic nanotube. The vertical dashed lines represent the incident (red) and scattered photons (blue). The double arrows indicate the resonance window.

2) The double-peak structure of the G'-band can also be seen when two different nanotube species are involved in the double resonance, with one of them in incident resonance while another in scattered resonance. Specifically, the lower-frequency component is associated with the scattered resonance while the higher-component is related to the incident resonance, according to the $\omega_{G'} = 2420 + 106E_{laser}$ relation [2].

Figure 4.16 shows a double-peak G'-band observed from an electrospun fibre along with the Kataura plot. The scattered photon has an energy of 1.63 eV when using the 633 nm incident laser ($E_{scattered} = 1.96$-0.33 eV). It can be seen from the Kataura plot that there is a group of nanotubes in the resonance window of the scattered photon. The double-peak G'-band observed from the electrospun fibres can therefore be explained as one nanotube in incident resonance and another group of nanotubes in scattered resonance. The nanotubes in resonance with the scattered G'-photon are not in resonance with the scattered RBM photon (the phonon emitted in an RBM

scattering process is ~0.02 eV), these nanotubes are thus not seen in the RBM region. The G'-band and RBM can be seen simultaneously only when incident resonance occurs [2].
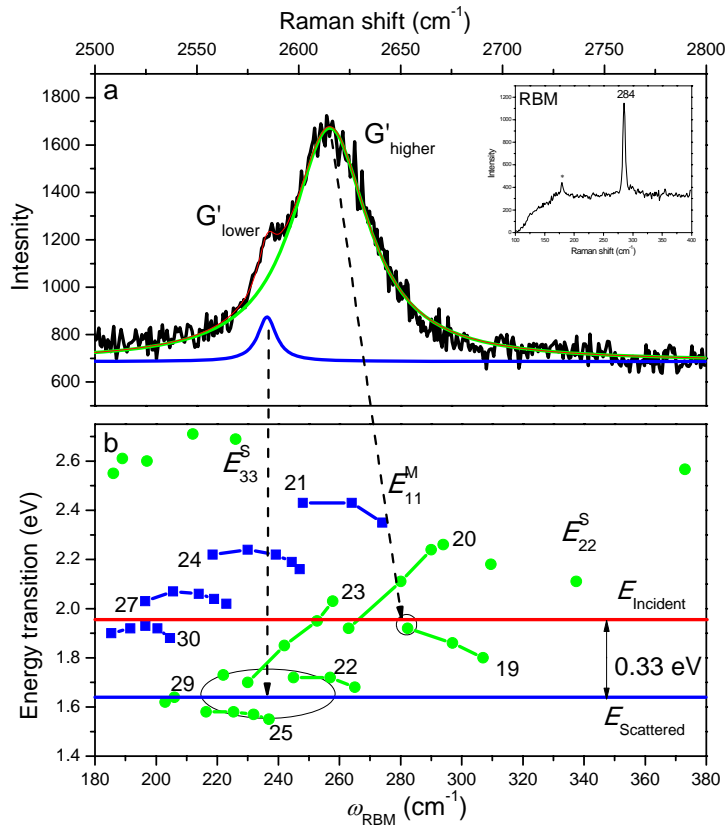
Figure 4.16 (a) Double-peak structure of the G'-band and the corresponding RBM peak observed from an electrospun fibre. (b) The experimental Kataura plot for isolated HiPco SWNTs showing two groups of nanotubes in incident resonance and scattered resonance, respectively. The red and blue lines in (b) indicate the energy of the incident photon and the scattered photon, respectively. The nanotubes in the oval are in resonance with the scattered photon.

3) In addition to the effect of E_{laser} on the $\omega_{G'}$, the nanotube diameter and the chiral angle also influence the G'-band frequency significantly, which is an important property of the SWNT G'-band. Another possibility for the double-peak structure is the presence of two (n, m) species that are both in resonance with the incident laser. The nanotubes display different G'-band frequencies due to their different diameters.

Two incident resonances, however, should give two peaks in the RBM region, which is not the case in Figure 4.5. When a double-peak RBM band is observed such

as the one shown in Figure 4.17a, the corresponding G'-band can be deconvolved to three peaks (Figure 4.17b). The two higher-frequency components correspond to the two nanotubes in incident resonance, while the peak at 2595 cm^{-1} originates from nanotubes in resonance with the scattered photon. The effects of both the diameter and the excitation energy on G'-band frequency are illustrated in Figure 4.17: the difference between the two higher-frequency peaks is due to the diameter dependence, while the difference between the 2595 cm^{-1} peak and the two higher-frequency peaks is attributed to the energy dependence.
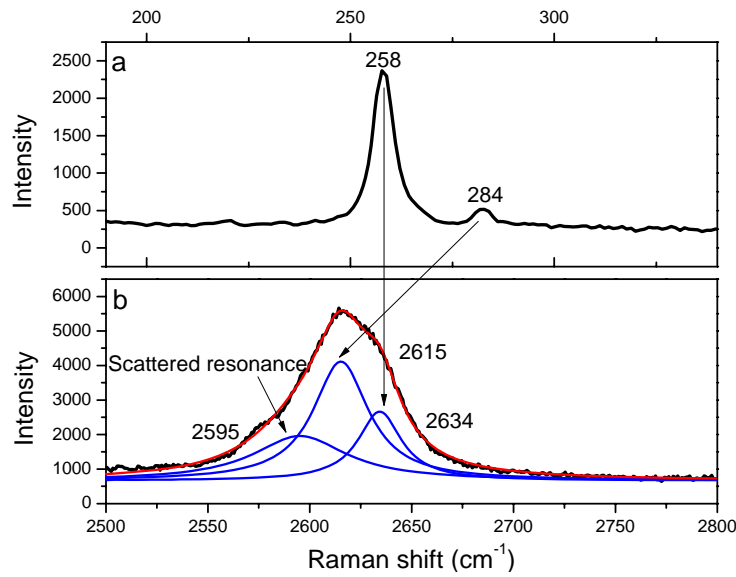
Figure 4.17 RBMs and the corresponding G'-band showing the incident resonance for two nanotubes and scattered resonance for another group of nanotubes. Excitation laser: 633 nm.

4.3.1.6 The $\omega_{G'}/d_t$ dependence

With a given E_{laser}, SWNTs display a range of G'-band frequencies due to the strong diameter and chiral angle dependence, a behaviour different from other sp^2 carbon based materials where a constant G'-band position is observed [2]. The chirality dependence of G'-band is attributed to the chirality dependence of the E_{ii} values. The dispersive behaviour of the G'-band overall is dependent on the quantized electronic states and the spring constant for the vibrations, which can be described as [26]:

$$\omega_{G'} = \omega_0 + \frac{C_i}{d_t} \tag{4.3}$$

where ω_0 is the frequency observed for 2D graphite. When considering the $\omega_{G'}/d_t$ dependence in a broad range of d_t such that different interband transitions are involved in resonance, the effect of spring constant plays a dominant role and a value of $C_i<0$ has been found, i.e. the $\omega_{G'}$ decreases as d_t decreases. This is associated with the softening of the spring constants for the vibrations as d_t decreases [26].

On the other hand, when analysing the $\omega_{G'}$ data within the same sub-band transition where the d_t varies in a small range, the quantized electronic states (double resonance effect) is the dominant effect. The value of C_i is greater than 0 in this case, which means the $\omega_{G'}$ decreases with increasing d_t. This is due to that the E_{ii} decreases as the nanotube diameter increases within a given E_{ii} branch, which leads to the resonance occurs at lower E_{laser} values. The value for the parameter C_i is different when different interband transitions are involved in the G'-band scattering. Souza Filho *et al.* determined a value of 34 nm cm^{-1} for E_{33}^S and 182 nm cm^{-1} for E_{44}^S, respectively [26]. No systematic study on the $\omega_{G'}/d_t$ relation for the resonance involving a E_{22}^S transition has been carried out before, and this study attempts to establish such a relation.

As discussed in Section 4.3.1.5, each (n, m) nanotube that is in incident resonance has a characteristic G'-band although the band frequency has been found to be spread over a relatively wide range. Figure 4.18 shows the G'-band frequency found from the PVA/SWNT electrospun fibres as a function of the nanotube diameter. Not enough data are available to give a statistical accuracy for the metallic nanotubes and the discussion is thus confined to the semiconducting nanotubes. The $\omega_{G'}$ value for each semiconducting nanotube is an average of at least five samples (except for the (8, 3) nanotube). It can be seen the nanotube diameter has a significant effect on the G'-band frequency, i.e. the $\omega_{G'}$ increases massively with increasing d_t. A least-square fit of Equation (4.3) to the data gives a relation: $\omega_{G'}= 2772-126/d_t$. In the first sense, this behaviour is in contrast to the analysis mentioned above where $\omega_{G'}$ is expected to decrease with increasing d_t. The expected negative dependence is based on the theoretical prediction that E_{ii} decreases as the diameter increases. The positive

dependence found here may not be too surprising, considering that the experimentally-determined value for E_{ii} does not decreases (actually increases slightly) with increasing d_t for these five semiconducting nanotubes as can be seen from Table 4.3. This apparent discrepancy is likely to arise from the interaction of nanotubes with the environment which has not been considered in the theoretical analysis.

The ω_0 value for 2D graphite, obtained by fitting the $\omega_{G'}$ data with Equation (4.3), of 2772 cm^{-1}, is higher than the accepted value (~2680 cm^{-1}). This is possibly brought about by the large variation of $\omega_{G'}$ within a single chirality. More $\omega_{G'}$ data for more nanotube species are needed to confirm the $\omega_{G'}/d_t$ dependence for the resonance involving a E_{22}^S transition.
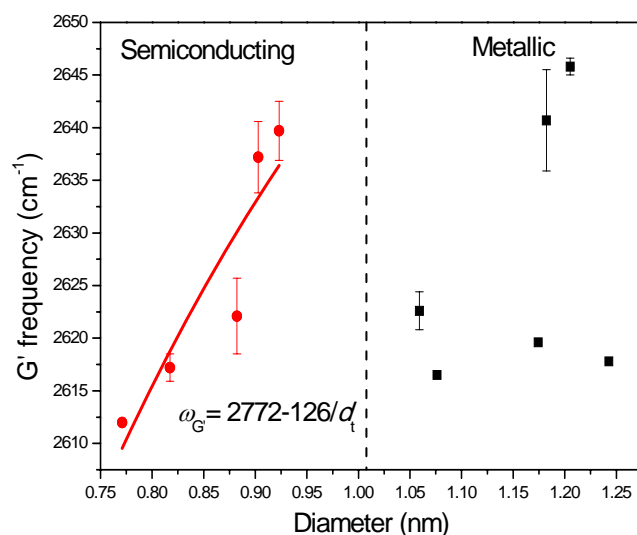
Figure 4.18 The G'-band frequency as a function of the diameter for nanotubes in resonance with the 633 nm laser. The red circles represent semiconducting nanotubes and black squares represent metallic nanotubes.

4.3.1.7 The G'-band linewidth

The G'-band linewidth is an indication of the state of dispersion of nanotubes. Cardenas *et al.* investigated the dependence of G'-band linewidth upon the aggregation state of nanotubes. They found that the linewidth decreases as the size of nanotube bundle decreases and the value for individual nanotubes is ~30 cm^{-1} [27]. Nanotubes dispersed in water using different sonication times were also examined by Raman spectroscopy in this study. Figure 4.19 shows SEM images of SWNTs for

different dispersion states and the evolution of the G'-band linewidth. It is evident that as the dispersion improves, the G'-band becomes narrower, which is consistent with Cardenas's findings [27].
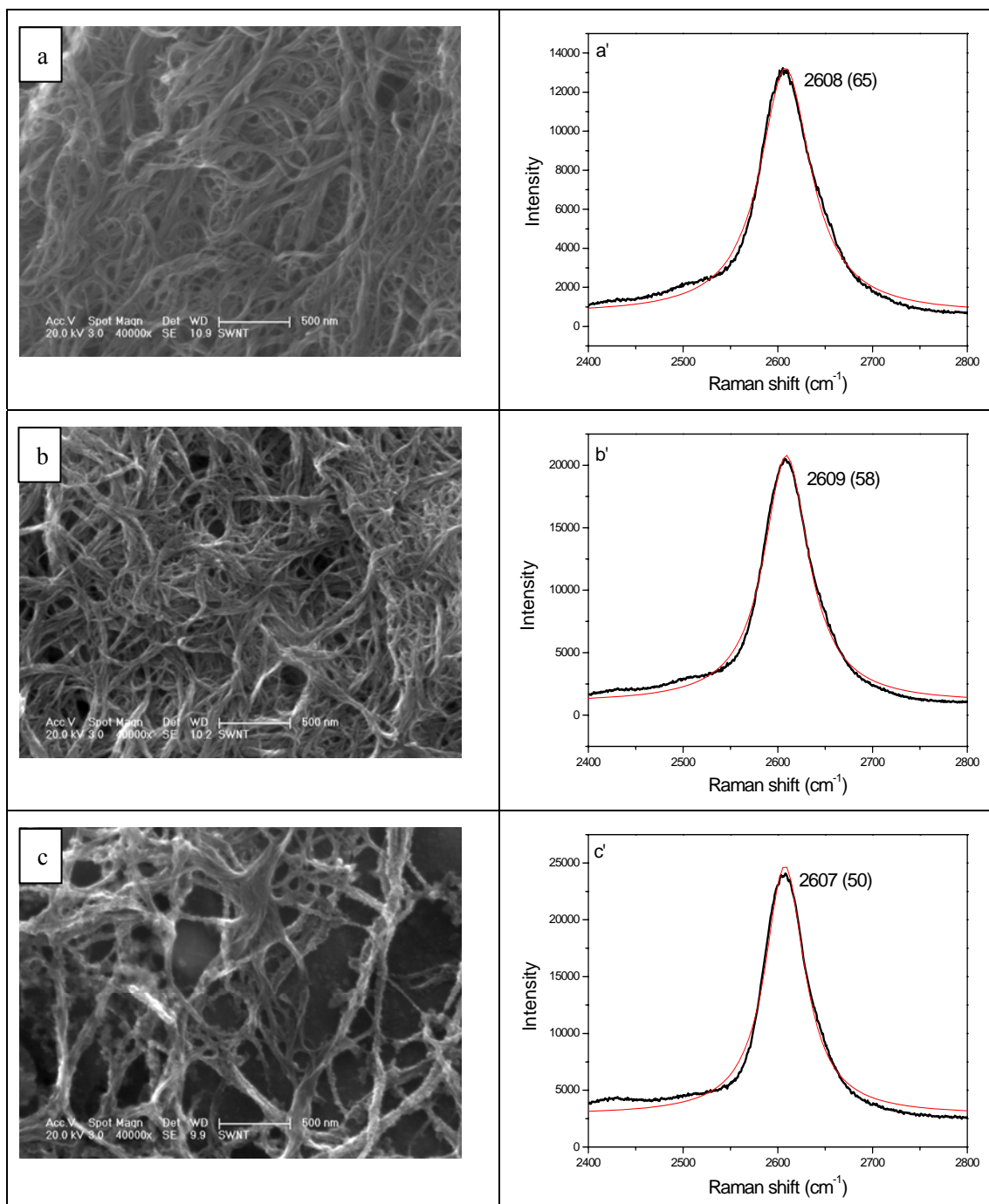
Figure 4.19 SEM micrographs and the corresponding G'-bands of SWNTs dispersed using different sonication times: (a) 0 min, (b) 2 min and (c) 30 min. The nanotubes were ultrasonicated in water and dried on SEM stubs for SEM and Raman measurements. The G' linewidths in cm^{-1} are indicated in brackets. Spectra were obtained using the 633 nm laser.

The G'-band lineshape observed from the electrospun fibres displayed a large variation, i.e. both single-peak and double-peak structures were observed when a single nanotube is in incident resonance. The spectral diversity may be due to the interaction of the nanotubes with the polymer matrix and different nanotube species being present in the laser spot. When a single-peak G'-band is seen, the linewidth ranges from 35 to 45 cm^{-1} which is much narrower than that of the powder (Figure 4.19). For the double-peak G'-band, the higher-frequency component of the G'-band which is assigned to the nanotube in incident resonance, exhibits a linewidth in the range of 18 - 45 cm^{-1} with most being below 35 cm^{-1}. This is similar to the linewidth observed for isolated SWNTs on a Si substrate [28], suggesting the presence of individual nanotubes in the electrospun fibres.

4.3.1.8 Summary

In summary, the single RBM peaks observed from the electrospun fibre allow Raman features of nanotube within a single chirality to be monitored, due to the resonance effect which enhances the Raman signal by $\sim10^3$ times. When a single RBM peak is observed, the Raman spectra show some features different from those of the SWNT powder and provide some evidence of single nanotubes in the fibres. The features that are believed to originate from single nanotubes are summarised as follows: 1) The RBMs: the band frequency was up-shifted by 1 - 6 cm^{-1} relative to that observed in the powder, and the linewidth was reduced from $\sim$11 cm^{-1} for the powder to $\sim$5 cm^{-1} for the individual nanotube. Furthermore, when using a 785 nm laser, the roping peak at 267 cm^{-1} which goes off-resonance when the nanotubes are dispersed individually, was absent in some areas in the electrospun fibres. 2) The G-band: The G$^-$ peak for semiconducting nanotubes became weaker and the G$^+$ peak became narrower, both features are typical for isolated individual nanotubes. 3) The G'-band displayed double-peak structure, and the frequency of the higher-wavenumber components increased with increasing nanotube diameter. The G'-band linewidth for the nanotubes in the electrospun fibres was much lower than that for the SWNT powder.

Evidence of individual nanotubes based solely on Raman spectra needs to be analysed carefully. By comparing the results in this study with those for individual nanotubes reported in the literature, it is safe to confirm the presence of individual nanotubes in the electrospun fibres because the Raman features meet the criteria for individualised nanotubes as described above and listed in Table 4.6.

Table 4.6 Raman criteria for individual SWNTs.

Band	Feature	Reference
RBMs	RBM frequencies are slightly higher and the linewidth are narrower for individualised nanotube than for bundles.	[2, 28]
	The 267 cm^{-1} peak vanishes when excited with the 785 nm laser.	[7, 8]
G-band	Linewidth: 5 - 10 cm^{-1} for the G$^+$ peak	[9, 20-22]
	Intensity: the G$^-$ peak at 1540 - 1580 cm^{-1} becomes weaker.	
G'-band	The linewidth decreases as the bundles size decreases and is 30 - 35 cm^{-1} for individual SWNTs.	[27]

4.3.2 Orientation of the nanotubes

Orientation of the nanotubes was characterised using polarized Raman spectroscopy. The nanotube G-bands obtained at different angles between the fibre axis and the axis of laser polarization are shown in Figure 4.20a. The intensities at different angles are normalised to that at 0° and plotted as a function of the angle as shown in Figure 4.20b. A line generated for a $I \propto \cos^4\varphi$ function (where φ is the angle between the fibre axis and the axis of laser polarization) which is expected to apply for perfect orientation of the nanotubes is also shown in Figure 4.20b [29]. The data scatter around the line due to the heterogeneity of the sample, making it difficult to perform quantitative analysis of the degree of alignment. The dramatic drop of Raman band intensity at 90° is, however, an indication of good orientation. As will be shown in Chapter 5, the nanotubes in electrospun fibres are almost perfectly aligned along the fibre axis.
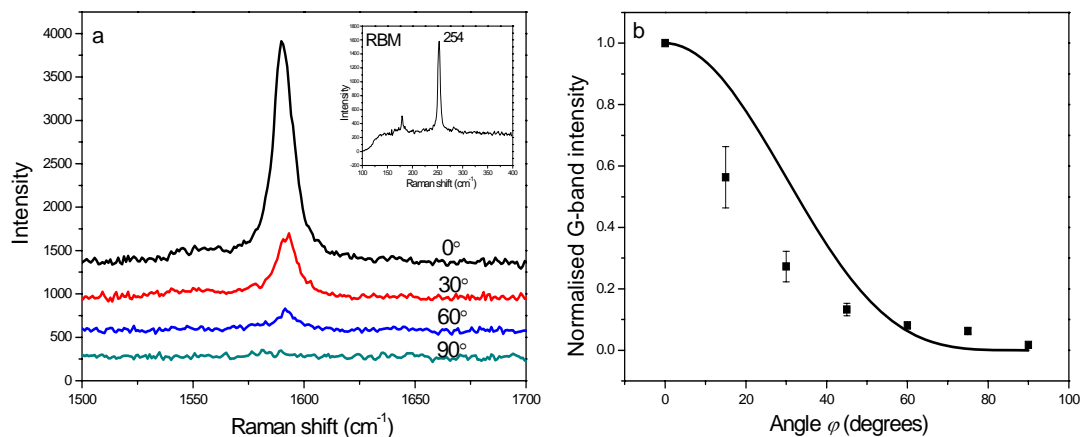
Figure 4.20 (a) Raman spectra of nanotubes at different angles between the fibre axis and the axis of laser polarisation. (b) The normalised intensity of the G-band as a function of the angle. Raman spectra were acquired with a VV configuration.

4.3.3 Deformation of individual nanotubes

Following the deformation process of a nanotube using Raman spectroscopy allows the electronic properties and mechanical reinforcing efficiency (in composites) to be monitored. Most deformation tests have been carried out to date on nanotube bundles which are an ensemble of nanotube chiralities, making it difficult to analyse the properties of a single chirality. With the Raman features and orientation of individual nanotubes in the electrospun fibres well established, we are now in a position to study the deformation process of individual nanotubes.

Deformation behaviours of individual nanotubes for 6 different chiralities were followed using Raman spectroscopy. Raman bands for these 6 nanotubes at different strain levels are shown in Figure 4.21. Some of the nanotubes that are listed in Tables 4.2 - 4.3 are absent in Figure 4.21 due to their low populations. It can be seen that for all nanotubes the RBM band frequency does not shift significantly during deformation, which is in agreement with the previous experimental findings and theoretical predictions [16]. The RBM intensity, on the other hand, scatters over a range with no clear trend observed. This is in contrast with Lucas's finding [30, 31], where the RBM intensity was found to change monotonically with the strain, with the changing trend and magnitude depending on nanotube chirality as well as the excitation laser. The

intensity change has been explained by Lucas *et al.* and well supported by theoretical calculations [16], that deformation can bring the E_{ii} closer to or further away from the E_{laser}. The apparent independence of the RBM intensity on the strain found in this case is possibly due to that the resonance window of these nanotubes has been broadened by some additional factors not taken into account in the theoretical calculation [32].
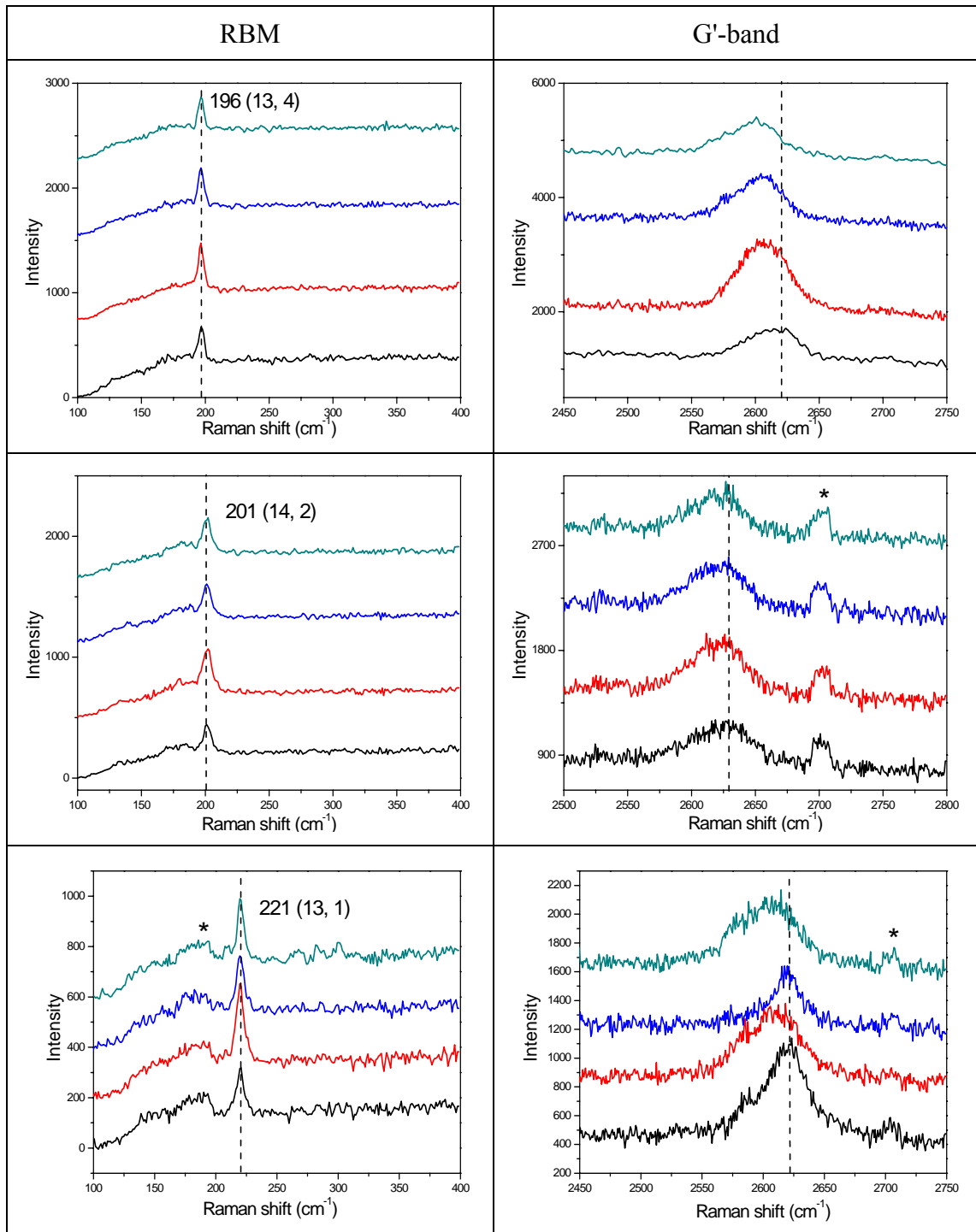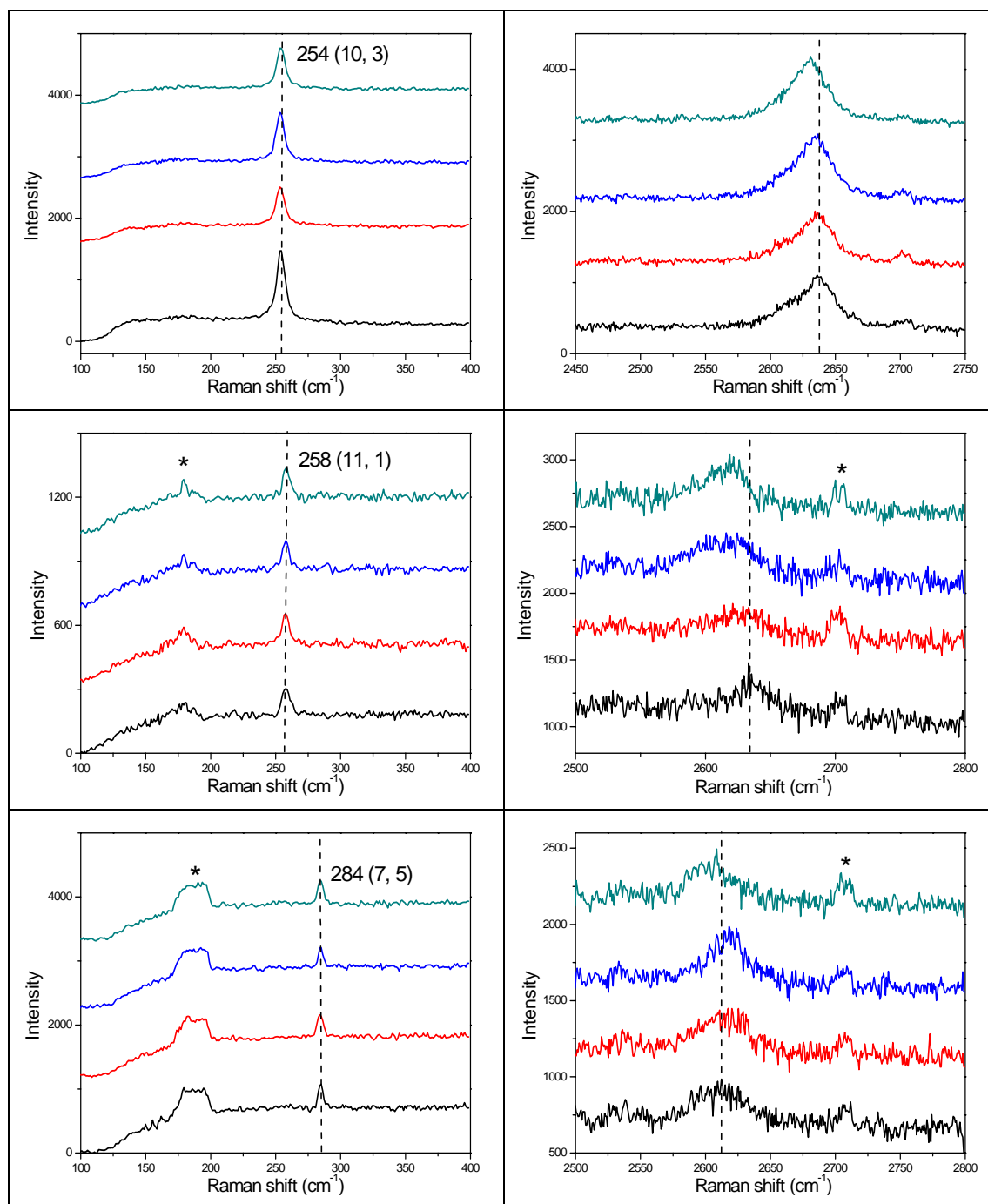
Figure 4.21 Raman bands of PVA/SWNT electrospun fibres at different strains. The strain levels are represented by the colour lines: ——0%, ——0.125%, ——0.25% and ——0.5%. The stars denote peaks from laser plasma lines. The spectra were offset for clarity.

The G'-band was also followed during deformation as it is particularly sensitive to the stress. The variation of the G'-band frequency for two (*n, m*) nanotubes under tensile strain is shown in Figure 4.22. It can be seen in the strain range of 0% - 0.6%,

the G'-bands for both nanotubes shift linearly with the strain and large band shift rates are observed, suggesting good efficiency of stress transfer in this range. When the strain exceeds 0.8%, the G'-band frequency scatters, which can be due to interfacial slippage in the composites [6] or yielding of the polymer matrix.
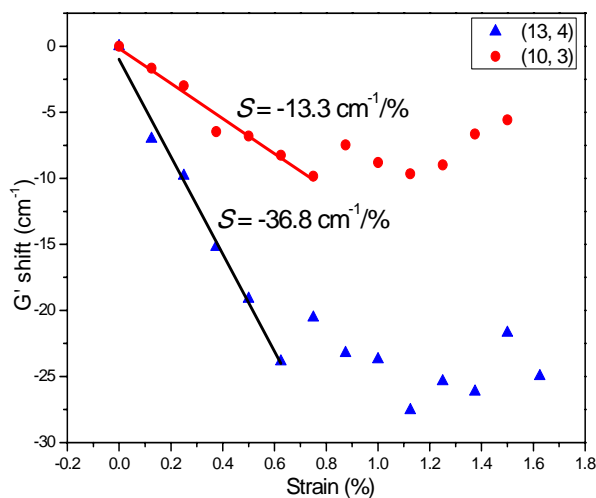
Figure 4.22 The G'-band frequency as a function of the fibre strain for two (n, m) nanotubes.

The shifts of G'-band wavenumber at 0.5% strain for the 6 nanotubes and the G'-band shift rates determined in the low strain range are listed in Table 4.7 (the shift rate for some of the nanotubes could not be determined due to the poor linearity). It is noted that the shift rate in the linear region differs from nanotube to nanotube, e.g. the shift rate of -36.0 cm^{-1}/% observed for the (13, 4) nanotube is almost 3× of that for the (10, 3) nanotube. It is thus speculated that the stress-induced G'-band shift rate for SWNTs is chirality-dependent. In fact, the chirality-dependence of Raman response to external perturbation has been observed by a number of groups in different situations. Gao *et al.* demonstrated a clear chirality-dependent Raman response to uniaxial strain that the G-band shift rate for individual nanotube increases with the decrease of chiral angle [33]. Very recently, Chang *et al.* also observed different G-band shift rates for different nanotubes [34]. Investigation of the deformation behaviour has been focused on the different shifts of the G-band for different chiralities, which can be understood on the basis of the effect of chiral angle on the projection of the strain vector onto the C-C bonds. No data on the G'-band shift for individual nanotubes have been reported

to the best of our knowledge, due possibly to that the G'-band is weaker than the G-band in most cases. As the G'-band frequency is related to the E_{ii} transition energy and the shift of E_{ii} under strain is dependent on the nanotube chirality [16], it would be reasonable to assume the G'-band shift rate is also chirality-dependent.

Table 4.7 The shift of G'-band at 0.5% strain for different nanotubes.

RBM frequency (cm^{-1})	Chirality (*n, m*)	Chiral angle (°)	Diameter (nm)	ΔG' (cm^{-1})	G' shift rate (cm^{-1}/%)
196	(13, 4)	13.0	1.20	-19.1±1.4	-36.0±2.5
201	(14, 2)	6.6	1.18	-0.7[a]	--
221	(13, 1)	3.7	1.06	-6±1.1	--
254	(10, 3)	12.7	0.92	-6.8±0.7	-13.1±1.7
258	(11, 1)	4.3	0.90	-15.5±2.6	--
284	(7, 5)	24.5	0.82	-7.3±0.7	-15.5[a]

--a: The standard deviation was not available.

The different G'-band shift rates observed here for different chiralities, however, may not reflect the actual difference among the nanotubes. This is because the strain experienced by the nanotube in the electrospun fibres might not be identical to the strain applied to the matrix even before the interface fails. End effects also need to be taken into account when deforming a short nanotube through stretching a polymer matrix. When applying a stress to a polymer matrix in which nanotubes are embedded, the stress is transferred to the nanotube through a shear mechanism at the nanotube-matrix interface. The strain (or stress) in a nanotube builds up from the nanotube ends to the maximum and plateaus at the midsection, giving rise to a shear-lag effect. A nanotube in the composite can be envisioned as a short solid fibre for approximation. The strain ε_{NT} at a position, *x* along the nanotube is given by [35]:

$$\varepsilon_{NT} = \varepsilon_m \left[1 - \frac{\cosh\left(2gs\dfrac{x}{l}\right)}{\cosh(gs)} \right] \qquad (4.4)$$

and the interfacial shear stress τ along the nanotube is given by:

$$\tau = \frac{1}{2} g \varepsilon_m E_{NT} \left[\frac{\sinh\left(2gs\dfrac{x}{l}\right)}{\cosh(gs)} \right] \quad (4.5)$$

where ε_m is the matrix strain, l is the length of a single nanotube, E_{NT} is the nanotube modulus which is taken as 1 TPa, s is the aspect ratio l/d_t of the nanotube, and g is a parameter that characterises the efficiency of stress transfer in the composites. The nanotube length is not known accurately, and the average value for individual HiPco SWNTs exfoliated by heavy ultrasonication, of ~150 nm [14], has been adapted here.

Figure 4.23 shows the strain profile along a nanotube when the matrix is subjected to a strain of 0.5%, assuming a diameter of 1 nm and the interfacial shear strength (IFSS) in the range of 10 - 100 MPa which is typical for a non-covalently bonded system [36]. It can be seen the strain (or stress) is non-uniform along the nanotube and for a given matrix strain, the maximum strain achieved in the nanotube depends on the IFSS. When a composite has a relatively poor interfacial adhesion (e.g. IFSS = 10 MPa), the maximum strain in the nanotube is far below the matrix strain, which means the mechanical reinforcing efficiency is rather low.
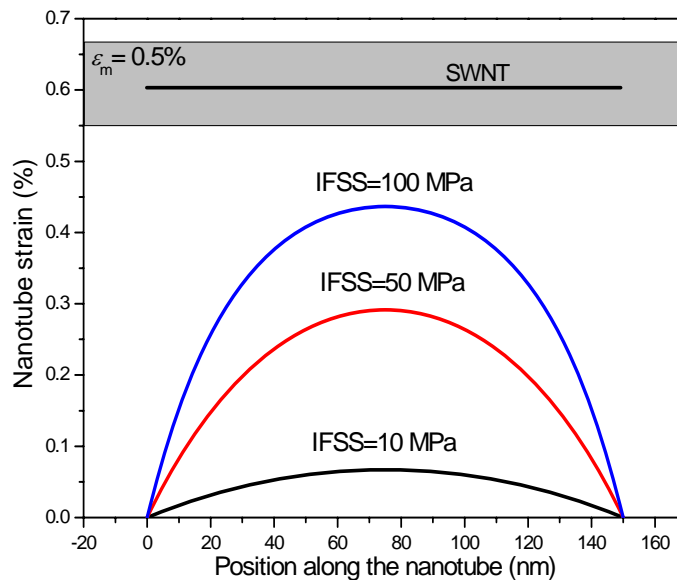
Figure 4.23 The strain distribution along a short nanotube in a polymer matrix.

A minimum length is needed to allow the strain in the nanotube to build up to the matrix strain, which is called the stress transfer length l_s. The stress transfer length increases with the increase of matrix strain. Assuming that the IFSS is 50 MPa, and the fibres is deformed in the strain range of 0 - 0.5% (elastic deformation), the stress transfer length is estimated to be roughly 500 nm for a SWNT with a diameter of 1 nm. To monitor the actual deformation behaviour of a single nanotube free from the end effects, as well as for efficient mechanical reinforcement would require a nanotube with a length of at least $10l_s$, which is roughly 5 μm.

4.4 Conclusions

Raman bands of SWNTs that were well dispersed in PVA electrospun fibres have been studied systematically in this chapter. Single RBM peaks were observed in the fibres, which allowed the properties of nanotubes with single chirality to be monitored. It has been found the features (including the frequency, the intensity and the linewidth) of Raman spectra of individual nanotubes were significantly different from those of nanotube bundles. The main differences are summarised as follows.

The RBM frequencies of nanotubes in electrospun fibres were similar to those in SDS/SWNT/water solutions and were up-shifted by 1 - 6 cm^{-1} relative to those in nanotube bundles in air. When using the 785 nm laser, single RBM peaks were observed and the "roping in" 267 cm^{-1} peak was absent, which is strong evidence that nanotubes have been isolated in the fibres. Chiralities were assigned to all of the RBM peaks observed in the electrospun fibres using an experimental Kataura plot.

As for the G-band, the G$^+$ peak became narrower which had a typical linewidth of 9 cm^{-1} and the G$^-$ peak became weaker in most cases. Debundling of nanotubes was also shown to reduce the G'-band linewidth. When a single RBM peak was seen, the G'-band exhibited either a single peak or more prevalently a double-peak structure. The double-peak structure was explained that along with the nanotube in incident resonance, there was another group of nanotubes in resonance with the scattered G'-photon. For the five semiconducting nanotubes that are in resonance with the 633

nm laser, the G'-band frequency increased with increasing diameter, which is thought to be related to the increase of E_{22} with nanotube diameter.

Orientation of nanotubes was characterised using polarized Raman spectroscopy. A dramatic decrease of the G-band intensity was observed when rotating the fibre from 0° to 90° with respect to the axis of laser polarisation, suggesting good orientation of the nanotubes in the electrospun fibres.

Tensile strain was applied to the nanotubes by stretching the electrospun fibres. The RBM frequency was found to be constant and the intensity scattered with no clear trend with strain. The G' shift per unit strain was found to be different for different chiralities. One possible reason for the different shift rates is the non-uniform distribution of stress along each individual nanotube. To compare the Raman band shift rate among different chiralities, as well as for efficient mechanical reinforcement would require nanotubes to be sufficiently long so that the stress is uniformly distributed in majority of a single nanotube. The minimum length was estimated to be roughly 5 μm assuming an IFSS of 50 MPa.

4.5 References

1. P. T. Araujo, P. B. Pesce, M. Dresselhaus, K. Sato, R. Saito and A. Jorio, *Resonance Raman spectroscopy of the radial breathing modes in carbon nanotubes,* Physica E, 2010, **42**, 1251-1261.

2. M. S. Dresselhaus, G. Dresselhaus, R. Saito and A. Jorio, *Raman spectroscopy of carbon nanotubes*, Phys. Rep., 2005, **409**, 47-99.

3. C. A. Cooper, R. J. Young and M. Halsall, *Investigation into the deformation of carbon nanotubes and their composites through the use of Raman spectroscopy*, Compos. Part A, 2001, **32**, 401-411.

4. Y. T. Shyng, *Interfacial micromechanics in model composites with high performance polymer fibres,* PhD Thesis, University of Manchester, 2006.

5. C. C. Kao, *Study of the deformation of single-walled carbon nanotube*

(SWNT)/epoxy composites using raman spectroscopy, PhD Thesis, University of Manchester, 2008.

6. P. Kannan, S. J. Eichhorn and R. J. Young, *Deformation of isolated single-wall carbon nanotubes in electrospun polymer nanofibres,* Nanotechnology, 2007, **18**, 235707-235713.

7. D. A. Heller, P. W. Barone, J. P. Swanson, R. M. Mayrhofer and M. S. Strano, *Using Raman spectroscopy to elucidate the aggregation state of single-walled carbon nanotubes,* J. Phys. Chem. B, 2005, **108**, 6905-6909.

8. S. K. Doorn, M. S. Strano, E. H. Haroz, K. L. Rialon, R. H. Hauge and R. E. Smalley, *Capillary electrophoresis separations of bundled and individual carbon nanotubes,* J. Phys. Chem. B, 2003, **107**, 6063-6069.

9. S. S. Karajanagi, H. Yang, P. Asuri, E. Sellito, J. S. Dordick and R. S. Kane, *Protein-assisted solubilization of single-walled carbon nanotubes,* Langmuir, 2006, **22**, 1392-1395.

10. S. Reich, C. Thomsen and P. Ordejon, *Electronic band structure of isolated and bundled carbon nanotubes,* Phys. Rev. B, 2002, **65**, 155411 1-11.

11. C. Fantini, A. Jorio, M. Souza, M. S. Strano, M. S. Dresselhaus and M. A. Pimenta, *Optical transition energies for carbon nanotubes from resonant Raman spectroscopy: Environment and temperature effects,* Phys. Rev. Lett., 2004, **93**, 147406 1-4.

12. M. S. Strano, *Probing Chiral Selective Reactions Using a Revised Kataura Plot for the Interpretation of Single-Walled Carbon Nanotube Spectroscopy*, J. Am. Chem. Soc., 2003, **125**, 16148-16153.

13. R. B. Weisman and S. M. Bachilo, *Dependence of optical transition energies on structure for single-walled carbon nanotubes in aqueous suspension: An empirical Kataura plot*, Nano Lett., 2003, **3**, 1235-1238.

14. S. M. Bachilo, M. S. Strano, C. Kittrell, R. H. Hauge, R. E. Smalley and R. B. Weisman, *Structure-assigned optical spectra of single-walled carbon nanotubes,* Science, 2002, **298**, 2361-2366.

15. S. Cui, *Characterisation and deformation of carbon nanotubes in polymer*

composites, PhD Thesis, University of Manchester, 2009.

16. M. Lucas, *Effect of deformation upon the intensity of the Raman radial breathing modes of single-wall carbon nanotubes in epoxy/SWNT composites,* PhD Thesis, University of Manchester, 2005.

17. F. Ding, A. R. Harutyunyan and B. I. Yakobson, *Dislocation theory of chirality-controlled nanotube growth*, Pro. Natl. Acad. Sci. USA, 2009, **106**, 2506-2509.

18. H. Dumlich and S. Reich, *Chirality-dependent growth rate of carbon nanotubes: A theoretical study*, Phys. Rev. B, 2010, **82**, 085421 1-5.

19. Y. Miyauchi, S. Chiashi, Y. Murakami, Y. Hayashida and S. Maruyama, *Fluorescence spectroscopy of single-walled carbon nanotubes synthesized from alcohol*, Chem. Phys. Lett., 2004, **387**, 198-203.

20. H. Kawamoto, H. Uchida, T. Kojima and M. Tachibana, *G band Raman features of DNA-wrapped single-wall carbon nanotubes in aqueous solution and air,* Chem. Phys. Lett., 2006, **432**, 172-176.

21. M. Paillet, P. Poncharal, A. Zahab and J. L. Sauvajol, *Vanishing of the breit-wigner-fano component in individual single-wall carbon nanotubes,* Phys. Rev. Lett., 2005, **94**, 237401 1-4.

22. A. Jorio, A. G. S. Filho, G. Dresselhaus, M. S. Dresselhaus, A. K. Swan, M. S. Unlu, B. B. Goldberg, M. A. Pimenta, J. H. hafner, C. M. Lieber and R. Saito, *G-band resonant Raman study of 62 isolated single-wall carbon nanotubes,* Phys. Rev. B, 2002, **65**, 155412 1-9.

23. A. G. S. Filho, A. Jorio, M. S. Dresselhaus, J. H. Hafner, C. M. Lieber and M. A. Pimenta, *Probing the electronic trigonal warping effect in individual single-wall carbon nanotubes using phonon spectra,* Chem. Phys. Lett., 2002, **354**, 62-68.

24. A. G. S. Filho, A. Jorio, A. K.Swan, M. S.Ünlü, B. B.Goldberg, R. Saito, J. H. Hafner, C. M. Lieber, M. A. Pimenta, G. Dresselhaus and M. S. Dresselhaus, *Anomalous two-peak G´-band Raman effect in one isolated single-wall carbon nanotube*, Phys. Rev. B, 2002, **65**, 085417 1-6.

25. I. O. Maciel, M. A. Pimenta, M. Terrones and A. Jorio, *The two peaks G' band in carbon nanotubes,* Phys. Stat. Sol, 2008, **245**, 2197-2200.

26. A. G. S. Filho, A. Jorio, G. Samsonidze, G. Dresselhaus, M. A. Pimenta, M. S. Dresselhaus, A. K. Swan, M. Ünlü, B. B. Goldberg and R. Saito, *Competing spring constant versus double resonance effects on the properties of dispersive modes in isolated single-wall carbon nanotubes,* Phys. Rev. B, 2003, **67**, 035427 1-7.

27. J. Cardenas, F. Juan and A. Gromov, *The effect of bundling on the G' Raman band of single-walled carbon nanotubes,* Nanotechnology, 2009, **20**, 465703 1-8.

28. A. Jorio, C. Fantini, M. S. S. Dantas, M. A. Pimenta, M. S. Dresselhaus, A. K. Swan and R. Saito, *Linewidth of the Raman features of individual single-wall carbon nanotubes,* Phys. Rev. B, 2002, **66**, 115411 1-8.

29. J. Hwang, H. H. Gommans, A. Ugawa, H. Tashiro, R. Haggenmueller, K. I. Winey, J. E. Fischer, D. B. Tanner and A. G. Rinzler, *Polarized spectroscopy of aligned single-wall carbon nanotubes,* Phys. Rev. B, 2000, **62**, R13310-R13313.

30. M. Lucas and R. J. Young, *Raman spectroscopic study of the effect of strain on the radial breathing modes of carbon nanotubes in epoxy/SWNT composites,* Compos. Sci. Technol., 2004, **64**, 2297-2302.

31. M. Lucas and R. J. Young, *Effect of uniaxial strain deformation upon the Raman radial breathing modes of single-wall carbon nanotubes in composites*, Phys. Rev. B, 2004, **69**, 085405 1-9.

32. S. B. Cronin, A. K. Swan, M. S. Ünlü, B. B. Goldberg, M. S. Dresselhaus and M. Tinkham, *Resonant Raman spectroscopy of individual metallic and semiconducting single-wall carbon nanotubes under uniaxial strain*, Phys. Rev. B, 2005, **72**, 035425 1-8.

33. B. Gao, L. Jiang, X. Ling, J. Zhang and Z. Liu, *Chirality-dependent Raman frequency variation of single-walled carbon nanotubes under uniaxial strain,* J. Phys. Chem. C, 2008, **112**, 20123-20125.

34. C. Chang, I. Hsu, M. Aykol, W. Hung, C. Chen and S. B. Cronin, *A new lower limit for the ultimate breaking strain of carbon nanotubes*, ACS Nano, 2010, **4**, 5095-5100.

35. D. Hull and T. W. Clyne, *An introduction to composite materials,* Cambridge: Cambridge University Press, 1996.

36. J. N. Coleman, U. Khan, W. J. Blau and Y. K. Gun'Ko, *Small but strong: A review of the mechanical properties of carbon nanotube–polymer composites,* Carbon, 2006, **44**, 1624-1652.

Chapter 5   PVA/SWNT composite fibres and films

5.1 Introduction

The efficiency of mechanical reinforcement by carbon nanotubes (CNTs) can be characterised by a parameter, the effective Young's modulus of nanotubes. One convenient way to measure it is to deform the CNT composites and measure the nanotube G'-band shift per unit strain. The Raman band shift rate is then converted to the nanotube modulus using the universal calibration of -0.05 cm^{-1}%$^{-1}$/GPa. This calibration was established by Cooper *et al*. by in-situ Raman spectroscopic study of a number of different carbon fibres [1]. They showed the G'-band shift rate was proportional to the carbon fibre modulus and assumed that the calibration was also valid for the stress-induced shift of the same G'-band in carbon nanotubes. This calibration has also been shown to apply to the stress-induced shift of the G'-band in single-layer graphene recently [2]. This is a simple yet powerful approach and has been used widely to evaluate the nanotube modulus. The approach they used, however, led to wide bounds in estimation of the effective modulus in CNT composites in which nanotubes were randomly distributed. This is because although they analysed the cases of both random two- and three-dimensional nanotube arrangements, they did not take into account laser polarisation effects in their analysis. In fact, the Raman shift rate has been found to depend on many factors such as the orientation distribution of nanotubes and the polarisation configuration in Raman spectrometer [3, 4]. A better understanding of the influence of these factors is needed if the shift rate is to be used in assessing the mechanical reinforcing efficiency.

To this end, poly(vinyl alcohol) (PVA) fibres containing highly aligned single-wall nanotubes (SWNTs) were prepared by both electrospinning and coagulation spinning as these two methods have been proved to be particularly effective in orienting nanotubes [5-7]. To study the effect of nanotube orientation on Raman band shift rate, another type of sample, isotropic films containing randomly-distributed nanotubes, was prepared by solution casting. The effect of molecular orientation upon stress transfer was investigated by Raman spectroscopy. It was found that the nanotube

Raman band shift rate is dependent on the angle between nanotube axis, strain axis and the direction of laser polarisation, and the angle-dependent Raman responsive behaviour also depends on the polarisation configuration in the Raman spectrometer. This phenomenon was explained by a mathematical model considering both the Poisson's contraction effect and the orientation-dependent Raman band intensity of the nanotubes (also known as the antenna effect).

5.2 Experimental

5.2.1 Materials and preparation of electrospun fibres and films

The materials and preparation of PVA/SWNT blend solutions were described in Section 3.2.1 and 3.2.2 in Chapter 3. The concentration of PVA in the blend solution was 14wt%, i.e. the same as that used in Chapter 4, but a higher concentration of nanotubes, of 0.2wt%, was used in this case. Electrospinning was carried out using the following conditions: electric voltage = 20 kV, flow rate = 0.02 ml/min and the needle-tip-to-collector distance = 8 cm. The fibres were collected using a rotary disk on which a poly(methyl methacrylate) (PMMA) beam (the dimensions of the beam were 6.8×1.4×0.25 cm) was attached, and the rotation speed was 1700 rpm. PVA/SWNT composite films were prepared by casting the blend solutions onto PMMA beams and were left for 12 h to dry.

5.2.2 Materials and preparation of coagulation-spun fibres

Larger PVA/SWNT fibres, with diameters ranging from 5 μm to 9 μm, were supplied by Professor Coleman's group, University of Dublin (Ireland). These fibres were produced using a coagulation spinning process. The PVA with an average molecular weight of 77,000 - 79,000 g/mol was purchased from J. T. Baker. The SWNTs were produced by a high-pressure decomposition of carbon oxide (HiPco) process and their concentration was 7.1wt% for all coagulation-spun fibres. Details of the preparation procedure can be found in Ref. [8].

5.2.3 Raman spectroscopy

Raman spectra were obtained and curve fitted using the same method as in Chapter 4. The laser power was ~1mW. The exposure time was set at 10 s and an accumulation of 5 times was used. A polarisation analyser and $\lambda/2$ plates were inserted before the microscope entrance and/or after the notch filter to select the polarisation for incident and scattered light. The position of the $\lambda/2$ plates and the analyser for each configuration were listed in Table 4.1 in Chapter 4.

5.2.4 SEM

A Philips XL30 FEG SEM was used to investigate the morphology of the fibres. For SEM observation, fibres deposited on aluminium foil were stuck to the SEM stubs which were then sputter coated with gold. SEM was operated with an accelerating voltage of 3 kV and images were acquired with a secondary electron mode.

5.2.5 Deformation testing

PVA/SWNT films and electrospun fibres were deposited directly on PMMA beams. These composites adhered to PMMA beam after the solvent evaporated and were deformed using a four-point bending rig (Figure 5.1) without any coating. For deformation testing of the PVA/SWNT coagulation-spun fibres, the fibres were placed on the PMMA beam at different angles between 0° and 90°, and coated by a thin layer of PMMA by casting a dilute chloroform solution of PMMA (2wt%). During deformation, the surface strain was measured using a resistance strain gauge. The strain ε was calculated according to the following equation:

$$\varepsilon = \frac{R_i - R_0}{2.08 \times R_i} \times 100\% \tag{5.1}$$

where R_0 is the initial electrical resistance of the strain gauge at 0% strain and R_i is the electrical resistance during deformation. The PMMA beam was deformed at a strain step of 0.04% and Raman spectra were collected at each strain level.
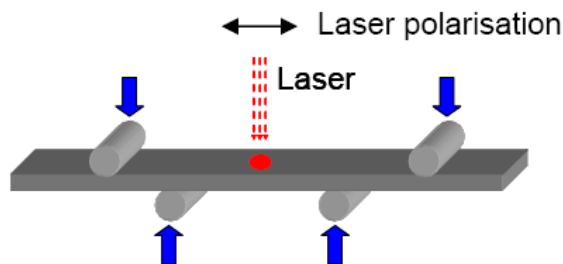
Figure 5.1 Schematic diagram of the four-point bending test [9].

5.2.6 Mechanical testing

The tensile testing was carried out using an Instron-1122 universal testing machine. Vacuum-oven-dried neat PVA and PVA/SWNT composite films were cut into a dumbbell shape which gave a gauge length of 20 mm and a width of 4 mm, and the thickness was around 0.12 mm (Figure 5.2). The samples were left in the mechanical testing room, in which the temperature was set at $23 \pm 0.1\,℃$ and a humidity set at $50 \pm 5\%$, for at least 48 hours prior to mechanical testing. Four samples were tested for each type of film.
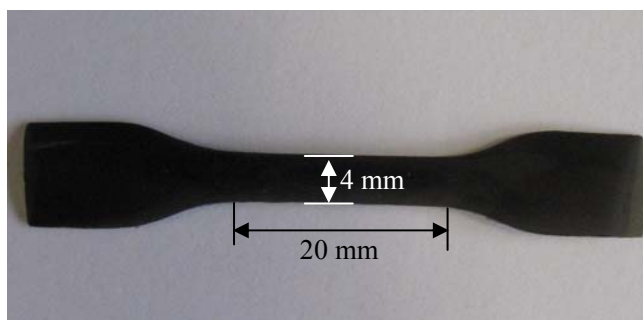
Figure 5.2 Dimensions of a PVA/SWT film sample for mechanical testing.

5.3 Results and discussion

5.3.1 Raman characterisation

Raman spectra of the original SWNT powder, a single PVA/SWNT electrospun fibre and a PVA/SWNT film are shown in Figure 5.3. With the resonant-enhanced signal, well-defined nanotube Raman bands including the RBMs, G-band and G'-band can be seen at a low loading of nanotubes. The G'-band frequency can be used to assess residual stress as it is most stress-sensitive. It was noted the G'-band position in

the electrospun fibres collected with a stationary stage was ~2 cm^{-1} higher than in the composite film while the G'-band position in fibres collected with a disk rotating at 1700 rpm was ~2 cm^{-1} lower than in the films. This suggests that the electrospinning process alone induces a small residual compression of the nanotubes in the fibres, possibly due to shrinkage as the solvent evaporates. In contrast, the nanotubes in fibres collected with a high-speed rotating disk are pre-stretched and have a slight residual tension that is not relaxed by solvent evaporation. Electrospun fibres collected with the rotating disk were used for further investigation.
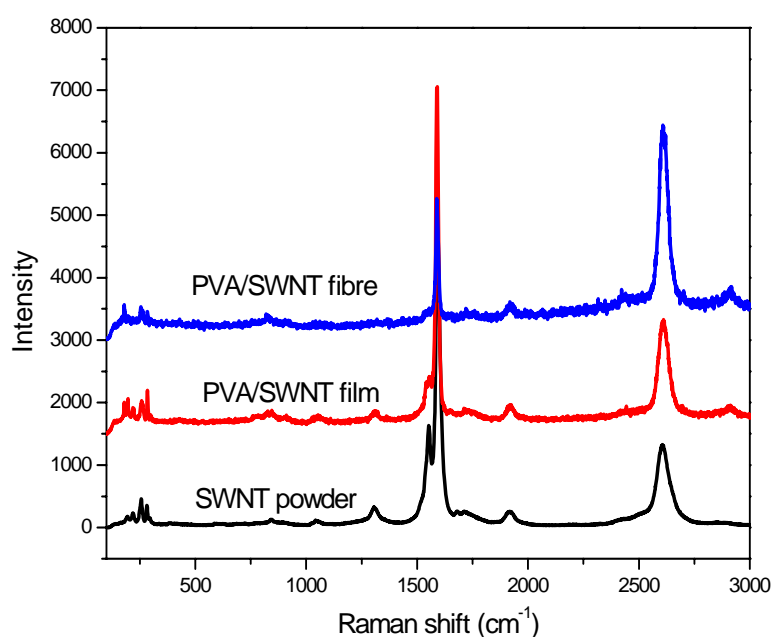
Figure 5.3 Raman spectra of the HiPco SWNT powder, PVA/SWNT film and PVA/SWNT electrospun fibre. Spectra were shifted vertically for clarity.

The nanotube G'-band linewidth is an indication of the aggregation state of nanotubes. The narrower G'-band corresponds to smaller nanotube bundles [10] as discussed in Chapter 4. It was noted the G' linewidth in the electrospun fibres was smaller than in composite films as can be seen from Table 5.1, which suggests a better dispersion of nanotubes in the electrospun fibres than in the films. The fibres and films were prepared using the same solution; the better dispersion in the fibres is therefore attributed to the extra exfoliation induced by the electrospinning process.

Table 5.1 Comparison of the frequency and linewidth of G'-band of the SWNT powder, PVA/SWNT film and electrospun fibre.

Material	G'-band frequency (cm^{-1})	G'-band linewidth (cm^{-1})
SWNT powder	2609	63 - 67
PVA/SWNT film	2610	52 - 54
PVA/SWNT electrospun fibre	2608 - 2614	35 - 50

Weak but resolvable Raman bands in the 600 - 1400 cm^{-1} region corresponding to PVA polymers can be seen in the electrospun fibres as shown in Figure 5.4. The assignments of the vibrational modes for these Raman peaks are listed in Table 5.2. This enables the use of Raman spectroscopy to investigate the orientation of both the polymers and nanotubes.
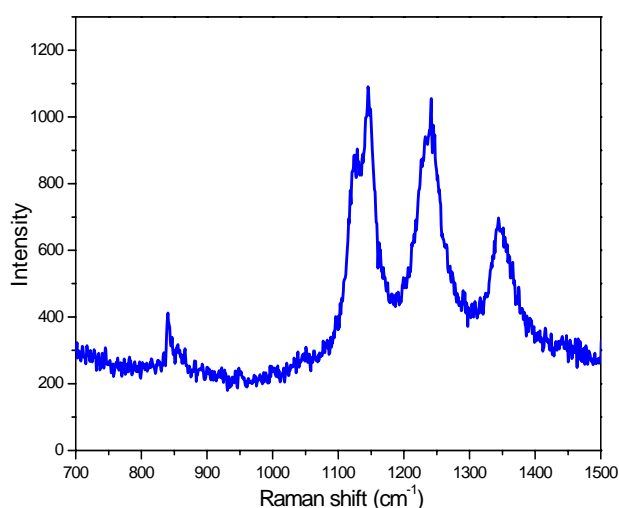
Figure 5.4 Raman spectrum obtained from a PVA/SWNT electrospun fibre using a 785 nm laser.

Table 5.2 Assignment of the vibrational modes of the PVA Raman bands [11, 12].

Peak position (cm^{-1})	Vibrational mode
852	C-C stretching
916	C-C stretching
1088	C-O stretching, O-H bending
1127	C-O stretching, O-H bending
1147	C-O stretching, C-C stretching
1349	C-H bending and O-H bending

The orientation of nanotubes in the composites was characterised using polarized Raman spectroscopy, following the methods described in Chapter 4. The sample was rotated from 0° to 90°, and Raman spectra were recorded at different angles, φ, between the sample axis and the axis of laser polarisation. There is no symmetry axis in the films so the angle 0° was defined arbitrarily. Figure 5.5 shows the normalised intensity of the nanotube G-band at different angles. Similar to the finding in Chapter 4, the G-band intensity in the electrospun fibre underwent a dramatic decrease when the angle increased from 0° to 90°. The orientation factor was determined by fitting the data using Equation (2.17) which was proposed by Liu *et al.* [13]. A least-square fit of the data in Figure 5.5a gave the orientation factor of 0.92, which suggests a high degree of alignment of nanotubes in the electrospun fibres. The strong drawing force exerted by electric field results in a high draw ratio in electrospinning jets and the nanotubes are thus almost perfectly aligned along the drawing direction.

Orientation of the nanotubes in the PVA/SWNT film was also investigated for comparison. It can be seen from Figures 5.5b, that the intensity of nanotube G-band does not change significantly when measured at different angles within the plane of the film relative to an arbitrarily-chosen axis, which indicates a random distribution of the nanotubes in the film.
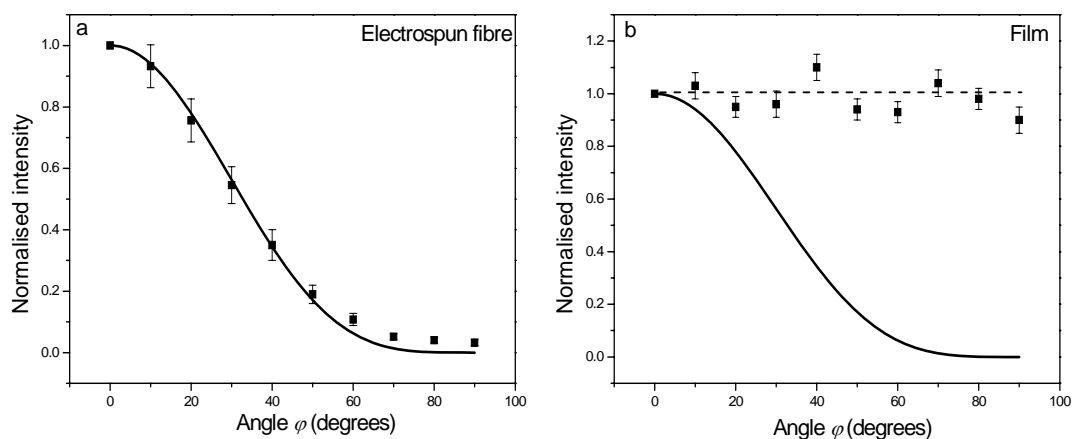

Figure 5.5 Variation of the nanotube G-band intensity as a function of the angle for: (a) PVA/SWNT electrospun fibre and (b) PVA/SWNT film. Raman spectra were obtained with a VV configuration. The intensities are normalised to the intensity at 0°, and the solid lines are generated for the function $\cos^4 \varphi$ which is expected for perfect orientation.

Along with the good orientation of nanotubes achieved in the electrospun fibres, polymer molecules could also be oriented under the strong electric forces together with the drawing force exerted by the rotating disk. Alignment of polymer molecules in electrospun fibres has been observed using Raman spectroscopy for a number of polymers such as poly(ethylene oxide) (PEO) [14] and Nylon [15]. The orientation of polymer molecules can be determined using Raman spectroscopy assuming that the depolarisation ratio for all samples that possess the same chemical structure is constant. The depolarisation ratio κ is defined as the ratio of the intensity obtained with an HV configuration to that obtained with a VV configuration [16]:

$$\kappa = \frac{I_{HV}}{I_{VV}} = \frac{1 - 2t + t^2}{8t^2 + 4t + 3} \tag{5.2}$$

where the configuration of laser polarisation is denoted by a pair of letters such as "VV", "VH", "HH" and "HV", in which the first and second letters denote the direction of the incident and scattered lasers, respectively. "V" and "H" indicate the lasers are parallel and perpendicular to the frame reference axis, respectively. The Raman band intensities obtained with different configurations are given by [16]:

$$I_{HH} = b\left\{\left[\left(8t^2 + 4t + 3\right)/15\right] + P_2\left[\left(8t^2 - 2t - 6\right)/21\right] + 3P_4\left[\left(8t^2 - 16t + 8\right)/280\right]\right\} \tag{5.3}$$

$$I_{VV} = b\left\{\left[\left(8t^2 + 4t + 3\right)/15\right] - 2P_2\left[\left(8t^2 - 2t - 6\right)/21\right] + P_4\left[\left(8t^2 - 16t + 8\right)/35\right]\right\} \tag{5.4}$$

$$I_{HV} = b\left\{\left[\left(t^2 - 2t + 1\right)/15\right] - P_2\left[\left(6t^2 + 4t - 2\right)/42\right] - P_4\left[\left(8t^2 - 16t + 8\right)/70\right]\right\} \tag{5.5}$$

where P_2 and P_4 are the second order and the fourth order orientation parameters, respectively. P_2 is also known as the Herman's orientation factor which has a value of 1 for perfect orientation, 0 for random distribution, and -0.5 for the vibration perpendicular to the main axis of the structure.

The He-Ne 633 nm laser was employed to characterise the orientation of polymer molecules. Figure 5.6 shows the PVA Raman bands obtained with different laser configurations, from which the variation of Raman band intensity with polarisation configuration can be seen. The C-C stretching 916 cm^{-1} band was chosen for determination of the polymer orientation as this band corresponds to the vibration along the molecular backbone [17] and is readily isolated from other peaks. The

depolarisation ratio of this band was examined with an isotropic PVA film from which a value of 0.53 was determined. The orientation factor for the polymer was determined using Equations (5.2)-(5.5) and was found to be 0.34, suggesting that the polymer molecules are only partially aligned along the fibre axis. It is thus evident that the nanotubes are much better oriented than the polymer molecules in the electrospun fibres, which is thought to be due to their higher rigidity and longer relaxation time than for the PVA molecules.
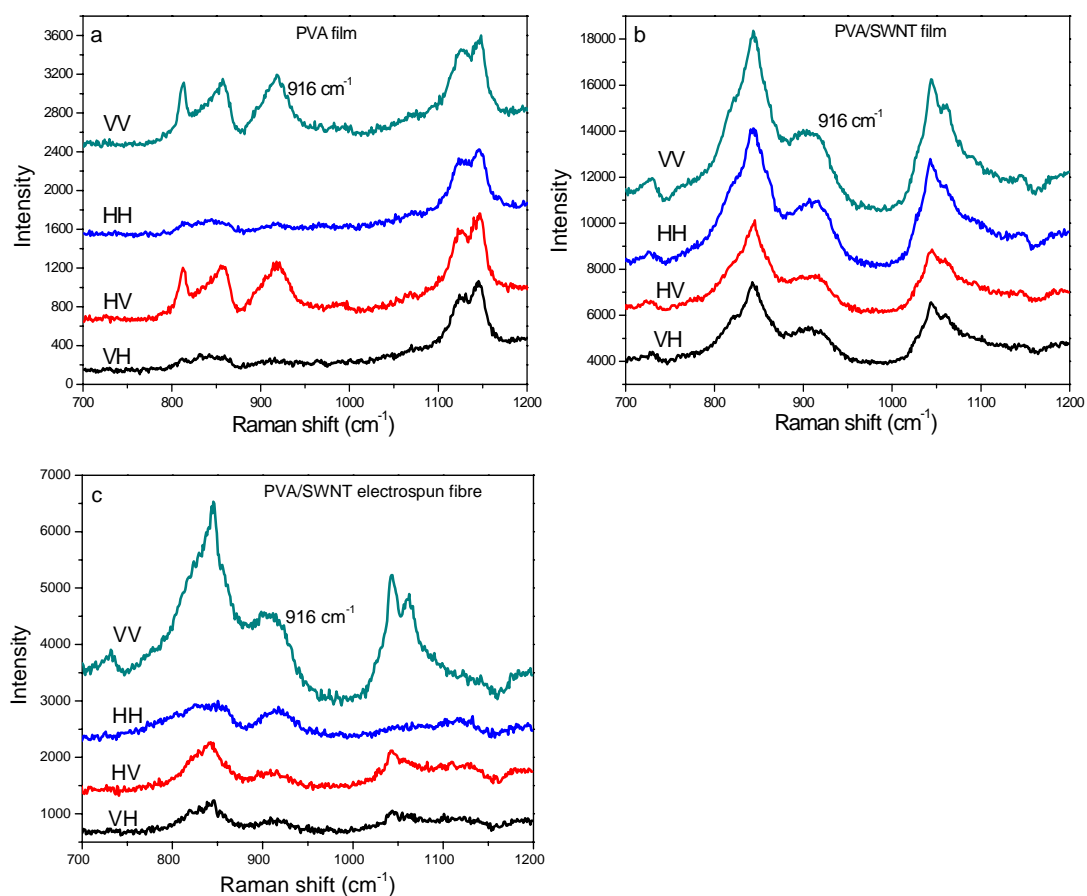
Figure 5.6 Polarized Raman spectra in 700 - 1200 cm^{-1} region for: (a) the PVA film, (b) the PVA/SWNT film and (c) the PVA/SWNT electrospun fibre for different configurations. Excitation laser: He-Ne 633 nm. The spectra were shifted vertically for clarity.

It is also possible to assess the crystallinity of the PVA polymers in the composite films and fibres using Raman spectroscopy. Iwamoto *et al*. demonstrated that the intensity of the PVA 1147 cm^{-1} peak increases while that of the 1127 cm^{-1} peak decreases with an increasing crystallinity of PVA [18]. They assigned the 1127 cm^{-1}

peak to an amorphous band and the 1147 cm^{-1} peak to a crystalline band. The relative intensity of these two bands can, therefore, serve as an indication of the crystallinity, i.e. a higher intensity ratio I_{1147}/I_{1127} indicates a higher crystallinity of the sample. Figure 5.7 shows Raman spectra of the PVA film, PVA/SWNT composite film and the PVA/SWNT composite fibre in the 1000 - 1200 cm^{-1} region. The intensity ratio I_{1147}/I_{1127} for the films and the electrospun fibres are listed in Table 5.3. It can be seen that incorporation of SWNTs does not influence the PVA crystallinity significantly in the films, while the crystallinity in the electrospun fibres is higher than that in both the neat PVA and composite films. This result is important because if there would be any mechanical reinforcement by nanotubes in the composite films, as will be discussed in the following section, it will be associated with the stress transfer to the nanotubes in the composites rather than due to a stiffer matrix.

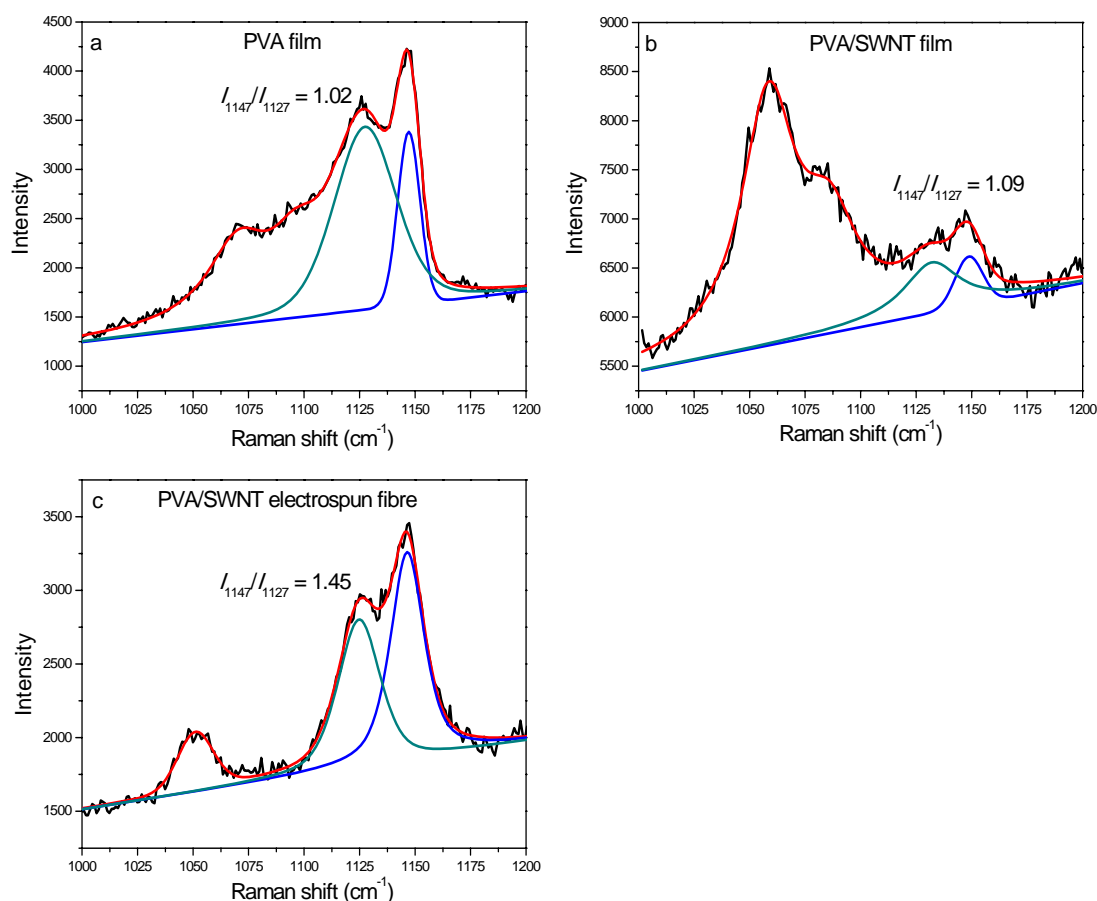*Figure 5.7 Raman spectra of: (a) a PVA film, (b) a PVA/SWNT composite film and (c) a PVA/SWNT composite fibre in the 1000 - 1200 cm^{-1} region showing the relative intensity between the 1127 cm^{-1} band and the 1147 cm^{-1} band. Excitation laser: near-infrared 785 nm.*

Table 5.3 Orientation factors of the nanotubes and polymers, and the crystallinity (which is characterised by the intensity ratio I_{1147}/I_{1127}) of PVA in different samples.

Material	Orientation factor P_2		Intensity ratio	G'-band shift rate
	PVA[a]	Nanotube[b]	I_{1147}/I_{1127}	(cm^{-1}/%strain)
PVA film	0	--	1.02	--
PVA/SWNT film	0.11	0.14	1.09	-23
PVA/SWNT electrospun fibre	0.32	0.92	1.45	-35

--a: Orientation factors determined using Equations (5.2) – (5.5).

--b: Orientation factors determined using Equation (2.17).

5.3.2 Stress-induced Raman band shift

The PVA/SWNT films and electrospun fibres were deformed using a four-point bending rig and the Raman bands were followed during deformation. Figure 5.8 shows the G'-band frequency as a function of the strain applied to the composite films and fibres. Good linearity between the band frequency and strain can be seen in the small strain range (< 0.4%) for both materials. The nanotube G'-band shift per unit strain, observed in the elastic deformation region in PVA/SWNT film, of -23 cm^{-1}/%strain, is to our knowledge one of the highest found in isotropic polymer/CNT films and is higher than in many CNT composite fibres. For example, Lachman *et al.* observed a shift rate of -3.6 cm^{-1}/% for their PVA/SWNT fibres [19], while Wang *et al.* observed a shift rate of -2.7 cm^{-1}/% for their PVA/SWNT films [20]. None of these works, however, indicated whether the polarisation analyser was in or not for their Raman measurements. The Raman band shift rates in isotropic films detected using a parallel-parallel (VV) laser configuration are slightly higher than those detected with Raman spectroscopy where the scattered laser is not polarized.
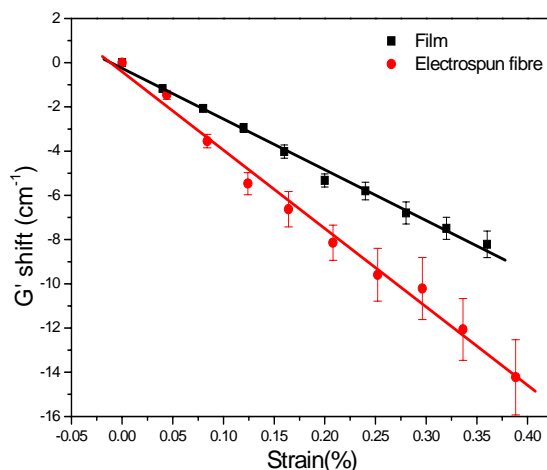
Figure 5.8 Variation of the G'-band position for nanotubes in the PVA/SWNT fibres and films as a function of strain. Raman spectra were obtained with a VV configuration.

The high shift rates found in these composite films are thought to be due to the good dispersion of nanotubes in the film as PVA can facilitate and stabilize the dispersion of nanotubes in a mechanism similar to a surfactant [21]. A controlled experiment was undertaken to assess the effect of dispersion upon Raman band shift rate. Figure 5.9 shows the nanotube G' shift rate and the G' linewidth observed in the films as a function of the sonication time for preparation of the blend solution. It can be seen the G' linewidth decreases with the sonication time, suggesting an improvement of the dispersion, which in turn results in an increase of the G'-band shift rate. The band shift rate is related to the effective modulus of nanotubes and it is known that the modulus of SWNT bundles decreases rapidly as the bundle size increases. For example, the modulus decreases from over 1 TPa for the nanotube rope with a diameter of 3 nm to 149 GPa for the rope with a diameter of 13.5 nm [22]. The strain-induced Raman band shift rate can thus serve as an indication of the dispersion state of nanotubes.

The electrospun fibres in Figure 5.8 exhibited an even higher Raman band shift rate, of -35 cm^{-1}/%strain, which is thought to be a consequence of the improved orientation of nanotubes and polymer molecules as compared to the films. The better dispersion of nanotubes in electrospun fibres than in the films might also be responsible for the higher band shift rate.
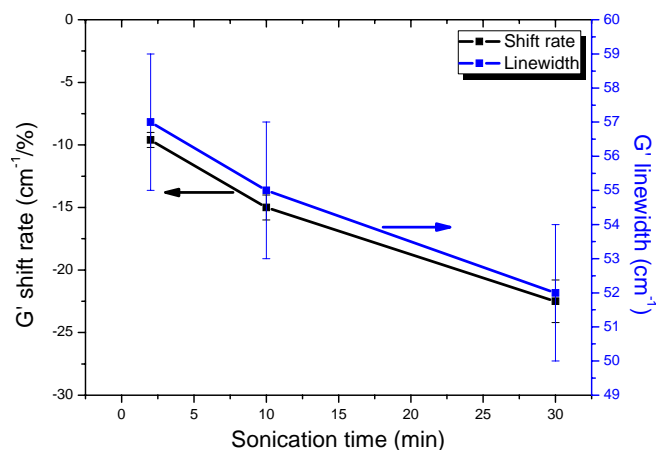
Figure 5.9 Nanotube G'-band shift rate and the linewidth as a function of sonication time for the PVA/SWNT films.

5.3.3 Mechanical properties

The high shift rate is indicative of good stress transfer in the composites, that ought also be reflected in mechanical reinforcement of the PVA by SWNTs. Mechanical testing was carried out with the film samples using an Instron testing machine and typical stress-strain curves are shown in Figure 5.10. For both the neat PVA and PVA/SWNT films, the stress increases linearly with the strain in the low strain range (< 2.5%) and the polymers yield at around 3% strain. The moduli of the films were calculated in the strain range of 0.5 - 2.5% where good linearity was observed. It was found that the modulus increased from 1.9 GPa for the neat PVA film to 2.3 GPa for the PVA/SWNT film (see Table 5.4) and the ultimate tensile strength increased from 36 MPa to 42 MPa with just 0.2% of SWNTs in the composite films.
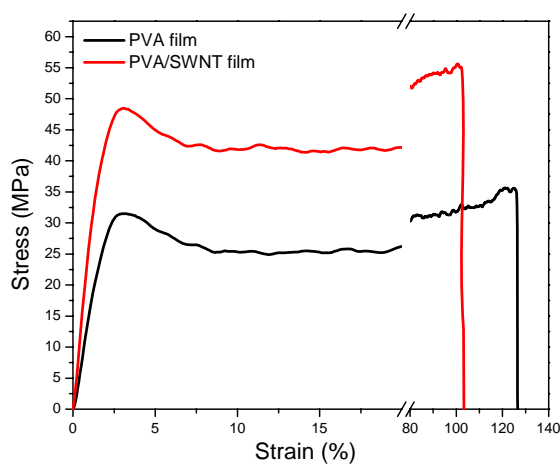
Figure 5.10 Typical stress-strain curves of the neat PVA and PVA/SWNT films.

Table 5.4 Mechanical properties of the neat PVA and PVA/SWNT films.

Material	Modulus (GPa)	Strength (MPa)	Elongation (%)
PVA film	1.9±0.2	36±5	130±10
PVA/SWNT film	2.3±0.3	42±6	110±13

The SEM image of the fracture surface of the composite film showed that nanotubes were pulled out from the matrix as illustrated in Figure 5.11. Visible charging of the sample, as indicated by the wrinkle of the polymers, was observed even with a low accelerating voltage at high magnification [23]. The typical diameter of the nanotube bundle protruding from the matrix seen from the SEM image is around 10 nm. It was difficult to distinguish smaller nanotubes from the polymers due to the charging effects (individual nanotubes are also below the resolution limit of this technique).
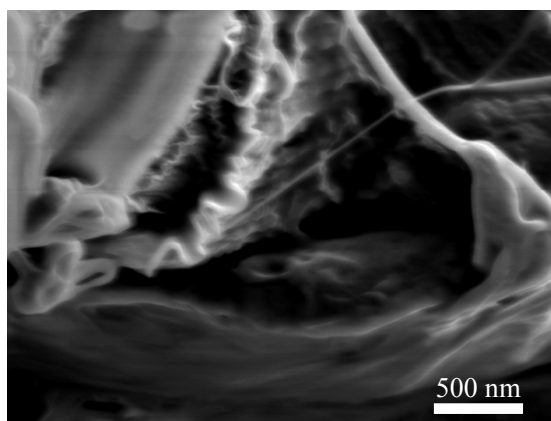
Figure 5.11 SEM micrograph of the fracture surface of the PVA/SWNT composite film.

5.3.4 Angular-dependence of the Raman band shift rate

The stress-induced Raman band shift for nanotubes has been found to be dependent on the polarisation configuration and the angle between the nanotube axis and the strain axis [3, 4, 24, 25]. A quantitative model describing the effect of these factors on the Raman band shift rate is required if the shift rate is to be used in assessing mechanical reinforcement by nanotubes. A detailed study was therefore undertaken to assess the level of stress-induced Raman band shift for the PVA/SWNT nanocomposite fibres and films as a function of the angles between the direction of

incident laser polarisation and the nanotube axis (α) and strain axis (ϕ). The definitions of these angles are shown in Figure 5.12 where the angle θ is defined as the angle between the strain axis and nanotube axis. Assuming that the nanotubes are randomly distributed in the plane of the film (two-dimensional distribution), then there is a relation between the angles: $\alpha = \phi + \theta$.
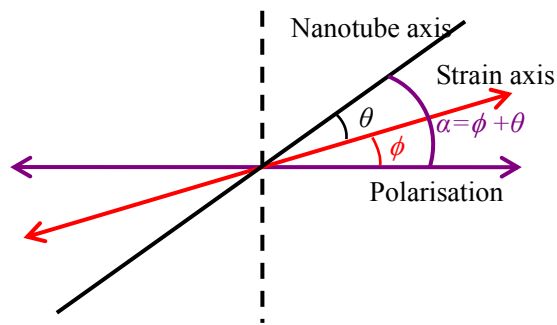
Figure 5.12 Schematic diagram of the angle between the nanotube axis, strain axis and the axis of laser polarisation in the same plane [25].

The G'-band shift was measured as a function of the strain for the nanotubes in the PVA/SWNT electrospun fibres and films in three different experimental arrangements (Figure 5.13). The slope of the lines, similar to those plotted in Figure 5.8, gives the G'-band shift rate. The band shift rate was determined as a function of the angle for three different geometries investigated.

1) Nanocomposite fibre ($\theta = 0°$ and ϕ varied). An electrospun fibre adhering to a PMMA beam was deformed axially ($\theta = 0°$) using the four-point bending rig. Since the strain direction is parallel to the fibre axis then $\phi \equiv \varphi$ (where φ is the angle between the sample axis and the axis of laser polarisation). This angle was changed relative to the direction of laser polarisation by rotating the rig on the Raman microscope stage and the G'-band shift rate with strain was recorded as a function of ϕ. Measurements were undertaken using two different polarisation configurations, VV and VH. When the VV configuration was used, it was difficult to go beyond 60° as the Raman signal became weak at higher angles, due to the $\cos^4\varphi$ dependence of the intensity (Figure 5.5a). It can be seen from Figure 5.13a, that the shift rates are constant with angle, suggesting that the nanotubes are always subject to the same

stress in this geometry. The band shift rate determined using the VH configuration revealed that the shift rate was also independent of the polarisation of the scattered light in this case.

2) Nanocomposite fibre ($\phi = 0°$ and θ varied). Stress was applied to single electrospun fibres lying at different angles on the PMMA beam and the G'-band shift rate determined as a function of θ, the angle between nanotube ($\equiv$ fibre) axis and strain axis, as shown in Figure 5.13b. The down-shift rate of the Raman band decreased as θ increased and the G'-band shift rate became positive when the angle exceeded 55°, suggesting that the nanotubes became subjected to compression at higher angles, due to the Poisson's contraction effect.

As the nanotubes are parallel to the fibre axis and the G'-band frequency decreases linearly with strain (Figure 5.8), the axial strain in nanotubes is assumed to be identical to the strain in the fibre in the low strain range (<0.4%), and the nanotube Raman band shift scales with the strain in the fibre. Andrews *et al*. showed that the Raman band shift rate for a fibre in a composite lying at an angle θ with respect to the strain axis, $S(\theta)$, is given by [26]:

$$S(\theta) = S_0 \left(\cos^2 \theta - v \sin^2 \theta \right) \tag{5.6}$$

where v is the Poisson's ratio of the matrix and S_0 is the band shift rate for the fibres parallel to the strain direction. Equation (5.6) can also be used to explain the angular-dependence of the G'-band shift rate for the nanotubes in the PVA nanocomposite fibres. The shift rate S_0 of the G'-band when $\theta = 0°$, i.e. all nanotubes are aligned parallel to the strain direction, can be seen to be -35 cm^{-1}/% in Figure 5.8. The values of Poisson's ratio for polymers are typically between 0.33 and 0.49 and are not known accurately for all polymers. The curve in Figure 5.13b is generated from Equation (5.6) assuming a Poisson's ratio of 0.4 for both the PMMA beam and PVA. It can be seen from Figure 5.13b that the data fall close to the curve. This confirms the validity of Equation (5.6) for the deformation of the electrospun fibres. The shift rate was again found to be independent of the laser configuration (i.e. the shift rate detected with a VH configuration is similar to the VV configuration).
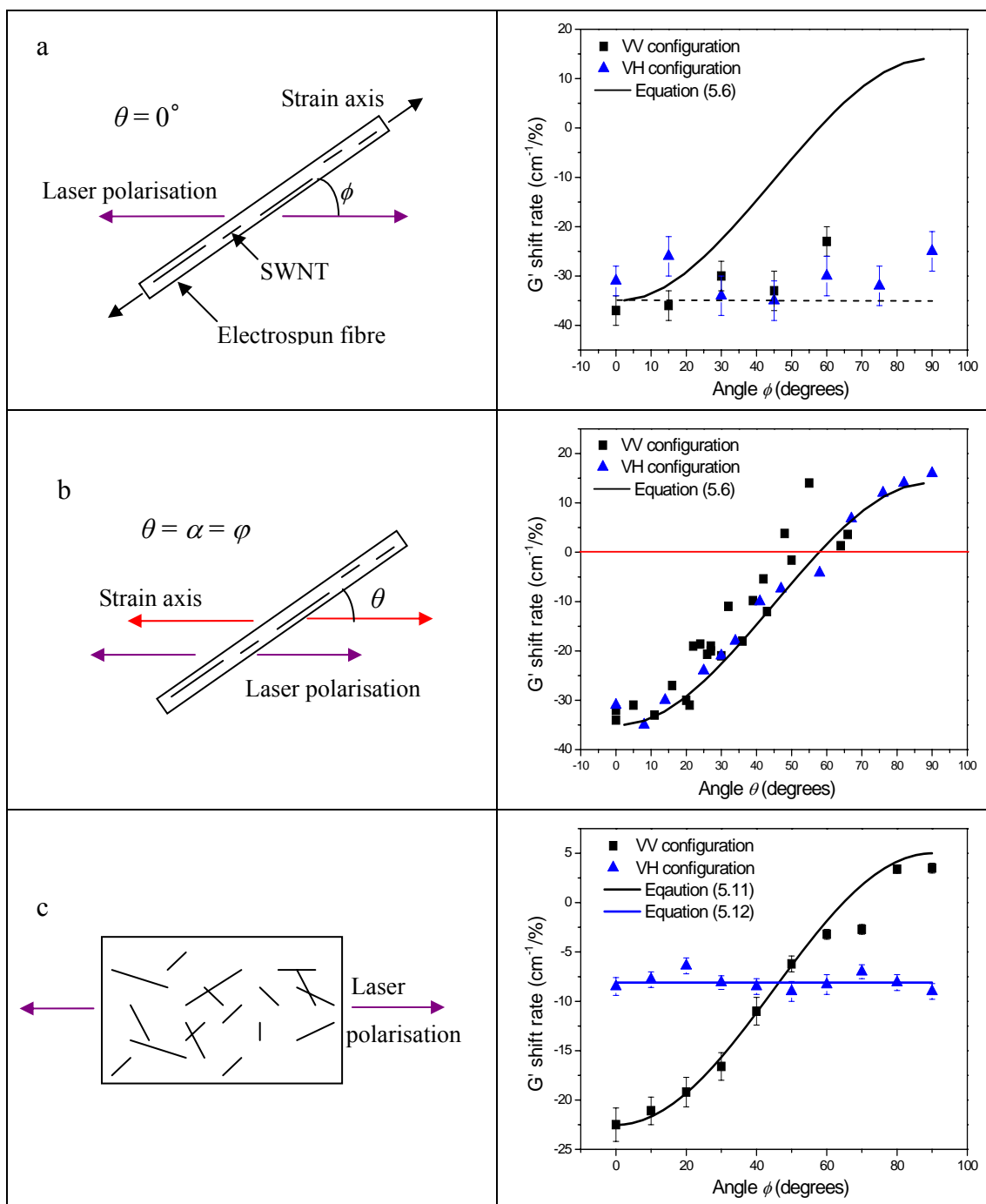
Figure 5.13 Nanotube G'-band shift rate as a function of the angle between: (a) strain axis and the axis of laser polarisation for electrospun fibre, (b) strain axis and nanotube axis for electrospun fibre and (c) strain axis and the axis of laser polarisation for isotropic film. The lines in (a) and (b) are generated for Equation (5.6) with $S_0 = -35$ cm^{-1}/%, and the lines in (c) are generated for Equation (5.11) and Equation (5.12) with $S_0 = -29.5$ cm^{-1}/% for VV and -27 cm^{-1}/% for VH configurations, respectively.

3) Nanocomposite film (ϕ varied). The nanocomposite film was deformed at different angles between the strain axis and the axis of laser polarisation (Figure 5.13c) and the G'-band shift monitored as a function of strain for two different polarisation configurations, VV and VH. When the VV configuration was used, the negative shift rate decreased as the angle ϕ increased and the shift rate became positive above 75°, again due to the Poisson's contraction effect.

Nanotubes contribute to the Raman band intensity differently when the VH configuration is used rather than in VV configuration. Because of this, a constant shift rate was observed at different angles for VH as can be seen from Figure 5.13c. These phenomena can be analysed quantitatively if both the contraction effect and the orientation dependence of Raman band intensity for nanotubes are taken into account.

The Raman band intensity is a contribution of nanotubes lying at all directions relative to the direction of laser polarization (the angle is denoted as α). Assuming the nanotubes are uniformly distributed in all directions, the proportion of nanotubes lying within an infinitesimal angle range, dα, with respect to the polarisation direction is $\frac{1}{\pi}\mathrm{d}\alpha$. The Raman band intensities obtained using different polarisation configurations are then given by [27, 28]:

$$I_{\mathrm{VV}}(\alpha) = \frac{1}{\pi}\int_0^\pi I_0 \cos^4 \alpha \mathrm{d}\alpha \tag{5.7}$$

$$I_{\mathrm{VH}}(\alpha) = \frac{1}{\pi}\int_0^\pi I_0^{'} \cos^2 \alpha \sin^2 \alpha \mathrm{d}\alpha \tag{5.8}$$

At a given angle ϕ, the intensity can be described as:

$$I_{\mathrm{VV}}(\phi) = \frac{1}{\pi}\int_0^\pi I_0 \cos^4(\theta + \phi)\mathrm{d}\theta \tag{5.9}$$

$$I_{\mathrm{VH}}(\phi) = \frac{1}{\pi}\int_0^\pi I_0^{'} \cos^2(\theta + \phi)\sin^2(\theta + \phi)\mathrm{d}\theta \tag{5.10}$$

for the VV and VH configurations, respectively, where I_0 and $I_0^{'}$ are parameters that give the maximum intensity for each configuration.

The possibility of reorientation of the nanotubes under strain needs to be taken into account as Equations (5.9) and (5.10) are invalid when the reorientation occurs. Bokobza *et al.* demonstrated that nanotubes in an elastomer can be oriented along the strain direction, giving rise to a change of the orientation distribution of the nanotubes

during deformation [29]. The strain applied to the electrospun fibres and films in this study was limited into a small range (<0.4%) to avoid any significant reorientation effect of the nanotubes. Figure 5.14 shows the G-band intensity as a function of the angle φ for the film subjected to 0.36% strain from which no significant alignment of nanotubes was observed. The composite film can, therefore, be envisioned as a random (in plane) system throughout the whole deformation process.
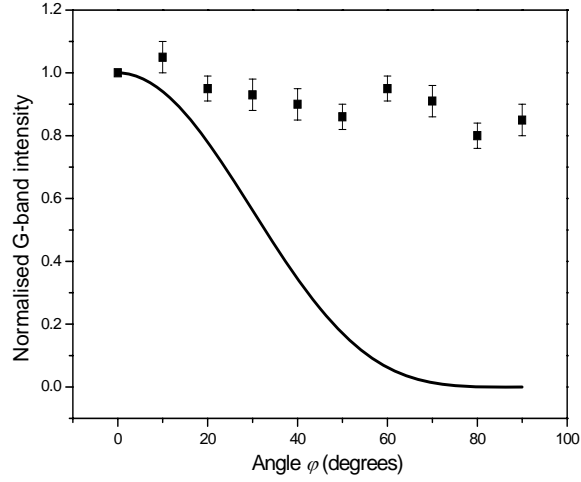
Figure 5.14 Normalised G-band intensity as a function of the angle for a PVA/SWNT film subjected to 0.36% strain.

The Raman band is a contribution of all nanotubes, thus the stress induced band shift is also a contribution of band shift for each individual nanotubes. The overall band shift can be considered as an intensity-weighted average of band shift for nanotubes lying at all angles. For nanotubes distributed randomly in two-dimensions in the film, the dependencies of the shift rates for the two different polarization configurations, VV and VH, upon the angle ϕ are given by:

$$S_{VV}(\phi) = \frac{\frac{1}{\pi} \int_0^\pi I_0 \cos^4(\theta + \phi) \times \left[S_0 \left(\cos^2 \theta - \nu \sin^2 \theta \right) \right] d\theta}{\frac{1}{\pi} \int_0^\pi I_0 \cos^4(\theta + \phi) d\theta} \qquad (5.11)$$

$$S_{VH}(\phi) = \frac{\frac{1}{\pi} \int_0^\pi I_0' \left[\cos^2(\theta + \phi) \sin^2(\theta + \phi) \right] \times \left[S_0 \left(\cos^2 \theta - \nu \sin^2 \theta \right) \right] d\theta}{\frac{1}{\pi} \int_0^\pi I_0' \left[\cos^2(\theta + \phi) \sin^2(\theta + \phi) \right] d\theta} \qquad (5.12)$$

where the Poisson's ratio v was taken as 0.40 for both the PVA and PMMA. Equations (5.11) and (5.12) were evaluated using Mathematica and least-squares fits of these equations to the experimental data in Figure 5.13c give S_0 = -29.5 cm^{-1}/% for the VV configuration and -27 cm^{-1}/% for the VH configuration, respectively.

5.3.5 Angular-dependence of the shift rate for incident laser misaligned at 5°

The sensitivity of the above analysis to the alignment of the laser polarisation was also examined. The λ/2 plate, which is a birefrigent crystal, can rotate the polarized light that makes an angle θ with respect to its fast axis by 2θ when the light passes through it (Figure 5.15). It is convenient to rotate the polarisation of a laser to any other desired polarisation. The λ/2 plate sitting in front of the notch filter (denoted as λ/2 Plate 1# in Figure 4.2) was rotated by ~2.5° (indicated as the red frame in Figure 5.15) to give deliberately a misalignment of 5° for the incident laser with respect to the frame reference axis. The Raman band shift rates were again recorded at different angles between the strain direction and the axis of laser polarisation.
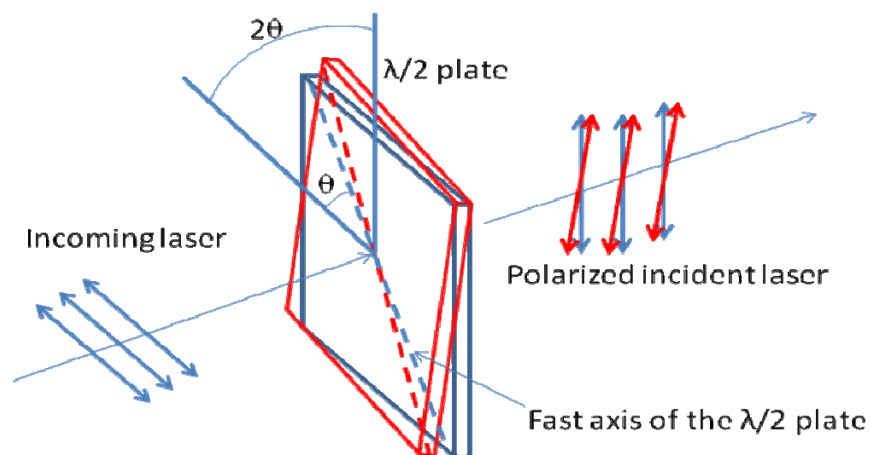
Figure 5.15 Schematic diagram of rotating the incident laser polarisation through rotating the λ/2 plate. The red arrows indicate the misorientation of the laser upon rotating the λ/2 plate.

Figure 5.16 shows the results obtained with 5° of misalignment of the incident laser. It can be seen the dependencies of G'-band shift rate upon angle as described by Equations (5.11) and (5.12), are sensitive to the alignment of the incident laser, and this effect is more significant for the VH configuration than for the VV configuration.

It is thus important to calibrate the alignment of laser polarisation accurately before performing any measurements.

A parameter $\Delta\phi$ was introduced to the 2-D model to account for the misalignment of the laser line in the instrument, and the modified equations are given by:

$$S_{VV}(\phi) = \frac{\frac{1}{\pi}\int_0^\pi I_0 \cos^4(\theta + \phi + \Delta\phi) \times \left[S_0\left(\cos^2\theta - \nu\sin^2\theta\right)\right]\mathrm{d}\theta}{\frac{1}{\pi}\int_0^\pi I_0 \cos^4(\theta + \phi + \Delta\phi)\mathrm{d}\theta} \qquad (5.13)$$

$$S_{VH}(\phi) = \frac{\frac{1}{\pi}\int_0^\pi I_0^{'}\left[\cos^2(\theta + \phi + \Delta\phi)\sin^2(\theta + \phi + \Delta\phi)\right] \times \left[S_0\left(\cos^2\theta - \nu\sin^2\theta\right)\right]\mathrm{d}\theta}{\frac{1}{\pi}\int_0^\pi I_0^{'}\left[\cos^2(\theta + \phi + \Delta\phi)\sin^2(\theta + \phi + \Delta\phi)\right]\mathrm{d}\theta} \qquad (5.14)$$

It can be seen from Figure 5.16, that these modified equations fit the experimental data well, which further verifies the validity of the 2-D model.

It should be noted that introduction of the parameter $\Delta\phi$ to account for the misalignment of laser in Equations (5.13) and (5.14) is valid only for small degrees of misalignment ($< 10°$). At higher degrees of misalignment, the orientation dependence of Raman band intensity for nanotubes may not follow the function $\cos^4(\theta+\Delta\phi)$ or $\cos^2(\theta+\Delta\phi)\sin^2(\theta+\Delta\phi)$, and other forms of equations should be used.
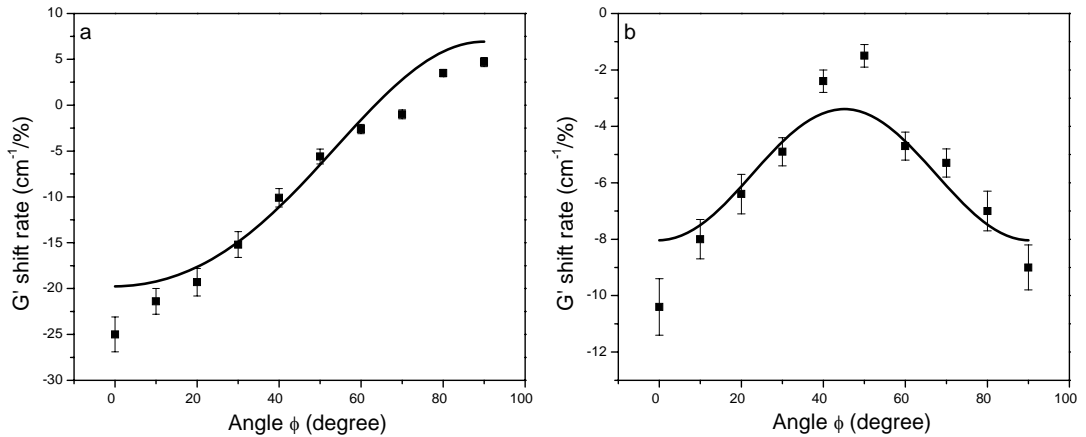

Figure 5.16 Stress-induced nanotube G'-band shift rate for the composite film as a function of the angle. Raman spectra were obtained with misaligned incident laser and detected with: (a) the VV configuration and (b) the VH configuration. The black and red lines are generated for Equation (5.13) (in (a)) and Equation (5.14) (in (b)) with $\Delta\phi = 5°$, respectively.

5.3.6 The effective modulus of nanotubes

Cooper *et al.* established a relation between the effective modulus of nanotubes E_{eff} and the G'-band shift rate S_0 which is given by [1]:

$$E_{\mathrm{eff}} = \frac{S_0}{-0.05} \qquad (5.15)$$

where the universal calibration of -0.05 cm^{-1}%$^{-1}$/GPa was derived from carbon fibres and assumed to apply to nanotubes. The effective modulus of nanotubes in CNT composites can then be determined if the shift rate S_0 is known. For the unidirectionally-aligned system (e.g. the electrospun fibres) it has been shown in Figure 5.13a that:

$$S_0 = S(0) \qquad (5.16)$$

where $S(0)$ is the shift rate obtained when the fibre is deformed parallel to the strain direction. While for the randomly-distributed system, S_0 can be estimated by fitting the shift rates obtained at different angles using Equations (5.11) and (5.12), or simply by substituting $\phi = 0°$ into these two equations which gives:

$$S_0 = 1.3 \times S_{\mathrm{VV}}(0) \qquad (5.17)$$

$$S_0 = 3.3 \times S_{\mathrm{VH}}(0) \qquad (5.18)$$

The effective modulus of nanotubes for composites containing randomly-distributed nanotubes can be determined using Equation (5.15) combined with Equations (5.17) and/or (5.18). It should be noted the correction factors 1.3 and 3.3 were derived assuming a Poisson's ratio of 0.4 and these factors depend on the Poisson's ratio of the polymer, e.g. for epoxy resin with a Poisson's ratio of 0.35, the correction factors are 1.28 and 3.0 for the VV and VH configurations, respectively. These correction factors are significantly lower than that determined by Cooper *et al.*, where a value between 3 and 9 was suggested [1].

Table 5.5 shows the values of E_{eff} determined using the different band shift rates, $S(0)$, along with Equations (5.15) - (5.18) where appropriate. It can be seen that the effective modulus of the nanotubes E_{eff} in the composites is in the range 530 - 700 GPa, i.e. about 60% of the accepted value of around 1000 GPa [30, 31]. It should be noted the value for absolute modulus of nanotubes is model-dependent as a SWNT

can be considered as a hollow cylinder. There is no unanimous agreement on the wall thickness and different assumptions of wall thickness give different modulus for the nanotubes. The most widely quoted value of 1000 GPa is derived assuming a thickness of 0.34 nm [32]. Assuming that the whole cross-section bears the force (i.e. conside a nanotube as a solid fibre) when subjected to uniaxial stress, then the nanotube modulus is less than 1000 GPa. For a nanotube with a diameter of 1 nm (which is typical of HiPco nanotubes), the modulus for its effective solid fibre is approximately 900 GPa. It can be seen the E_{eff} achieved in PVA/SWNT composite fibres and films is close to this value, suggesting a very high efficiency of stress transfer in these composites.

The slightly lower value for the nanocomposite films may be due to all of the nanotubes not lying exactly in plane. The discrepancy with the accepted value can further be accounted for by factors such as SWNT bundling and finite length effects. These effects will reduce the effective modulus below the nanotube Young's modulus E_{NT} such that:

$$E_{eff} = \eta_l E_{NT} \qquad (5.19)$$

where the parameter η_l accounts for the reduction in effective modulus of nanotubes due to the nanotubes both having finite length and being bundled. This parameter will be reduced if the nanotubes become shorter and increase as the dispersion is improved (Figure 5.9). This parameter is therefore useful in being able to gage the efficiency of reinforcement in the absence of orientation effects.

Table 5.5 Calculated effective modulus of the nanotubes based on the G'-band shift rate detected at $\phi = 0°$ (i.e. laser polarization parallel to the strain direction).

Material	Laser polarisation configuration	Shift rate (cm^{-1}/%strain)	Effective modulus (GPa)
PVA/SWNT electrospun fibre	VV	-35	700
PVA/SWNT film	VV	-23	600
PVA/SWNT film	VH	-8	530

It is possible to estimate the mechanical properties such as the modulus E_c of the composite film using the simple rule of mixtures for fibre-reinforced composites [33]:

$$E_c = \eta_o V_{NT} E_{eff} + (1 - V_{NT}) E_m \qquad (5.20)$$

where η_o is a factor that takes into account the effect of the orientation of the reinforcing fibres (nanotubes in this case) which is unity for a perfectly-aligned system and is found to be 3/8 for a 2-D random system [1, 34]. The volume fraction V_{NT} of nanotubes will be roughly the same as the weight fraction, i.e. 0.2%, since the SWNTs and PVA have about the same density ~1.3 g/cm^3. If E_{eff} is taken as 620 ± 80 GPa, $V_{NT} \sim 0.002$ and E_m is taken as 1.9 ± 0.2 GPa, η_o is taken as 3/8, substituting these values into Equation (5.20) gives a 2.3 ± 0.2 GPa for E_c, which agrees well with the experimental result in Table 5.4. This demonstrates that this is a self-consistent method to evaluate the reinforcing efficiency of randomly-distributed nanotubes.

5.3.7 Coagulation-spun PVA/SWNT fibres

It has been demonstrated that good orientation of nanotubes can be achieved in electrospinning process due to the strong electric forces. Coagulation spinning is another effective method to orient nanotubes in polymer/nanotube fibres and good mechanical properties have been achieved in PVA/SWNT coagulation-spun fibres. For example, Minus *et al*. prepared PVA/SWNT fibres with a tensile strength of 2.6 GPa [35] while Dalton *et al*. observed a Young's modulus of 80 GPa for their fibres [36]. Moreover, the alignment of nanotubes can be controlled by drawing the coagulation-spun fibres to different ratios. This provides an excellent system for investigating the effect of orientation upon the Raman band shift rate and the effective modulus of nanotubes. The properties of PVA/SWNT coagulation-spun fibres supplied by Professor Coleman's group (University of Dublin, Ireland) [8] are presented here as a comparison to the electrospun fibres.

The as-spun fibres are straight with reasonably uniform diameter. The fibrils which make up the as-spun fibre are loosely stacked as shown in Figure 5.17a. When in the wet state, the fibres can be drawn up to 63% (the draw ratio (DR) is defined as: DR =

$(l_f-l_0)/l_0)$. Fibres with higher DRs possess a more dense structure and are more uniform in diameter as can be seen from Figure 5.17b.
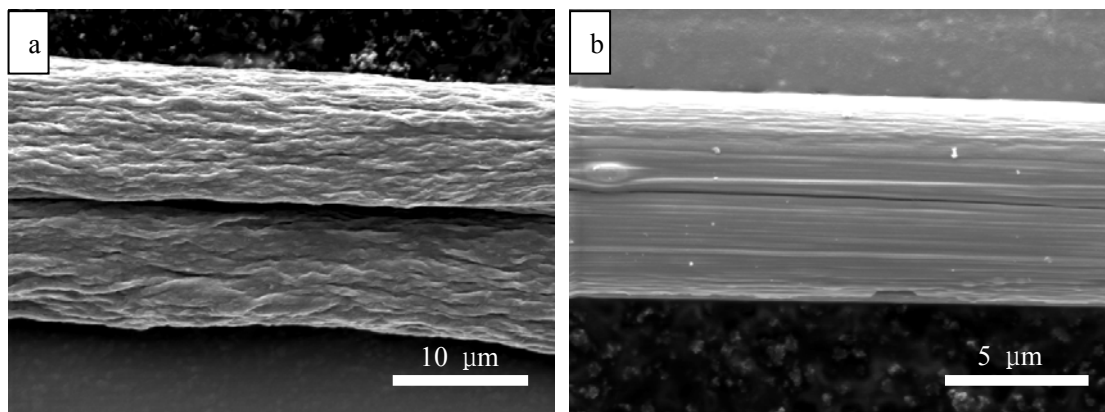
Figure 5.17 SEM images of the PVA/SWNT coagulation-spun fibre: (a) an undrawn fibre and (b) a fibre with a DR of 63%.

Figure 5.18 shows the nanotube G-band at different angles between the fibre axis and the axis of laser polarisation for an undrawn fibre (Figure 5.18a) and a fibre with a DR of 63% (Figure 5.18b). The decrease of G-band intensity with increasing angle indicates good orientation of nanotubes in these fibres and it is evident that the orientation of nanotubes in the drawn fibres is better than in the undrawn fibres. It was also noted the G-band frequency increased slightly when the angle increased from 0° to 90°. This is because nanotubes absorb the light polarized parallel to the nanotube axis at ~20 times stronger than that for perpendicularly-polarized light. The strong absorption causes heating of the nanotubes at 0° and lowers the G-band frequency.

Figure 5.18 The nanotube G-band of PVA/SWNT coagulation-spun fibres acquired at different angles relative to the axis of laser polarisation: (a) an undrawn fibre and (b) a fibre with a DR of 63%. Spectra were obtained with the VV configuration and shifted vertically for clarity.

The orientation factors for the nanotubes were determined using Equation (2.17) as described in Chapter 2 [13] and the results are shown in Figure 5.19. It can be seen the orientation factor increases from ~0.75 for the undrawn fibre to ~0.9 for the fibres wit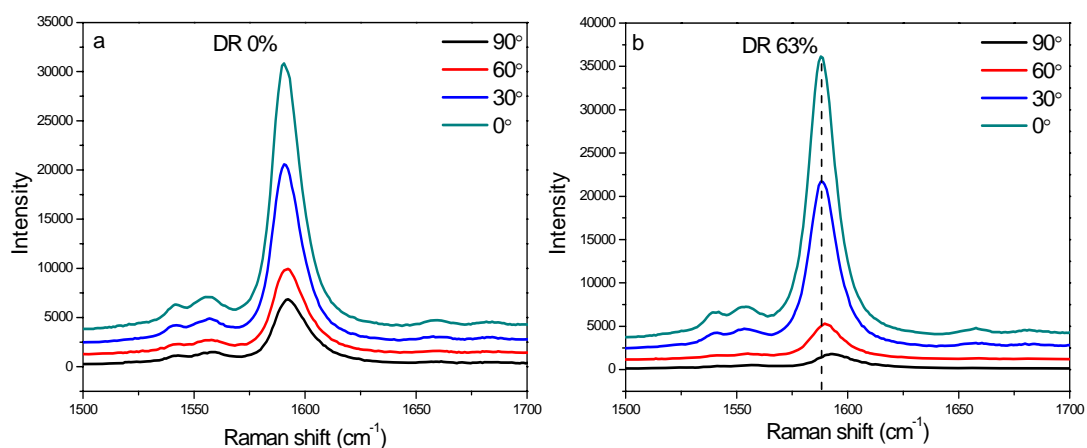h a DR of 63%. The degree of alignment of the nanotubes in fibres with a DR of 63% is close to that found in the electrospun fibres (which is 0.92) which have essentially a DR of over 10,000 [15]. This indicates drawing of the coagulation-spun fibre in the wet state is quite effective in orientating nanotubes, but drawing the fibre to higher than 63%, if it is possible, would not improve the orientation significantly.
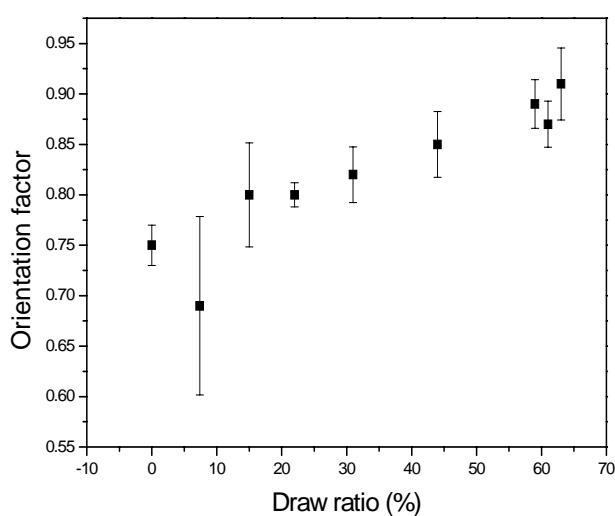
Figure 5.19 Orientation factor for the nanotubes as a function of the draw ratio of the coagulation-spun fibres.

The coagulation-spun fibres were placed on top of the PMMA beam at different angles and covered with a PMMA solution. The fibres were effectively embedded in PMMA polymers after the solvent evaporated and off-axis stress was applied to the fibres using a four-point bending rig. The stress-induced G'-band shift rate was measured in an experimental arrangement the same as that shown in Figure 5.12b. Figure 5.20 shows the shift rates at different angles between the fibre axis and the strain direction for the fibres with DRs of 0% and 63%. Curves generated for Equations (5.6) and (5.11), i.e. the dependence for perfectly-aligned system and randomly-distributed system, respectively, are also shown in Figure 5.20. It can be seen from Figure 5.20b for the highly-aligned fibre, that all the data points fall close

to the curve generated for Equation (5.6), indicating all nanotubes are subjected to the same stress and is controlled by the Poisson's contraction effect. The shift rate detected at 0°, of -26 cm^{-1}/%, corresponds to an effective modulus of 520 GPa according to Equations (5.15) and (5.16) for nanotubes in the coagulation-spun fibres with a DR of 63%. On the other hand, the data points for the undrawn fibre (poorer orientation) deviate from the Poisson's contraction line at high angles and lie in somewhere between the two lines (Figure 5.20a), which can be understood that the relatively poorer orientation leads to that all nanotubes not bearing the same stress. This suggests that the angular-dependence of Raman band shift rate, described by Equation (5.6), is sensitive to the alignment of nanotubes in the composites. It is therefore another qualitative method to assess the orientation of nanotubes although it is less straightforward yet requires considerably more measurements.
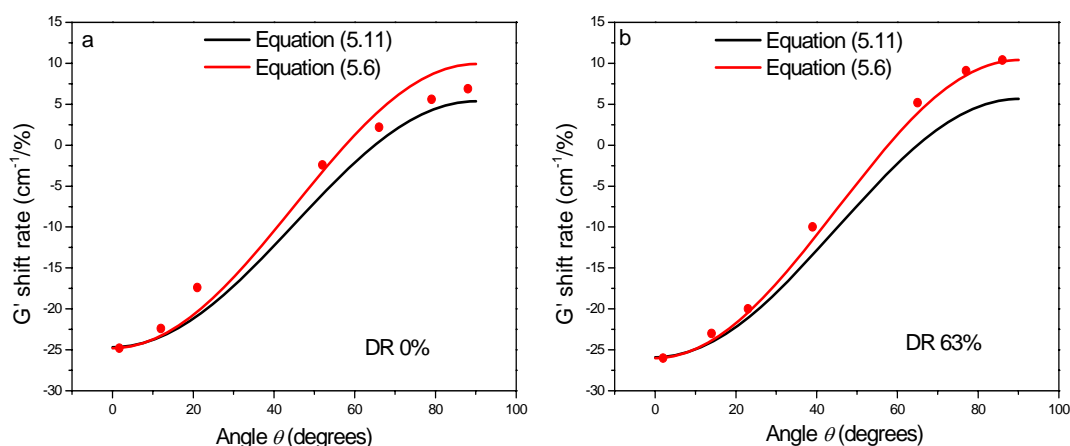
Figure 5.20 The nanotube G'-band shift rate as a function of the angle between the fibre axis and strain direction for coagulation-spun fibre with a DR of: (a) 0% and (b) 63%. Spectra were obtained with a VV configuration.

5.4 Conclusions

PVA/SWNT composite films were produced by solution casting and composite fibres were fabricated by both electrospinning and coagulation spinning. Raman spectroscopy has been demonstrated to be extremely powerful in characterising these materials.

The electrospinning process can debundle the nanotubes efficiently and exerts a

small residual compression of the nanotubes in the fibre. Polarized Raman spectroscopy showed that the nanotubes are highly aligned and the polymer molecules are partially aligned along the axis of the electrospun fibres. Crystallinity of the PVA polymer was characterised by the intensity ratio I_{1147}/I_{1127} and it was found that nanotubes do not nucleate the PVA to crystallise significantly in the composite film whereas the crystallinity increases upon electrospinning. Mechanical testing of the neat and composite films showed that the modulus of PVA is increased by 21% and the tensile strength is improved by 16% by adding 0.2% of HiPco SWNTs.

Large Raman band shift rates were observed in the composite films and electrospun fibres and it was found that the shift rate depends strongly on the angle between the nanotube axis, strain axis and the axis of laser polarisation. For randomly-distributed nanotubes, the Raman band shift rates obtained at different angles were fitted with a quantitative model considering both the Poisson's contraction effect and the orientation dependence of Raman band intensity. For highly-aligned nanotubes such as in the electrospun fibres and coagulation-spun fibres with high draw ratios, the angular-dependence of Raman band shift was explained with the Poisson's contraction effect. While for partially-aligned nanotubes such as in the undrawn coagulation-spun fibres, the shift rate-angle curve lies in somewhere between the curves for perfect orientation and that for random distribution. A model which correlates the Raman band shift rate with the effective modulus of nanotubes was also established. The calculated effective modulus, in turn, allows the estimation of the composite modulus and it was found that the composite modulus estimated using this method is consistent with the experimental data.

5.5 References

1. C. A. Cooper, R. J. Young and M. Halsall, *Investigation into the deformation of carbon nanotubes and their composites through the use of Raman spectroscopy*, Compos. Part A, 2001, **32**, 401-411.

2. T. M. G. Mohiuddin, A. Lombardo, R. R. Nair, A. Bonetti, G. Savini, R. Jalil, N.

Bonini, D. M. Basko, C. Galiotis, N. Marzari, K. S. Novoselov, A. K. Geim and A. C. Ferrari, *Uniaxial strain in graphene by Raman spectroscopy: G peak splitting, Gruneisen parameters, and sample orientation,* Phys. Rev. B, 2009, **79**, 205433 1-8.

3. M. D. Frogley, Q. Zhao and H. D. Wagner, *Polarized resonance Raman spectroscopy of single-wall carbon nanotubes within a polymer under strain,* Phys. Rev. B, 2002, **65**, 113413 1-4.

4. J. R. Wood, Q. Zhao and H. D. Wagner, *Orientation of carbon nanotubes in polymers and its detection by Raman spectroscopy*, Compos. Part A, 2001, **32**, 391-399.

5. J. Ji, G. Sui, Y. Yu, Y. Liu, Y. Lin, Z. Du, S. Ryu and X. Yang, *Significant improvement of mechanical properties observed in highly aligned carbon-nanotube-reinforced nanofibers,* J. Phys. Chem. C, 2009, **113**, 4779-4785.

6. P. Kannan, S. J. Eichhorn and R. J. Young, *Deformation of isolated single-wall carbon nanotubes in electrospun polymer nanofibres*, Nanotechnology, 2007, **18**, 235707-235713.

7. K. Wong, M. Zinke-Allmanga, J. L. Hutter, S. Hrapovi, J. Luong and W. Wan, *The effect of carbon nanotube aspect ratio and loading on the elastic modulus of electrospun poly(vinyl alcohol)-carbon nanotube hybrid fibers,* Carbon, 2009, **47**, 2571-2578.

8. F. M. Blighe, K. Young, I. A. Kinloch, L. Deng, R. J. Young and J. N. Coleman, *The effect of nanotube content and fiber drawing on the mechanical properties of coagulation spun polymer-nanotube composite fibers*, Adv. Funct. Mater., 2011, **In press**.

9. S. Cui, *Characterisation and deformation of carbon nanotubes in polymer composites,* PhD Thesis, University of Manchester, 2009.

10. J. Cardenas, F. Juan and A. Gromov, *The effect of bundling on the G' Raman band of single-walled carbon nanotubes,* Nanotechnology, 2009, **20**, 465703 1-8.

11. A. Martinelli, A. Matic, P. Jacobsson, L. Börjesson, M. A. Navarra, A. Fernicola, S. Panero and B. Scrosati, *Structural analysis of PVA-based proton conducting membranes*, Solid State Ionics, 2006, **177**, 2431-2435.

12. C. Yang, J. Yang and C. Wu, *Poly (vinyl alcohol)/poly (vinyl chloride) composite polymer membranes for secondary zinc electrodes*, J. Power Sources, 2009, **191**, 669-677.

13. T. Liu and S. Kumar, *Quantitative characterization of SWNT orientation by polarized Raman spectroscopy*, Chem. Phys. Lett., 2003, **378**, 257-262.

14. M. V. Kakade, S. Givens, K. Gardener, K. H. Lee, B. Chase and J. F. Rabolt, *Electric field induced orientation of polymer chains in macroscopically aligned electrospun polymer nanofibers,* J. Am. Chem. Soc., 2007, **129**, 2777-2782.

15. L. M. Bellan and H. G. Craighead, *Molecular orientation in individual electrospun nanofibers measured via polarized Raman spectroscopy*, Polymer, 2008, **49**, 3125-3129.

16. S. Frisk, R. M. Ikeda, D. B. Chase and J. F. Rabolt, *Determination of the molecular orientation of poly(propylene terephthalate) fibers using polarized raman spectroscopy: A comparison of methods*, Appl. Spectrosc., 2004, **58**, 279-286.

17. A. Martinelli, A. Matic, P. Jacobsson, L. Börjesson, M. Navarra, A. Fernicola, S. Panero and B. Scrosati, *Structural analysis of PVA-based proton conducting membranes,* Solid State Ionics, 2006, **177**, 2431-2435.

18. R. Iwamoto, M. Miya and S. Mima, *Determination of crystallinity of swollen poly(Vinyl Alcohol) by laser Raman spectroscopy*, J. Polym. Sci. Polym. Phys., 1979, **17**, 1507-1515.

19. N. Lachman, C.Bartholome, P. Miaudet, M. Maugey, P. Poulin and H. D. Wagner, *Raman response of carbon nanotube/PVA fibers under strain,* J. Phys. Chem. C, 2009, **113**, 4751-4754.

20. Z. Wang, *Reinforcing efficiency of carbon nanotubes in Poly(vinyl alcohol) composites,* PhD thesis, Queen Mary, University of London, 2007.

21. X. Zhang, T. Liu, T. Screekumar, S. Kumar, X. Hu and K. Smith, *Gel spinning of PVA/SWNT composite fibre*, Polymer, 2004, **45**, 8801-8807.

22. J. P. Salvetat, G. A. D. Briggs, J. M. Bonard, R. R. .Bacsa, A. J. Kulik, T. Stockli, N. A. Burnham and L. Forro, *Elastic and shear moduli of single-walled carbon nanotube ropes*, Phys. Rev. Lett., 1999, **82**, 944-947.

23. P. Kannan, *Stress transfer in carbon nanotube composite films and fibres,* PhD Thesis, University of Manchester, 2008.

24. W. Qiu, Y. Kang, Z. Lei, Q. Qin and Q. Li, *A new theoretical model of a carbon nanoube strain sensor*, Chin. Phys. Lett., 2009, **26**, 080701 1-5.

25. C. C. Kao, *Study of the deformation of single-walled carbon nanotube (SWNT)/epoxy composites using raman spectroscopy,* PhD Thesis, University of Manchester, 2008.

26. M. C. Andrews, R. J. Day, X. Hu and R. J. Young, *Dependence of fibre strain on orientation angle for off-axis fibres in composites*, J. Mater. Sci. Lett., 1992, **11**, 1344-1346.

27. J. Hwang, H. H. Gommans, A. Ugawa, H. Tashiro, R. Haggenmueller, K. I. Winey, J. E. Fischer, D. B. Tanner and A. G. Rinzler, *Polarized spectroscopy of aligned single-wall carbon nanotubes*, Phys. Rev. B, 2000, **62**, R13310-R13313.

28. H. H. Gommans, J. W. Alldredge, H. Tashiro, J. Park, J. Magnuson and A. G. Rinzler, *Fibers of aligned single-walled carbon nanotubes: Polarized Raman spectroscopy,* J. Appl. Phys., 2000, **88**, 2509-2514.

29. L. Bokobza. *New investigations on carbon nanotube-reinforced elastomers*, ECCM-14 proceeding, 2010, Budapest, Hungary.

30. M. F. Yu, B. S. Files, S. Arepalli and R. S. Ruoff, *Tensile loading of ropes of single wall carbon nanotubes and their mechanical properties*, Phys. Rev. Lett., 2000, **84**, 5552-5555.

31. M. F. Yu, O. Lourie, M. J. Dyer, K. Moloni, T. F. Kelly and R. S. Ruoff, *Strength and breaking mechanism of multiwalled carbon nanotubes under tensile load*, Science, 2000, **287**, 637-640.

32. A. Sears and R. C. Batra, *Macroscopic properties of carbon nanotubes from molecular-mechanics simulations*, Phys. Rev. B, 2004, **69**, 235406 1-10.

33. D. Hull, *An Introduction to Composite Materials*, Cambridge University Press, 1981.

34. H. Krenchel, *Fibre reinforcement*, Copenhagen: Akademisk, 1964.

35. M. L. Minus, H. G. Chae and S. Kumar, *Single wall carbon nanotube templated*

oriented crystallization of poly(vinyl alcohol), Polymer, 2006, **47**, 3705-3710.

36. A. B. Dalton, S. Collins, E. Munoz, J. M. Razal, V. H. Ebron, J. P. Ferraris, J. N. Coleman, B. G. Kim and R. H. Baughman, *Super-tough carbon-nanotube fibres - These extraordinary composite fibres can be woven into electronic textiles*, Nature, 2003, **423**, 703-703.

Chapter 6   Poly(p-phenylene terephthalamide)/SWNT composite fibres

6.1 Introduction

High-performance fibres, which usually have high strength and high modulus, have been becoming very important materials both in academic research and industrial applications since the 1960s [1]. Poly(p-phenylene terephthalamide) (PPTA) fibres, which are made up of oriented bundles of rig-rod polymer molecules, are an important aramid high-performance fibre. Figure 6.1 shows the chemical structure of PPTA polymer and the basic chemical reaction that involved in the preparation of this polymer.
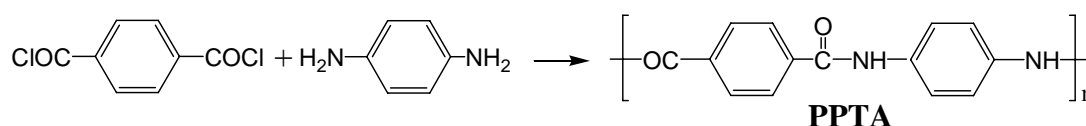
Figure 6.1 Chemical structure and preparation of PPTA.

PPTA fibres possess a high degree of crystallinity and molecular orientation in their structure, which is achieved by the lyotropic liquid crystalline phase being formed in the spinning dope combined with the unique dry-jet wet spinning technique as shown in Figure 6.2 [2, 3]. The development of molecular orientation during fibre spinning as shown in Figure 6.2b is crucial for the performance of the fibres [2]. In the spinning process, the shear force induces the liquid crystalline domains to orient along the flow direction when the spinning dope is extruded through a spinneret. As the domain passes through the spinneret some deorientation occurs, but the molecules are again oriented before reaching the coagulation bath because of the spinning tension [2].

The high degree of crystallinity and orientation and rig-rod like structure confer PPTA fibres with excellent mechanical properties. Typical values of the Young's modulus for commercial PPTA fibres such as Twaron and Kevlar fibres are in the range of 80 -140 GPa and the strength values vary from 2 to 3.5 GPa. There is still a

gap between the actual modulus (140 GPa) and the crystallite modulus (220 GPa) measured using X-ray diffraction [4]. It is desirable but great challenge to enhance the high-performance PPTA fibres.
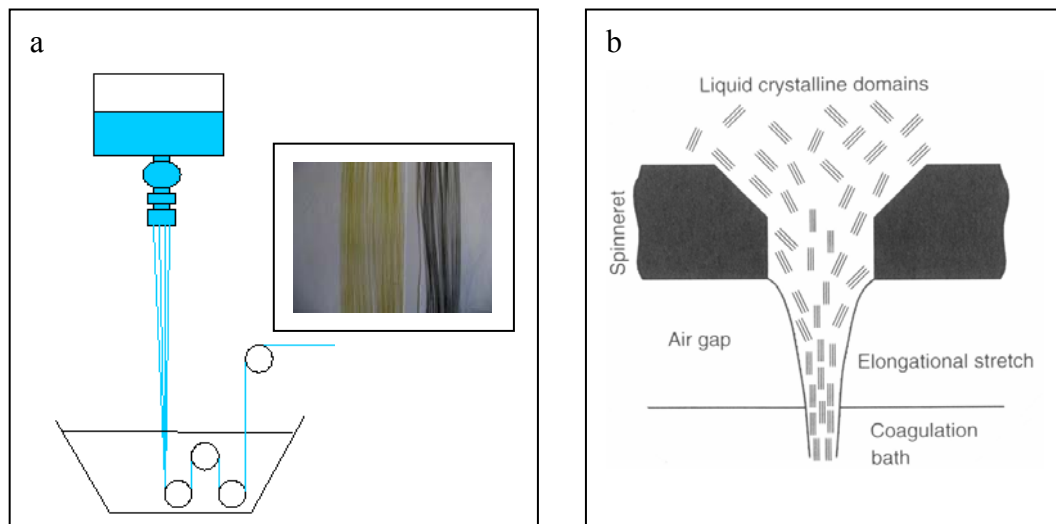

Figure 6.2 (a) Schematic of the dry-jet wet spinning process and (b) development of the orientation of the molecules in the fibre. The insert in (a) shows a picture of the neat PPTA fibres (yellow) and PPTA/SWNT composite fibres (black) [3].

Carbon nanotubes (CNTs) are now believed to be the ultimate reinforcing filler for polymers due to their extraordinary mechanical properties [5, 6]. They have been shown to have a reinforcing effect for a range of polymers such as poly(vinyl alcohol) (PVA) [7] and poly(methyl methacrylate) (PMMA) [8], but are less efficient in enhancing high-performance polymers and only a few successful examples have been reported [9, 10]. Recently, O'Connor *et al*. prepared Kevlar/nanotube composite fibres by swelling of Kevlar fibre in a suspension of multi-wall carbon nanotubes in a solvent N-methylpyrrolidone (NMP). It was found that the Young's modulus of the Kevlar fibre was not improved while the strength was increased moderately at 1% loading of nanotubes [10].

Although the conventional dry-jet wet spinning process for preparation of PPTA fibres is believed to be feasible and is suitable for mass-production of PPTA/SWNT composite fibres, little work has been published to date. In this chapter, the effect of

nanotubes on the structure and mechanical properties of PPTA fibres that were spun using a dry-jet wet spinning process was investigated. We demonstrate that important issues involved in mechanical reinforcement, such as the dispersion of nanotubes, the orientation of both nanotubes and polymer molecules, and the interfacial stress transfer can be assessed using Raman spectroscopy.

6.2 Experimental

6.2.1 Materials

The neat PPTA and PPTA/SWNT fibres used in this study were supplied by Professor van der Zwaag's group in TU Delft (Netherlands). The fibres were spun using a dry-jet wet spinning process with concentrated sulphuric acid as the solvent. Fibres with different draw ratios (DRs), which are defined as the ratios of the take-up speed to the dope extruding speed were prepared to understand the influence of processing conditions on properties of the fibres. The fibres with different DRs are denoted in this study as DR2, DR4, DR8, DR10, DR11 and DR12. During the spinning process, the fibres were spun at a fixed dope extruding speed and collected at different take-up speeds. For example, the DR2 fibres were collected at a speed of 50 m/min, while the DR12 fibres were collected at a speed of 300 m/min.

The nanotubes used to prepare PPTA/SWNT composite fibres were pristine HiPco SWNTs, and the concentration of nanotubes was 0.5wt% for all composite fibres.

6.2.2 Mechanical testing

For tensile testing of single PPTA/SWNT fibres, the fibres were mounted onto a paper frame with a window with a gauge length of 50 mm. Both ends of the fibre were fixed using a quick-setting epoxy resin to achieve good adhesion and prevent slippage of the fibre during mechanical testing. Figure 6.3 shows a schematic of the sample. The samples were left in the mechanical testing room, in which the temperature was set at $23 \pm 0.1°C$ and a humidity set at $50 \pm 5\%$, for at least 48 h prior to mechanical testing. Tensile testing was carried out using an Instron-1122 universal

testing machine. The machine was equipped with a 1 N load cell and the crosshead speed was set at 0.5 mm/min. The sample was mounted onto the testing machine to ensure the fibre axis was parallel to the loading axis. Both sides of the paper frame were burnt away prior to mechanical testing. At least 15 samples for each type of fibre were tested.
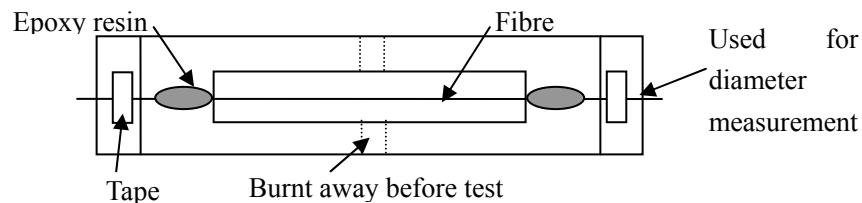

Figure 6.3 Schematic of the sample for single fibre mechanical testing [3].

6.2.3 Raman spectroscopy

Raman spectra were obtained and curve fitted using the same method as in Chapter 4 and a He-Ne 633 nm laser was used in this study. For single-fibre deformation testing, a tensile rig shown in Figure 4.1 in Chapter 4 was used for stretching the paper card on which the fibre was mounted. The strain was recorded using a micrometre attached to the rig, and the force applied on the fibre was recorded using a transducer. Raman spectra were taken at each strain level.

Polarized Raman spectroscopy was employed for orientation analysis. The position of the half-wave plate and polarisation analyser for each polarisation configuration were listed in Table 4.1 in Chapter 4. A rotational stage was used to rotate the sample relative to the axis of laser polarisation.

6.2.4 Fibre surface characterization and diameter measurement

A JEOL Scanning Electron Microscope 6300 (SEM) was used to observe the fibre surface and to measure the diameter of the fibres. Images were acquired with a secondary electron mode. The SEM image was calibrated with a standard graticule sample provided by Agar Scientific Ltd prior to any measurement. The standard sample has an area with 2160 lines/mm and is suitable for magnifications from 1000 upwards as shown in Figure 6.4.
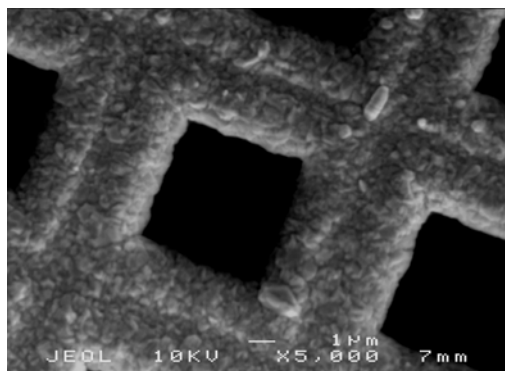
Figure 6.4 SEM micrograph of a standard graticule calibration sample.

6.3 Results and discussion

6.3.1 Structure of the composite fibres

The surface morphology of the fibres was characterised using SEM and a typical SEM image of a PPTA/SWNT fibre is shown in Figure 6.5. Generally, the surface was smooth and the cross-section appeared to be circular, but some irregularities such as particles and defects were also seen on the surface. These irregularities are thought to originate from the perturbation in the spinning process. Small variations of the spinning conditions such as change of the viscosity of the spinning dope and the temperature of coagulation bath can cause surface irregularities, which may in turn degrade the mechanical properties of the fibres significantly. For example, delamination may occur on a minor defect on the fibre surface when subjected to external stress [3].

Figure 6.5 SEM micrograph of a PPTA/SWNT DR11 fibre.

Figure 6.6 shows the Raman spectra of a neat PPTA fibre, the original SWNTs and

a PPTA/SWNT composite fibre. Characteristic Raman bands of nanotubes including the RBMs, G-band and G'-band can be seen from the spectrum of the composite fibres, and the 1610 cm^{-1} peak which corresponds to stretchi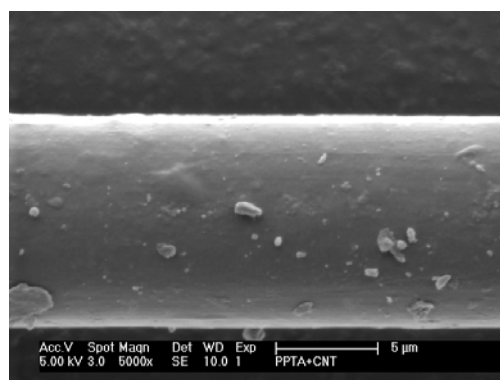ng vibration of C-C in the benzene ring of PPTA polymer can also be isolated. This enables the use of Raman spectroscopy for further characterisation of both the polymers and nanotubes.
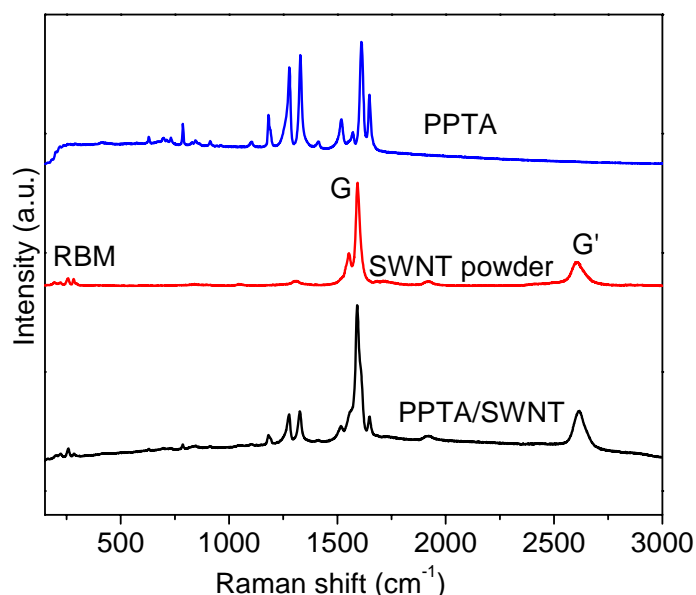
Figure 6.6 Raman spectra of the neat PPTA fibre, SWNT powder and the PPTA/SWNT composite fibre. The spectra were offset for clarity.

Table 6.1 lists the nanotube Raman bands observed from the composite fibres and the original SWNTs. Two features can be found by comparing the spectra obtained from these two materials:

1) The G'-band of the composite fibres is higher in frequency (up to 6 cm^{-1}) than that of the original SWNT powder in air, indicating residual compressive stress of the nanotubes in the fibre. It is common that in stiff polymers such as in PMMA and epoxy resin, embedded nanotubes undergo significant mechanical compression during the polymer curing processes [11] and so could also happen during coagulation in this case.

2) Multiple RBM peaks are observed in the spectrum of the composite fibres and their frequencies are slightly higher (up to 3 cm^{-1}) than those of the nanotube powder; in addition, the linewidth of the G'-band of composite fibres is smaller than that of the

nanotube powder but is larger than that of isolated individual nanotubes as found in Chapter 4. As has been demonstrated in Chapter 4, the G'-band linewidth decreases as the size of nanotube bundle decreases and the value for individual nanotubes is ~30 cm^{-1} [12]. The G'-band linewidth seen from the PPTA/SWNT composite fibres suggests the nanotubes were exfoliated to some extent but were still in bundles rather than in isolated state even though the processing conditions had been optimized to exfoliate them.

Table 6.1 Comparison of nanotube Raman bands obtained using a 633 nm laser for the PPTA/SWNT fibres and SWNT powder.

Material	RBM position (cm^{-1})	G'-band position (cm^{-1})	G'-band linewidth (cm^{-1})
HiPco SWNT powder	189, 193, 199, 201, 215, 221, 250, 257, 262, 284, 298	2609	63 - 67
PPTA/SWNT fibres	196, 221, 254, 286, 301	2611 - 2615	51 - 55

The state of dispersion of nanotubes is an important factor that determines the mechanical properties of the composites. To examine the distribution of nanotube bundles in the composite fibres, the Raman band intensity was mapped out by scanning the laser over the fibre surface. Mapping of the Raman band intensity can serve as a measure of the dispersion state since the intensity increases with the quantity of nanotubes in the laser spot. To eliminate the effect of laser focus upon the Raman band intensity, intensity ratio of the nanotube G-band to the PPTA 1610 cm^{-1} peak (I_G/I_{1610}) was used in this study. It can be seen from Figure 6.7, that the intensity ratio is generally uniform at different locations on the fibre, suggesting that the nanotube bundles were well dispersed on the micron scale. Fibres with higher DRs also showed uniform distribution of nanotubes on the micron scale.
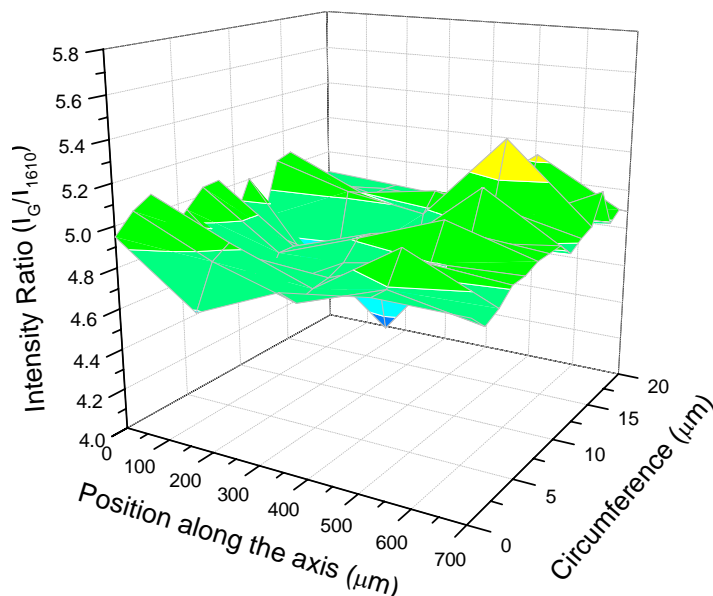
Figure 6.7 Intensity ratio of the nanotube G-band to the PPTA 1610 cm^{-1} band along a PPTA/SWNT fibre with a DR of 2, showing the uniform distribution of SWNTs.

The orientation of nanotubes was characterised using polarized Raman spectroscopy following the method described in Chapter 4. The Raman band intensity was recorded at different angles φ between the fibre axis and the axis of laser polarisation. Equation (2.17) (see Section 2.7.2 in Chapter 2) which describes the orientation-dependence of Raman band intensity was then used to fit the experimental data to give the orientation factor for the nanotubes [13]. To determine the polymer orientation quantitatively, either the Raman band intensities at different angles (for a complete procedure see [14]) or the depolarisation ratio coupled with the intensities obtained with different polarisation configurations (for a simplified model see [15]) are required. The depolarisation ratio for isotropic PPTA polymer is not available and thus a qualitative parameter $P = 1- I_{HH}/I_{VV}$ was employed to characterise the orientation in this work. For polymers, the ratio of Raman band intensity obtained with the HH configuration to that obtained with the VV configuration, I_{HH}/I_{VV}, decreases with increasing degree of alignment [15] (see Section 4.2.4 in Chapter 4 for definition of the polarisation configurations). Hence, a higher value of P indicates a better orientation of polymer molecules. This qualitative parameter has been proved to be a simple yet effective way to assess the relative molecular orientation of polymers

that possess the same structure [15]. The configuration of laser polarisation used in this study is depicted in Figure 6.8.
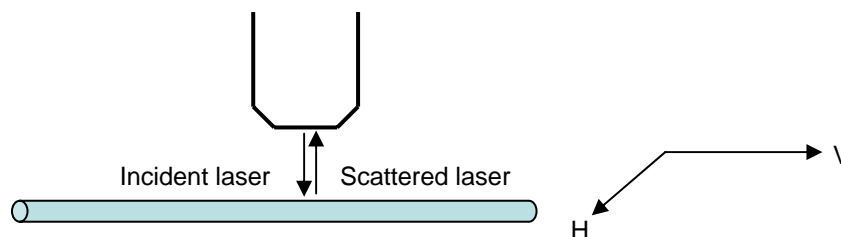
Figure 6.8 Schematic diagram of the configuration of the laser polarisation.

Figure 6.9 shows the Raman spectra of a composite fibre obtained at different angles with respect to the axis of laser polarisation and the spectra of a neat PPTA fibre obtained with different polarisation configurations. The dramatic decease of the G-band intensity when increasing the angle (Figure 6.9a) and the different intensities observed with different polarisation configurations (Figure 6.9b) indicate that both the nanotubes and polymer molecules are aligned parallel to the fibre axis.
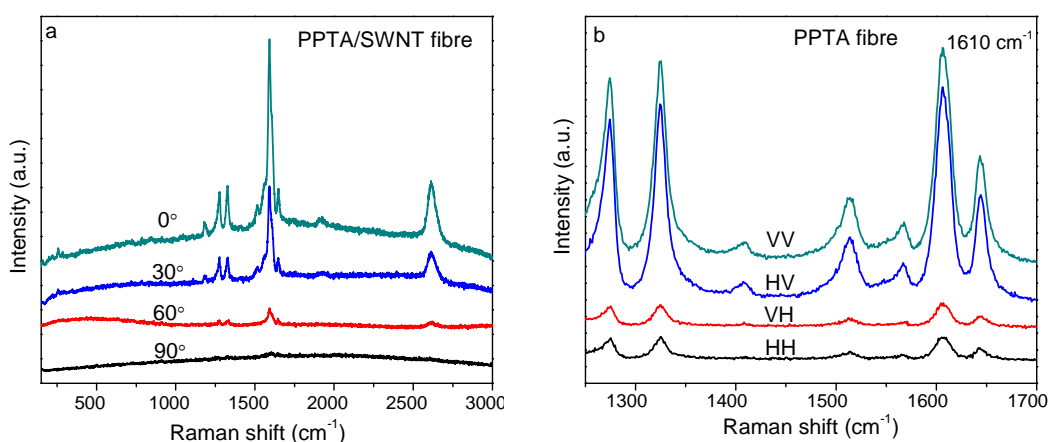
Figure 6.9 Raman spectra of: (a) a composite fibre at different angles relative to the axis of laser polarisation and (b) a neat fibre for different polarisation configurations. The DR is 11 for both fibres. The spectra were shifted vertically for clarity.

The normalised intensities of the G-band relative to the intensity at 0º, as well as the lines generated for a $\cos^4\varphi$ function, which is expected for perfect orientation of nanotubes, are illustrated in Figure 6.10. Also shown in Figure 6.10 is the resulting fit of Equation (2.17) to the data for a DR11 fibre using the best-fit parameters for

$<P_2(\cos\beta)>$ and $<P_4(\cos\beta)>$ (β is the angle between the nanotube axis and the fibre axis, and P_2 and P_4 are the second-order and fourth-order orientation factors, respectively. See Section 2.7.2 in Chapter 2 for details.) and it can be seen the function fits the data very well.
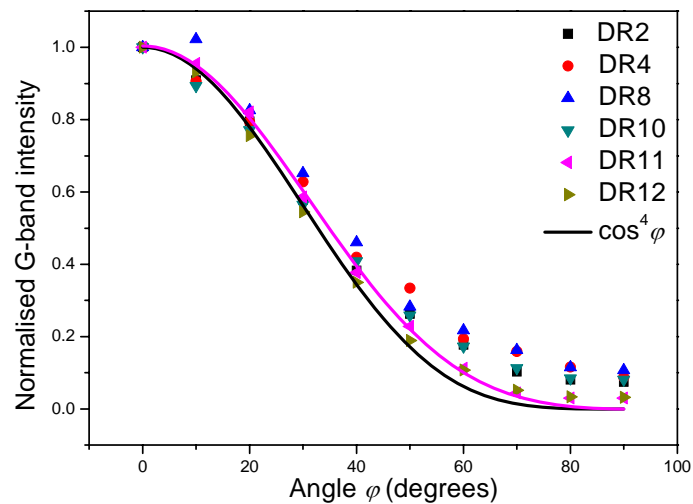
Figure 6.10 Variation of the nanotube G-band intensity as a function of the angle φ. The intensities are normalised to the intensity at 0°. The black curve is generated for a cos⁴φ function. The red curve is a fitting curve for a DR11 fibre using Equation (2.17).

The orientation factor $<P_2(\cos\beta)>$ for the nanotubes and the qualitative orientation parameter P for PPTA are plotted as a function of the fibre DR as shown in Figure 6.11. The large standard deviation in the orientation parameter for nanotubes is due to probing different areas while rotating the sample. It can be seen the orientation of both the nanotubes and polymer molecules generally increases with the fibre DR. It is also noted the orientation of the polymers in the composite fibres with a DR of 2 is higher than that in the neat fibre of the same DR, while for fibres with higher DRs the polymer molecules are better oriented in the neat fibres than in the composite fibres. The change of polymer orientation by adding nanotubes may have direct effect on the mechanical performance of the composite fibres, which will be discussed later. It remains unclear at this stage how the nanotubes influence the arrangement of the polymer chains in the composite fibres.
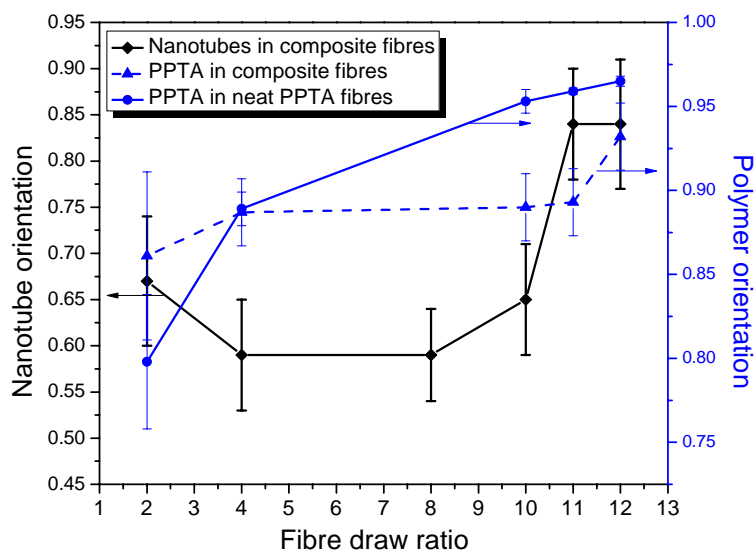
Figure 6.11 Orientation factors for nanotubes and polymers as a function of fibre DR for the composite fibres and neat PPTA fibres.

6.3.2 Mechanical properties

The mechanical properties of the fibres were determined using an Instron machine. The typical stress-strain curves for the neat PPTA and PPTA/SWNT fibres are shown in Figure 6.12 and it can be seen the variation of stress with strain appears roughly linear until fibre breaks. A closer inspection reveals that the slope in these curves decreases when the strain exceeds 0.5% and increases after 1%. This phenomenon is more pronounced for fibres with a lower DR, which can be seen more clearly by differentiating the stress over strain which gives rise to the modulus-strain curves, as shown in Figure 6.12c. The decrease of modulus in the strain range of 0.5% - 1.0% is due to yielding of the polymers. According to Northolt's theory [16], the stress acting on the domain in the fibre causes not only extension of the domain along the chain direction but also the rotation of the chain axis which is brought about by the shear stress between adjacent domains that possess different molecular orientations. Yielding of the fibre is caused by plastic shearing of chains as a result of the disruption of secondary interchain bonds [16]. It was noted the yielding of the fibre becomes less obvious as the orientation improves.
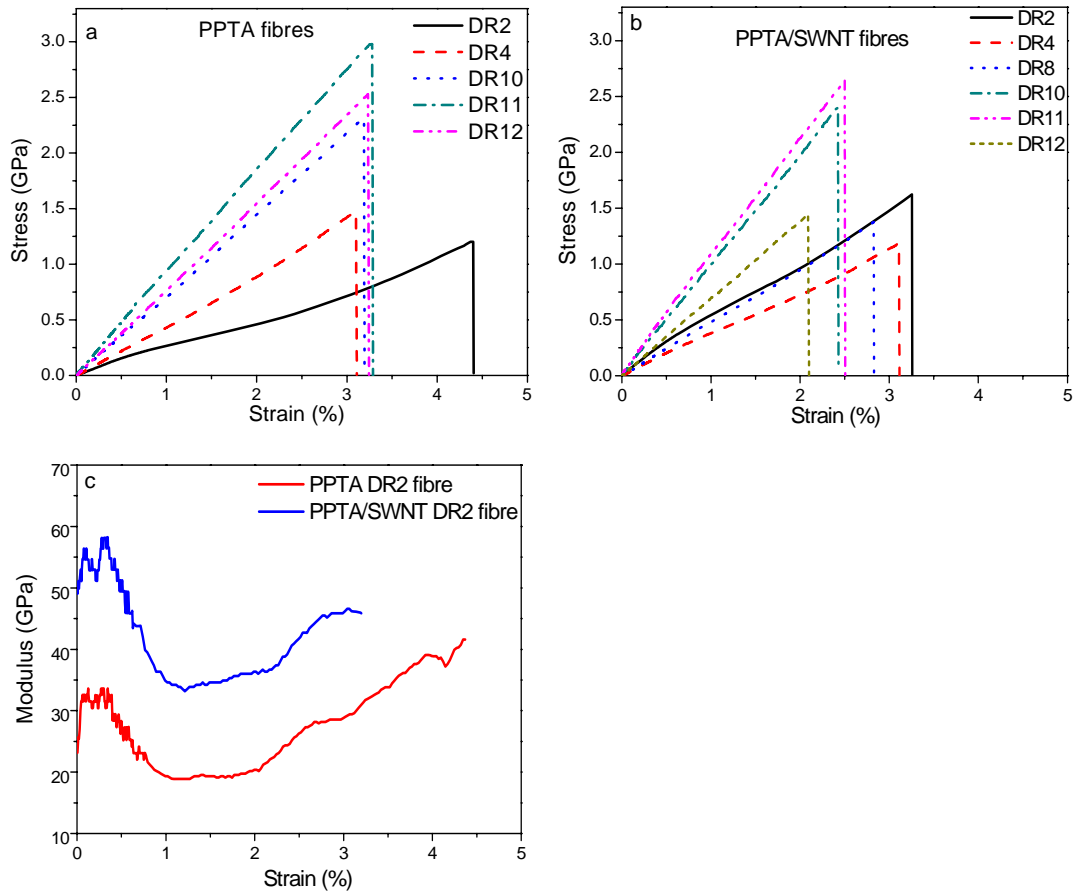
Figure 6.12 Typical stress-strain curves of: (a) neat PPTA fibres and (b) PPTA/SWNT fibres. (c) The fibre modulus as a function of strain for DR2 fibres.

The increase of modulus beyond 1% strain is thought to be due to the increase of molecular orientation under strain. The orientation of polymer molecules of DR2 fibres was monitored during deformation as shown in Figure 6.13. It can be seen the molecular orientation in both the neat PPTA fibres and composite fibres increases significantly during tensile deformation. Strain-induced reorientation of the polymers was also observed in the fibres with higher DRs but the improvements were less significant as compared to the DR2 fibres.
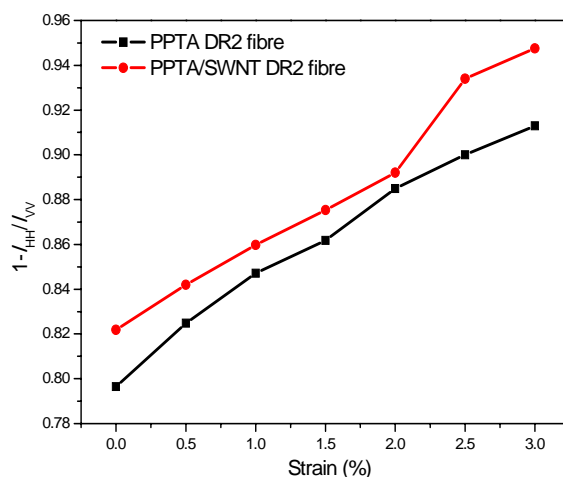
Figure 6.13 Molecular orientation of PPTA polymers in the neat PPTA fibres and composite fibres with a DR of 2 during tensile deformation.

The Young's moduli of the fibres were determined in the strain range of 0 - 0.5% where good linearity was observed. The fibre diameter and mechanical parameters including the modulus, tensile strength and elongation at break are presented as a function of DR as shown in Figure 6.14 and listed in Table 6.2. It can be seen that the modulus and tensile strength increases with the fibre DR for both types of fibre. For the neat PPTA fibres, the modulus and strength increase from 45 GPa and 1.7 GPa to 112 GPa and 3.3 GPa, respectively, and the mechanical properties of the neat fibres with DRs higher than 10 are comparable to those of commercial Kevlar and Twaron fibres [3]. For the composite fibres, the modulus and strength increase from 52 GPa and 1.3 GPa to 99 GPa and 1.9 GPa, respectively. As expected, the elongation at break for both types of fibre decreases with the increase of DR. The increase of modulus and strength with the fibre DR can be understood on the basis of the improvement of orientation for both the polymer molecules and the nanotubes upon drawing.

It was found that the Young's modulus of composite fibres was improved by 15% relative to the neat fibre with a DR of 2. For fibres with higher DRs, the mechanical properties were degraded, an effect that has also been observed for other polymer/CNT composites [17]. It should be noted that mechanical reinforcement of polymers has been achieved mostly on relatively low-modulus polymers to date, and mechanical degradation of polymers by pristine nanotubes has also been reported

where poor dispersion of nanotubes and weak interfacial interactions occur [17-20].
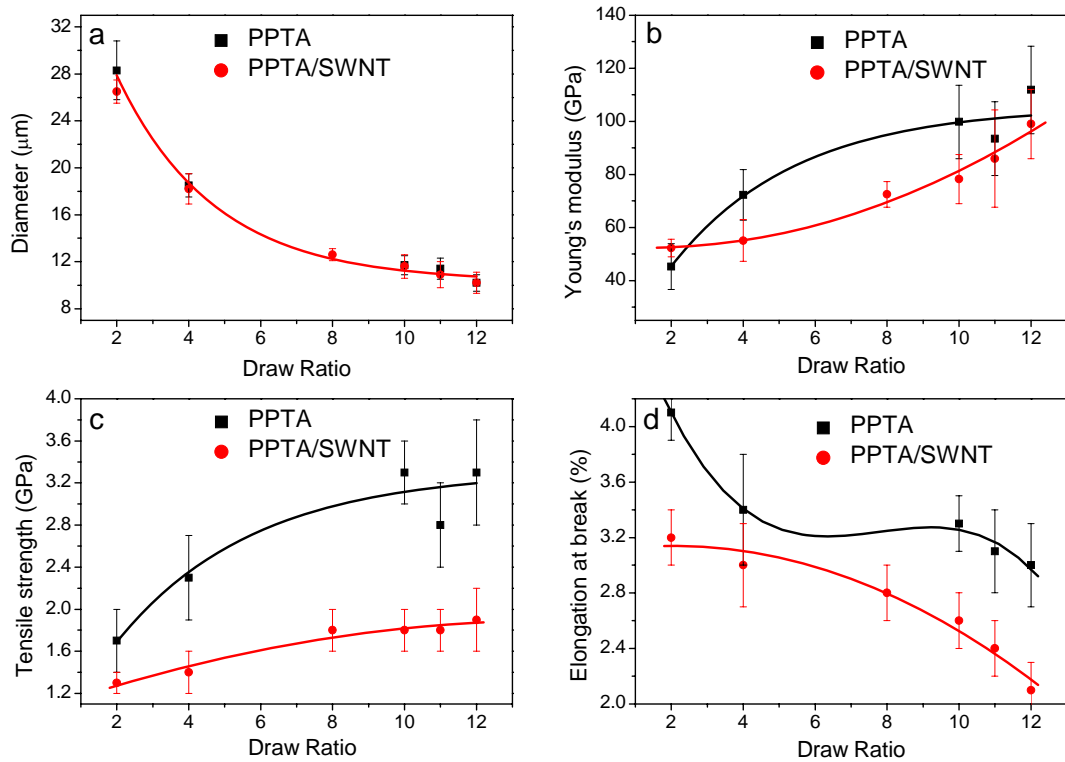
Figure 6.14 Mechanical properties of the neat PPTA and PPTA/SWNT fibres.

Table 6.2 Mechanical properties of the neat PPTA and PPTA/SWNT fibres.

Fibre	DR	Diameter (μm)	Modulus (GPa)	Strength (GPa)	Elongation at break (%)
PPTA	2	28.3±2.5	45±9	1.7±0.3	4.1±0.2
	4	18.5±1.0	72±9	2.3±0.4	3.4±0.4
	10	11.0±0.8	100±14	3.3±0.3	3.3±0.2
	11	11.4±0.9	93±13	2.8±0.4	3.1±0.3
	12	10.1±0.7	112±16	3.3±0.5	3.0±0.3
PPTA/SWNT	2	26.5±1.0	52±3	1.3±0.1	3.2±0.2
	4	18.2±1.3	55±8	1.4±0.2	3.0±0.3
	8	12.6±0.5	72±5	1.8±0.2	2.8±0.2
	10	11.6±1.1	78±9	1.8±0.2	2.6±0.2
	11	10.9±1.0	86±18	1.8±0.2	2.4±0.2
	12	10.2±0.9	99±13	1.9±0.3	2.1±0.2

Along with the importance of dispersion, molecular orientation is thought to be another important factor that determines the mechanical properties of the fibres. The moduli of the composite fibres are presented as a function of the orientation of both nanotubes and PPTA polymers as shown in Figure 6.15a. Also shown in Figure 6.15b is the change of modulus of the composite fibres relative to the neat fibres ($\Delta E = E_{Composite} - E_{Neat}$) as a function of the difference in PPTA orientation ($\Delta P = P_{Composite} - P_{Neat}$). It can be seen from Figure 6.15a, that the composite modulus is more strongly dependent on the orientation of polymer molecules than on the nanotube orientation. Figure 6.15b illustrates that the Young's modulus increases when the orientation of polymers improves relative to the neat fibre (e.g. for the DR2 fibres) and reduces when the orientation of polymers deteriorates. This indicates that the orientation of polymer molecules plays a dominant role in mechanical properties of these composite fibres.
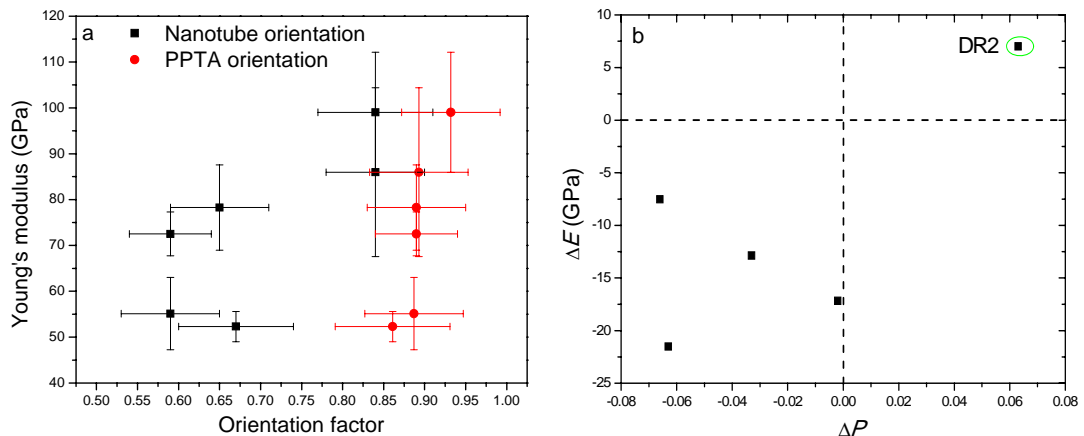
Figure 6.15 (a) Modulus of the composite fibres as a function of nanotube orientation and PPTA orientation. (b) Difference in modulus between the composite fibres and the neat fibres as a function of the difference in PPTA orientation.

6.3.3 Interfacial effects

Raman spectroscopy was also employed to follow the deformation behaviour of the composite fibres. Figure 6.16 shows the variation of band frequency for both the nanotube G'-band and PPTA 1610 cm^{-1} peak as a function of the tensile strain for the composite fibres (only the data for DR2 and DR11 fibres are presented here for

clarity). It can be seen the PPTA 1610 cm^{-1} peak shifts to lower wavenumber monotonically with increasing strain up to fibre fracture. On the other hand, the nanotube G'-band frequency was found to decrease as the strain increases until it reaches ~0.3%, and the downshift of the G'-band ceases when the strain exceeds 0.6%. The strain at which the Raman band frequency-strain deviates from a straight line is slightly different for fibres with different DRs, but the transition strains are all well below the yield strain of the fibres shown in Figure 6.12. The transition is therefore an indication of interfacial slippage, which could be a result of interfacial sliding at the CNT/CNT interface and/or the polymer/CNT interface [21].
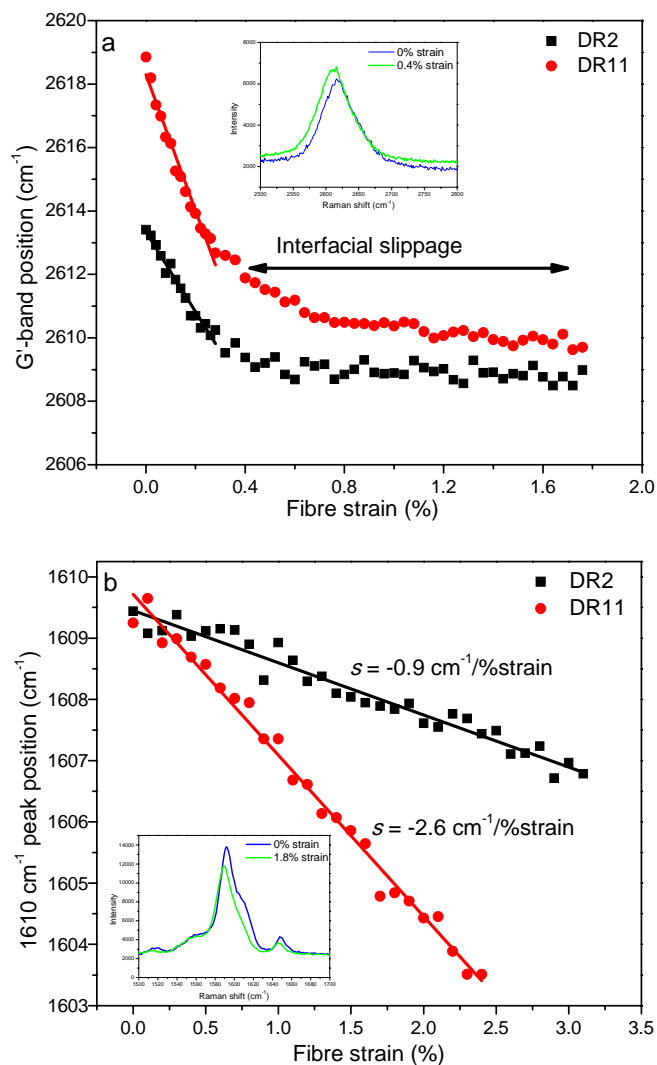
Figure 6.16 Variation of the Raman band frequency as a function of the strain for the composite fibres with different DRs: (a) the nanotube G'-band and (b) the PPTA 1610 cm^{-1} peak. The insets show the G'-band and 1610 cm^{-1} peak at different strain levels for the DR11 fibres.

Since the shear modulus of the PPTA fibre is around 1.4 GPa [16], then the strain at which the interfacial sliding occurs, of 0.3%, corresponds to an interfacial shear stress of roughly 4.2 MPa. Previous experimental and theoretical results suggested that the interfacial shear strength (IFSS) for the CNT/CNT interface is in the range of 0.08 - 0.66 MPa [22], while the IFSS for the polymer/CNT interface in a non-covalently bonded system is around 50 - 100 MPa [5, 23, 24]. An IFSS of 2.5 MPa was also predicted by Frankland *et al.* for polyethylene composites [25]. The interfacial failure at 0.3% strain in the PPTA/SWNT composite fibres is therefore likely to be due to sliding at the polymer/CNT interface and this represents a relatively weak interfacial adhesion for CNT composites. The weak polymer/CNT interface in the composite fibres was revealed by SEM observations of the fracture surface as shown in Figure 6.17. The SEM image shows that rigid SWNT ropes with diameters of 30 - 70 nm were pulled out from the matrix, which also suggests relatively low aspect ratios for the nanotube ropes (it should be noted, however, the exsitence of smaller nanotubes could not be excluded as it was difficult to distinguish nanotubes from the polymers due to the charging effects at higher magnifications). The reinforcing efficiency could be improved by further exfoliating the nanotubes into smaller bundles.

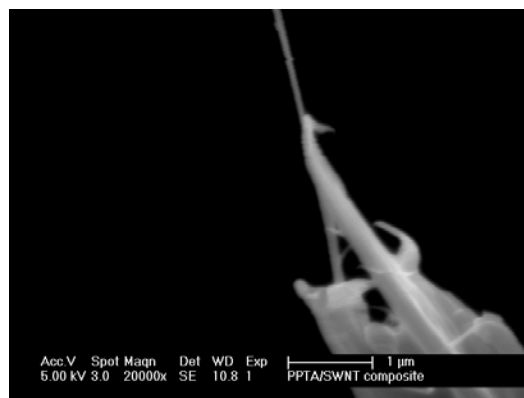*Figure 6.17 SEM micrograph of the fracture surface of a PPTA/SWNT fibre with a DR of 2.*

Raman band shift rates for fibres with different DRs are listed in Table 6.3. The shift rates were found to increase with the draw ratio as well as the modulus of the fibres, due probably to the improved orientation of both the nanotubes and polymers for fibres with higher DRs. The G'-band shift rate varies from 12.5 to 22 cm^{-1}/% in the

composite fibres, which translates to an effective nanotube modulus ranging from 250 to 440 GPa according to Equations (5.15) and (5.16) (in Chapter 5).

It is then possible to estimate the modulus of the composite fibres using the rule of mixtures as given by Equation (5.20) in Chapter 5. The orientation factor η_o is taken as 1 in the PPTA/SWNT fibres, the volume fraction of SWNTs V_{NT} is taken as 0.5% as the density of nanotubes is close to that of the PPTA, the effective nanotube modulus E_{eff} is taken as 440 GPa and the modulus of the neat PPTA fibre E_m is taken as 100 GPa (e.g. for a DR11 fibre). Substituting these values to Equation (5.20) gives approximately only 2% increase of modulus of the PPTA fibres for the nanotube concentration employed here. Moreover, the matrix in the composites was probably degraded compared to the neat PPTA due to the poorer molecular orientation. It is therefore not too surprising to observe a negative reinforcing effect in the composite fibres even though high efficiency of stress transfer was observed.

Table 6.3 Strain-induced Raman band shift rate (cm^{-1}/%strain) for the fibres with different DRs.

Fibre	DR	G'-band [a]	G-band [a]	1610 cm^{-1}	1648 cm^{-1}
PPTA	2			-0.7±0.02	--
	4			-1.7±0.2	-1.0±0.2
	10			-3.6±1.3	-1.6±0.4
	11			-3.9±0.2	-1.6±0.2
	12			-3.8±0.3	-1.5±0.1
PPTA/SWNT	2	-12.4±0.7	-7.1±0.1	--	--
	4	-14.8±2.0	-7.8±1.0	--	--
	8	-15.8±1.9	-7.9±1.3	--	--
	10	-18.1±2.6	-8.9±0.9	--	--
	11	-22.0±1.5	-9.5±1.4	-2.4±0.2	-1.3±0.2
	12	-16.2±0.5	-8.6±1.0	--	--

--a: The band shift rates were calculated using the data in the strain range of 0 - 0.2%.

The overall down-shift of the G'-band during deformation is a measure of the

maximum stress transferred to the nanotubes. A comparison of the nanotube G'-band shift rates together with the final down-shifts reported in the literature is listed in Table 6.4. It is difficult to compare the shift rate for different composite systems as it depends on the nanotube orientation, the preparation method as well as the properties of the polymer matrix. Despite the significant variations in Raman band shift rate observed in different composites, however, the final shift of the nanotube G'-band is comparable, which suggests a similar interfacial shear strength in these non-covalently bonded nanocomposites.

Table 6.4 Nanotube G'-band shift rate and the final shift in different composites.

Polymer	CNT type	Functionality	Shift rate $(cm^{-1}/\%strain)$	Maximum shift (cm^{-1})	Reference
PVA	Elicarb	Pristine	-3.7	~-7	[26]
		-COOH	-5.6	~-8	
PVA	HiPco	Pristine	-23	~-8	Chapter 5
Epoxy	HiPco	Pristine	-13	-8	[27]
Polystyrene	SWNT	Annealed	~-9.5	-7	[28]
Polycarbonate	Undiym Inc	Pristine	-6	-2.6	[29]
		PCA-functionalized	-8.5	-4	
Poly(methyl methacrylate)	HiPco	Pristine	-15	-4	[30]
PPTA/SWNT DR2	HiPco	Pristine	-12.5	-4	This work
PPTA/SWNT DR11	HiPco	Pristine	-23	-8	This work

The reversibility of deformation of the composite fibres was investigated by loading and unloading on the fibres to different strain levels. Two cycles of loading were applied at each strain level and the response of the G'-band are shown in Figure 6.18. In the cyclic loading within the strain range of 0 - 0.2% (Figure 6.18a and 6.18c), the

G'-band shifts to higher wavenumber in the unloading process following almost the same path as the loading line, and the curves for the second cycle overlap with the first ones, indicating a reversible deformation process [30]. When the strain is recovered back from 1% where most interfacial sliding has been activated, the G'-band returns in a different path such that hysteresis is observed. For the DR2 fibres, the shift rate in the initial stage of the unloading curve is similar to the loading curve, and the second cycle begins with a slightly smaller shift rate, showing reversible behaviour again. All these indicate that breakdown of the interface in the composite fibres is a gradual process. For a DR11 fibre as shown in Figure 6.18d, the Raman shift rate in the unloading curve is smaller than in the loading curve, and the shift rate in the second loading cycle is also smaller than in the first loading curve. This implies that the breakdown of the interface in the first loading cycle is more significant for fibres with a higher DR than with lower DRs (Figure 6.18b).
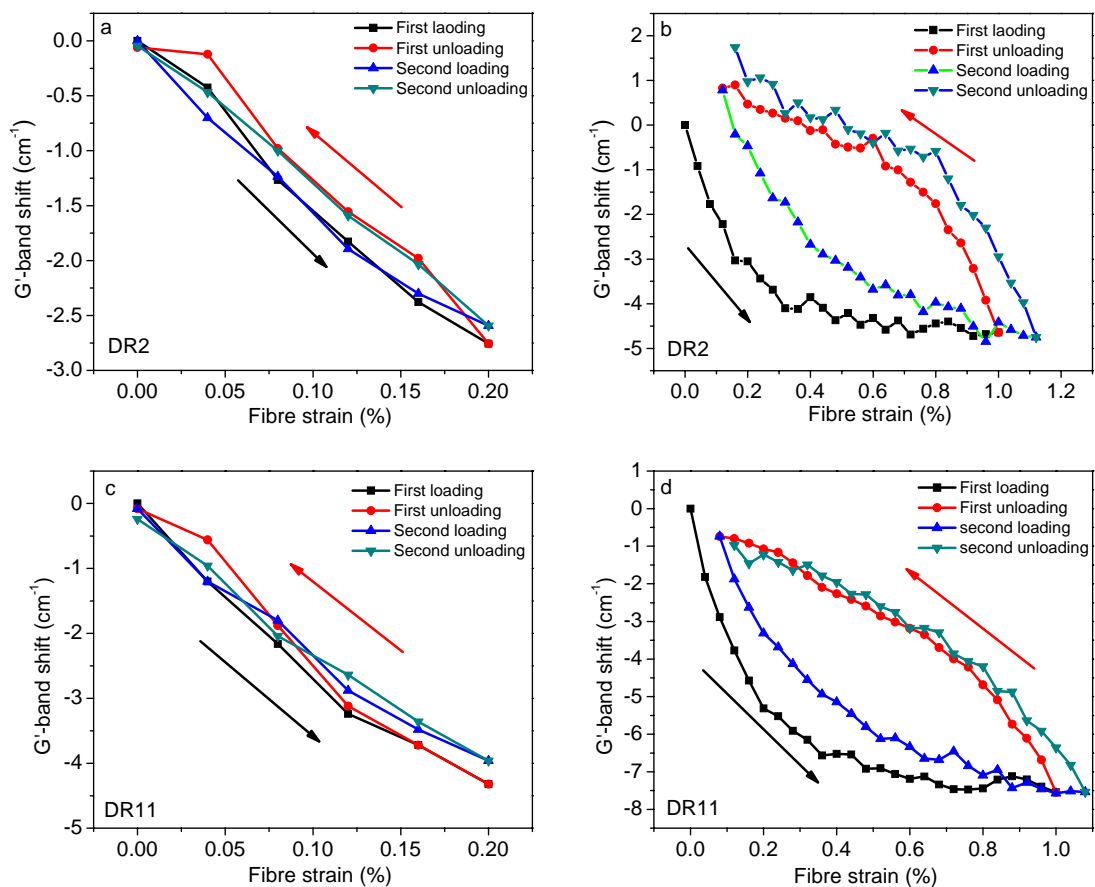

Figure 6.18 Variation of the G'-band under cyclic loading for PPTA/SWNT fibres with different DRs: (a) and (b) DR2; and (c) and (d) DR11.

After being fully unloaded from 1% strain, the G'-band in the composite fibre with a DR of 2 is about 1.7 cm^{-1} higher than the initial position prior to cyclic loading (Figure 6.19b). The up-shift of G' frequency suggests a 0.34 GPa of residual compressive stress upon unloading according to the universal calibration for stress-induced shift of the G'-band [27]. This residual stress is thought to arise from the friction between the mismatched nanotube and the matrix. In addition, the interfacial sliding results in an approximately 0.84 MJ/m^3 of energy dissipation in the loading-unloading cycle (the energy dissipation was calculated from the area of the loop between loading and unloading stress-strain curves following the method described in Ref. [31]), which is about 50% higher than in the neat PPTA fibre. The frictional sliding in the composite fibres increases the energy dissipated during cyclic loading relative to the neat fibres and this may be useful in structural damping applications [24].

6.4 Conclusions

PPTA/SWNT composite fibres spun using a dry-jet wet spinning process were characterised using Raman spectroscopy. Mapping of the relative intensity of the nanotube G-band and the PPTA 1610 cm^{-1} peak showed a good dispersion of nanotubes on the micron scale in the composite fibres, while on the nanoscale, the nanotubes are in bundles with relatively large diameters. Improvement in the modulus was observed in the composite fibres with a DR of 2 compared to the neat PPTA fibres with the same DR, but the mechanical properties of the composite fibres with higher DRs are poorer than those of the neat fibres. Orientation analysis showed that the incorporation of nanotubes improves the orientation of polymers for fibres with a DR of 2 but degrades the matrix orientation at higher DRs. The change of orientation of polymers has direct effect on mechanical properties of the composite fibres.

In-situ Raman spectroscopy study during fibre deformation revealed good stress transfer from the matrix to nanotubes in the small strain range and the interface fails when the strain exceeds 0.6%. Cyclic loading on the fibres indicated reversible

deformation within the strain range of 0 - 0.2% and a gradual breakdown of the interface when subjected to higher strains. The interfacial failure in the first loading cycle is more significant for the fibres with higher DRs than for lower DR fibres.

6.5 References

1.   W. Y. Yeh, *Structure-property Relationship in engineering polymer fibres,* PhD Thesis, University of Manchester, 1995.

2.   D. Lu, *Structure/property relationships in aromatic polyamide fibres,* PhD Thesis, University of Manchester, 1991.

3.   Y. T. Shyng, *Interfacial micromechanics in model composites with high performance polymer fibres,* PhD Thesis, University of Manchester, 2006.

4.   W. Y. Yeh and R. J. Young, *Molecular deformation processes in aromatic high modulus polymer fibres,* Polymer, 1999, **40**, 857-870.

5.   J. N. Coleman, U. Khan, W. J. Blau, and Y. K. Gun'Ko, *Small but strong: A review of the mechanical properties of carbon nanotube–polymer composites,* Carbon, 2006, **44**, 1624-1652.

6.   J. N. Coleman, U. Khan, and Y. K. Gun'Ko, *Mechanical reinforcement of polymers using carbon nanotubes,* Adv. Mater., 2006, **18**, 689-706.

7.   J. N. Coleman, M. Cadek, R. Blake, V. Nicolosi, K. P. Ryan, C. Belton, A. Fonseca, J. B. Nagy, Y. K. Gun'ko, and W. J. Blau, *High-performance nanotube-reinforced plastics: Understanding the mechanism of strength increase,* Adv. Func. Mater., 2004, **14**, 791-798.

8.   D. Blond, V. Barron, M. Ruether, K. P. Ryan, V. Nicolosi, W. J. Blau, and J. N. Coleman, *Enhancement of Modulus, Strength, and Toughness in Poly(methyl methacrylate)-Based Composites by the Incorporation of Poly(methyl methacrylate)-Functionalized Nanotubes,* Adv. Funct. Mater., 2006, **16**, 1608-1614.

9.   S. Kumar, T. D. Dang, F. E. Arnold, A. R. Bhattacharyya, B. G. Min, X. F. Zhang, R. A. Vaia, C. Park, W. W. Adams, R. H. Hauge, R. E. Smalley, S. Ramesh, and P. A. Willis, *Synthesis, structure, and properties of PBO/SWNT composites,*

Macromolecules, 2002, **35**, 9039-9043.

10. I. O'Connor, H. Hayden, J. N. Coleman, and Y. K. Gun'ko, *High-strength, high-toughness composite fibers by swelling Kevlar in nanotube suspensions,* Small, 2009, **5**, 466-469.

11. M. D. Frogley, D. Ravich, and H. D. Wagner, *Mechanical properties of carbon nanoparticle-reinforced elastomers,* Compos. Sci. Technol., 2003, **63**, 1647-1654.

12. J. Cardenas, F. Juan, and A. Gromov, *The effect of bundling on the G' Raman band of single-walled carbon nanotubes,* Nanotechnology, 2009, **20**, 465703 1-8.

13. T. Liu and S. Kumar, *Quantitative characterization of SWNT orientation by polarized Raman spectroscopy,* Chem. Phys. Lett., 2003, **378**, 257-262.

14. D. I. Bower, *Investigation of molecular orientation distribution by polarized Raman-scattering and polarized fluorescence,* J. Polym. Sci. B., 1972, **10**, 2135-2153.

15. S. Frisk, R. M. Ikeda, D. B. Chase, and J. F. Rabolt, *Determination of the molecular orientation of poly(propylene terephthalate) fibers using polarized raman spectroscopy: A comparison of methods,* Appl. Spectrosc., 2004, **58**, 279-286.

16. M. G. Northolt, J. J. M. Baltussen, and B. Schaffers-Korff, *Yielding and hysteresis of polymer fibres,* Polymer, 1995, **36**, 3485-3492.

17. A. R. Bhattacharyy, T. V. Sreekumar, T. Liu, S. Kmar, L. M. Errison, R. H. Haug, and R. E. Smalley, *Crystallization and orientation studies in polypropylene/single wall carbon nanotube composite,* Polymer, 2003, **44**, 2373-2377.

18. P. M. Ajayan, L. S. Schadler, C. Giannaris, and A. Rubio, *Single-walled carbon nanotube-polymer composites: strength and weakness,* Adv. Mater., 2000, **12**, 750-753.

19. M. Manchado, L. Valentini, J. Biagiotti, and J. M. Kenny, *Thermal and mechanical properties of single-walled carbon nanotubes-polypropylene composites prepared by melt processing,* Carbon, 2005, **43**, 1499-1505.

20. B. Vigolo, B. Vincent, J. Eschbach, P. Bourson, J. F. Mareche, E. McRae, A. Mller, A. Soldatov, J. Hiver, A. Dahoun, and D. Rouxel, *Multiscale characterization of single-walled carbon nanotube/polymer composites by coupling Raman and Brillouin spectroscopy,* J. Phys. Chem. C, 2009, **113**, 17648-17654.

21. P. Kannan, S. J. Eichhorn, and R. J. Young, *Deformation of isolated single-wall carbon nanotubes in electrospun polymer nanofibres,* Nanotechnology, 2007, **18**, 235707-235713.

22. J. Cumings and A. Zettl, *Low-friction nanoscale linear bearing realized from multiwall carbon nanotubes,* Science, 2000, **289**, 602-604.

23. A. Barber, S. Cohen, and H. Wagner, *Measurement of carbon nanotube polymer interfacial strength,* Appl. Phys. Lett., 2003, **82**, 4140-4142.

24. J. Suhr, N. Koratkar, P. Keblinski, and P. Ajayan, *Viscoelasticity in carbon nanotube composites,* Nature Mater., 2005, **4**, 134-137.

25. S. J. V. Frankland, A. Caglar, D. W. Brenner, and M. Griebel, *Molecular simulation of the influence of chemical cross-links on the shear strngth of carbon nanotube-polymer interfaces,* J. Phys. Chem. B, 2002, **106**, 3046-3048.

26. N. Lachman, C.Bartholome, P. Miaudet, M. Maugey, P. Poulin, and H. D. Wagner, *Raman response of carbon nanotube/PVA fibers under strain,* J. Phys. Chem. C, 2009, **113**, 4751-4754.

27. C. A. Cooper, R. J. Young, and M. Halsall, *Investigation into the deformation of carbon nanotubes and their composites through the use of Raman spectroscopy,* Compos. Part A, 2001, **32**, 401-411.

28. T. E. Chang, A. Kisliuk, S. M. Rhodes, W. J. Brittain, and A. P. Sokolov, *Conductivity and mechanical properties of well-dispersed single-wall carbon nanotube/polystyrene composite,* Polymer, 2006, **47**, 7740-7746.

29. T. J. Simmons, J. Bult, D. P. Hashim, R. J. Linhardt, and P. M. Ajayan, *Noncovalent functionalization as an alternative to oxidative acid treatment of single wall carbon nanotubes with applications for polymer composites,* ACS Nano, 2009, **3**, 865-870.

30. M. Mu, S. Osswald, Y. Gogotsi, and K. I. Winey, *An in situ Raman spectroscopy study of stress transfer between carbon nanotubes and polymer,* Nanotechnology, 2009, **20**, 335703 1-7.

31. C. C. Kao and R. J. Young, *Assessment of interface damage during the deformation of carbon nanotube composites,* J. Mater. Sci., 2010, **45**, 1425-1431.

Chapter 7   Carbon nanotube fibres

7.1 Introduction

Fibres made up of neat carbon nanotubes (CNTs) are expected to have excellent properties due to the extraordinary mechanical and electrical properties of their component elements. There are generally two methods to spin neat CNT fibres [1]: 1) spinning from lyotropic solutions of nanotubes and 2) solid state drawing from either vertical arrays of CNTs or directly from a furnace reactor. The CNT fibres spun using these techniques have a Young's modulus of typically a few GPa and the strength on the order of MPa [2-4], which are far lower than those of individual nanotubes.

The mechanical properties can be improved by optimizing the composition and structure of the fibres. In terms of the fibre composition, it was found that greater proportion of single-wall carbon nanotubes (SWNTs) in the fibre leads to higher modulus and strength [5]. As for the microstructure, the SWNT fibres spun from lyotropic solutions in super acids consist of highly-aligned fibrillar "super ropes", which results in a high modulus (130 GPa) but only a moderate strength (0.2 GPa) [2]. CNT fibres spun directly from the furnace reactor possess continuous network structure, and high modulus and strength have been achieved for these fibres [5]. The large voids within the fibres also provide access through which polymers can diffuse into, which gives rise to good bonding between the fibres and polymers [6].

A better understanding of the structure/property relationships for CNT fibres is required to fulfil the potential of nanotubes. Raman spectroscopy can provide unique information on the microstructure and deformation behaviour of CNT fibres. In this chapter, the composition and nanotube orientation of CNT fibres and the stress transfer both within the fibres and in composites were investigated using Raman spectroscopy.

7.2 Experimental

7.2.1 Materials

CNT fibres were supplied by Professor Windle's group in University of Cambridge. They were spun directly from an aerogel formed during synthesis of CNTs in a chemical vapour deposition (CVD) process, and the detailed procedure was described in Refs. [7, 8].

7.2.2 Characterisation

Raman spectra were obtained using a Renishaw 1000 system. Three lasers, with the wavelength of 514 nm, 633 nm and 830 nm were used to excite Raman scattering in the sample. The spectra were taken with a 50× objective lens which gives a laser spot size of 2 μm on the specimen. The laser power was ~1mW. The exposure time was set at 10 s and an accumulation of 5 times was used.

For deformation testing of single free-standing fibre, the home-made tensile rig shown in Figure 4.1 in Chapter 4 was used to stretch the paper card on which the fibre was mounted. The strain was recorded using a micrometre attached to the rig and the force applied to the fibre was recorded using a transducer.

To prepare poly(methyl methacrylate) (PMMA)/CNT composites, CNT fibres were placed on a PMMA beam and covered by a thin layer of PMMA by casting a dilute chloroform solution of PMMA (2wt%) onto the beam. The composites were then deformed using the four-point-bending rig shown in Figure 5.1 in Chapter 5.

A Philips XL30 FEG SEM was used to investigate the morphology of the CNT fibres. For SEM observation, the fibres were stuck to the stub and sputter coated with a thin layer of gold. SEM was operated with an accelerating voltage of 5 kV and images were acquired with a secondary electron mode.

7.3 Results and discussion

7.3.1 Structure of the fibres

The surface morphology and structure of the CNT fibres was examined using SEM

as shown in 7.1. The diameter is non-uniform and the cross-section is not always circular along the fibre, which makes it difficult to define the dimensions of the fibre. The internal structure consists of an oriented network of bundles, some that branch and rejoin [8]. The nanotube bundles have diameters typically in the range of 10 to 100 nm and can be tens of μm long. They are loosely stacked and a large free volume exists in the fibre, making the fibre extremely light (~0.4 g/km). Ma *et al.* also observed a network structure in their CVD-grown CNT fibres which have a modulus of 9-15 GPa and a strength of ~0.5 GPa [9]. They elucidated that the network structure formed during nanotube growth is important for the mechanical performance of the fibre: the fibre strength is dominated by the strength of the networks' junction rather than the straight nanotube bundles. The network structure could also play an important role in mechanical properties of the CNT fibres in this case.
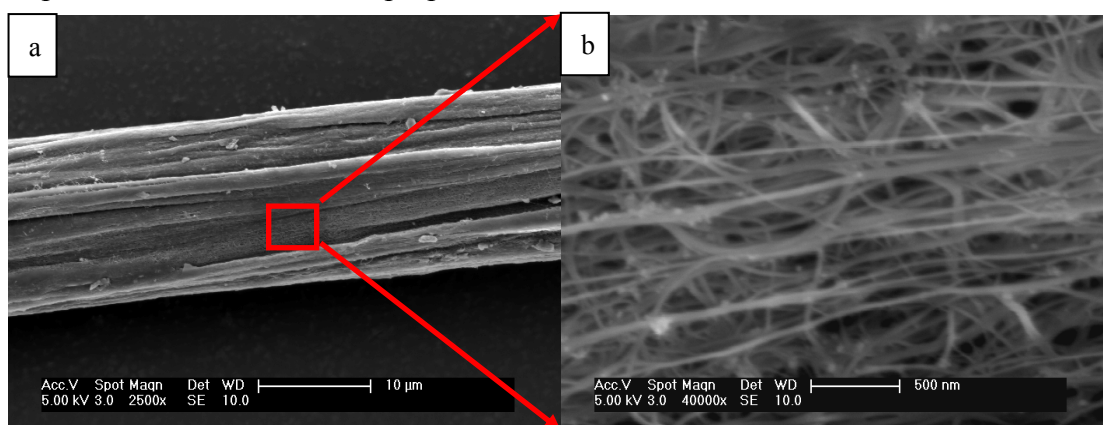
Figure 7.1 SEM images of a CNT fibre showing the network structure and orientation of nanotubes.

7.3.2 Raman spectra of the CNT fibres

A typical Raman spectrum obtained from a CNT fibre using a 633 nm laser is shown in Figure 7.2. Raman radial breathing mode (RBM) peaks in the frequency range of 142 - 262 cm^{-1} were observed at different locations in the fibre, which suggests the presence of SWNTs with the diameter ranging from 0.9 to 1.8 nm in the fibre (assuming a relation $\omega_{RBM} = 248/d_t$ for a rough estimation). The main peak of the G-band is located at 1586 cm^{-1} and a shoulder is seen on the higher-wavenumber side of this peak. It is known that the G-band frequency and lineshape for different

types of nanotubes are different: for SWNTs, the main peak is mostly located at 1591 cm^{-1} and other peaks are usually seen on the lower-wavenumber side; for double-wall carbon nanotubes (DWNTs) and multi-wall nanotubes (MWNTs), the main G-peak is generally found at 1586 - 1588 cm^{-1} and 1582 cm^{-1}, respectively, and side peaks are weak for both types of nanotube. The G-band observed in this case is possibly a composite feature of all types of nanotube. In fact, previous studies on these fibres using transmission electron microscopy (TEM) showed that the fibre consists of all types of nanotube but predominantly of collapsed DWNTs with an effective diameter greater than 5 nm [8].
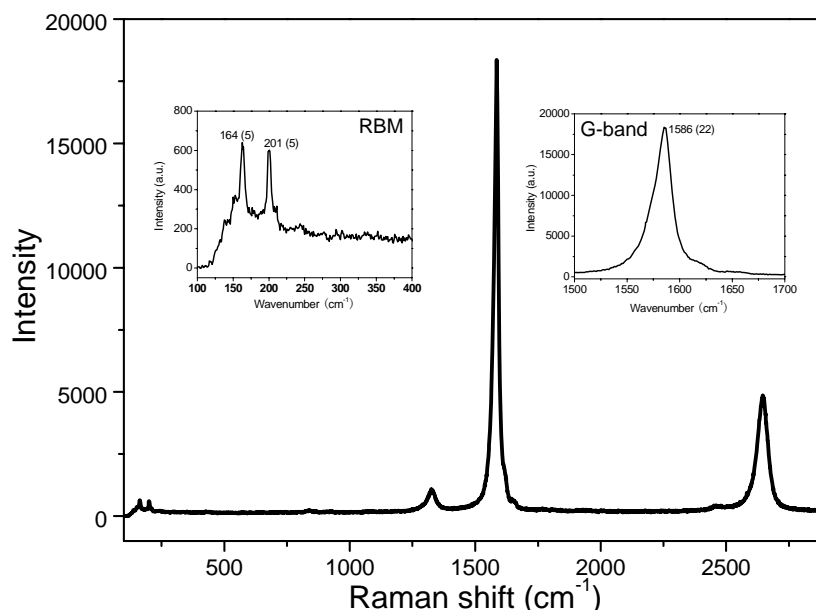
Figure 7.2 Typical Raman spectra obtained from the CNT fibre using a 633 nm laser. Inserts show the RBM peaks and G-band, and the numbers in parenthesis indicate the linewidth.

Figure 7.3 shows the RBMs and their corresponding G'-bands observed using different lasers. The G'-band shows single-peak structure in most cases but double-peak structure was also seen from some areas in the fibre. It is likely the double-peak G'-bands originate from DWNTs as the fibres consist of predominantly large DWNTs [8], but it is also possible that the double-peak strucutre is due to two types of nanotube both in resonance with the laser.
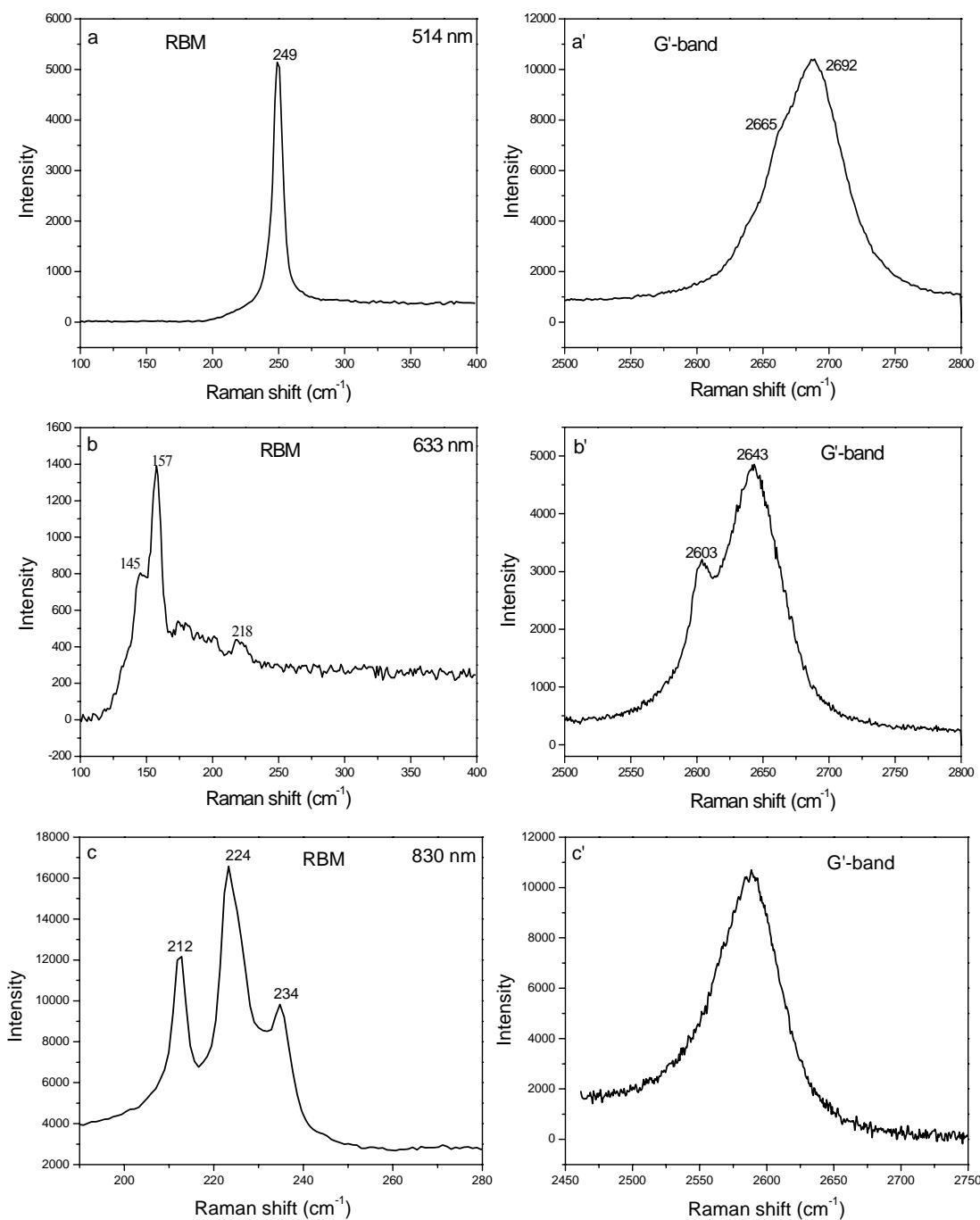
Figure 7.3 Raman spectra obtained using different lasers for the CNT fibres: (a) 514 nm, (b) 633 nm, and (c) 830 nm.

The assignment of chiralities of the RBM peaks observed in the CNT fibres are listed in Table 7.1. The E_{ii} values used for identification of the nanotube chirality were calculated using the tight-binding model developed by Lucas *et al.* [10]. There are several possible chiralities for some of the peaks and unique assignment was made using the additional information provided by the variation of the RBM intensity

during deformation, which will be discussed further in section 7.3.7.

Table 7.1 Assignment of chiralities of the RBM peaks observed from the CNT fibres.

Laser	ω_{RBM} (cm^{-1})	(n, m)	d_t (nm)[b]
Argon 514 nm	249	(10, 4)	1.00
	253	(11, 2)	0.98
	262	(12, 0)	0.95
He-Ne 633 nm	142	(15, 10), (16, 9), (19, 5)	1.75
	153	(20, 1)[a]	1.62
	156	(12, 11)[a]	1.59
	163	(18, 2), (19, 0)	1.52
	192	(12, 6)	1.29
	197	(13, 4)[a]	1.26
	212	(10, 7), (11, 5)	1.17
	217	(12, 3)[a]	1.14
IR 830 nm	193	(11, 7), (10, 8)	1.28
	212	(13, 2), (14, 0)	1.17
	222	(13, 2), (14, 0)	1.12
	231	(11, 4)	1.07
	236	(12, 1)	1.05

--a: The unique assignment was made considering the RBM intensity variation during deformation [10].

--b: The diameters were calculated using the equation: $\omega_{RBM} = 248/d_t$.

7.3.3 Distribution of the Raman bands along the fibres

The homogeneity of the fibres was investigated by scanning the laser along the fibre such that the Raman band frequencies were mapped out. Figure 7.4 shows the distribution of the band frequencies over a length of 250 μm. Different RBM peaks were observed from different areas and the G- and G'-band frequencies were found to scatter over a relatively broad range, again suggesting that the fibres are composites of

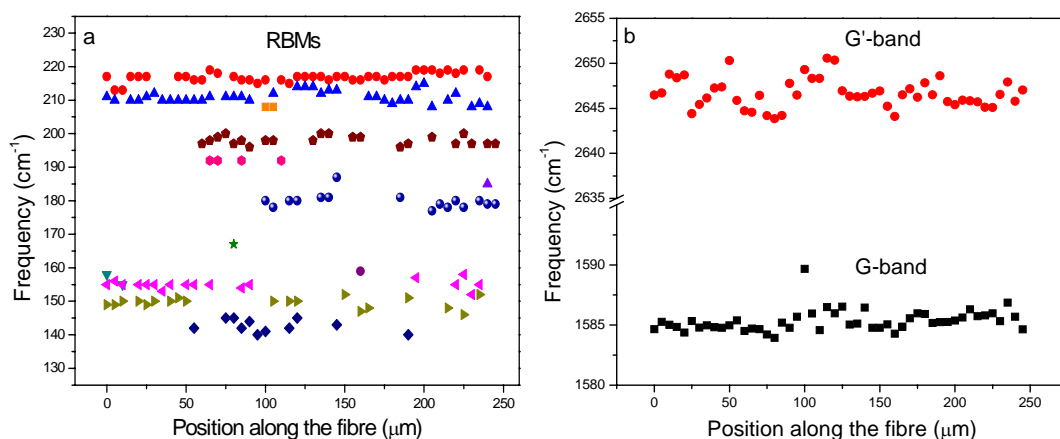different types of nanotube and vary in composition at different locations [8].

Figure 7.4 Distribution of the Raman bands in a CNT fibre examined using a 633 nm laser, showing the heterogeneous composition of the fibre.

7.3.4 Orientation analysis

The orientation of nanotubes in the fibres was characterised using polarized Raman spectroscopy with a VV configuration. The intensities of a RBM peak at 213 cm^{-1} and the G-band from the same spot were plotted as a function of the angle φ between the fibre axis and the axis of laser polarisation as shown in Figure 7.5. It can be seen the RBM peak intensity undergoes a sharper decrease than the G-band intensity when the angle increases from 0° to 90°. While the data points for the RBM peak fall close to the line generated for a $\cos^4\varphi$ function which is expected for perfect orientation [11], the data points for the G-band deviate from this function. The intensity ratio $I_{90°}/I_{0°}$ is 0.05 for the RBM peak and 0.29 for the G-band.

The difference in relative intensity of the RBM and G-band observed at different angles is due to that all types of nanotube (i.e. SWNTs, DWNTs and MWNTs) contribute to the G-band while only the SWNT contributes to the RBM peak. It is well established that for SWNT Raman bands that are resonantly enhanced, all the Raman bands lose their intensities to the same extent through the $I \propto \cos^4\alpha$ function when increasing the angle α (where α is the angle between the nanotube axis and the direction of laser polarisation, and this function can be replaced by $I \propto \cos^4\varphi$ when $\alpha \equiv \varphi$ which indicates the nanotubes are perfectly aligned along the fibre axis) [11, 12].

For MWNTs the G-band exhibits a maximum intensity at $\alpha = 0^{\circ}$, and a minimum intensity which is about 1/3 of the maximum intensity, is observed at $\alpha = 55^{\circ}$ [13]. The difference in the orientation-dependence of the Raman band intensity between these two types of nanotube is due to the strong relaxation of the depolarisation effect in MWNTs [13].

The dramatic drop of the RBM intensity at 90° shown in Figure 7.5c suggests a good orientation for this particular SWNT. Different degrees of alignment were, however, observed at different locations. In some areas the Raman band intensity remained almost constant when rotating the sample, which suggests a random distribution of the nanotubes. The heterogeneity of the nanotube orientation observed using Raman spectroscopy is consistent with the SEM observations.
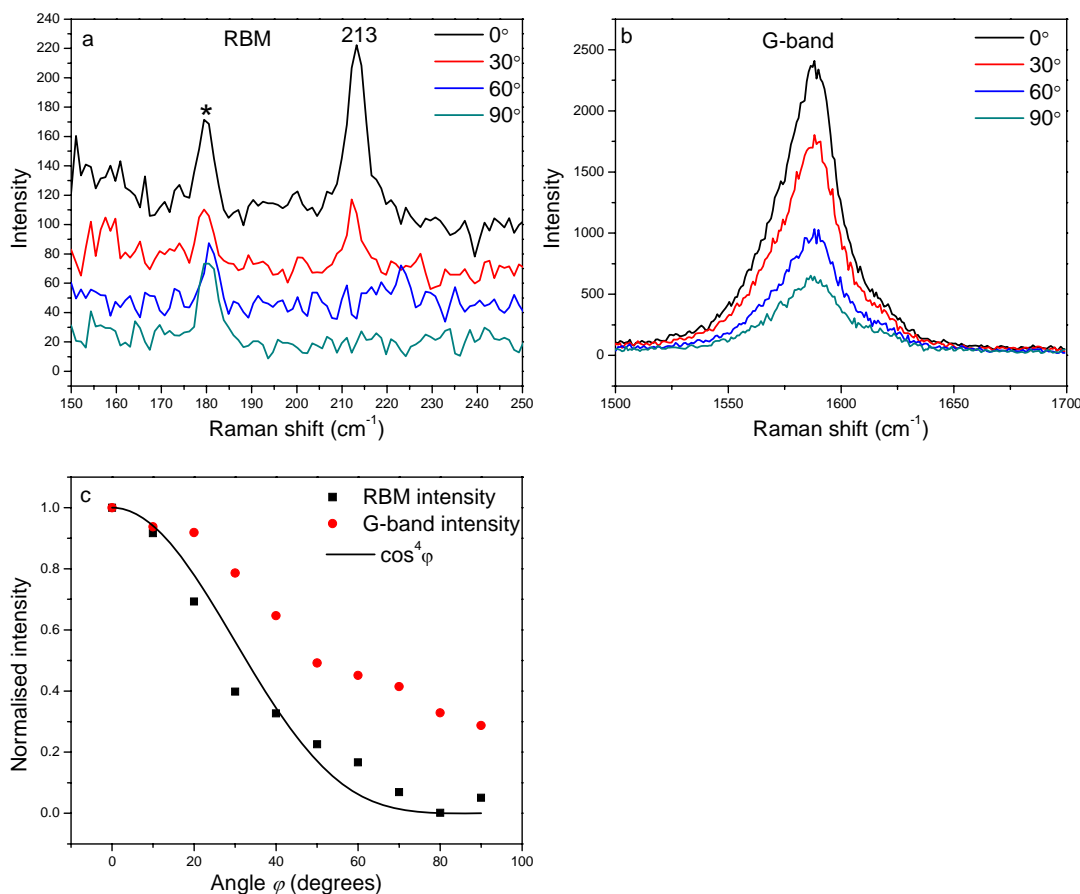

Figure 7.5 (a) RBM and (b) G-band at different fibre angles relative to the direction of laser polarisation. (c) Normalised RBM and G-band intensity as a function of the angle. The intensities are normalised to the intensity at 0°. The black line is generated with a function of $\cos^4 \varphi$. The star denotes the peaks from laser plasma lines.

7.3.5 Single fibre deformation

7.3.5.1 The response of G'-band

A single free-standing fibre was deformed using the tensile rig and the RBM peaks and the G'-band were followed during deformation as shown in Figure 7.6. The RBM peak served as a marker which helped to return to the same point in the fibre after applying the strain.

The G'-band was found to shift to lower wavenumber linearly with strain until the strain reached 0.6%, above which the shift rate became smaller and the band shift stopped when the strain exceeded 1%. The data were fitted approximately with a linear function in the low strain range (< 0.6%) and the initial slope was -23.3 cm^{-1}/%strain. The down-shift of the G'-band was accompanied with a broadening effect during tensile deformation, suggesting an uneven distribution of stress among the nanotubes probed.

The large Raman band shift rate is an indication of good stress transfer, which suggests the main effect of the strain applied to the fibre is to extend the nanotube bundles and not to induce free movement of the mesh. Ma *et al.* observed a similar deformation behaviour but with smaller Raman band shift rates for their SWNT films and fibres [14]. They ascribed the small band shift rates as a result of free movement of the meshes rather than axial extension of the nanotubes and suggested that the plateau stage of the band shift due to only the strongest junctions of the meshes bearing load at the high strains [14]. The high shift rate observed in this case is due to most nanotube bundles are preferentially aligned along the drawing direction and only a small fraction of the nanotubes entangled over the bundles to form the network as is indicated by the SEM images (Figure 7.1).

The decrease of G'-band shift rate with increasing strain is associated with different deformation mechanisms in different strain ranges, i.e. elastic deformation in the low strain range and plastic deformation at high strains. Typical stress-strain curves adapted from Ref. [8] for the fibres are shown in Figure 7.7, from which the elastic deformation and plastic deformation regions can be seen. Previous work by Motta *et al.* determined the maximum Young's modulus and tensile strength to be 60 N/tex

(~130 GPa assuming a density of 2.1 g/cm^3) and 1.1 N/tex (~2.1 GPa), respectively [8], while the average values for the modulus and strength were seen to be ~10 GPa and 0.6 GPa, respectively [5].
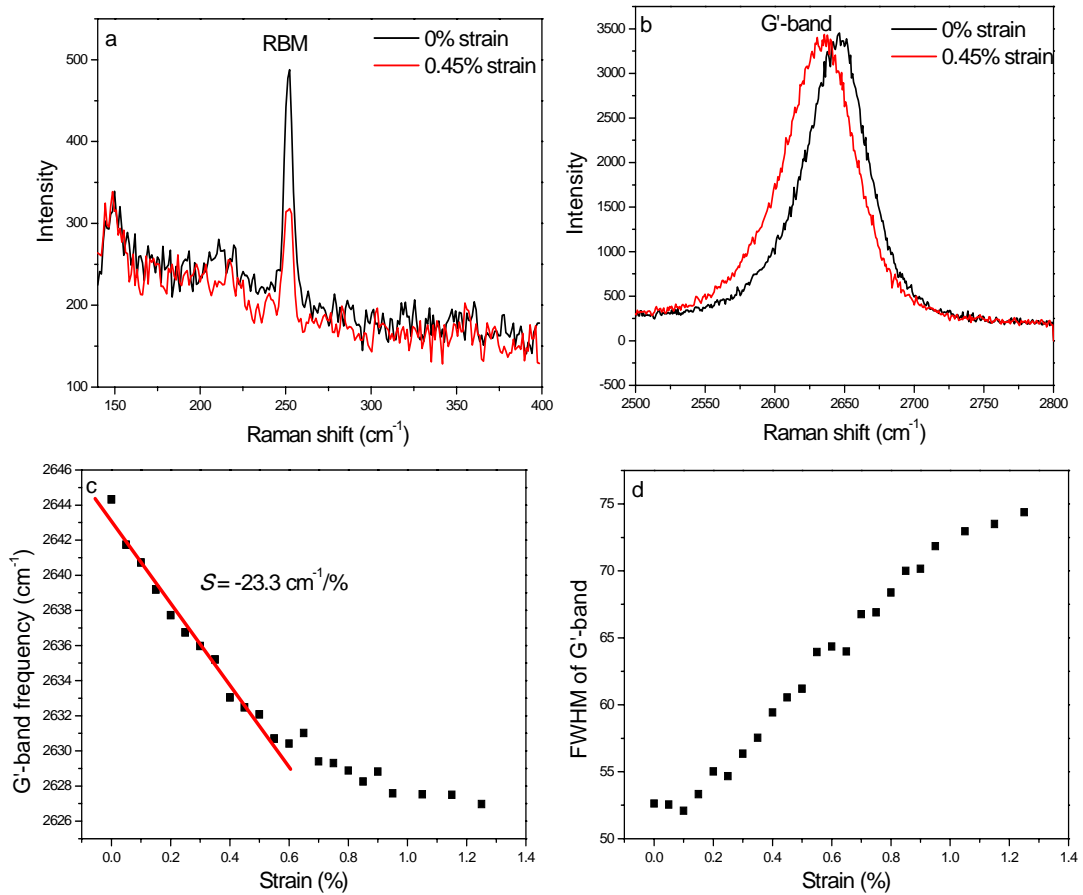

Figure 7.6 (a) RBM and (b) G'-band of the CNT fibre at different strains. (c) Variation of the G' frequency and (d) variation of the G' linewidth as a function of the fibre strain.
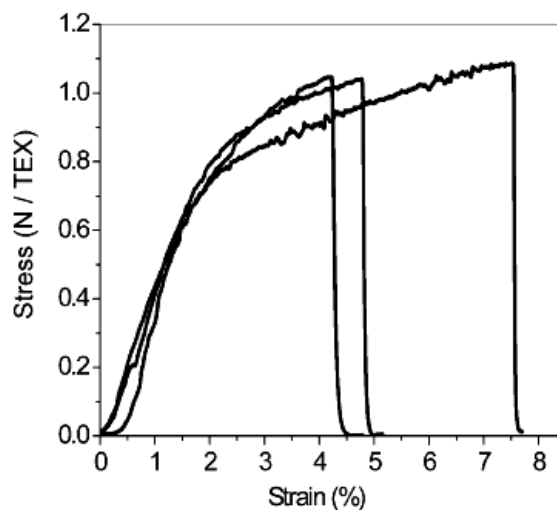

Figure 7.7 Typical stress-strain curves of the CNT fibres [8].

In the low strain range (0 - 2% strain in Figure 7.7), the nanotube bundles carry most of the load and the bundles extend linearly with the strain, giving rise to the elastic deformation behaviour. As the strain exceeds a certain point, some weak junctions break and nanotube bundles begin to slide over each other and only the relatively strong junctions carry the load, which results in the plastic deformation behaviour [9, 14]. Optical images of the fracture surface provide evidence of the intertube slippage during deformation as shown in Figure 7.8.
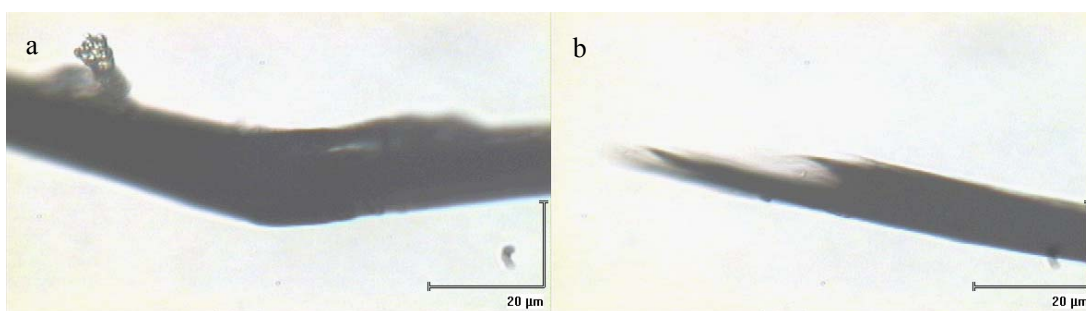
Figure 7.8 Optical micrographs of a strained CNT fibre showing the fracture process of the fibre.

The CNT fibres are composites of all types of nanotubes but the G'-band seen in Figure 7.6 is dominated by SWNTs due to the resonance enhancement. The large G'-band shift rate, of -23.3 cm^{-1}/%, suggests an effective modulus of at least 460 GPa for the SWNTs according to Equations (5.15) and (5.16) (in Chapter 5). Such a high nanotube modulus, however, results in only moderate fibre modulus. One possible reason is the volume fraction of high-modulus SWNT which are embedded in networks of low-modulus material such as MWNTs, is too low. Increasing the fraction of SWNTs in the fibres would improve the mechanical properties, which can be achieved by optimizing the processing conditions to favour the formation of SWNTs. One effective approach is to use a lower concentration of iron content and smaller particles in the feedstock, which has been demonstrated by Motta *et al.* in Ref. [5].

7.3.5.2 Stress distribution in the strained fibres

To assess the stress distribution in the fibres, the strain was halted during deformation and the G'-band frequency was measured at different locations. Figure

7.9a shows the variation of the G'-band frequency as a function of the fibre strain. In this sample, a shift rate of -23.8 cm^{-1}/% was determined in the low strain range. It was observed that after fracture of the fibre, the G'-band shifted back to around 2645 cm^{-1}, which is about 4 cm^{-1} higher than the average initial G'-band frequency prior to deformation. This suggests the initial fibre had a residual tension of ~0.17% strain before applying any load.

The G'-band frequencies acquired from 15 random points in the strained fibre at different strains are shown in Figure 7.9b. The strain levels for the curves are 0%, 0.17%, 0.67% and 1.17% from the top to the bottom. The values of strain in Figure 7.9b have been corrected to take into account the residual tension in the fibre. It can be seen the G'-band frequency scatters over a relatively large range when the fibre is deformed, suggesting a non-uniform distribution of stress, which is thought to be related to the heterogeneous composition and structure of the fibre.
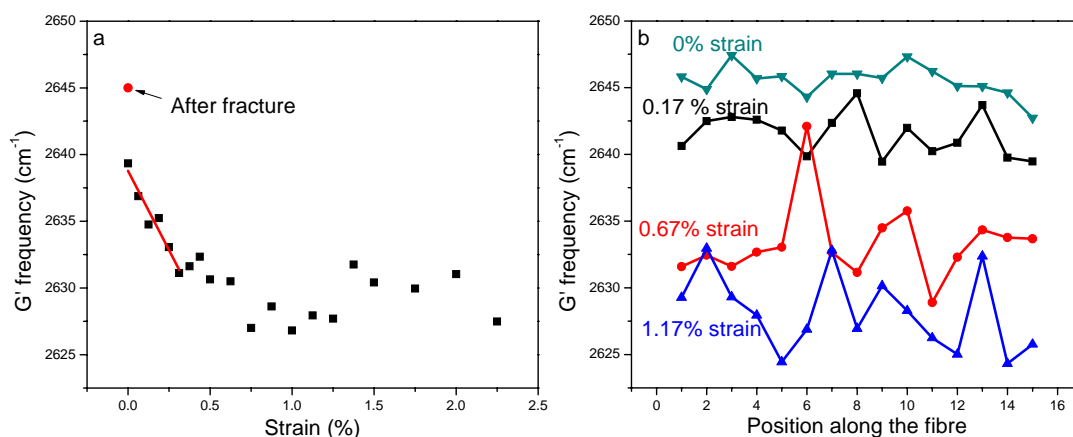
Figure 7.9 (a) The G'-band frequency as a function of the fibre strain. (b) Distribution of the G'-band frequency in a single CNT fibre at different strain levels.

The stress distribution was quantified by the standard deviation of the G'-band frequency as listed in Table 7.2. It can be seen the standard deviation increases with the increase of strain, which indicates the stress is more unevenly distributed at higher strains. The stress concentration in fibres is possibly responsible for the relatively low fibre strength, which can be overcome by making a more uniform composition and structure for the fibre.

Table 7.2 Distribution of the G'-band frequency along the fibre at different strain levels.

	0% strain	0.17% strain	0.67% strain	1.17% strain
Mean value (cm^{-1})	2646	2642	2633	2628
Standard deviation (cm^{-1})	1.2	1.6	2.9	2.9

7.3.6 PMMA/CNT fibre composites

To investigate the stress transfer in PMMA/CNT fibre composites, the CNT fibres were placed on a PMMA beam and covered with a PMMA solution. The fibres were effectively embedded in the polymer matrix after drying and the composites were then deformed using a four-point bending rig. Figure 7.10 shows the G'-band frequency as a function of the strain in both tension and compression. The deformation behaviour is similar to the free-standing fibre but a larger band shift rate is observed in the composite. The band shift rate, of -33.6 cm^{-1}/%strain, is exceptionally high and approaches the largest band shift rate (-37.5 cm^{-1}/%) for individual nanotubes reported to date [16]. The large Raman band shift rate observed here is an indication of high efficiency of stress transfer from the matrix to the CNT fibre and is probably due to the infiltration of PMMA into the fibre such that mechanical interlocks form in the composites. Mora *et al.* demonstrated that uncured epoxy can diffuse into voids within the fibre structure, giving rise to large interface areas in the composites [6]. They observed that the composite failed through nanotube bundle pull-out rather than through fibre pull-out. It was found the pulled out bundles were covered by epoxy, suggesting good adhesion between the two phases [6] and this could also occur for the PMMA/CNT fibre composites. The strong interfacial adhesion which originates from the mechanical interlocks is beneficial for mechanical performance of the composites.
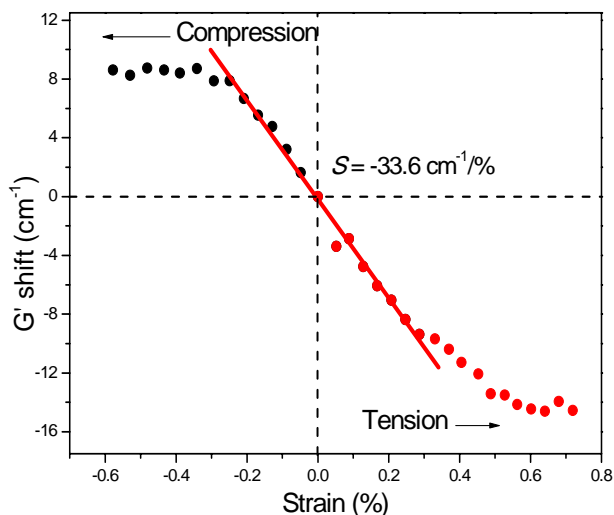
Figure 7.10 Variation of the G'-band frequency as a function of strain for the PMMA/CNT fibre composite.

The strain applied to the composite was decreased and the Raman bands were followed to examine the reversibility of the deformation process. Figure 7.11 shows the variation of the frequency and linewidth of the G'-band under a cyclic loading. When the strain recovers back from 0.6% at which interfacial sliding has been partially activated, the G'-band returns in a different path such that hysteresis is observed. After being fully unloaded from 0.6% strain, the G'-band is about 2.2 cm^{-1} higher than its original pre-strain position which is due to the friction between the mismatched nanotube and matrix. The G'-band linewidth displays a similar behaviour, i.e. it reverts back when the strain is released but it is slightly higher than its original pre-strain value when fully unloaded. This suggests the deformation within this strain range is generally reversible but the interface is gradually damaged during cyclic loading.

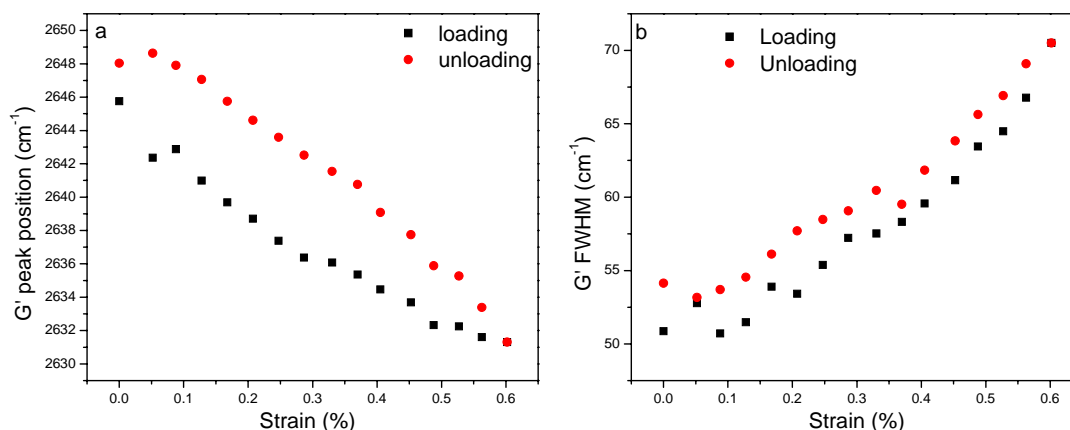*Figure 7.11 Variation of the: (a) G'-band frequency and (b) linewidth during cyclic loading.*

7.3.7 Effect of deformation on the RBM intensity

The RBM intensity was found to vary during deformation of the CNT fibres, with the variation trend and magnitude depending on the nanotube chirality. For example, the 153 cm^{-1} and 163 cm^{-1} peaks increase in intensity while the 217 cm^{-1} peak intensity decreases during tensile deformation as shown in Figure 7.12. The intensity variation is due to the strain-induced modification of electronic structure of the nanotubes. Deformation can bring the electronic transition energy (E_{ii}) of nanotubes closer to or further away from the excitation energy of the laser, which results in an increase and decrease of the RBM intensity, respectively. This provides valuable information on electronic structure which helps to assign the nanotube chirality of the RBMs. For example, there are two possible candidates, the (15, 8) and (20, 1) nanotubes for the 153 cm^{-1} peak, if one considers only the nanotube diameter and the E_{33} energy. The response of E_{33} energy to the strain for these two nanotubes is different, however, as shown in Figure 7.12e (the E_{33} energies were calculated using the tight binding model considering the nearest-neighbour interaction (TB1), following Lucas's method [10]). It can be seen the E_{33} energy of the (15, 8) nanotube moves further away from the E_{laser} upon deformation while that of the (20, 1) nanotube moves closer to E_{laser}, from which a decrease and increase of the RBM intensity is expected for these two nanotubes, respectively. The (20, 1) nanotube shows a behaviour consistent with the experimental observation and is therefore

assigned to the 153 cm^{-1} peak. Using this method, some other RBM peaks were assigned uniquely and the results are listed in Table 7.1. The assignment of nanotube chiralities is helpful in understanding the electronic properties of the CNT fibre, although the actual properties are beyond the scope of this study.
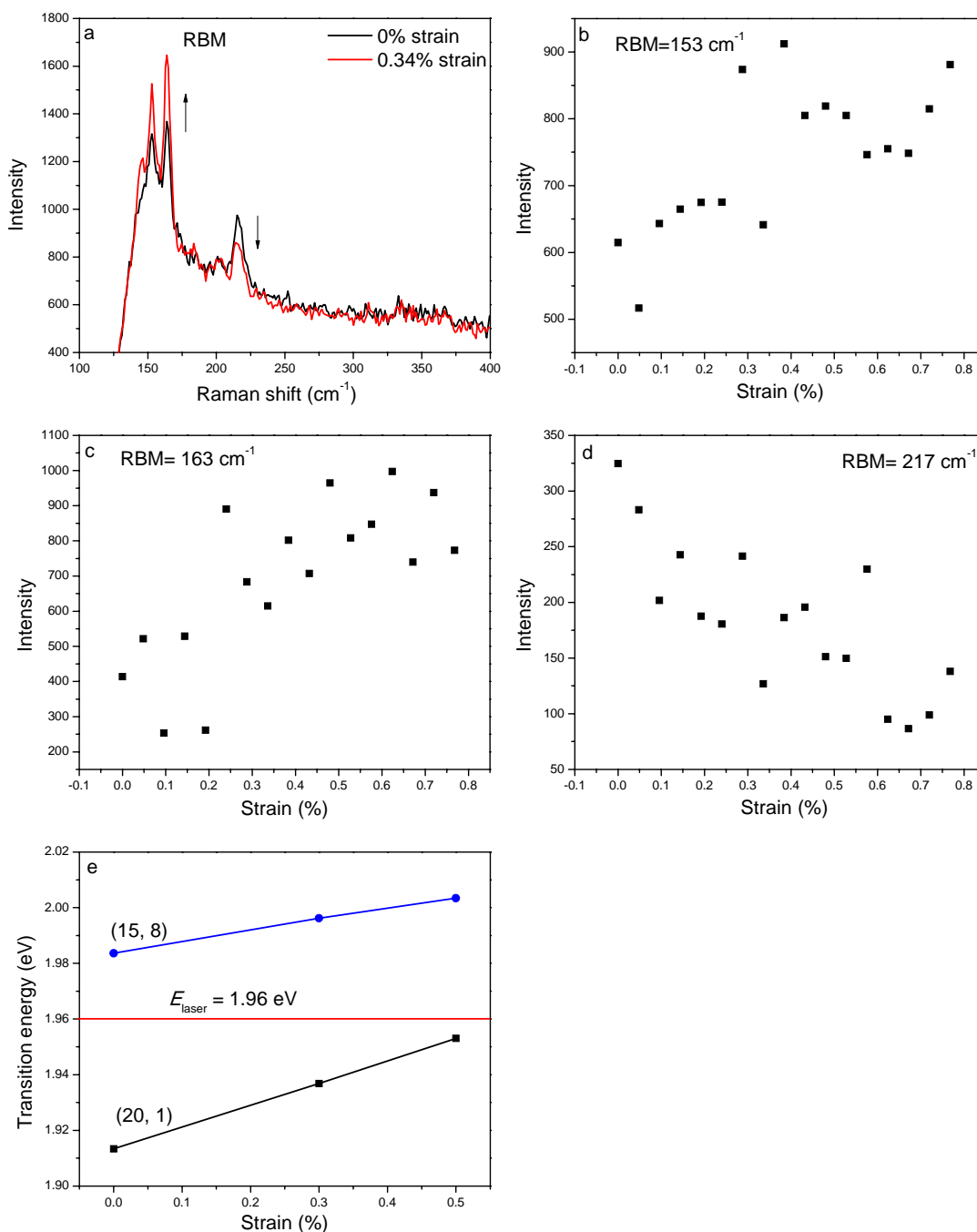

Figure 7.12 (a) RBMs of the CNT fibre at different strains. (c)-(d) Variation of the RBM intensity as a function of strain. (e) Variation of the E_{33} energies for two (n, m) nanotube species as a function of strain. The red line indicates the energy of the excitation laser.

Finally, it is interesting to compare the structure and properties of CNT fibres with those of polymer fibres as nanotubes can be considered as essentially a rigid rod polymer [1]. Fibres based on rod-like and rigid rod polymers such as poly(p-phenylene terephthalamide) (PPTA) and poly(p-phenylene benzobisoxazole) (PBO) are characterised as high-performance fibres and have fibrillar structures. The individual fibril possesses a diameter of a few hundred nm and a length of 200 - 400 nm and the microfibrils are highly aligned along the fibre axis [1]. The CNT fibres spun from an acid solution have a fibrillar structure analogous to that of PBO fibres [1, 2] and have a relatively high modulus (120 GPa) [2]. The fibres used in this study which were spun directly from the CVD furnace, however, possess a network structure which is apparently different from the structure of polymer fibres. The loose stacking of nanotubes and weak interbundle interaction in the CNT fibres result in poor mechanical properties as compared to commercial PPTA and PBO fibres. On the other hand, the porous structure allows the infiltration of polymers into the CNT fibres which enhance the efficiency of stress transfer from the polymer matrix to the CNT fibres.

7.4 Conclusions

The microstructure and micromechanical process of CNT fibres were investigated using Raman spectroscopy. It was found the fibres consist of both SWNTs and MWNTs and vary in composition in different areas. The fibres exhibit good efficiency of interbundle stress transfer and the stress is unevenly distributed in the fibre due probably to the heterogeneous composition and structure. Increasing the fraction of SWNTs in the fibres would improve the mechanical properties, which can be achieved by optimizing the processing conditions to favour the formation of SWNTs. On the other hand, the the large free volume in the fibre provides access for mechanical interlocking between the fibre and the polymers, which results in an exceptionally-high efficiency of stress transfer in PMMA/CNT fibre composites and suggests the promising potential of CNT fibres in reinforcing polymers.

7.5 References

1. M. J. Green, N. Behabtu, M. Pasquali, and W. W. Adams, *Nanotubes as polymers,* Polymer, 2009, **50**, 4979-4997.

2. L. M. Ericson, H. Fan, H. Q. Peng, V. A. Davis, W. Zhou, W. F. Hwang, R. H. Hauge, J. E. Fischer, and R. E. Smalley, *Macroscopic, neat, single-walled carbon nanotube fibers,* Science, 2004, **305**, 1447-1450.

3. K. Jiang, Q. Li, and S. Fan, *Nanotechnology: Spinning continuous carbon nanotube yarns,* Nature, 2002, **419**, 801-801.

4. M. Zhang, K. R. Atkinson, and R. H. Baughman, *Multifunctional carbon nanotube yarns by downsizing an ancient technology,* Science, 2004, **306**, 1358-1361.

5. M. Motta, Y. L. Li, I. A. Kinloch, and A. H. Windle, *Mechanical properties of continuously spun fibers of carbon nanotubes,* Nano Lett., 2005, **5**, 1529-1533.

6. R. J. Mora, J. J. Vilatela, and A. H. Windle, *Properties of composites of carbon nanotube fibres,* Compos. Sci. Technol., 2009, **69**, 1558-1563.

7. Y. L. Li, I. A. Kinloch, and A. H. Windle, *Direct spinning of carbon nanotube fibers from chemical vapor deposition synthesis,* Science, 2004, **304**, 276-278.

8. M. Motta, A. Moisala, I. A. Kinloch, and A. H. Windle, *High performance fibres from dog bone carbon nanotubes,* Adv. Mater., 2007, **19**, 3721-3726.

9. W. Ma, L. Liu, Z. Zhang, R. Yong, P. M. Ajayan, and S. Xie, *High-Strength Composite Fibers: Realizing True Potential of Carbon Nanotubes in Polymer Matrix through Continuous Reticulate Architecture and Molecular Level Couplings,* Nano Lett., 2009, **9**, 2855-2861.

10. M. Lucas, *Effect of deformation upon the intensity of the Raman radial breathing modes of single-wall carbon nanotubes in epoxy/SWNT composites,* PhD Thesis, University of Manchester, 2005.

11. J. Hwang, H. H. Gommans, A. Ugawa, H. Tashiro, R. Haggenmueller, K. I. Winey, J. E. Fischer, D. B. Tanner, and A. G. Rinzler, *Polarized spectroscopy of aligned single-wall carbon nanotubes,* Phys. Rev. B, 2000, **62**, R13310-R13313.

12. H. H. Gommans, J. W. Alldredge, H. Tashiro, J. Park, J. Magnuson, and A. G.

Rinzler, *Fibers of aligned single-walled carbon nanotubes: Polarized Raman spectroscopy,* J. Appl. Phys., 2000, **88**, 2509-2514.

13. A. M. Rao, A. Jorio, M. A. Pimenta, M. S. S. Dantas, R. Saito, G. Dresselhaus, and M. S. Dresselhaus, *Polarized Raman study of aligned multiwalled carbon nanotubes,* Phys. Rev. Lett., 2000, **84**, 1820-1823.

14. W. Ma, L. Liu, T. Zhang, and S. Xie, *Monitoring a micromechanical process in macroscale carbon nanotube films and fibers,* Adv. Mater., 2008, **20**, 1-6.

15. S. Cui, I. A. Kinloch, R. J. Young, L. Noé, and M. Monthioux, *The effect of stress transfer within double-walled carbon nanotubes upon their ability to reinforce composites,* Adv. Mater., 2009, **21**, 3591-3595.

16. S. B. Cronin, A. K. Swan, M. S. Ünlü, B. B. Goldberg, M. S. Dresselhaus, and M. Tinkham, *Resonant Raman spectroscopy of individual metallic and semiconducting single-wall carbon nanotubes under uniaxial strain,* Phys. Rev. B, 2005, **72**, 035425 1-8.

Chapter 8   Conclusions and suggestions for future work

8.1 Conclusions

8.1.1 Electrospinning of PVA and PVA/SWNT

Electrospinning is a complex process which is influenced by a large variety of parameters. Smooth and circular PVA and PVA/SWNT fibres can be spun in a broad range of conditions, i.e. with a PVA concentration of 6 - 14%, a voltage of 10 - 25 kV, and a tip-to-collector distance of 6 - 20 cm. It was demonstrated among the four processing conditions (polymer concentration, electric voltage, tip-to-collector distance and nanotube concentration) considered, the polymer concentration had the most significant effect on fibre diameter.

Macroscopically-aligned fibres were collected using both electrostatic and mechanical methods. A pair of parallel electrodes sitting on an insulator substrate can direct the electric field such that isolated fibres spanning over a paper frame can be obtained. A rotating disk which makes use of the tangential force on its sharp edge was also found to align the fibres efficiently.

8.1.2 Raman spectroscopy of individual SWNTs

Single RBM peaks were observed from electrospun PVA/SWNT fibres, which enabled the properties of nanotubes of single chirality to be monitored. It was found the features (including the frequency, intensity and linewidth) of Raman spectra of individual nanotubes were significantly different from those of nanotube bundles.

The RBM frequencies of nanotubes in electrospun fibres were similar to those in SDS/SWNT/water solutions and were up-shifted by 1 - 6 cm^{-1} relative to those in nanotube bundles in air. When using the 785 nm laser, single RBM peaks were observed and the "roping in" 267 cm^{-1} peak was absent, which is strong evidence that nanotubes have been isolated in the fibres. Chiralities were assigned to all of the RBM peaks observed in the electrospun fibres using an experimental Kataura plot.

As for the G-band, the G^+ peak became narrower which had a typical linewidth of 9 cm^{-1} and the G^- peak became weaker in most cases. Debundling of nanotubes was also

shown to reduce the G'-band linewidth. When a single RBM peak was seen, the G'-band exhibited either a single peak or more prevalently a double-peak structure. The double-peak structure was explained that along with the nanotube in incident resonance, there was another group of nanotubes in resonance with the scattered G'-photon. For the five semiconducting nanotubes that are in resonance with the 633 nm laser, the G'-band frequency increased with increasing diameter, which is thought to be related to the increase of E_{22} with nanotube diameter.

Orientation of nanotubes was characterised using polarized Raman spectroscopy. A dramatic decrease of the G-band intensity was observed when rotating the fibre from 0° to 90° with respect to the axis of laser polarisation, suggesting good orientation of the nanotubes in the electrospun fibres.

Tensile strain was applied to the nanotubes by stretching the electrospun fibres. The RBM frequency was found to be constant and the intensity scattered with no clear trend with strain. The G' shift per unit strain was found to be different for different chiralities. One possible reason for the different shift rates is the non-uniform distribution of stress along each individual nanotube. To compare the Raman band shift rate among different chiralities, as well as for efficient mechanical reinforcement would require nanotubes to be sufficiently long so that the stress is uniformly distributed in majority of a single nanotube. The minimum length was estimated to be roughly 5 μm assuming an IFSS of 50 MPa.

8.1.3 Orientation-dependence of the Raman band shift rate

PVA/SWNT composite films were produced by solution casting and composite fibres were fabricated by both electrospinning and coagulation spinning.

The electrospinning process can debundle the nanotubes efficiently and exerts a small residual compression of the nanotubes in the fibre. Polarized Raman spectroscopy showed that the nanotubes are highly aligned and the polymer molecules are partially aligned along the axis of the electrospun fibres. Crystallinity of the PVA polymer was characterised by the intensity ratio I_{1147}/I_{1127} and it was found that nanotubes do not nucleate the PVA to crystallise significantly in the composite film

whereas the crystallinity increases upon electrospinning. Mechanical testing of the neat and composite films showed that the modulus of PVA is increased by 21% and the tensile strength is improved by 16% by adding 0.2% of HiPco SWNTs.

Large Raman band shift rates were observed in the composite films and electrospun fibres and it was found that the shift rate depends strongly on the angle between the nanotube axis, strain axis and the axis of laser polarisation. For randomly-distributed nanotubes, the Raman band shift rates obtained at different angles were fitted with a quantitative model considering both the Poisson's contraction effect and the orientation dependence of Raman band intensity. For highly-aligned nanotubes such as in the electrospun fibres and coagulation-spun fibres with high draw ratios, the angular-dependence of Raman band shift was explained with the Poisson's contraction effect. While for partially-aligned nanotubes such as in the undrawn coagulation-spun fibres, the shift rate-angle curve lies in somewhere between the curves for perfect orientation and that for random distribution. A model which correlates the Raman band shift rate with the effective modulus of nanotubes was also established. The calculated effective modulus, in turn, allows the estimation of the composite modulus and it was found that the composite modulus estimated using this method is consistent with the experimental data.

8.1.4 PPTA/SWNT composite fibres

A case study with PPTA/SWNT composite fibres using Raman spectroscopy revealed the effect of dispersion and orientation of nanotubes and the interfacial adhesion on mechanical properties of the composite fibres. Dispersion of nanotubes on the micron scale was assessed by mapping the Raman intensity along the fibre, while the dispersion on the nanoscale was examined by close inspection of the RBMs and G'-band and the fracture surface. Improvement in the modulus was observed in the composite fibres with a DR of 2 compared to the neat PPTA fibres with the same DR, but the mechanical properties of the composite fibres with higher DRs are poorer than those of the neat fibres. Orientation analysis showed that the incorporation of nanotubes improves the orientation of polymers for fibres with a DR of 2 but degrades

the matrix orientation at higher DRs. The change of orientation of polymers has direct effect on mechanical properties of the composite fibres.

In-situ Raman spectroscopy study during fibre deformation revealed good stress transfer from the matrix to nanotubes in the small strain range and the interface fails when the strain exceeds 0.6%. Cyclic loading on the fibres indicated reversible deformation within the strain range of 0 - 0.2% and a gradual breakdown of the interface when subjected to higher strains. The interfacial failure in the first loading cycle is more significant for the fibres with higher DRs than for lower DR fibres.

8.1.5 Carbon nanotube fibres

The microstructure and micromechanical process of CNT fibres were investigated using Raman spectroscopy. It was found the fibres consist of both SWNTs and MWNTs and vary in composition in different areas. The fibres exhibit good efficiency of interbundle stress transfer and the stress is unevenly distributed in the fibre due probably to the heterogeneous composition and structure. Increasing the fraction of SWNTs in the fibres would improve the mechanical properties, which can be achieved by optimizing the processing conditions to favour the formation of SWNTs. On the other hand, the the large free volume in the fibre provides access for mechanical interlocking between the fibre and the polymers, which results in an exceptionally-high efficiency of stress transfer in PMMA/CNT fibre composites and suggests the promising potential of CNT fibres in reinforcing polymers.

8.2 Suggestions for future work

8.2.1 Chirality-dependence of the Raman band shift

In this work, investigation of the effect of nanotube chirality on the stress-induced Raman band shift was undertaken by exfoliating nanotube bundles into individual ones. This method brings uncertainty in nanotube length and requires tedious search for individual nanotubes due to the low loading. A recent work demonstrated that HiPco SWNTs which are mixtures of nanotubes of different chiralities can be readily

sorted to give fractions enriched in different (n, m) species using a density-gradient ultracentrifugation process [1]. Using this separation method, nanotubes of single chirality can be incorporated into polymer nanofibres. This allows the nanotube length to be pre-measured before embedding into the polymers and ensures the Raman signal to be collected from a single chirality in the composite nanofibres, which would make the study of the effect of nanotube chirality on the stress-induced Raman band shift more reliable. Raman spectroscopy equipped with a tuneable laser would be needed to bring different (n, m) species in resonance so that nanotubes with different chiralities can be monitored.

8.2.2 Interlayer stress transfer in double-wall nanotubes

Double-wall nanotubes (DWNTs), the thinnest MWNTs, provide an ideal model material for investigation of the interaction between the coaxial graphene layers and the shielding effect of outer wall on their inner structure. Cui *et al.* demonstrated that the efficiency of stress transfer from the outer wall to the inner wall during deformation was rather poor [2]. The DWNTs used in their work had the outer walls greater than 1.2 nm and relatively large inner walls. A recent work showed that very small nanotubes (the smallest nanotube observed was a (5, 0) nanotube which had a diameter of 0.41 nm) can be grown inside HiPco SWNTs which have an average diameter of 1.1 nm [3]. It would be interesting to investigate the interlayer stress transfer in such small DWNTs and to compare the efficiency of interlayer stress transfer in DWNTs that have different outer wall diameters. To carry out this investigation, a tuneable laser would be needed to bring both the outer wall and inner wall in resonance simultaneously.

8.2.3 High-performance polymer/SWNT fibres

It has been shown that PBO/SWNT composite fibres prepared by in-situ polymerization have promising mechanical properties [4]. It would be interesting to study the high-performance PBO/SWNT fibre using the methods demonstrated in this project. For exapmle, to determine the effective modulus of nanotubes in the fibre by

measuring the stress-induced Raman band shift rate, to investigate the effects of dispersion and orientation of nanotubes on the mechanical performance of the composite fibres and to assess the interfacial strength by monitoring the onset of interfacial slippage.

8.2.4 Graphene composites

Single-layer graphene sheets are one-atom-thick two-dimensional layers of sp^2-bonded carbon. They were first discovered in 2004 and are now attracting increasingly attention. Investigations on this novel and amazing material are still at the starting line and there are some aspects to be exploited in the framework of graphene composites: 1) The structural aspects of graphene are of great importance and microscopic corrugations have been observed for most suspended and supported graphene sheets [5]. Chen et al. applied heat treatment to introduce compression on the graphene and employed Raman spectroscopy to study the mechanism of ripple formation [6]. An alternative way to apply compression loading to the graphene sheets is to bend them using a four-point bending rig which gives more precise strains, rippling of the graphene can therefore be investigated. 2) It is important to determine the edge chirality and crystal orientation of the graphene [7]. This can be undertaken by studying the orientation-dependence of Raman band shift (particularly the G^+ and G^- peaks) during deformation of the graphene, similar to the work described in Chapter 5. The deformation testing carried out at different angles and polarisation configurations not only reveals the interfacial stress transfer in the graphene composites, but also enables the electronic structures of graphene to be probed. 3) It might also be interesting to exfoliate the graphite flakers into graphene sheets by electrospinning, through which rolling and curvature effect of the graphene sheets in the nanofibres would possibly be observed.

8.3 References

1. S. Ghosh, S. M. Bachilo and R. B. Weisman, *Advanced sorting of single-walled*

carbon nanotubes by nonlinear density-gradient ultracentrifugation, Nature Nanotech., 2010, **5**, 443-450.

2.   S. Cui, I. A. Kinloch, R. J. Young, L. Noé and M. Monthioux, *The effect of stress transfer within double-walled carbon nanotubes upon their ability to reinforce composites,* Adv. Mater., 2009, **21**, 3591-3595.

3.   W. Plank, R. Pfeiffer, C. Schaman, H. Kuzmany, M. Calvaresi, F. Zerbetto and J. Meyer, *Electronic structure of carbon nanotubes with ultrahigh curvature,* ACS Nano, 2010, **4**, 4515-4522.

4.   S. Kumar, T. D. Dang, F. E. Arnold, A. R. Bhattacharyya, B. G. Min, X. F. Zhang, R. A. Vaia, C. Park, W. W. Adams, R. H. Hauge, R. E. Smalley, S. Ramesh and P. A. Willis, *Synthesis, structure, and properties of PBO/SWNT composites*, Macromolecules, 2002, **35**, 9039-9043.

5.   C. H. Lui, L. Liu, K. F. Mark, G. W. Flynn and T. F. Heinz, *Ultraflat graphene,* Nature, 2009, **462**, 339-341.

6.   C. C. Chen, W. Bao, J. Theiss, C. Dames, C. N. Lau and S. B. Cronin, *Raman spectroscopy of ripple formation in suspended graphene,* Nano Lett., 2009, **9**, 4172-4176.

7.   C. Cong, T. Yu and H. Wang, *Raman study on the G mode of graphene for determination of edge orientation,* ACS Nano, 2010, **4**, 3175-3180.